

NEW TECHNIQUES FOR PRECISION ATOM
INTERFEROMETRY AND APPLICATIONS TO FUNDAMENTAL
TESTS OF GRAVITY AND OF QUANTUM MECHANICS

A DISSERTATION
SUBMITTED TO THE DEPARTMENT OF PHYSICS
AND THE COMMITTEE ON GRADUATE STUDIES
OF STANFORD UNIVERSITY
IN PARTIAL FULFILLMENT OF THE REQUIREMENTS
FOR THE DEGREE OF
DOCTOR OF PHILOSOPHY

Tim Kovachy
May 2016

© 2016 by Timothy Light Kovachy. All Rights Reserved.
Re-distributed by Stanford University under license with the author.



This work is licensed under a Creative Commons Attribution-
Noncommercial 3.0 United States License.
<http://creativecommons.org/licenses/by-nc/3.0/us/>

This dissertation is online at: <http://purl.stanford.edu/fv109wq1863>

I certify that I have read this dissertation and that, in my opinion, it is fully adequate in scope and quality as a dissertation for the degree of Doctor of Philosophy.

Mark Kasevich, Primary Adviser

I certify that I have read this dissertation and that, in my opinion, it is fully adequate in scope and quality as a dissertation for the degree of Doctor of Philosophy.

Peter Graham

I certify that I have read this dissertation and that, in my opinion, it is fully adequate in scope and quality as a dissertation for the degree of Doctor of Philosophy.

Leo Hollberg

Approved for the Stanford University Committee on Graduate Studies.

Patricia J. Gumpert, Vice Provost for Graduate Education

This signature page was generated electronically upon submission of this dissertation in electronic format. An original signed hard copy of the signature page is on file in University Archives.

Abstract

Light-pulse atom interferometry—in which quantum mechanical atomic wave packets are split along two paths and later recombined and made to interfere by sequences of optical pulses—is a remarkably sensitive technique for measuring inertial forces, allowing it to be a valuable tool for applications ranging from fundamental tests of gravity to geodesy and inertial navigation. The inertial sensitivity of an atom interferometer is proportional to its enclosed spacetime area—that is, the product of the spatial separation between the two interferometer paths and the interferometer duration. Therefore, new techniques that allow this spacetime area to be increased are essential in order for atom interferometry to reach its full potential. In this thesis, I describe the development of such techniques.

We approach the problem of increasing the interferometer spacetime area on two fronts. First, we implement new methods to increase the momentum transferred by the beam splitters of the interferometer. The velocity difference and therefore the spatial separation of the interferometer paths are proportional to this momentum transfer. Conventional atom optics techniques involve beam splitters that transfer two photon momentum recoils ($2\hbar k$) to the atoms. I will discuss our realization of large momentum transfer (LMT) beam splitters that transfer up to $100\hbar k$. Second, we have built a 10 m tall atomic fountain that allows the total interferometer duration to be increased to 2 s. Ultimately, we combined LMT atom optics with long-duration atom interferometry in the 10 m atomic fountain, leading to very large spacetime area atom interferometers. In these very large area atom interferometers, the separation between the two atomic wave packets that respectively travel along the two

interferometer paths reaches distances of up to 54 cm. Therefore, in addition to offering greatly increased inertial sensitivity, these interferometers probe the quantum mechanical wavelike nature of matter in a new macroscopic regime. I will discuss the techniques we devised to overcome the many technical challenges associated with such interferometers, which in other apparatus have prevented interference from being maintained for path separations larger than 1 cm. I will also describe initial results from the use of our very large area interferometers to test the equivalence principle with ^{85}Rb and ^{87}Rb and our plans for further progress in this direction.

Very large area atom interferometry requires high laser power and extremely cold atom sources. We have developed a novel high power, frequency doubled laser source at 780 nm that is suitable for atom optics. Also, we have implemented a sequence of matter wave lenses to prepare and measure atomic ensembles with record-low effective temperatures of 50 pK. In addition to applications in atom interferometry, we expect that such an atom source will be broadly useful for a wide range of experiments.

Acknowledgements

First, I would like to thank my advisor Mark Kasevich. Mark's unfailing optimism and enthusiasm have been a source of inspiration throughout my years as a graduate student, and his prescient guidance has been essential to the success of the experiments described in this thesis. On many occasions, he has identified a subtle experimental challenge many years before we ultimately encountered it and helped us make sure that the apparatus was designed to overcome this challenge (for example, absolute ac Stark shift compensation). I appreciate that Mark is not afraid to think big and to take on ambitious experiments, and his vision has been largely responsible for the growth of atom interferometry into the vibrant field it is today.

The results I will present have all been a team effort, and I have been fortunate to work with an amazing group of people over the years, in rough chronological order: Jason Hogan, Dave Johnson, Sheng-wey Chiow, Alex Sugarbaker, Susannah Dickerson, Hui-Chun Chien, Peter Asenbaum, Chris Overstreet, and Christine Donnelly. All of our team members are not only excellent researchers from whom I have learned much, but also great people who have made my time in graduate school a lot of fun.

I have also enjoyed the company of the rest of the Kasevich group (the K-Team), whether over lunchtime conversations or on group ski trips. The other members of the K-Team are: Brannon, Thomas, Stewart, Catherine, Seth, Christoph, Gunnar, David, Patrick, Nick, Mike, Olaf, Kaspar, Jan, Sean, Nils, Raj, Onur, Geert, Igor, Jongmin, and Josh.

I am also grateful for the hard work of the group staff—Ping, Sha, and Beth—who are always available to help out. I am lucky that our lab is right next to the machine shop. I appreciate the friendly attitudes of the machinists—Karlheinz, Mehmet, John,

Matt, and Scott—who have on many occasions generously taken the time to answer my machining questions.

Being a teaching assistant (TA) has been a fun and rewarding part of my time in graduate school. I thank the Professors for whom I TA’ed—Leo Hollberg, Roger Blandford, and Mark Kasevich—for the opportunity to be a part of their courses and for their guidance. I also thank Chaya Nanavati and Rick Pam for their teaching advice.

I greatly appreciate financial support from the Fannie and John Hertz Foundation, the National Science Foundation Graduate Research Fellowship Program, and the Stanford Graduate Fellowship Program.

Finally, I thank my parents Susan and Eddie, my brother Ben, and my wife Vanessa for their love and support.

Contents

Abstract	iv
Acknowledgements	vi
1 Introduction	1
1.1 Introduction to Atom Interferometry	1
1.1.1 Beam Splitters and Mirrors for Atoms: A Simplified Treatment Using the Two Level Atom	1
1.1.2 Beam Splitters and Mirrors for Atoms: The Three Level Atom	5
1.1.3 The Phase Shift of an Atom Interferometer: Simple Example Using a Perturbative Treatment	10
1.1.4 The Phase Shift of an Atom Interferometer: Formal Treatment	12
1.2 Large Momentum Transfer (LMT) Atom Optics	15
1.2.1 Motivation for LMT Atom Optics	15
1.2.2 Methods for LMT Atom Optics	16
1.2.3 Challenges of Large Area Atom Interferometry	22
1.3 Differential Measurement Strategies and Applications of Atom Inter- ferometry	24
1.3.1 Overview of Atom Interferometry Applications	24
1.3.2 Differential Measurement Strategies	24
1.3.3 Tests of the Equivalence Principle	25
1.3.4 Tests of Quantum Mechanics at Macroscopic Scales	26
1.3.5 Gravitational Wave Detection	28

1.4	Matter Wave Lensing	32
1.5	Organization of This Thesis	34
2	Apparatus	36
2.1	Ten Meter Atomic Fountain	36
2.2	^{87}Rb Cold Atom Source	39
2.2.1	Overview of cold atom preparation	39
2.2.2	Magneto-Optical Trap (MOT)	41
2.2.3	Evaporative Cooling	45
2.2.4	Optical Pumping Before Evaporation	49
2.2.5	Optical Lattice Launch	50
2.2.6	Water Cooling of Quadrupole Coils and Repair of Leaks	52
2.3	Dual Species $^{87}\text{Rb}/^{85}\text{Rb}$ Cold Atom Source	52
2.3.1	Upgraded MOT Laser System	52
2.3.2	Dual Species Evaporative Cooling	57
2.4	Atom Optics: High Power Frequency Doubled Laser System	58
2.4.1	Why Frequency Doubling?	58
2.4.2	Frequency Doubling Optics Setup	59
2.4.3	Optical Spectrum of Atom Optics Laser Beams	63
2.4.4	Doubling Crystal Aging	74
2.5	Imaging	75
2.6	Timing System	78
2.7	Magnetic Shielding	80
2.7.1	Importance of Magnetic Shielding	80
2.7.2	Challenges of Building a Tall Magnetic Shield	80
2.7.3	Eliminating the Magnetic Field Spikes: The Welded Shield	85
2.8	State Preparation	86
2.9	Time Orbiting Potential (TOP) Trap Current Stabilization	93
3	102 Photon Large Momentum Beam Splitters	97
3.1	Overview	97
3.2	Experimental Results	98

3.3	Outlook	107
4	Adiabatic-rapid-passage Bragg diffraction	110
4.1	Overview	110
4.2	Experimental Results	114
4.3	Outlook	120
5	43 W Quasi-Continuous Laser Source at 780 nm	122
5.1	Overview	122
5.2	Experimental Results	124
5.3	Outlook	128
6	Atom Lensing to Picokelvin Temperatures	130
6.1	Overview	130
6.2	Experimental Results	132
6.3	Overview of theoretical background and analysis details	143
6.4	Time evolution of the Wigner function in a delta-kick cooling sequence	143
6.4.1	Free space evolution	143
6.4.2	Time evolution during the delta kick	144
6.4.3	Time evolution from the lens to detection	149
6.4.4	Classical correspondence of observables calculated using the Wigner function	149
6.4.5	Evaluation of position-momentum cross moments	155
6.4.6	Modified Cauchy-Schwarz inequality for symmetrized operators	157
6.5	Aberrations	157
6.5.1	Harmonic lens	162
6.5.2	Gaussian aberrations	164
6.5.3	High spatial frequency aberrations	166
6.5.4	Scaling of aberration contributions to cloud size with lens duration	168
6.6	Point spread function	171
6.7	Spontaneous heating rate limit	172
6.7.1	Heating from a classicalizing modification to quantum mechanics	172

6.7.2	Analogous classical model: Fokker-Planck equation with a stochastic force	174
6.7.3	Stochastic modifications of the trajectories	175
6.7.4	Delta-kick sequence with stochastic modification	176
7	Atom Interferometry at the Macroscale	181
7.1	Overview	182
7.2	Experimental Results	184
7.3	Methods	190
7.3.1	Atom source	190
7.3.2	Atom optics	191
7.3.3	Absolute light shift compensation	191
7.3.4	Contrast metrics data analysis	192
7.3.5	Spatial interference fringes	195
7.4	Outlook	195
8	Theory of Atom Optics with Optical Lattices	200
8.1	Overview	201
8.2	The Hamiltonian in Different Frames	203
8.3	Phase Evolution Under the Adiabatic Approximation	208
8.4	Calculating Corrections to the Adiabatic Approximation Using the Method of Perturbative Adiabatic Expansion	213
8.5	An Example of Perturbative Adiabatic Expansion: Calculating the Non-Adiabatic Correction to the Phase Shift Evolved During a Lattice Beam Splitter	217
8.6	Applications: Atom Interferometers Using Optical Lattices as Waveguides	224
8.6.1	Gravimetry and gravity gradiometry	225
8.6.2	Tests of atom charge neutrality	230
8.6.3	Measurements of $\frac{\hbar}{m}$ and of isotope mass ratios	232
8.6.4	Gyroscopes	233
8.7	Outlook	235

8.8 Additional Calculation: Boosting Between Different Frames	236
8.9 Additional Calculation: Generalizing to the Case of a Finite Wavepacket	237
8.10 Additional Calculation: Perturbative Adiabatic Expansion at Higher Orders	241
9 Current Work: Equivalence Principle Test	243
9.1 Overview	244
9.2 Magnetic Lensing and Launching of the Dual Species Cloud	244
9.3 Atom Optics for the Dual Species Interferometer	245
9.4 Imaging the Output Ports of Dual Species Interferometers	248
9.5 Preliminary Dual Species Interferometry Data	250
9.5.1 The Differential Signal	250
9.5.2 Preliminary Analysis: Maximum Likelihood Estimation of the Differential Phase	251
9.5.3 Phase Shear Readout	253
9.6 Consideration of Systematic Effects	254
9.7 Upgrades Underway	256
10 Conclusion	258
Bibliography	260

List of Tables

6.1	Stochastic variable correlations with initial distribution.	176
6.2	Noise averages of stochastic variable correlations.	176
7.1	Comparison of superposition parameters to other matter wave interference experiments.	197

List of Figures

1.1	Diagram of a Raman transition.	7
1.2	Spacetime diagram of a three pulse Mach-Zehnder interferometer with pulse spacing T	10
1.3	Diagrams of Bragg transitions.	20
1.4	Schematic and sensitivity curve of a proposed satellite based atomic gravitational wave detector.	29
1.5	Strain sensitivity as a function of frequency for an AGIS detector with a more ambitious set of parameters that could be realized further into the future.	31
1.6	Effect of high spatial frequency perturbations on the performance of a lens.	33
2.1	Photographs of 10 m atomic fountain apparatus.	38
2.2	Diagram of the 10 m tower apparatus.	40
2.3	Optics layout for MOT lasers.	43
2.4	z axis optics layout.	46
2.5	Circuit for quickly ‘snapping’ on and off current through the inductive quadrupole coils.	48
2.6	Example of a joint between square copper wire like that used for the quadrupole coils and a hose connector.	53
2.7	Updated MOT laser optics path for the optimized dual species source.	55
2.8	Home designed mounts for Thorlabs 2 W TA modules.	56
2.9	High power laser box optics layout.	61
2.10	Photographs of high power laser system.	64

2.11	30 GHz frequency chain for atom optics phase modulation.	67
2.12	Schematic of the atom optics spectrum.	70
2.13	Atom optics lasers amplitude and phase control.	72
2.14	Doubling crystal aging.	75
2.15	Two different imaging lens systems that we have used in our apparatus.	79
2.16	Initial magnetic shield design.	81
2.17	Comparison of the initial segmented shield and the welded shield. . .	82
2.18	Finite element simulation of the initial segmented three layer magnetic shield.	83
2.19	Comparison of the measured and simulated magnetic fields inside the segmented shield.	84
2.20	Photograph of the millimeter-sized gap between a shield segment and a joining band.	86
2.21	Apparatus for controllably lowering a fluxgate magnetometer down the center of the magnetically shielded region.	87
2.22	Welded shield magnetic fields.	88
2.23	Diagram of state preparation microwave transitions for ^{85}Rb	91
2.24	Microwave chain for ^{85}Rb	92
2.25	TOP coil current stabilization circuit diagram.	94
3.1	Diagram of sequential multiphoton Bragg atom optics.	99
3.2	Images of clouds subjected to $30\hbar k$ LMT momentum kicks.	101
3.3	Output ports of LMT interferometers.	104
3.4	Parametric plot of simultaneous $30\hbar k$ interferometer outputs.	108
4.1	Schematic of adiabatic rapid passage multiphoton Bragg pulses. . . .	112
4.2	Simulations of adiabatic rapid passage multiphoton Bragg pulses. . .	113
4.3	Transfer efficiency of adiabatic rapid passage multiphoton Bragg pulses.	116
4.4	$10\hbar k$ tanh pulse diffraction efficiency versus detuning of a π -pulse and a $\pi/2$ -pulse.	118
4.5	Simulations of ARPMB Mach-Zehnder interferometers.	119
4.6	$10\hbar k$ Mach-Zehnder interferometer results.	121

5.1	Schematic of the coherently combined frequency doubling setup.	124
5.2	Frequency doubling results.	127
5.3	Beam quality measurement.	128
6.1	Schematic of the lensing experiment.	134
6.2	Comparison of the dipole lens beam intensity profile after numerical paraxial wave propagation of the measured profile by (a) 0.25 m and (b) 16.25 m.	135
6.3	Cloud size versus dipole lens duration.	137
6.4	Effect of Gaussian aberrations on lensing.	140
6.5	Magnetic lensing in the TOP trap.	142
7.1	Fountain interferometer.	183
7.2	Wave packets separated by 54 cm.	184
7.3	Fluorescence images of output ports.	186
7.4	Contrast metrics.	188
7.5	Spatial interference fringes.	189
7.6	Dependence of contrast on absolute light shift compensation.	198
7.7	Examples of data showing interference contrast.	199
8.1	The physical setup for applying a periodic potential.	205
8.2	Numerical simulation of a lattice acceleration that transfers $10\hbar k$ of momentum.	211
8.3	Non-adiabatic correction to the phase difference between an arm that is accelerated by an experimentally plausible lattice beam splitter and an arm that is not accelerated.	221
8.4	Array of lattice gravimeters.	231
8.5	Conjugate interferometer geometry that could be used to measure $\frac{\hbar}{m}$	234
9.1	Oscillations in a dual species magnetic lens.	246
9.2	Transfer efficiency for dual species LMT atom optics.	249
9.3	Data for a $2\hbar k$ dual species interferometer with $T = 1.04$ s.	250
9.4	Data for a $10\hbar k$ dual species interferometer with $T = 1.04$ s.	252

Chapter 1

Introduction

This chapter provides an introduction to the concepts of atom optics and atom interferometry. When atoms are cooled to ultracold temperatures, using methods such as those described in Ch. 2, their quantum mechanical wavelike nature can be exploited to perform experiments typically associated with light. These quantum mechanical matter waves can be manipulated with the atomic equivalents of lenses, beam splitters, and mirrors. Much of the work in this thesis is focused on using atomic matter waves for interferometry. I will provide an overview of atom interferometry and discuss some of its applications to precision measurement and fundamental physics tests.

1.1 Introduction to Atom Interferometry

1.1.1 Beam Splitters and Mirrors for Atoms: A Simplified Treatment Using the Two Level Atom

Atom interferometry is conceptually analogous to optical interferometry. In both cases, an incident wave is split into two paths by a beam splitter. The two paths are later redirected back toward each other with mirrors and overlapped on a final beam splitter to produce an interference pattern. It has long been known how to make beam splitters and mirrors for optical beams. Work to develop and improve beam splitters and mirrors for atoms has been underway for the past several decades.

The two most widely used techniques for atom interferometry respectively rely on material gratings and optical pulses to manipulate the atomic wavefunctions [1]. Our work has focused on the optical pulse technique, often referred to as light-pulse atom interferometry, and so I will focus the discussion here on this method.

A discussion of atom optics for light pulse atom interferometry naturally begins with consideration of the standard quantum mechanical treatment of the two level atom. Although the two level atom is a simplified picture, it captures much of the essential physics. We consider an atom with two levels $|1\rangle$ and $|2\rangle$ that have frequency difference $\omega_0 \equiv \omega_2 - \omega_1$. We will analyze the effect of the electric dipole interaction [2] of the atom with an electric field $\mathbf{E} = \mathbf{E}_0 \cos(\phi - \omega_0 t)$ at the location of the atom (ϕ is the local phase of the field). Under the electric dipole approximation, we neglect effects arising from variation of the field over the spatial extent of the atom's electron orbitals, as this spatial extent is typically much smaller than an optical wavelength. For simplicity, we have assumed that the field oscillates on resonance with the atomic transition. The electric dipole interaction is characterized by an interaction Hamiltonian $H_{\text{int}} = -\hat{\mu} \cdot \mathbf{E}$, where $\hat{\mu}$ is the electric dipole operator for the atom. We write the state of the atom in terms of amplitudes of the two states:

$$|\psi(t)\rangle = c_1(t)|1\rangle + c_2(t)|2\rangle. \quad (1.1)$$

Defining a Rabi frequency $\Omega \equiv -\frac{1}{\hbar} \langle 2 | \hat{\mu} \cdot \mathbf{E} | 1 \rangle$, the dynamical equations for the two amplitudes are

$$\begin{aligned} \frac{dc_1(t)}{dt} &= -ic_2(t)\Omega \cos(\phi - \omega_0 t)e^{-i\omega_0 t} = -ic_2(t)\frac{\Omega}{2}(e^{-i\phi} + e^{-i(2\omega_0 t - \phi)}) \\ \frac{dc_2(t)}{dt} &= -ic_1(t)\Omega \cos(\phi - \omega_0 t)e^{i\omega_0 t} = -ic_1(t)\frac{\Omega}{2}(e^{i\phi} + e^{i(2\omega_0 t - \phi)}) \end{aligned} \quad (1.2)$$

We can simplify these equations by making the rotating wave approximation, dropping the rapidly oscillating terms at frequency $2\omega_0$ [2]. This approximation assumes that $\omega_0 \gg \Omega$, which is typically the case for atomic systems. The dynamical equations then reduce to

$$\begin{aligned}\frac{dc_1(t)}{dt} &= -i\frac{\Omega}{2}e^{-i\phi}c_2(t) \\ \frac{dc_2(t)}{dt} &= -i\frac{\Omega}{2}e^{i\phi}c_1(t),\end{aligned}\tag{1.3}$$

which admit the simple solution

$$\begin{aligned}c_1(t) &= c_1(0) \cos\left(\frac{\Omega t}{2}\right) - ie^{-i\phi}c_2(0) \sin\left(\frac{\Omega t}{2}\right) \\ c_2(t) &= -ie^{i\phi}c_1(0) \sin\left(\frac{\Omega t}{2}\right) + c_2(0) \cos\left(\frac{\Omega t}{2}\right).\end{aligned}\tag{1.4}$$

These equations correspond to sinusoidal oscillation of population between the two states (see Fig. 1.1(b)). This can be quickly seen by considering the case where all the population begins in $|1\rangle$, so that $c_1(0) = 1$ and $c_2(0) = 0$. The populations $p_1(t) = |c_1(t)|^2$ and $p_2(t) = |c_2(t)|^2$ then evolve as

$$\begin{aligned}p_1(t) &= \cos^2\left(\frac{\Omega t}{2}\right) \\ p_2(t) &= \sin^2\left(\frac{\Omega t}{2}\right).\end{aligned}\tag{1.5}$$

There are two especially interesting times t with respect to Eq. (1.5). If the pulse area Ωt is equal to $\pi/2$ (we call this a $\pi/2$ -pulse), then the population is evenly divided between $|1\rangle$ and $|2\rangle$. This corresponds to the operation

$$\begin{aligned}|1\rangle &\longrightarrow \frac{1}{\sqrt{2}}(|1\rangle - ie^{i\phi}|2\rangle) \\ |2\rangle &\longrightarrow \frac{1}{\sqrt{2}}(-ie^{-i\phi}|1\rangle + |2\rangle).\end{aligned}\tag{1.6}$$

Until this point, we have not paid attention to the external degrees of freedom of

the atom. It is now important to note that the excitation of atomic population from $|1\rangle$ to $|2\rangle$ via an electric dipole interaction corresponds to the stimulated absorption of a photon from the driving field [2]. By conservation of momentum, the photon's momentum is necessarily transferred to the atom. For example, if the field arises from a laser beam propagating in a particular direction, then the atom will receive a single photon momentum kick in that direction. Where k is the laser wave number, the momentum kick has magnitude $\hbar k$. For the Rb atoms that we work with, and laser light near the 780 nm D₂ transition, the corresponding recoil velocity ($\hbar k/m$ for atomic mass m) is about 6 mm/s (for Rb atoms, 6 mm/s corresponds to an effective temperature of 400 nK). State $|2\rangle$ should be associated with this additional recoil velocity¹. The $\pi/2$ -pulse therefore divides the atomic state into two parts with different velocities, making it a beam splitter.

The second interesting time t occurs when $\Omega t = \pi$ (a π -pulse). A π -pulse yields the operation

$$\begin{aligned} |1\rangle &\longrightarrow -ie^{i\phi}|2\rangle \\ |2\rangle &\longrightarrow -ie^{-i\phi}|1\rangle, \end{aligned} \tag{1.7}$$

fully swapping the population between the two states. We describe this as a mirror operation, as population is ‘reflected’ from one state to the other, along with the corresponding momentum kick.

Note that the transfer of population from one state to the other is associated with a phase factor: $e^{i\phi}$ for $|1\rangle \longrightarrow |2\rangle$ and $e^{-i\phi}$ for $|2\rangle \longrightarrow |1\rangle$. We can interpret the phase factor as follows. When the atom absorbs a photon from the field ($|1\rangle \longrightarrow |2\rangle$), the local phase ϕ of the field is imprinted onto the atom’s state. When the atom emits a photon into the field, the atom receives the conjugate phase factor. These imprinted phases play a crucial role in determining the response of the interferometer phase shift to inertial effects.

¹The de-excitation of population from $|2\rangle$ to $|1\rangle$ corresponds to stimulated emission of a photon into the field. The atom then receives a momentum kick $\hbar k$ in the direction opposite to the laser beam propagation, losing the momentum that it had gained upon initial excitation.

1.1.2 Beam Splitters and Mirrors for Atoms: The Three Level Atom

The example of the two level atom discussed in Sec. 1.1.1 illustrates many of the key features of light-pulse beam splitters and mirrors. However, for the alkali atoms that have so far been most widely used in atom interferometry, there are some additional details that are important to consider². For the Rb atoms that we use, population in optically excited states rapidly decays via spontaneous emission (the decay rate is $\Gamma = 2\pi \times 6$ MHz for the D₂ line transitions that we use). An atom that undergoes spontaneous emission does not contribute to the interference signal—it receives a photon recoil momentum kick in a random direction that typically removes it from an ultracold atom ensemble that is well below the recoil temperature [2]. Therefore, we want to avoid using an optically excited state as one of the states in a two level system.

Instead, we turn to the quantum mechanical problem of the three level atom. We consider an optically excited state $|e\rangle$ and two long-lived, lower energy states $|1\rangle$ and $|2\rangle$ with a comparatively small frequency difference. For Rb, states $|1\rangle$ and $|2\rangle$ could correspond to the two ground state hyperfine levels, which have a microwave frequency splitting. For appropriate parameters, it is possible to create an effective two level system from the three level atom, with $|1\rangle$ and $|2\rangle$ coupled by two-photon optical transitions and $|e\rangle$ acting as an intermediary state that contains only a small amount of atomic population [4].

To be concrete, let us say that an upward propagating laser beam with frequency ω_{up} and local phase ϕ_{up} couples $|1\rangle$ and $|e\rangle$ with Rabi frequency Ω_1 and detuning from resonance $\Delta \equiv \omega_{\text{up}} - (\omega_e - \omega_1)$, and a downward propagating laser beam with frequency ω_{down} and local phase ϕ_{down} couples $|2\rangle$ and $|e\rangle$ with Rabi frequency Ω_2 and a similar detuning approximately equal to Δ (i.e., $\omega_{\text{down}} - (\omega_e - \omega_2) \approx \Delta$). In the limit where $\Delta \gg \Omega_1, \Omega_2, \Gamma$, and if the frequency difference $\omega_{\text{up}} - \omega_{\text{down}}$ is on resonance with

²There has been recent interest in using atomic species that have narrow optical clock transitions, such as Sr, for atom interferometry with reduced sensitivity to laser phase noise, with the clock transition being used for atom optics. In this case, the two level atom would be the relevant description, with the two states being the lower and excited optical clock states [3].

the frequency difference between states $|1\rangle$ and $|2\rangle$, then within good approximation the dynamics proceed as for the resonantly driven two level atom described in Sec. 1.1.1 [4]. The system is described by an analogue to Eq. (1.4), with an effective Rabi frequency $\Omega_{\text{eff}} \equiv \frac{\Omega_1 \Omega_2}{2\Delta}$ and a phase factor equal to the difference of the local phases ϕ_{up} and ϕ_{down} of the upward and downward propagating beams³:

$$\begin{aligned} c_1(t) &= c_1(0) \cos\left(\frac{\Omega_{\text{eff}} t}{2}\right) - ie^{-i(\phi_{\text{up}} - \phi_{\text{down}})} c_2(0) \sin\left(\frac{\Omega_{\text{eff}} t}{2}\right) \\ c_2(t) &= -ie^{i(\phi_{\text{up}} - \phi_{\text{down}})} c_1(0) \sin\left(\frac{\Omega_{\text{eff}} t}{2}\right) + c_2(0) \cos\left(\frac{\Omega_{\text{eff}} t}{2}\right). \end{aligned} \quad (1.8)$$

As for the two level atom, beam splitters and mirrors can be realized by $\pi/2$ -pulses and π -pulses, respectively, with the pulse area defined in terms of the effective Rabi frequency Ω_{eff} . The transfer of population from one state to the other is now associated with the modified phase factors $e^{i(\phi_{\text{up}} - \phi_{\text{down}})}$ for $|1\rangle \rightarrow |2\rangle$ and $e^{-i(\phi_{\text{up}} - \phi_{\text{down}})}$ for $|2\rangle \rightarrow |1\rangle$. These phase factors can be understood as arising from two-photon transitions that couple $|1\rangle$ and $|2\rangle$. For transfer from $|1\rangle \rightarrow |2\rangle$, population is transferred from $|1\rangle \rightarrow |e\rangle$ by stimulated absorption of a photon from the upward propagating beam, imprinting phase ϕ_{up} . Stimulated emission of a photon into the downward propagating beam transfers the population from $|e\rangle \rightarrow |2\rangle$, imprinting phase $-\phi_{\text{down}}$, and yielding a total imprinted phase of $(\phi_{\text{up}} - \phi_{\text{down}})$. The inverse of this process yields a total imprinted phase of $-(\phi_{\text{up}} - \phi_{\text{down}})$ for transfer from $|2\rangle \rightarrow |1\rangle$.

In an actual multilevel atom, there are typically several closely spaced excited states $|e\rangle$ that contribute to the coupling of states $|1\rangle$ and $|2\rangle$. The observed effective Rabi frequency then consists of a sum of the individual contributions from this collection of optically excited states.

The fact that we are now considering two-photon transitions as opposed to the single photon transitions considered in Sec. 1.1.1 affects the momentum kicks associated with the two states. For transfer from $|1\rangle \rightarrow |2\rangle$, the absorption of the photon

³We ignore light shifts for the moment. We will discuss them in detail in Sec. 1.2.2.

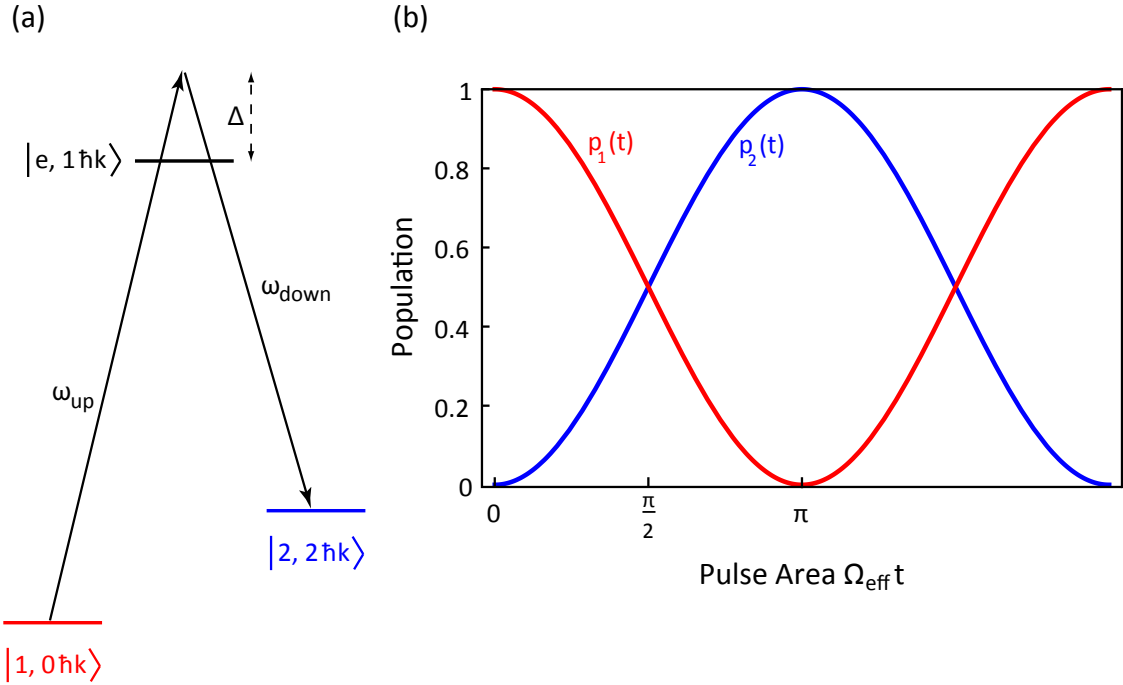


Figure 1.1: Diagram of a Raman transition. (a) The Raman transition couples two hyperfine ground states $|1\rangle$ and $|2\rangle$ through an intermediate optically excited state $|e\rangle$. Atomic population initially in $|1\rangle$ with upward momentum $0\hbar k$ undergoes stimulated absorption of a photon from an upward propagating laser beam with frequency ω_{up} followed by stimulated emission of a photon into a downward propagating laser beam with frequency ω_{down} , yielding a total upward momentum kick of $2\hbar k$ in addition to the internal state change from $|1\rangle$ to $|2\rangle$. (b) The atomic population undergoes a sinusoidal oscillation between the states $|1, 0 \hbar k\rangle$ and $|2, 2 \hbar k\rangle$ as the pulse area $\Omega_{\text{eff}} t$ is increased. For $\Omega_{\text{eff}} t = \pi/2$, the Raman transition acts as a 50/50 beam splitter for the two states. For $\Omega_{\text{eff}} t = \pi$, the Raman transition acts as a mirror, interchanging population between the two states.

from the upward propagating beam gives the atom a momentum kick $\hbar k$ in the upward direction. The stimulated emission of a photon into the downward propagating beam gives the atom another upward kick of $\hbar k$. So state $|2\rangle$ should be associated with an upward momentum kick of $2\hbar k$.

If, as suggested above, states $|1\rangle$ and $|2\rangle$ correspond to the two ground state hyperfine levels of our Rb atoms, these two-photon transitions are known as Raman transitions. The use of Raman transitions for beam splitters and mirrors in an atom interferometer (with Na atoms) was first demonstrated by Kasevich and Chu in 1991 [5], and Raman transitions remain a widely used and versatile tool for atom optics to this day. A schematic of a Raman transition is illustrated in Fig. 1.1

Another possibility is that $|1\rangle$ and $|2\rangle$ do not correspond to different internal atomic states, but only to different external momentum states differing by momentum $2\hbar k$ (see Fig. 1.3). This situation is known as a Bragg transition [6]. For a Bragg transition, it makes sense to relabel states $|1\rangle$ and $|2\rangle$ as $|p_0\rangle$ and $|p_0 + 2\hbar k\rangle$, where p_0 is the initial vertical momentum of the atom. Conservation of energy provides a resonance condition for $\omega_{\text{up}} - \omega_{\text{down}}$ in the case of a Bragg transition. When atomic population is transferred from $|p_0\rangle$ to $|p_0 + 2\hbar k\rangle$, there is an external kinetic energy gain of

$$\Delta E = \frac{(p_0 + 2\hbar k)^2}{2m} - \frac{p_0^2}{2m} = 2p_0 \frac{\hbar k}{m} + 2 \frac{\hbar^2 k^2}{m} = 2p_0 v_r + 4\hbar\omega_r, \quad (1.9)$$

where $v_r \equiv \frac{\hbar k}{m}$ and $\omega_r \equiv \frac{\hbar k^2}{2m}$ are respectively the recoil velocity and the recoil frequency associated with a single photon momentum kick. Meanwhile, the atom gains energy $\hbar(\omega_{\text{up}} - \omega_{\text{down}})$ from the laser fields. Since the internal state of the atom does not change, all of the energy gained from the laser fields necessarily goes into the kinetic energy gain ΔE . Therefore,

$$\omega_{\text{up}} - \omega_{\text{down}} = \frac{\Delta E}{\hbar} = 2 \frac{p_0}{\hbar} v_r + 4\omega_r. \quad (1.10)$$

For both the Raman and Bragg cases, it is important to consider the spontaneous emission loss rate arising from residual atomic population in $|e\rangle$. For a laser beam spectral component with single photon Rabi frequency Ω and detuning Δ , the induced

excited state population for $\Delta \gg \Omega, \Gamma$ is [2]

$$P_e = \frac{\Omega^2}{4\Delta^2}. \quad (1.11)$$

The corresponding spontaneous emission loss rate is

$$R = \Gamma P_e = \Gamma \frac{\Omega^2}{4\Delta^2}. \quad (1.12)$$

If this spectral component pairs with a second spectral component of comparable Rabi frequency to drive a two-photon transition, as discussed above the effective Rabi frequency is $\Omega_{\text{eff}} = \frac{\Omega^2}{2\Delta}$. To drive a π -pulse, the light must be pulsed on for a time $t_\pi = \frac{\pi}{\Omega_{\text{eff}}}$. This leads to a fraction of the atoms $L_\pi \sim R t_\pi$ being lost to spontaneous emission during a π -pulse. The loss scales as

$$L_\pi \sim \Gamma \frac{\Omega^2}{4\Delta^2} \frac{\pi}{\frac{\Omega^2}{2\Delta}} \sim \frac{\Gamma}{\Delta}. \quad (1.13)$$

This suggests that in order to minimize spontaneous emission losses, the detuning Δ should be made as large as possible. There are additional constraints that make it undesirable to have Δ be arbitrarily large. The single photon Rabi frequency Ω is proportional to the electric field amplitude, so Ω_{eff} is proportional to the laser intensity and inversely proportional to Δ . If arbitrarily high laser power were available, a fixed t_π could be maintained as Δ is increased by turning up the laser power⁴. We want t_π to be short enough so that the pulse is not excessively Doppler selective. From fundamental properties of the Fourier transform, the width of the range of detunings over which a π -pulse can maintain high transfer efficiency is inversely proportional to t_π . If this width becomes too narrow, the majority of the atoms will not be efficiently transferred due to the finite velocity spread of the cloud, which leads to Doppler shifts away from resonance. For our typical atom sources, we do not want t_π to be longer than $\sim 100 \mu\text{s}$. In practice, the laser power is limited, constraining the maximum detuning that can be used.

This discussion indicates that higher laser power is generally helpful for atom

⁴Using a smaller laser beam waist can also increase the intensity, but it is typically desirable not to make the waist too small to avoid laser intensity inhomogeneities across the atom cloud.

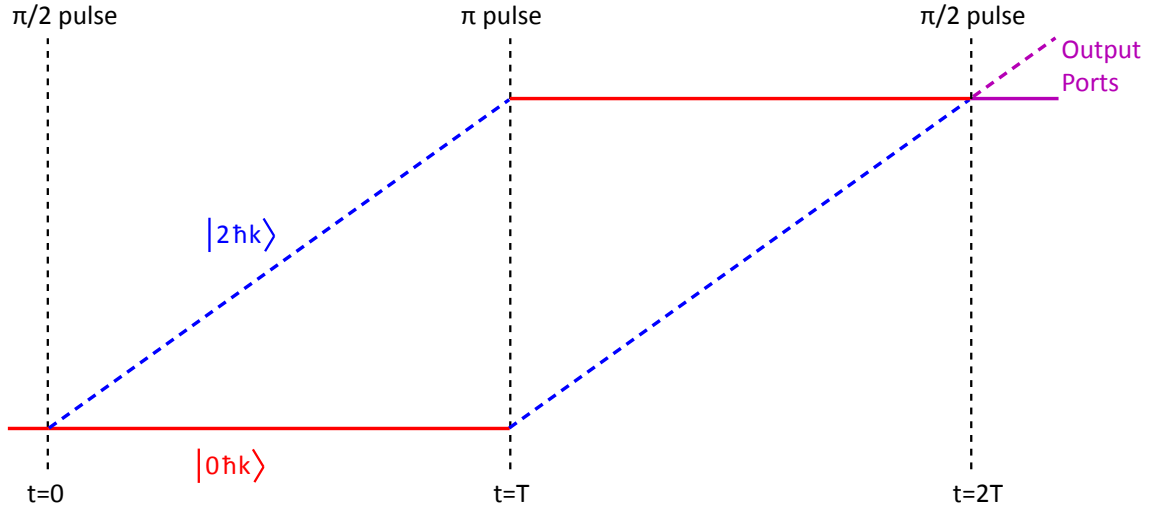


Figure 1.2: Spacetime diagram of a three pulse Mach-Zehnder interferometer with time between pulses (pulse spacing) T .

optics, as it allows for the reduction of spontaneous emission losses while maintaining the same effective Rabi frequency. We have therefore expended significant effort to build a high power, frequency doubled laser system, as discussed in Sec. 2.4 and in Ch. 5. Chapter 5 details the demonstration of an unprecedented 43 W laser source at 780 nm (the wavelength of the Rb D₂ line) that is suitable for atom optics.

1.1.3 The Phase Shift of an Atom Interferometer: Simple Example Using a Perturbative Treatment

In order to assess possible applications for atom interferometry, it is necessary to know how the interferometer phase shift depends on various quantities of interest, such as inertial forces. As a start, we will perform a simple phase shift calculation for a spatially and temporally constant gravitational acceleration g . In Sec. 1.1.4, we will give an overview of the more formal method for calculating phase shifts in more general situations.

We consider a Mach-Zehnder interferometer with time between pulses (pulse spacing) T . At time $t = 0$, a beam splitter ($\pi/2$ -pulse) splits the initial matter waves into a superposition of two paths with vertical momentum differing by $2\hbar k$. These two paths drift apart for time T . At time $t = T$, a mirror (π -pulse) interchanges the momenta of the two interferometer arms, so that they start to move back toward each other. At time $t = 2T$, the two arms spatially overlap and are interfered by a final beam splitter. The normalized populations P_1 and P_2 in the two interferometer output ports depend on the interferometer phase shift $\Delta\phi$ as

$$\begin{aligned} P_1 &= \frac{1}{2} + \frac{1}{2}C \cos(\Delta\phi) \\ P_2 &= \frac{1}{2} - \frac{1}{2}C \cos(\Delta\phi), \end{aligned} \quad (1.14)$$

where C is the interferometer contrast, which ranges between zero and one depending on the quality of the interference. Figure 1.2 shows a schematic of such a Mach-Zehnder interferometer.

The atoms move in a potential $U(z) = mgz$, where m is the atomic mass. To perform a ‘back-of-the-envelope’ phase shift calculation, we will neglect the effect of this potential on the atomic trajectories, and assume that the interferometer phase shift comes entirely from integrating the Lagrangian over the two interferometer arms. This approach is motivated by the Feynman path integral approach to quantum mechanics, and it turns out that our ‘back-of-the-envelope’ approximation is formally justified as a perturbative method that gives exactly the correct answer for the simple situation considered here [7]. The Lagrangian is given by $\mathcal{L} = \frac{1}{2}m\dot{z}^2 - mgz$. Due to the symmetry of the interferometer, the integral of the kinetic energy term is the same over both paths and cancels from the interferometer phase shift. The phase shift is then determined by the difference between the gravitational potential term integrated over the upper versus the lower path:

$$\Delta\phi = \phi_{\text{upper}} - \phi_{\text{lower}} = \left(-\frac{1}{\hbar} \int_{\text{upper path}} mgz \right) + \left(\frac{1}{\hbar} \int_{\text{lower path}} mgz \right) \quad (1.15)$$

$$= -\frac{m}{\hbar} g \int_0^{2T} \Delta z(t) dt, \quad (1.16)$$

where $\Delta z(t) \equiv z_{\text{upper}}(t) - z_{\text{lower}}(t)$ is the spatial separation of the upper and lower paths.

The phase shift is proportional to the enclosed spacetime area $\int_0^{2T} \Delta z(t) dt$ of the interferometer. For the interferometer geometry we are considering, the enclosed spacetime area is equal to $\Delta z_{\text{max}} T$, where Δz_{max} is the maximum path separation reached during the interferometer. Therefore,

$$\Delta\phi = -\frac{m}{\hbar} g \Delta z_{\text{max}} T. \quad (1.17)$$

Since $\Delta z_{\text{max}} = \frac{2\hbar k}{m} T$, we can alternatively write

$$\Delta\phi = -2kgT^2. \quad (1.18)$$

This phase shift calculation demonstrates that to increase the acceleration sensitivity of an atom interferometer, the enclosed spacetime area should be increased. This can be achieved by increasing the pulse spacing T or by implementing beam splitters that transfer many photon recoils of momentum instead of just two. We will discuss large area interferometers in detail in Sec. 1.2.

1.1.4 The Phase Shift of an Atom Interferometer: Formal Treatment

In Sec. 1.1.3, the phase shift from a gravitational acceleration g was calculated using a simple perturbative method that ignored the effect of g on the atomic trajectories. To calculate phase shifts in a general and formal framework, it is necessary to explicitly account for modifications to the atomic trajectories from external forces. The discussion here will provide a summary of a formal method for calculating phase

shifts, following the treatment in [7] and in [8].

Generally speaking, contributions to the interferometer phase shift can arise from several sources. The first class of contributions, familiar from Sec. 1.1.3, comes from taking the difference of the Lagrangian integrated over the two interferometer arms. This is called the propagation phase, which we denote $\Delta\phi_{\text{prop}}$:

$$\Delta\phi_{\text{prop}} = \left(\frac{1}{\hbar} \int_{\text{upper path}} \mathcal{L} \right) - \left(\frac{1}{\hbar} \int_{\text{lower path}} \mathcal{L} \right). \quad (1.19)$$

Second, recall from Sec. 1.1.2 that the local phase of the laser field at the location of the atom is imprinted on the atom's wavefunction when momentum is transferred during beam splitter or mirror pulses. The difference of the net imprinted phase for the two interferometer arms is called the laser phase, $\Delta\phi_{\text{laser}}$. For each interferometer path, the local phase is evaluated at the classical center of mass position of that path at the time when a given atom optics pulse occurs. Where $\phi_{\text{imprint}}(\mathbf{r}_i^{\text{upper}})$ is the imprinted phase on the upper path from atom optics pulse i and $\phi_{\text{imprint}}(\mathbf{r}_i^{\text{lower}})$ is the imprinted phase on the lower path from pulse i ($\mathbf{r}_i^{\text{upper}}$ and $\mathbf{r}_i^{\text{lower}}$ are the positions along the upper and lower paths at which the local phase is evaluated for pulse i), the laser phase is

$$\Delta\phi_{\text{laser}} = \left(\sum_i \phi_{\text{imprint}}(\mathbf{r}_i^{\text{upper}}) \right) - \left(\sum_i \phi_{\text{imprint}}(\mathbf{r}_i^{\text{lower}}) \right). \quad (1.20)$$

Finally, if the two paths do not perfectly overlap at the end of the interferometer, there is an additional contribution called the separation phase, $\Delta\phi_{\text{sep}}$. Where $\bar{\mathbf{p}}_{\text{final}}$ is the mean canonical momentum of the two interferometer paths in a given output port⁵ after the final beam splitter and $\mathbf{r}_{\text{final}}^{\text{upper}} - \mathbf{r}_{\text{final}}^{\text{lower}}$ is the separation between the upper and lower paths when the final beam splitter is applied, the separation phase is

$$\Delta\phi_{\text{sep}} = -\frac{1}{\hbar} \bar{\mathbf{p}}_{\text{final}} \cdot (\mathbf{r}_{\text{final}}^{\text{upper}} - \mathbf{r}_{\text{final}}^{\text{lower}}). \quad (1.21)$$

⁵In general, $\Delta\phi_{\text{laser}}$ and $\Delta\phi_{\text{sep}}$ can individually differ depending on which interferometer output port is considered. However, their sum $\Delta\phi_{\text{laser}} + \Delta\phi_{\text{sep}}$ is the same for both output ports [8].

The total phase shift is the sum of these three contributions:

$$\Delta\phi = \Delta\phi_{\text{prop}} + \Delta\phi_{\text{laser}} + \Delta\phi_{\text{sep}} \quad (1.22)$$

We can now calculate the phase shift for the example interferometer considered in Sec. 1.1.3 using this formal method. When the effect of g on the atomic trajectories is taken into account, the kinetic energy term in the propagation phase is no longer zero. In fact, it cancels with the potential energy term to yield $\Delta\phi_{\text{prop}} = 0$. This cancellation is closely related to the fact that the gravitational potential is independent of path. The two interferometer arms overlap perfectly at the end, so $\Delta\phi_{\text{sep}} = 0$. The entire phase shift therefore comes from the laser phase. Accounting for the positions of the freely falling trajectories of the interferometer arms at each of the three atom optics pulses, the laser phase, and hence full phase shift, is

$$\Delta\phi = -2kgT^2, \quad (1.23)$$

in agreement with the result from the treatment in Sec. 1.1.3. It is interesting to note that in the perturbative treatment of Sec. 1.1.3, the phase shift comes from the propagation phase calculated using the unmodified trajectories, while for the full treatment this same phase shift instead enters through the laser phase. This is an example of a more general method of calculating phase shifts from perturbing potentials—in perturbation theory, the change in the phase shift is calculated by integrating the perturbing potential over the unperturbed interferometer trajectories [7]. In general, there will also be terms in the formal phase shift calculation that enter through the propagation phase. One such example is the gravitational curvature term

$$\Delta\phi_{\text{curvature}} = -\frac{\hbar(2k)^2}{2m} T_{zz} T^3, \quad (1.24)$$

which arises from the curvature of the gravitational field, quantified by the vertical gravity gradient T_{zz} . Specifically, T_{zz} is the first vertical derivative of the vertical gravitational acceleration.

1.2 Large Momentum Transfer (LMT) Atom Optics

1.2.1 Motivation for LMT Atom Optics

For atom interferometry to reach its ultimate potential, it is desirable to realize ultra-sensitive atom interferometers via large enclosed spacetime area $\Delta z_{\max} T$, where Δz_{\max} is the maximum path separation reached during the interferometer and T is the interferometer pulse spacing. As shown in Sec. 1.1.3, the acceleration sensitivity scales proportionally with the enclosed spacetime area. One way to increase the enclosed spacetime area is to implement beam splitters that lead to larger momentum splittings between the two interferometer arms than the $2\hbar k$ momentum splitting of standard light-pulse atom optics. Beam splitters and mirrors that deliver $n\hbar k$ momentum kicks to the atoms, with $n > 2$, are commonly called large momentum transfer (LMT) atom optics. The path separation Δz_{\max} , and hence the interferometer area, is proportional to n , as a larger momentum splitting allows the two interferometer paths to separate by a larger distance over a given time T .

Since Δz_{\max} is proportional to T , the interferometer area is proportional to T^2 . In addition to implementing interferometers with LMT atom optics, we would therefore like to make T as large as possible. For terrestrial experiments, T is limited by the height over which the atoms can freely fall before hitting the bottom of the apparatus. Maximizing T has motivated us to construct a 10 m atomic fountain for atom interferometry and others to perform atom interferometry in a freely falling capsule that takes advantage of the microgravity environment provided by the 146 m tall drop tower at the Center of Applied Space Technology and Microgravity (ZARM) in Bremen [9].

One of the major goals of the work presented in this thesis was to demonstrate atom interferometers that have both very large momentum transfer ($n \sim 100$) and very long interrogation time ($T > 1$ s). There were a number of technical challenges associated with these very large area interferometers. Even for short T , it has been a major challenge for the field to implement LMT atom optics that efficiently transfer

many momentum kicks to the atoms without washing out the interference signal due to dephasing from the atom-light interaction. Sources of dephasing include laser intensity and velocity dependent atom-optics-induced phase shifts (the laser intensity dependent phase shifts couple to laser intensity variations across the atom cloud) and wavefront imperfections in the atom optics laser beams. As discussed in Sec. 1.2.3, it becomes significantly more difficult to mitigate the harmful effects of such technical imperfections as n becomes larger and T becomes longer.

1.2.2 Methods for LMT Atom Optics

There are a number of different methods for LMT atom optics, each with its own set of advantages and disadvantages. It is useful to have this variety of methods available, as there are many applications of atom interferometry that can benefit from LMT atom optics, and the optimal method may depend on the specific constraints imposed by a particular situation. We will now discuss several of these methods.

Sequential Raman Transitions

One way to create an LMT beam splitter involves a sequence of Raman transitions [10]. One implementation of a sequential Raman LMT beam splitter, which we realized in the 10 m atomic fountain apparatus [11, 12], consists of an initial $\pi/2$ -pulse that splits the interferometer arms in momentum by $2\hbar k$, and a subsequent sequence of π -pulses that increase this momentum splitting by selectively delivering additional $2\hbar k$ momentum kicks to one of the arms. As in Sec. 1.1.2, we denote the two ground state hyperfine levels of the Rb atoms as $|1\rangle$ and $|2\rangle$. Before the beam splitter, let us say that all the population is in state $|1\rangle$ with momentum p_0 . For convenience, we will incorporate the momentum into the state label, so that the initial state is $|1, p_0\rangle$. The initial $\pi/2$ -pulse creates a superposition of two interferometer arms, one in state $|1, p_0\rangle$ and the second in state $|2, p_0 + 2\hbar k\rangle$. A π -pulse then transfers the second arm from $|2, p_0 + 2\hbar k\rangle \rightarrow |1, p_0 + 4\hbar k\rangle$. Additional π -pulses can further accelerate the second arm by driving the sequence of transitions $|1, p_0 + 4\hbar k\rangle \rightarrow |2, p_0 + 6\hbar k\rangle \rightarrow |1, p_0 + 8\hbar k\rangle$ and so on.

Because Raman transitions involve two different internal states, the resonance condition for $\omega_{\text{up}} - \omega_{\text{down}}$ differs from that in Eq. (1.10) for the case of Bragg transitions. For pulses that deliver upward momentum kicks while changing the internal state from $|1\rangle \rightarrow |2\rangle$ ($|2\rangle \rightarrow |1\rangle$), the frequency difference ω_{21} between states $|2\rangle$ and $|1\rangle$ must be added to (subtracted from) $\omega_{\text{up}} - \omega_{\text{down}}$:

$$\omega_{\text{up}} - \omega_{\text{down}} = 2\frac{p_i}{\hbar}v_r + 4\omega_r + \omega_{21} \quad (\text{for } |1, p_i\rangle \rightarrow |2, p_i + 2\hbar k\rangle) \quad (1.25)$$

$$\omega_{\text{up}} - \omega_{\text{down}} = 2\frac{p_i}{\hbar}v_r + 4\omega_r - \omega_{21} \quad (\text{for } |2, p_i\rangle \rightarrow |1, p_i + 2\hbar k\rangle). \quad (1.26)$$

Assuming a configuration in which the laser beams are not retroreflected⁶, if one Raman transition $|1, p_i\rangle \rightarrow |2, p_i + 2\hbar k\rangle$ ($|2, p_i\rangle \rightarrow |1, p_i + 2\hbar k\rangle$) is on resonance, its neighboring Raman transitions $|2, p_i - 2\hbar k\rangle \rightarrow |1, p_i\rangle$ and $|2, p_i + 2\hbar k\rangle \rightarrow |1, p_i + 4\hbar k\rangle$ ($|1, p_i - 2\hbar k\rangle \rightarrow |2, p_i\rangle$ and $|1, p_i + 2\hbar k\rangle \rightarrow |2, p_i + 4\hbar k\rangle$) will be detuned from resonance by a large frequency difference of magnitude $\sim 2\omega_{21}$. This implies that a Raman transition involves a very pure two level system that is not significantly polluted by neighboring transitions. We will see that Bragg transitions behave as pure two level systems under a narrower range of conditions, a feature with both advantages and disadvantages.

An important effect for Raman transitions is the optically-induced change of the frequency difference ω_{21} between the two hyperfine states from ac Stark shifts (also called light shifts). These shifts directly couple to the pulse transfer efficiency and phase, as they affect the resonance condition. AC Stark shifts change the energies of states $|1\rangle$ and $|2\rangle$ via off-resonant coupling to the excited state $|e\rangle$. We consider the ac Stark shift on state $|i\rangle$ ($i = 1$ or 2) from a spectral component with frequency ω_j and single-photon Rabi frequency Ω_{ji} coupling $|i\rangle$ and $|e\rangle$. For detuning $\Delta_{ji} \equiv \omega_j - (\omega_e - \omega_i)$ of ω_j from the $|i\rangle \rightarrow |e\rangle$ transition, the ac Stark shift of the energy of $|i\rangle$ is [4]

⁶In the retroreflected case, neighboring Raman transitions can be driven by the mirror image of the on-resonance laser beam pair. In this case, the neighboring transitions are detuned by an amount $\sim 4\frac{p_i}{\hbar}v_r$, which can be large for a sufficiently high offset momentum p_i .

$$\Delta E_{ji}^{\text{AC}} = \hbar \frac{\Omega_{ji}^2}{4\Delta_{ji}} \quad (1.27)$$

for $\Delta_{ji} \gg \Omega_{ji}, \Gamma$. Note that the ac Stark frequency shift has the same order of magnitude as the two-photon Rabi frequency $\frac{\Omega_{ji}^2}{2\Delta_{ji}}$ associated with the spectral component ω_j we are considering. Because of the hyperfine splitting between $|1\rangle$ and $|2\rangle$ (6.8 GHz for ^{87}Rb , 3 GHz for ^{85}Rb), Δ_{j1} and Δ_{j2} are different, leading to a differential ac Stark between the two hyperfine levels.

The total ac Stark shift arises from summing the individual shifts $\Delta E_{ji}^{\text{AC}}$ over all the spectral components ω_j present in the laser beams. To optimize transfer efficiency and minimize residual phase shifts, it is desirable to have this total shift be zero. One technique is to adjust the power ratio between the two atom optics beams driving the Raman transitions so that the net differential ac Stark from the two beams cancels [13]. For this method, there is still typically an absolute ac Stark shift of each level—this shift is just the same for the two levels. We describe this situation as having relative but not absolute ac Stark shift compensation. It is also possible to set the spectrum of each atom optics beam so that the absolute ac Stark shift from that beam of each individual hyperfine level is zero (zero absolute ac Stark shift necessarily implies zero relative shift). Having each individual beam be ac Stark shift compensated has the advantage of eliminating residual ac Stark shifts from relative intensity variations or mode mismatches of the two beams. Moreover, as discussed in Sec. 1.2.3, absolute ac Stark shift compensation is important for large area atom interferometry.

Sequential and Multiphoton Bragg Transitions

Another approach to LMT atom optics is to use Bragg transitions. One way in which this can be done is analogous to the sequential Raman method described above, but with the two-photon Raman transitions replaced by two-photon Bragg transitions. An advantage of Bragg transitions is that they do not experience unwanted detunings from ac Stark shifts, as the internal state of the atom does not change. Another effect of the fact that Bragg transitions do not change the internal state is that,

in comparison to Raman transitions, they behave as pure two-level systems over a narrower set of experimental parameters. To understand this, if a Bragg transition $|p_i\rangle \rightarrow |p_i + 2\hbar k\rangle$ is on resonance, we note that the neighboring Bragg transitions $|p_i - 2\hbar k\rangle \rightarrow |p_i\rangle$ and $|p_i + 2\hbar k\rangle \rightarrow |p_i + 4\hbar k\rangle$ are detuned by $\pm 8\omega_r$ (from Eq. (1.10)). For Rb, $\omega_r \approx 2\pi \times 4$ kHz, which is much smaller than the hyperfine splitting by which neighboring Raman transitions are detuned. In order to avoid strong coupling to the neighboring Bragg transitions, the two-photon Rabi frequency should be significantly below $8\omega_r$. This constraint on the Rabi frequency limits how quickly momentum can be transferred to the atoms and the Doppler width of the atoms that can be efficiently transferred. For the latter reason, Bragg transitions require colder atom sources than do Raman transitions.

The fact that neighboring Bragg transitions are detuned by only a modest amount naturally leads to the possibility of driving higher order, multiphoton Bragg transitions [14, 15, 16]. A $2n$ photon Bragg transition couples states $|p_0\rangle$ and $|p_0 + 2n\hbar k\rangle$, using momentum states at $2\hbar k$ intervals in between as intermediary states (see Fig. 1.3). By extension of the argument used to derive Eq. (1.10), the resonance condition for the $|p_0\rangle \rightarrow |p_0 + 2n\hbar k\rangle$ multiphoton Bragg transition is

$$\omega_{\text{up}} - \omega_{\text{down}} = \frac{1}{n} \frac{1}{\hbar} \left[\frac{(p_0 + 2n\hbar k)^2}{2m} - \frac{p_0^2}{2m} \right] = 2 \frac{p_0}{\hbar} v_r + 4n\omega_r \quad (1.28)$$

It is possible to drive highly efficient transfer from $|p_0\rangle \rightarrow |p_0 + 2n\hbar k\rangle$ with multiphoton Bragg transitions, but there is typically significant population in the intermediate momentum states in the middle stages of the pulse. For this reason, the dynamics of multiphoton Bragg transitions are more complex than those of a pure two level system, raising the possibility of stronger intensity dependent phase shifts.

Multiphoton Bragg transitions have the advantage of being able to transfer momentum more quickly and with fewer pulses than two-photon Bragg transitions. Since multiphoton Bragg transitions are higher order processes, the laser intensity that it takes to drive them while keeping spontaneous emission losses acceptably low increases rapidly with n [17, 18]. With limited laser intensity, one option is to perform sequences of multiphoton Bragg transitions of intermediate order. As described in

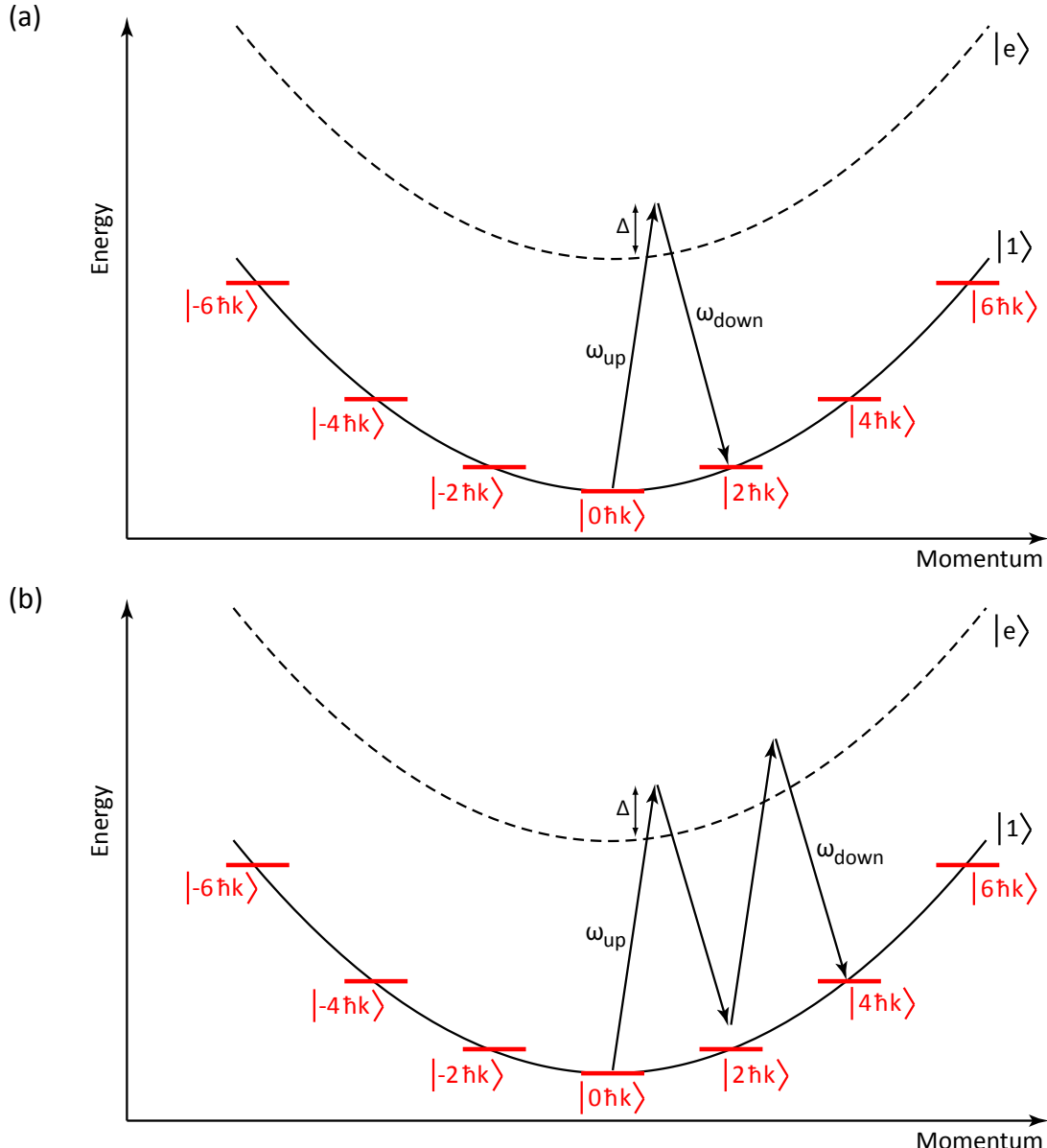


Figure 1.3: Diagrams of Bragg transitions. (a) Bragg transition that transfers $2\hbar k$ of momentum. Two momentum states with the same internal state $|1\rangle$ are coupled via an intermediate excited state $|e\rangle$. The transition arises from stimulated absorption of a photon from an upward propagating laser beam with frequency ω_{up} followed by stimulated emission of a photon into a downward propagating laser beam with frequency ω_{down} . Since the internal state does not change, the resonance condition is determined by the quadratic dependence of the external kinetic energy on momentum. (b) Multiphoton Bragg transition that transfers $4\hbar k$ of momentum. The transition arises from stimulated absorption of two photons from the ω_{up} beam and stimulated emission of two photons into the ω_{down} beam.

Ch. 3, we used sequential $6\hbar k$ multiphoton Bragg atom optics to demonstrate atom interferometers with momentum splittings between the arms of up to $102\hbar k$. This work was performed in a test apparatus with short interrogation time ($T \sim 10$ ms). For later work with very large area atom interferometers in the 10 m atomic fountain (see Ch. 7), we used sequential $2\hbar k$ Bragg transitions.

Adiabatic Rapid Passage Methods

Adiabatic rapid passage (ARP) is a commonly used technique to make the transfer between two states more robust against variations in Rabi frequency and detuning [19, 20, 21]. A key feature of ARP is that during an ARP pulse, the detuning is swept across resonance. Variations of ARP techniques can be combined with Raman [22] or Bragg transitions. In Ch. 4, we demonstrate atom interferometers using multiphoton Bragg transitions with enhanced transfer efficiency via the use of ARP. Another LMT method, which we analyze in detail in Ch. 8, is to adiabatically accelerate atoms in an optical lattice [23, 24, 25, 26], which can be understood as inducing sequential $2\hbar k$ ARP Bragg transitions [27].

ARP atom optics techniques are especially useful for applications in which it is difficult to make the laser intensity and transition resonance frequency constant from shot-to-shot or over the atom ensemble in a single shot. Such applications could include mobile atom-interferometry-based inertial sensors for use outside the laboratory. For example, with ARP techniques, high transfer efficiency can be achieved with a larger spread in Doppler detunings, allowing the use of hotter ensembles that contain more atoms and take less time to cool. ARP transitions require greater pulse area than their non-ARP counterparts (typically at least several times more), which leads to a proportional increase in the spontaneous emission loss, so an important tradeoff to take into account is the efficiency gain from the use of ARP versus the efficiency loss from spontaneous emission. Moreover, as discussed in Ch. 4 and Ch. 8, ARP generally leads to additional velocity and laser intensity dependent phase shifts. The analysis in Ch. 8 gives reason for optimism that these phase shifts can be controlled at an acceptable level for very large area interferometers using optical lattice manipulations of the atoms. It will be interesting to experimentally investigate

such interferometers in the 10 m atomic fountain in future work.

1.2.3 Challenges of Large Area Atom Interferometry

As mentioned in Sec. 1.2.1, a major technical obstacle for the realization of LMT atom interferometers has been the difficulty of preventing the interference signal from being washed out by dephasing from the LMT atom optics interactions. This task becomes dramatically more difficult for large path separation Δz_{\max} and long pulse spacing T , which is reflected in the fact that our 10 m atomic fountain is the only apparatus so far in which interference contrast has been maintained for path separations greater than 1 cm (see Tab. 7.1).

One of the key challenges for very large area atom interferometry is to prevent dephasing from laser intensity dependent phase shifts. For instance, all the LMT methods discussed in Sec. 1.2.2 are susceptible to ac Stark shifts of the atomic energies. In contrast to Raman transitions, Bragg transitions avoid the additional concern of intensity dependent detunings from the relative ac Stark shifts between the two hyperfine levels. However, both Raman and Bragg based atom optics are sensitive to the absolute ac Stark shift of each level.

In practice, the transverse laser beam profile always has intensity variations across the atom ensemble. Through the absolute ac Stark shift, these intensity variations exert spatially dependent forces and imprint spatial phase ripples on the atom cloud. If Δz_{\max} is small, this is not too much of a concern, as these disturbances from the absolute ac Stark shift will be common to the two wave packets that respectively travel along the two interferometer arms and will therefore not cause dephasing. However, once Δz_{\max} grows to tens of centimeters, as in the work described in Ch. 7, these disturbances are no longer common to the two interferometer arms. This is because for large Δz_{\max} , perturbations to the transverse laser intensity profile change between the two widely separated interferometer wave packets due to diffraction. Moreover, for larger momentum transfer, the atom optics lasers need to be kept on longer and/or have a higher intensity, thereby increasing the overall size of any intensity dependent phase perturbations. For the work in Ch. 7, we found it essential to implement a

spectrum that compensated the absolute ac Stark shift for each atom optics laser beam. The generation of this spectrum is discussed in detail in Sec. 2.4.3.

In addition to intensity dependent phase shifts, another concern is phase perturbations arising from wavefront imperfections of the atom optics laser beams. Whenever a laser beam delivers a photon recoil momentum kick to an atomic wave packet, the wavefront of the laser beam is imprinted on the wave packet's phase profile (using the terminology of Sec. 1.1.4, this can be understood as spatially dependent laser phase). Since many photon recoil kicks are delivered for LMT atom optics, these phase perturbations are imprinted many times. The amplitude of the total phase perturbation imprinted on atomic wave packet scales with the amount of momentum transferred. Since the two interferometer arms receive momentum kicks at different times spaced by T , the imprinted phase perturbations will not necessarily be common to the two interferometer arms. For example, differential imprinted phase profiles between the two arms can arise from expansion or transverse motion of the atom cloud over the pulse spacing T , effects which are magnified for longer T .

Another challenge for large area atom interferometry is the realization of efficient atom optics transfer efficiency. For long T , the atom cloud has more time to expand and can reach a size comparable to the width of the laser beams, leading to less efficient transfer due to Rabi frequency inhomogeneities. Moreover, atom optics that transfer more momentum are naturally more sensitive to Rabi frequency inhomogeneities. The use of wider laser beams can help to ameliorate this problem. This involves a tradeoff, however, since maintaining constant Rabi frequency while making the beams wider requires closer detuning, leading to increased spontaneous emission losses. In order to reduce the influence of large scale laser intensity and wavefront inhomogeneities in interferometers with long T , it is generally helpful to use an atom source that is transversely cold. Methods for generating such atom sources are discussed in Sec. 1.4 and Ch. 6.

1.3 Differential Measurement Strategies and Applications of Atom Interferometry

1.3.1 Overview of Atom Interferometry Applications

Atom interferometry has found a wide range of applications, ranging from the practical to the fundamental. Atom interferometers can be used as precise sensors of accelerations [13], rotations [28, 29], and gravity gradients [30]. In addition, atom interferometry is a valuable tool for measuring fundamental constants [31, 32] and performing fundamental physics tests, such as tests of the equivalence principle [33, 34, 35, 36], other aspects of general relativity [37], quantum mechanics at macroscopic scales [38, 9], and cosmological principles through the potential implementation of atomic gravitational wave observatories [39, 40]. Here I will introduce several of the applications on which our work has focused.

1.3.2 Differential Measurement Strategies

For many applications of atom interferometry, a crucial measurement strategy is to implement a simultaneous differential measurement. In many cases—such as gravity gradiometry [30], tests of the equivalence principle [33, 34, 35, 37], gyroscopy and gyrocompassing using point source interferometry [29, 41], and gravitational wave detection [39, 40]—the signal of interest is differential in nature. To understand the concept behind simultaneous differential measurement, consider a collection of parallel interferometers labelled by index i ,

$$|\psi_1\rangle_i + e^{i\phi_i} |\psi_2\rangle_i, \quad (1.29)$$

where $|\psi_1\rangle_i$ and $|\psi_2\rangle_i$ respectively correspond to the wavepackets associated with the two arms of interferometer i , and ϕ_i is the phase with which interferometer i interferes. These parallel interferometers, corresponding to sub-ensembles of the entire collection of atoms being used for interferometry in a given experimental shot, could represent different atom clouds separated over a long baseline [30], clouds of different

atomic species [33, 34, 35], or different parts of a single atom cloud [9, 29]. For example, in [29] a measurement of the differential phase between parallel interferometers corresponding to the left and right side of a single atom cloud was used to make a high-precision gyroscope.

Because of the high inertial sensitivity of atom interferometers, the individual phases ϕ_i can vary by large amounts from shot-to-shot due to vibrations [9, 29]. However, it is possible to make this vibration-induced phase noise cancel to a high degree as a common mode in the differential phase shifts $\phi_i - \phi_j$ of the simultaneous interferometers [42]. The simultaneity of the interferometers is critical for common mode cancellation to work. If the interferometers were not run simultaneously, different phase shifts ϕ_i and ϕ_j would not experience the noise in a common way, so that the differential signals of interest, $\phi_i - \phi_j$, would be noisy.

1.3.3 Tests of the Equivalence Principle

The equivalence principle is fundamental to our understanding of gravity. There are several variations of the equivalence principle, each of which makes successively stronger claims [43]. In this thesis, I will focus on the weak equivalence principle, which states that all objects fall under gravity at the same rate. From this point on, when I write equivalence principle, I will be referring to the weak equivalence principle.

Simultaneous atom interferometers that use different atomic species provide a way to test the equivalence principle by comparing the gravitational accelerations of the different species. Current research in our 10 m atomic fountain is aimed at testing the equivalence principle with dual interferometers using ^{85}Rb and ^{87}Rb . From the discussion in Sec. 1.3.2, it is essential that these dual interferometers be simultaneous so that the effects of vibration cancel as a common mode in the differential acceleration signal $g_{87} - g_{85}$ between the two species. We have implemented a dual species $^{85}\text{Rb}/^{87}\text{Rb}$ atom source and have recently begun to carry out large area dual species interferometry. Progress toward our test of the equivalence principle is described in Ch. 9.

1.3.4 Tests of Quantum Mechanics at Macroscopic Scales

The realization of interferometers with massize particles is a dramatic manifestation of the fundamentally quantum mechanical wave nature of matter and the related concept of quantum superposition. The quantum mechanical features of such interferometers can be illustrated with a simple thought experiment. Imagine the analog of an interferometer for a collection of classical billiard balls. In classical mechanics, the closest possible counterpart to a beam splitter is a switch that randomly directs each billiard ball into one of two paths with equal probability. Since classical particles have definite trajectories, each billiard ball must take one path or the other. The two paths eventually overlap on a second switch that, with equal probability, randomly places each billiard ball into one of two output ports. If many billiard balls are run through this contraption, half the balls will end up in one outport port and half will end up in the other output port, up to small deviations from counting statistics. The situation in quantum mechanics is very different. Instead of following from classical probabilities, the population distribution of the two output ports can behave as if two wavelike amplitudes corresponding to propagation along the two interferometer arms are superposed at the final beam splitter, allowing the output ports to vary between full constructive and destructive interference. In this situation, each of the particles that runs through the interferometer and is ultimately detected necessarily has quantum mechanical amplitude in both interferometer paths, and the distinctly nonclassical behavior of the interferometer output ports arises from the superposition and interference of such amplitudes [44].

In order to realize this ideal wavelike behavior, with the population varying between the two interferometer output ports with perfect contrast over a set of experimental shots, the particles must all contribute in phase to the interference for each experimental shot. In the notation of Eq. (1.29), the phases ϕ_i of each sub-ensemble of particles must all be the same. Additionally, to observe interference, the quantum states $|\psi_1\rangle_i$ and $|\psi_2\rangle_i$ corresponding to the two interferometer arms for each sub-ensemble i cannot become orthogonal. The ability to make all particles contribute to the interferometer in phase is directly related to the ability of the interferometer to perform differential measurements, as it implies that the differential phases

$\phi_i - \phi_j$ between different sub-ensembles are well-controlled, and therefore that any differential phase perturbation that is accumulated as the particles travel over the interferometer paths will be directly reflected in the interference pattern observed by resolving different sub-ensembles (e.g., using spatially resolved detection to observe a differential interferometer phase shift between the left and right halves of an atom cloud induced by the Earth's rotation as in [29]).⁷

It can be thought of as intuitively bothersome that quantum mechanics predicts the possibility of the wavelike behavior described above for massive particles, especially when the interferometer path separation, the interferometer duration, and/or the masses of the particles involved enter the macroscopic realm. In stark contrast to classically intuitive notions, the interference is a fundamentally nonlocal effect, involving the well-correlated superposition of widely separated trajectories for each massive particle. The somewhat counter-intuitive nature of matter wave interferometry has led to speculation about whether quantum mechanics breaks down at sufficiently macroscopic scales, preventing the observation of interference contrast for matter wave interferometers with macroscopic enclosed spacetime area and/or macroscopic particle mass [38, 9]. In practice, we know that it is highly challenging to prevent contrast loss arising from non-common environmental disturbances to the wavepackets associated with each interferometer arm as they propagate over paths separated by large distances for long times (e.g., see Sec. 1.2.3). Perhaps there are fundamental mechanisms that prevent such disturbances from being common for sufficiently macroscopic interferometers. Generally speaking, such mechanisms might couple to the motional degrees of freedom and/or any other degrees of freedom associated with a particle. With continued improvement in matter wave optics, matter wave interferometry can continue to probe quantum mechanics in increasingly macroscopic regimes.

⁷A situation in which each differential phase shift $\phi_i - \phi_j$ is non-zero but well-controlled is closely related to the situation in which all the phase shifts ϕ_i are equal. This is because in the aforementioned case, compensating differential phase shifts could, at least in principle, be applied to each $\phi_i - \phi_j$ to make all the sub-ensemble phase shifts equal, and the differential phase signals would be preserved in the knowledge of the compensations applied.

1.3.5 Gravitational Wave Detection

Gravitational wave observatories offer a new way to study fundamental questions in astrophysics and cosmology [45]. Atom interferometry has the potential to be a valuable tool for gravitational wave detection and to complement existing and planned gravitational wave detectors that use laser interferometry and macroscopic proof masses [46, 47, 48, 49]. Possible advantages of atomic gravitational wave detectors include the ideal features of freely falling, neutral atoms as inertial proof masses, the ability to enhance the signal with LMT atom optics, and the ability to implement pulse sequences that are insensitive to laser phase noise [3]. Proposals for atomic gravitational wave detectors involve simultaneously operated pairs of atom interferometers separated over long baselines, with the atom optics lasers shared by both interferometers [39, 40]. The gravitational wave signal enters as a differential phase shift $\Delta\phi_{\text{GW}}$ between the two interferometers. For a three-pulse Mach-Zehnder interferometer sequence with pulse spacing T , a fully general relativistic calculation shows this differential phase shift to be

$$\Delta\phi_{\text{GW}} = 2k_{\text{eff}}hL \sin^2\left(\frac{\omega T}{2}\right) \sin(\theta_{\text{GW}}), \quad (1.30)$$

where $k_{\text{eff}} = n\hbar k$ is the effective interferometer k -vector corresponding to the number n of photon momentum recoils transferred by the LMT beam splitters, h is the gravitational wave strain, L is the baseline length, ω is the gravitational wave frequency, and θ_{GW} is the gravitational wave phase. Equation (1.30) assumes that the wavelength of the gravitational wave is much larger than L [39].

A ‘back-of-the-envelope’ estimate of the scaling of this phase shift can provide some (not fully rigorous) physical intuition for its origin. We will think of the gravitational wave strain as inducing a time-dependent oscillation $\sim hL \sin(\omega t)$ in the distance between the two atomic test masses separated over the baseline L . This corresponds to a relative acceleration $a_{\text{GW}} \sim -hL\omega^2 \sin(\omega t)$ between the two test masses. The differential phase shift between the two interferometers reflects this relative acceleration via the known interferometer acceleration response from Eq. (1.23), yielding

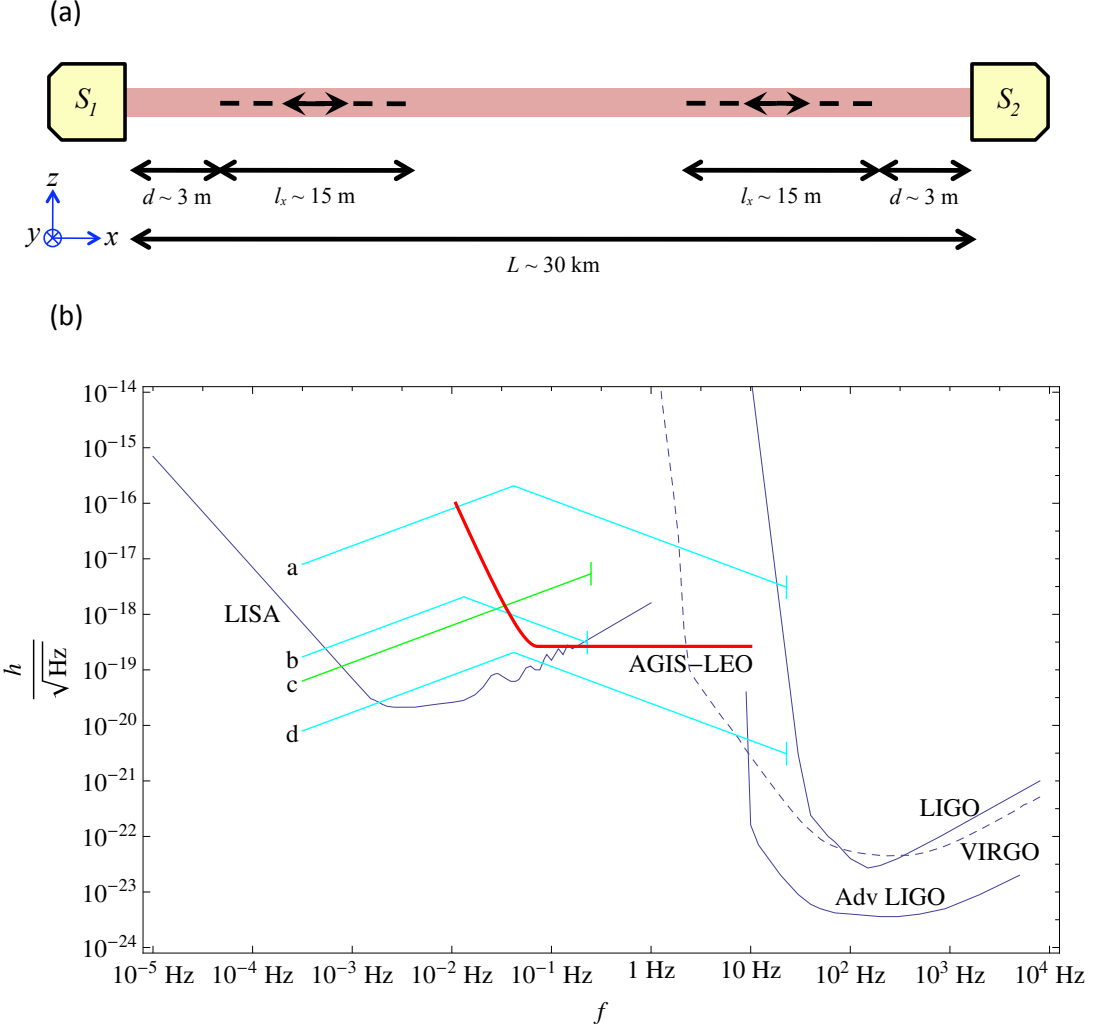


Figure 1.4: Schematic and sensitivity curve of a proposed satellite based atomic gravitational wave detector. (a) Diagram of a baseline for a proposed atomic gravitational wave interferometric sensor in low Earth orbit (AGIS-LEO). Atom interferometers are run near a pair of satellites separated by an $L = 30$ km baseline. Each individual interferometer has a longitudinal spatial extent of approximately 15 m. (b) Strain sensitivity as a function of frequency for this detector (red curve). Interferometer parameters are beam splitter momentum $\hbar k_{\text{eff}} = 200\hbar k$, pulse spacing $T = 4$ s, and phase sensitivity $\delta\phi = 10^{-4} \text{ rad}/\sqrt{\text{Hz}}$. Curves a-d show gravitational wave source strengths after integrating over the lifetime of the source or one year, whichever is shorter: (a) represents inspirals of 10^3 solar mass (M_\odot), $1M_\odot$ intermediate mass black hole binaries at 10 kpc, (b) inspirals of $10^5 M_\odot$, $1M_\odot$ massive black hole binaries at 10 Mpc, (c) white dwarf binaries at 10 kpc, and (d) inspirals of $10^3 M_\odot$, $1M_\odot$ intermediate mass black hole binaries at 10 Mpc. Figures are from [40].

$$\Delta\phi_{\text{GW}} \sim -k_{\text{eff}}a_{\text{GW}}T^2 \sim k_{\text{eff}}hL\omega^2T^2 \sin(\theta_{\text{GW}}), \quad (1.31)$$

where we associate ωt with the phase θ_{GW} of the gravitational wave. Equation (1.30) displays the same scaling if we Taylor expand in the limit $\omega T \ll 1$.

In [40], we performed a detailed analysis of possible experimental parameters for a satellite based atomic gravitational wave interferometric sensor (AGIS). Figure 1.4(a) shows a schematic of the proposed apparatus. The two interferometers along a given baseline are respectively carried out near two satellites separated over the baseline. The atom optics pulses come from lasers on the satellites. We analyzed a broad range of possible noise backgrounds—including rotations, laser wavefront and atom distribution fluctuations, and Newtonian gravitational backgrounds from the Earth and from satellite position jitter—and associated mitigation strategies. For example, we designed a specialized five-pulse interferometer sequence to reduce the sensitivity of the interferometer to background rotations and gravity gradients. The largest Newtonian gravitational background arises from non-spherical Earth gravity inhomogeneities, which are a significant systematic effect for frequencies below 30 mHz. The effect of these inhomogeneities on the AGIS sensor orbiting at an altitude of 1000 km was estimated using a spherical harmonic model of the near-Earth gravity field [40]. Lunar tidal forces are also a significant effect below 1 mHz. Our analysis showed that free Earth oscillations would not be a significant measurement background, nor would the effect of gravitational waves on masses within the Earth. I will not repeat the detailed analysis of [40] in this thesis. Figure 1.4(b) shows a calculated strain sensitivity curve for a proposed set of interferometer parameters that could be feasible for satellites in low Earth orbit (LEO) based on the analysis in [40]. Figure 1.5 shows a strain sensitivity curve with a more ambitious set of parameters that might be realized in the further future, with the aim of showing potential for improvements as technology continues to develop. For comparison, sensitivity curves for existing (LIGO [46], Advanced LIGO [47], and VIRGO [48]) and proposed (LISA [49]) laser interferometry detectors with macroscopic proof masses are also included. Much of the work in this thesis has been motivated in part by developing techniques for the

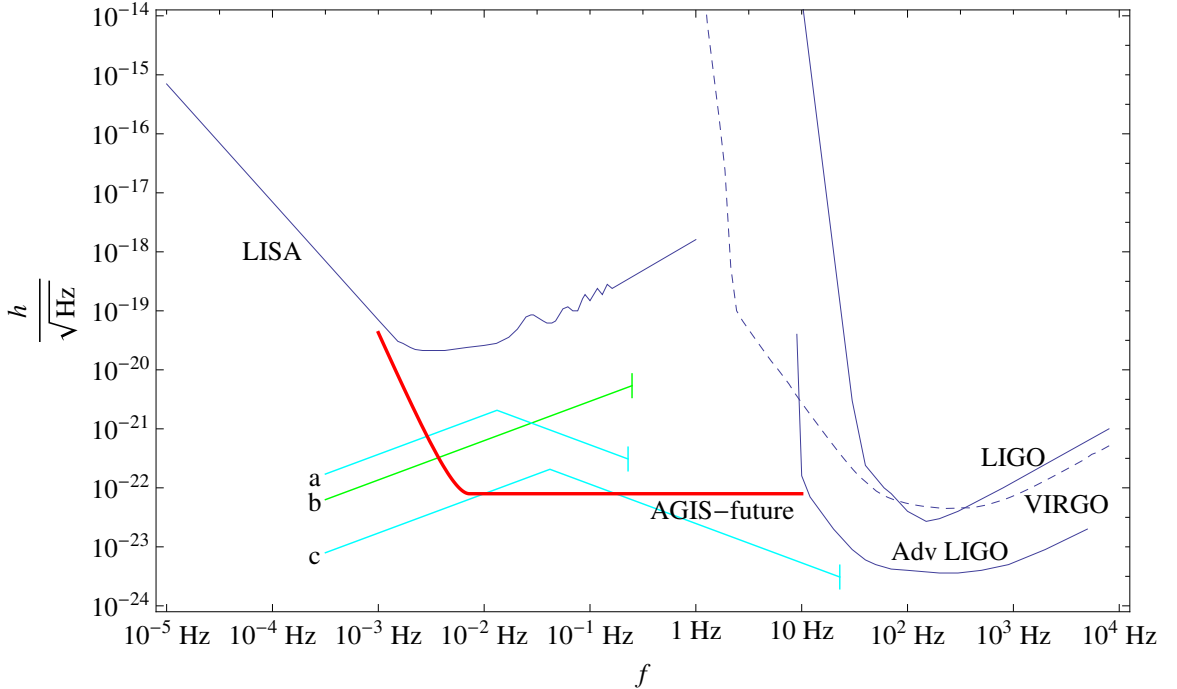


Figure 1.5: Strain sensitivity as a function of frequency for an AGIS detector with a more ambitious set of parameters that could be realized further into the future (red curve). Interferometer parameters are baseline $L = 10^4$ km, beam splitter momentum $\hbar k_{\text{eff}} = 200\hbar k$, pulse spacing $T = 40$ s, and phase sensitivity $\delta\phi = 10^{-5}$ rad/ $\sqrt{\text{Hz}}$. Curves a-c show gravitational wave source strengths after integrating over the lifetime of the source or one year, whichever is shorter: (a) represents inspirals of $10^5 M_\odot$, $1M_\odot$ massive black hole binaries at 10 Gpc, (b) white dwarf binaries at 10 Mpc, and (c) inspirals of $10^3 M_\odot$, $1M_\odot$ intermediate mass black hole binaries at 10 Gpc. Figure is from [40].

very large area interferometers that would be required for an atomic gravitational wave detector.

1.4 Matter Wave Lensing

Gaining improved control of physical systems by making them increasingly cold has led to many important advances [50, 51, 52]. As discussed in Sec. 1.2.3, from the point of view of atom interferometry, transversely cold atom sources⁸ are critical for very large area interferometers, especially envisioned space-based interferometers with pulse spacings of tens of seconds that would be valuable for applications such as gravitational wave detection [39, 40]. The atom source for the 10 m atomic fountain uses evaporative cooling to reach effective temperatures of 20 nK for ^{87}Rb atoms. To reach even lower temperatures, we make use of a technique that we refer to as lensing due to its conceptual similarity to collimating light with a lens [53].

To perform lensing on an atomic ensemble, an initially small atom cloud is allowed to freely expand for a time $t_{\text{expansion}}$. It is useful to think of the lensing process in a phase space picture. For sufficient expansion time, the atom cloud will enter the point source limit, where the position and velocity will be proportionally correlated through the relation $x \approx vt_{\text{expansion}}$. A harmonic potential $V(x) = \frac{1}{2}kx^2$ is then pulsed on for a short time δt , corresponding to a position dependent restoring force $F(x) = -kx$. Because of the position-velocity correlation, the force as a function of velocity can be expressed as $F(v) \approx -kv t_{\text{expansion}}$, leading to a velocity dependent impulse $F(v)\delta t \approx -kv t_{\text{expansion}}\delta t$. If this velocity dependent impulse is equal to $-mv$ (m is the atomic mass) for each velocity v , implying that $\delta t = \frac{m}{kt_{\text{expansion}}}$, then all the atoms are brought to rest. This process is analogous to collimating light from a point source with a lens, where the role of the harmonic potential is played by the parabolic phase profile imprinted by the lens. We refer to the example just described, with the harmonic lensing potential applied for a short time, as the thin lens limit. Lensing can

⁸For the purposes of this thesis, we define ‘cold’ from the perspective of the effective temperature that quantifies the mean kinetic energy of the atoms [2], as this is the relevant quantity for the applications we consider, as well as for many other applications (see Ch. 6.)

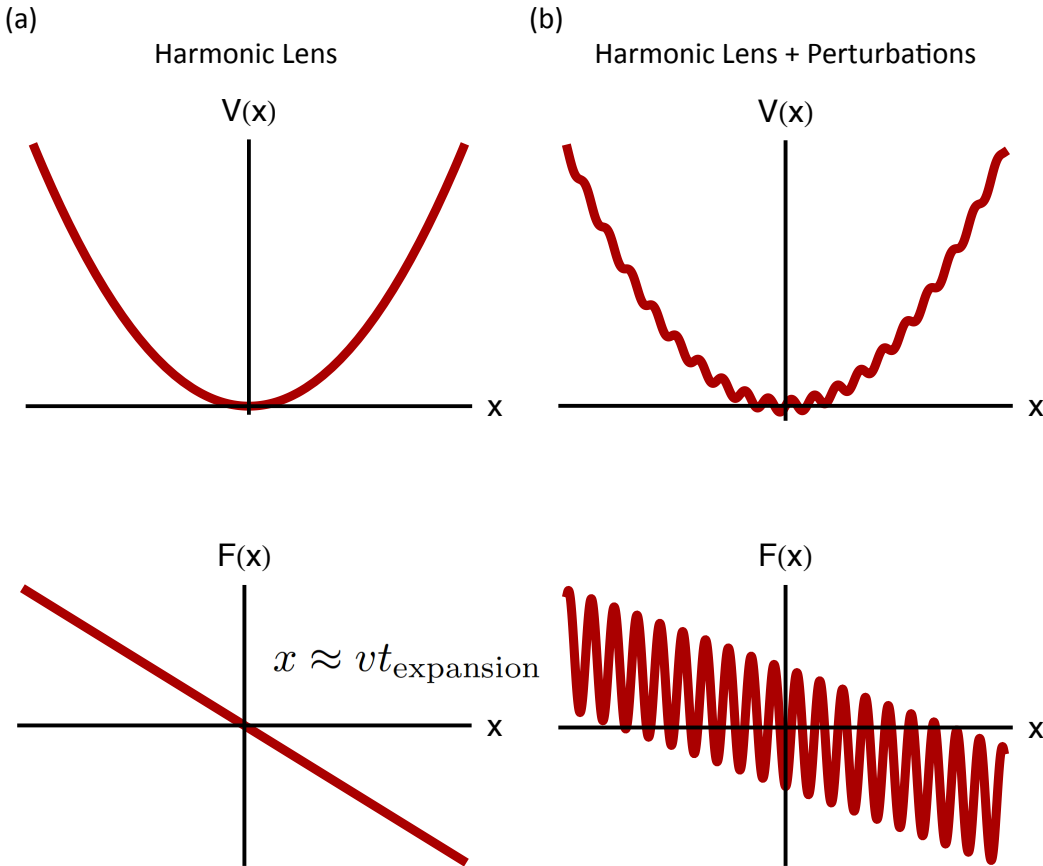


Figure 1.6: Effect of high spatial frequency perturbations on the performance of a lens. (a) Harmonic potential $V(x)$ and force $F(x)$ associated with an ideal lens. (b) Potential and force when high spatial frequency perturbations are added to the ideal lens. Even if the perturbations to the potential have a comparatively small amplitude, the resulting perturbations to the force can be large because they are proportional to the spatial frequency. These force perturbations can lead to significant distortion of the atom cloud.

also be performed in the thick lens limit, where atoms from a point source expand against a constant harmonic potential. All velocities reach a turning point at the same time, at which point the harmonic potential is suddenly turned off.

There are practical limitations to how well a lens can collimate an ensemble of atoms. First, the size of the atom cloud before expansion will never be zero, so there will always be deviations from the perfect point source limit. To be as far into the point source limit as possible, it is useful to have a long expansion time. This makes our 10 m atomic fountain ideally suited to lensing, as discussed in Ch. 6. Second, just as in standard optics, it is difficult to make a perfect lens (i.e., a perfect harmonic potential). Potentials are generally harmonic only near the center, and anharmonicities in the lensing potential cause the performance of the lens to be degraded by aberrations. As shown in Fig. 1.6, high spatial frequency perturbations to the lensing potential are especially harmful. This is because the resulting spurious forces are proportional to the spatial frequency. The work presented in Ch. 6 discusses the limitations of lensing in detail and demonstrates methods to mitigate them.

1.5 Organization of This Thesis

This thesis is organized as follows. Chapter 2 describes our 10 m atomic fountain apparatus, including the atom source and the atom optics laser system that allows us to perform atom interferometry. The theses of previous graduate students who have worked on this apparatus, Jason Hogan [54], David Johnson [55], Susannah Dicker-son [11], and Alex Sugarbaker [12], are also valuable references. Chapters 3 and 4 present earlier work that demonstrated new atom optics techniques in a test apparatus. Relevant aspects of the test apparatus are discussed in these chapters. Chapter 3 discusses the realization of large area atom interferometers that use sequential multiphoton Bragg transition to reach large momentum splittings of $102\hbar k$. Chapter 4 discusses the combination of adiabatic rapid passage (ARP) techniques with multi-photon Bragg transitions to make these Bragg transitions more robust against pulse imperfections. Chapter 5 reports on a novel high power, frequency doubled laser system at 780 nm that has applications in atom optics. Chapter 6 describes a matter

wave lensing experiment in the 10 m atomic fountain that prepares atomic ensembles with ultra-low 50 pK effective temperatures. Chapter 7 presents results from very large area atom interferometry in the 10 m atomic fountain, with pulse spacings of 1 s and path separations of up to 54 cm. Chapter 8 contains a theoretical analysis of atom optics techniques based on manipulations of the atoms with optical lattices, which could lead to interferometers with even larger enclosed spacetime areas as well as interferometers that maintain a high sensitivity with a small size. Finally, Chapter 9 discusses current work toward an equivalence principle test using ^{85}Rb and ^{87}Rb .

Chapter 2

Apparatus

This chapter describes the 10 m atomic fountain apparatus and the experimental features that allow it to be used for atom interferometry. We begin by discussing the methods for generating ultracold atoms and launching them up along the full height of the fountain. Subsequently, we describe additional aspects of the apparatus, including the lasers that are used for atom optics and the magnetic shielding of the fountain. Much of the work in this thesis was performed only with ^{87}Rb atoms. For the equivalence principle test, we made a number of changes to the apparatus to better accommodate ^{85}Rb , which I will describe.

2.1 Ten Meter Atomic Fountain

A key differentiating aspect of our apparatus that enables many of the results presented in this thesis is the 10 m height of the atomic fountain into which the atoms are launched. The tall atomic fountain allows atoms to undergo several seconds of free fall, which is crucial for achieving matter wave lensing to record-low effective temperatures (quantifying the mean kinetic energy) of tens of picokelvin (Ch. 6), atom interferometers with macroscopic enclosed spacetime area (Ch. 7), and improved sensitivity in atomic tests of the equivalence principle (Ch. 9). Our lab is able to accommodate this atomic fountain because the lab has an 8 m deep pit extending into the floor. A photograph of the apparatus from a view looking down into the pit

is shown in Fig. 2.1(a), and a view looking up from the bottom of the pit is shown in Fig. 2.1(b). The atom source (see Sec. 2.2) is located at the bottom of the pit. The atoms are cooled and trapped in a 3D magneto-optical trap (MOT) loaded by a 2D MOT, and subsequently undergo evaporative cooling. The 3D MOT vacuum chamber is attached to an upward-extending 8.8 m long vacuum tube made from aluminum, with a 10 cm diameter. An optical lattice launches the atoms upward into this vacuum tube. A solenoid is wound directly around the outer circumference of the vacuum tube. We drive 34 mA of current through the solenoid to generate a uniform bias field of 130 mG that establishes a quantization axis for the atoms. The vacuum tube is surrounded by a three-layer, cylindrical magnetic shield to reduce external magnetic fields (see Sec. 2.7.1). The entire structure is supported by an 80/20 tower, as shown in Fig. 2.1.

Figure 2.2(a) presents a CAD model of the apparatus. Ultra high vacuum ($< 10^{-10}$ Torr) is maintained in the 3D MOT chamber and the atomic fountain by a pair of ion pumps, one at the bottom of the tower and one at the top. When the atoms fall back to the bottom of the fountain at the end of an experimental sequence, into a detection region just above the 3D MOT, they are imaged using fluorescence detection and CCD cameras (see Sec. 2.5). Figure 2.2(b) shows a schematic of the z axis beam path for the MOT and for the atom optics beams used to drive Bragg transitions. The beam line is expanded to a radial waist of 2 cm by a telescope. The input lens to the telescope has a focal length of 50 mm, and the primary lens has a focal length of 786 mm. The input lens is located in an optics enclosure above the tower (we call this the z box), and the primary lens is mounted in vacuum inside the upper ion pump. The two atom optics beams are overlapped with orthogonal linear polarizations, which are subsequently circularized by a $\lambda/4$ waveplate. The beams are retroreflected by a mirror at the bottom of the pit. This mirror is mounted on a piezo tip-tilt stage and is rotated between interferometer pulses to compensate for Coriolis forces from the Earth's rotation [29]. Another $\lambda/4$ waveplate is mounted in front of the retroreflection mirror, so that σ^- circular polarization is rotated to σ^+ circular polarization, and vice versa. Bragg transitions are driven by counter-propagating frequency pairs with the same circular polarization. Therefore, this $\lambda/4$ waveplate

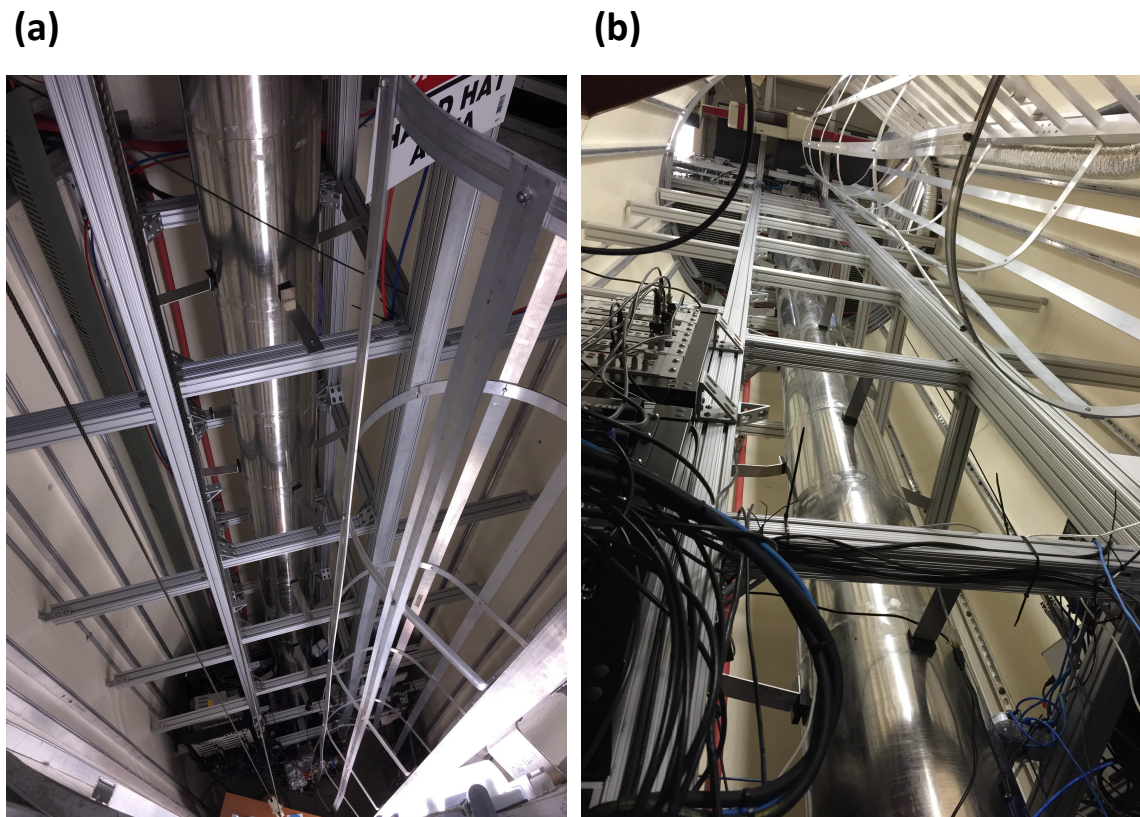


Figure 2.1: Photographs of 10 m atomic fountain apparatus. (a) Looking down at the bottom of the 8 m deep pit where the atom source is located. The atoms are launched upward into the atomic fountain, which is housed inside a magnetic shield (the tall metal cylinder). (b) Looking up from the bottom of the pit. Some of the lasers for cooling and manipulating the atoms are located at the top of the tower. In the upper right corner of the photograph, the ladder that we use to climb into and out of the pit is visible. An 80/20 tower supports the atomic fountain.

ensures that one frequency component from each of the two atom optics beams drives the Bragg transitions.

2.2 ^{87}Rb Cold Atom Source

2.2.1 Overview of cold atom preparation

To prepare ultracold atoms to be launched into the 10 m tower, we initially cool and confine $4 - 7 \times 10^9$ atoms in a 3D magneto-optical trap (MOT). The 3D MOT is loaded by a 2D MOT for approximately 4 s. The 2D MOT cools atoms in two transverse dimensions and uses a separate vacuum chamber from the 3D MOT. The 2D MOT and 3D MOT chambers are connected along the longitudinal direction by a differential pumping stage, which consists of a 5 cm long graphite tube with a 3 mm diameter (graphite is used because it is an alkali getter and should therefore improve the differential pumping performance [56]). The differential pumping stage allows the pressure of the background Rb vapor to be multiple orders of magnitude higher in the 2D MOT chamber ($\sim 10^{-7}$ Torr) than in the 3D chamber ($< 10^{-10}$ Torr). Therefore, the 2D MOT can capture and cool atoms comparatively quickly and use them to load the 3D MOT, while the ultra high vacuum (UHV) in the 3D MOT chamber is not compromised. Maintaining UHV in the 3D MOT chamber is critical, since atoms in the background gas can collide with the ultracold atoms, decreasing the lifetime of the ultracold ensemble.

Following the 3D MOT loading, the atoms are transferred into a tight quadrupole magnetic trap and cooled with forced microwave evaporation. Subsequently, the atoms are further cooled by evaporation in a time-orbiting potential (TOP) trap. We then suddenly weaken the TOP trap to subject the atoms to a magnetic lensing sequence. In the lensing sequence, the atom cloud expands against an approximately harmonic potential, trading off increased size for reduced kinetic energy. This process is analogous to the collimation of an initially diverging optical beam as it travels through a thick lens (hence the name ‘magnetic lens’). The magnetic lens is discussed in greater detail in Chapter 6.

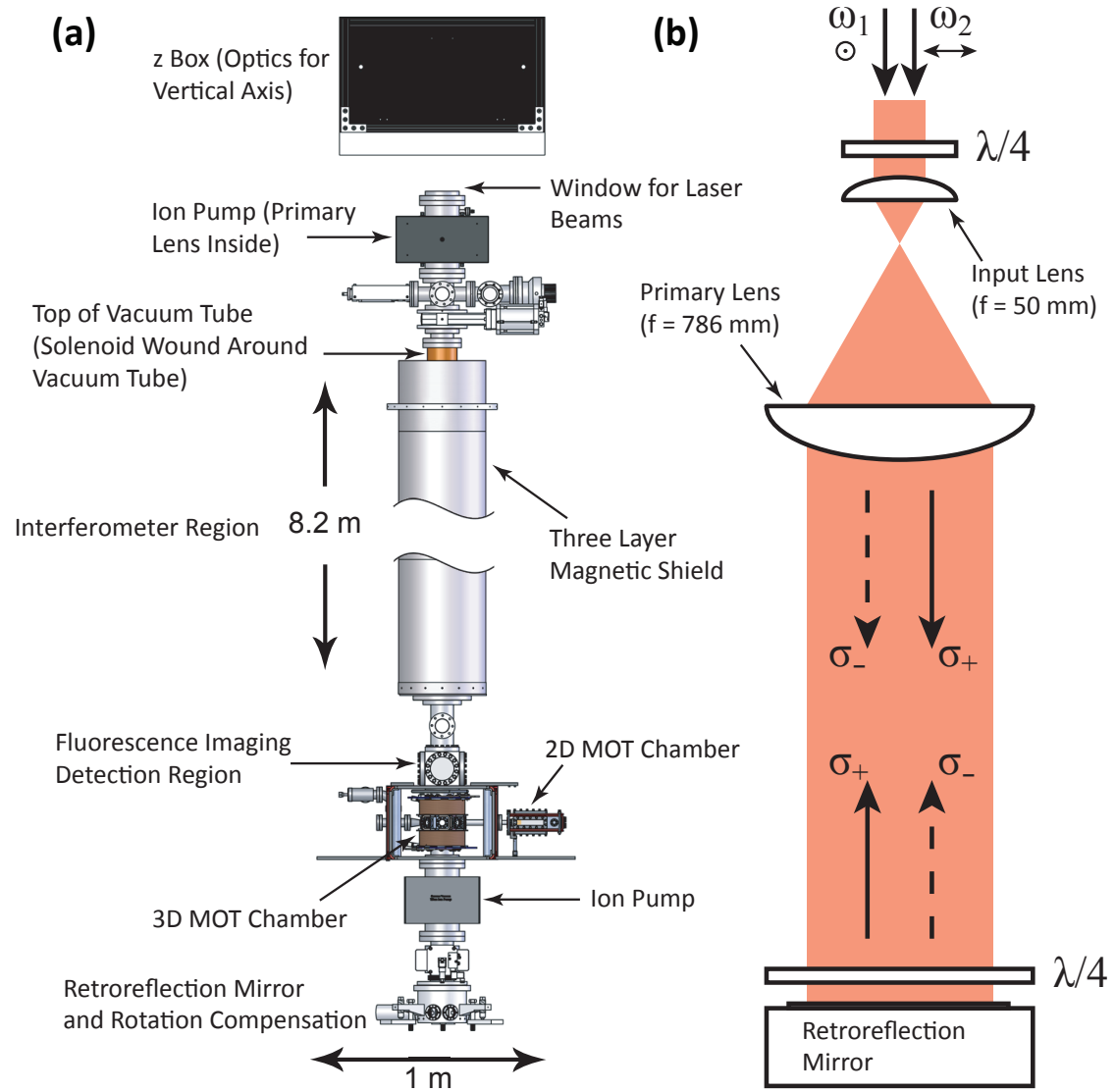


Figure 2.2: Diagram of the 10 m tower apparatus. (a) CAD model of the apparatus. (b) Optics for the z axis MOT path and the atom optics beams. A telescope expands the radial beam waist to 2 cm. The two atom optics beams are labeled as ω_1 and ω_2 . Modified from [12].

2.2.2 Magneto-Optical Trap (MOT)

A MOT cools and traps atoms by providing both damping and restoring forces on the atoms arising from photon scattering. In the 3D MOT, three counter-propagating pairs of laser beams intersect along orthogonal directions (the 2D MOT has two beam pairs). The key concept behind the damping force is that each laser beam is red-detuned from an atomic resonance. Thus, an atom with a given velocity will see the laser beam propagating counter to its velocity blue-shifted onto resonance. The atom will therefore preferentially receive photon momentum kicks that oppose its motion. The restoring force arises from a proper combination of magnetic field gradients and laser beam polarizations. Counter-propagating beam pairs are made to have orthogonal circular polarizations (σ^+ and σ^-). Magnetic fields shift the resonances for σ^+ and σ^- transitions in opposite directions. The σ^+ beam will therefore be shifted closer to resonance on one side of a magnetic field zero, and the σ^- beam will be shifted closer to resonance on the other side of the magnetic field zero. If the beams are oriented appropriately, an atom displaced from the magnetic field zero will receive photon momentum kicks back toward the field zero from one of the two beams [2].

In our apparatus, the magnetic field gradients for the 3D MOT are generated by a pair of vertically oriented quadrupole coils (see Fig. 6.1(a)). For the 3D MOT, we run 6 A of current through the quadrupole coils. Three additional coil pairs (in the x , y , and z directions, with z being vertical) are used to trim bias magnetic fields and stray magnetic field gradients. The current in each of the six trim coil is independently controllable. The magnetic field gradients for the 2D MOT are generated by two additional pairs of anti-Helmholtz coils.

A crucial ingredient for the MOT is a laser system that generates all the necessary optical frequencies. For ^{87}Rb (^{85}Rb), the cooling occurs on the $F = 2 \rightarrow F' = 3$ ($F = 3 \rightarrow F' = 4$) D_2 line transition. These cooling transitions are closed, so in principle one might hope that no other frequencies are necessary. However, there is a small probability of off-resonant excitation of the $F = 2 \rightarrow F' = 2$ ($F = 3 \rightarrow F' = 3$) transition. Selection rules allow population in $F' = 2$ ($F' = 3$) to decay into the lower hyperfine ground level, $F = 1$ ($F = 2$), where population would eventually accumulate without any additional optical frequencies. In order to prevent this from

happening, we pump population out of the lower hyperfine ground level using light resonant with a repump transition. A repump transition must involve an excited state hyperfine level that can decay into the upper hyperfine ground level, $F = 2$ ($F = 3$). We use the $F = 1 \longrightarrow F' = 2$ ($F = 2 \longrightarrow F' = 3$) transition for repump.

To generate and deliver the necessary cooling and repump light for the 2D MOT and 3D MOT, we use a combination of phase modulators and optical amplifiers. The MOT light all originates from a Newport Vortex external cavity diode laser that we use as the master laser. The master laser is locked using saturation absorption spectroscopy 480 MHz blue of the crossover resonance between the ^{85}Rb $F = 3 \longrightarrow F' = 2$ and $F = 3 \longrightarrow F' = 4$ transitions. We ultimately need to split the master laser light into many paths, and because the master laser only emits 20 mW of power, we amplify the light with an Eagleyard Photonics tapered amplifier (TA) and subsequently spatially filter it using propagation through an optical fiber. After the optical fiber, there is ~ 150 mW of optical power.

The master light is then split into several directions in order to generate the frequency content needed for the MOT. An array of $\lambda/2$ waveplates and polarizing beam splitter cubes divides the light into four paths: the repump path, the ^{87}Rb cooling path, the ^{85}Rb cooling path, and the optical pumping path. The waveplate angles determine the relative powers in each path. Light directed into the repump path is coupled into a Photline Technologies fiber phase modulator that sinusoidally modulates the light at 2.526 GHz. The master laser frequency is specially chosen so that the +1 phase modulation sideband is resonant with the ^{85}Rb repump transition, and the +2 sideband is resonant with ^{87}Rb repump transition. This choice was made to avoid the need for separate repump paths for ^{85}Rb and ^{87}Rb . The relative power in the ^{85}Rb and ^{87}Rb repump sidebands is controlled by adjusting the rf power driving the phase modulator with a voltage controlled attenuator (VCA). The 2.526 GHz rf source is a computer controlled Analog Devices VCO.

The ^{87}Rb cooling path initially passes through a double-passed acousto-optic modulator (AOM) that downshifts the frequency by 480 MHz. Some of the light is then split off into a separate path that is used for a saturation absorption frequency lock. The remaining light is coupled into a phase modulator that downshifts the frequency

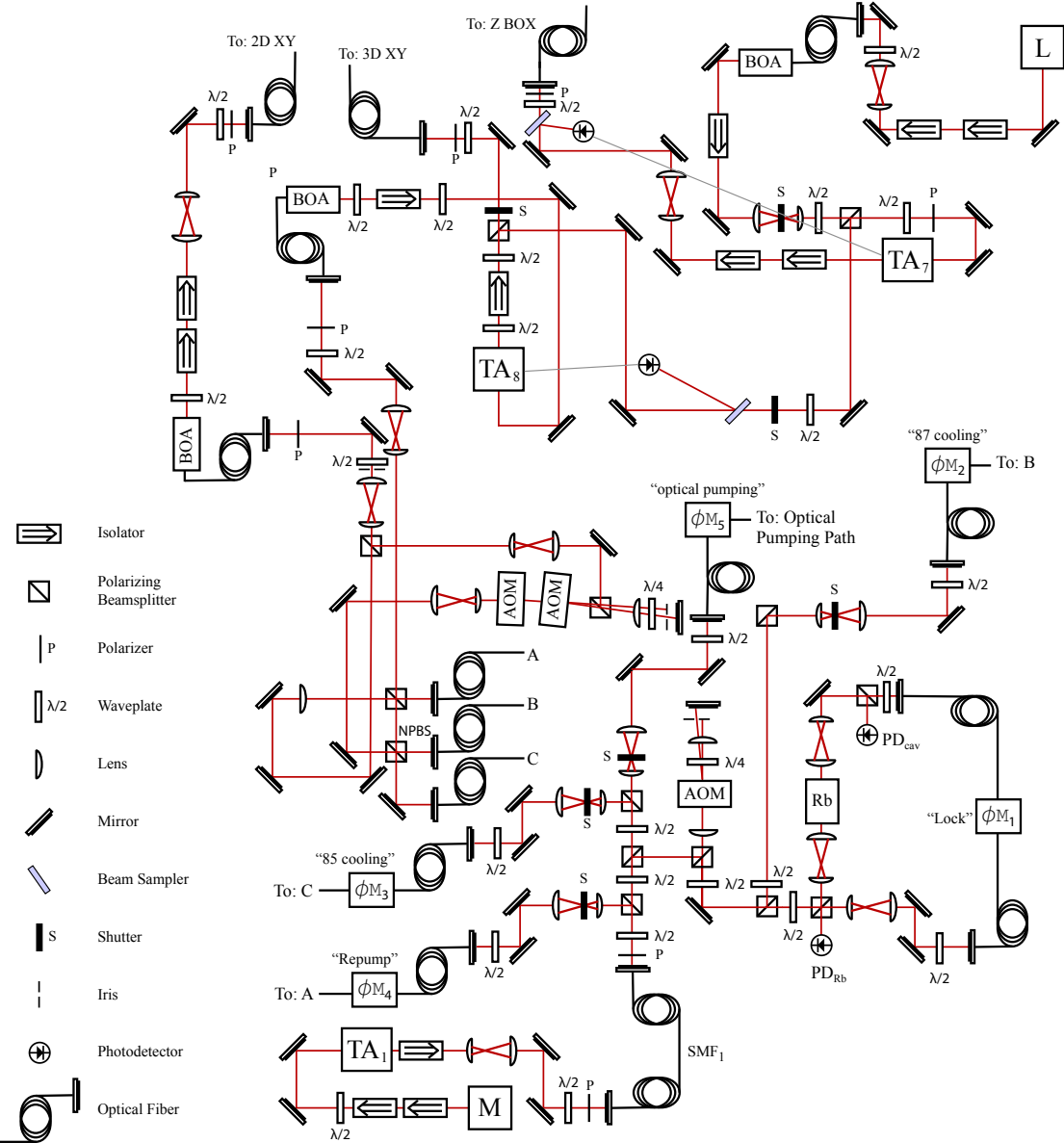


Figure 2.3: Optics layout for MOT lasers. Light originating from a master laser (labeled M) is divided into several paths which are independently phase modulated (fiber phase modulators are labeled ϕM) to generate the necessary frequencies. Light is amplified by BOAs and TAs at various stages. After the phase modulators, light is sent via optical fibers to the bottom of the pit for the 2D and 3D MOTs (fibers labeled 2D XY and 3D XY) and to the top of the pit for the z axis of the 3D MOT (fiber labeled z box). Light from a separate master laser for the optical lattice (labeled L) is also sent to the z box. Updated from [12].

by ~ 1050 MHz so that it is slightly red-detuned from the ^{87}Rb cooling transition. This is achieved using serrodyne frequency modulation instead of the usual sinusoidal frequency modulation, which allows for efficient wideband frequency shifting. The serrodyne waveform is generated by sinusoidally driving a Picosecond Pulse Labs nonlinear transmission line [57]. The frequency source for the ^{87}Rb cooling phase modulator is a Marconi Instruments frequency generator that is mixed with a programmable direct digital synthesizer (DDS) for frequency agility.

The ^{85}Rb cooling path is coupled directly into a third phase modulator that down-shifts the frequency by ~ 400 MHz. The 400 MHz source is a frequency quadrupled DDS channel. Finally, the optical pumping path is coupled into a fourth phase modulator. We discuss the optical pumping procedure in greater detail in Sec. 2.2.4. For experiments that did not use ^{85}Rb , no power was directed into the ^{85}Rb cooling path.

After the phase modulators, the repump path, the ^{87}Rb cooling path, the ^{85}Rb cooling path are combined and directed along two separate paths, using a combination of polarizing and non-polarizing beam splitters. The first of these paths provides light for the 2D MOT. The optical power in the 2D MOT path is amplified to ~ 40 mW by a Thorlabs booster optical amplifier (BOA) and sent to the atom source at the bottom of the pit via optical fiber. There, the light is further amplified to ~ 600 mW by a TA. The cooling light for the 2D MOT path is sent through a pair of AOMs in the push-pull configuration before being combined with the repump light. This allows the cooling light detuning to be independently adjusted for the 2D MOT without affecting the detuning for the 3D MOT. This feature is important, since we empirically find that the loading rate optimizes when the 2D MOT detuning is 4 MHz smaller than the 3D MOT detuning. The 3D MOT detuning is typically 10 MHz for ^{87}Rb and 17 MHz for ^{85}Rb .

The second path provides light for the 3D MOT. The optical power is first amplified by a BOA so as to have sufficient power to seed a TA. After amplification by the TA, most of the light is sent to the x and y axes of the 3D MOT chamber via optical fiber. A small fraction of the light is picked off before this fiber, amplified by another TA, and sent via a separate fiber to the top of the 10 m tower (the z box). In the z box, the light is amplified by a TA and then sent down the atomic fountain and

retroreflected at the bottom of the pit, providing the z axis light for the 3D MOT. A $\lambda/4$ waveplate in front of the retroreflection mirror causes the circularly polarized light to change helicity upon retroreflection, as is necessary for a MOT (see Fig. 2.2(b)). The ratio between repump and cooling powers in the 2D/3D MOT paths is set by projecting the light onto a single polarization axis using an absorptive polarizer just before amplification by each path's respective BOA. Before the polarizer, the cooling and repump light have orthogonal polarizations, with an overall angle set by a $\lambda/2$ waveplate. A diagram of the optics layout for the MOT lasers is shown in Fig. 2.3.

2.2.3 Evaporative Cooling

After loading the 3D MOT (typically $4\text{-}7 \times 10^9$ atoms), we transfer the atoms into a tight quadrupole magnetic trap in order to perform forced microwave evaporative cooling. The transfer process has several stages. For the moment, I will focus on the case with ^{87}Rb only. First, we ramp the detuning of the 3D MOT cooling light to 46 MHz over 30 ms in order to decrease the temperature. Second, we depump the atoms into the $F = 1$ hyperfine level by illuminating the atoms with a 1 ms pulse of light resonant with the $F = 2 \longrightarrow F' = 1$ transition, with the repump light shuttered. Light at the depump frequency is generated by switching the rf input for the ^{87}Rb cooling phase modulator to a 1.458 GHz source. During the depump pulse, we simultaneously perform optical pumping within the $F = 1$ hyperfine level to the $F = 1, m_F = -1$ magnetic sublevel, which is the state we use for evaporation (it is the only magnetically trapped $F = 1$ sublevel). The optical pumping procedure is detailed in Sec. 2.2.4. Finally, we ‘snap up’ the current through the quadrupole coils to 58 A in 700 μs using an LC resonator circuit (the coils are the inductor in this circuit). In comparison to a more gradual increase in current, this ‘snap up’ procedure increases the phase space density of the atoms transferred into the magnetic trap. The dependence of the radial quadrupole field gradient on the current is 0.87 G/cm/A. Similarly, we use a second capacitor in order to quickly remove current from the quadrupole coils when we ‘snap off’ the magnetic trap at the end of the magnetic lensing sequence.

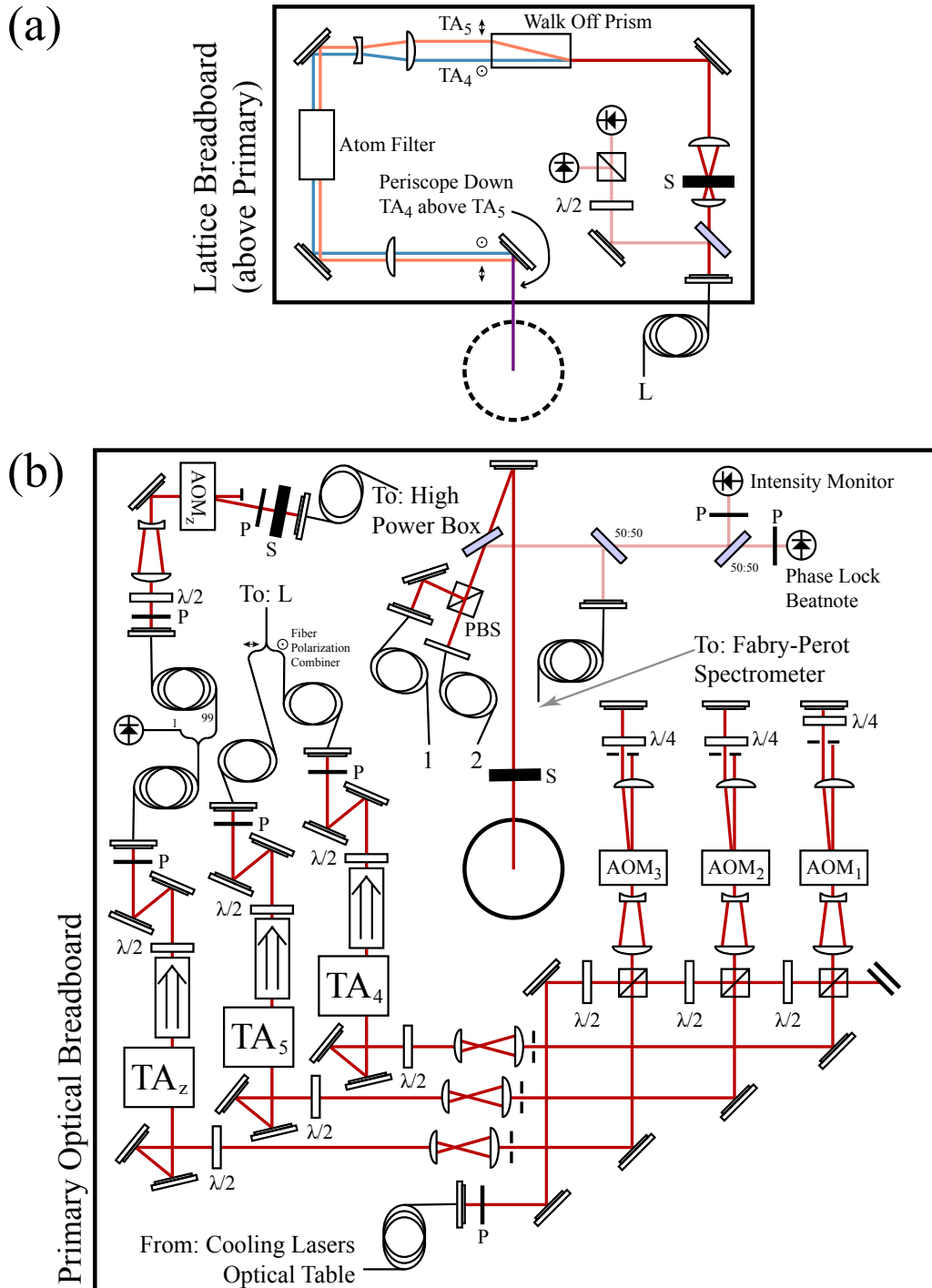


Figure 2.4: z axis optics layout. TA₄ and TA₅ amplify the two lattice paths, while TA_z amplifies cooling light for the z axis of the 3D MOT. The z axis MOT light is coupled into a fiber and combined with one of the atom optics laser beam paths in a separate optics setup. The atom optics paths enter the z box via the fibers labeled 1 and 2 and are directed downward into the atomic fountain. Updated from [12].

The LC resonator circuits are shown in Fig. 2.5. In order to quickly ‘snap up’ the trap, a low current/high voltage power supply keeps a capacitor charged at 650 V (charge circuit in Fig. 2.5). The ‘snap up’ occurs when an IGBT (Powerex CM450DX-24S, rated for 450 A and 1200 V) closes to connect the high voltage terminal of the capacitor to the quadrupole coils, which have an inductance of 4 mH. This begins an LC oscillation, during which the energy stored in the capacitor is converted into current through the coils. A diode (Powerex A390PB, rated for 400 A and 1200 V) placed between the capacitor and the IGBT prevents the current from reversing direction and oscillating back into the capacitor. Once the current has oscillated into the coils, we command the quadrupole coil power supply to this exact current value, so that the current is maintained. A diode in front of the supply prevents current from flowing into the supply during the ‘snap up’ procedure. The ‘snap off’ of the quadrupole current is realized by suddenly opening a second IGBT that connects the supply to the coils. The current then undergoes an LC ring from the coils into a second capacitor (discharge circuit in Fig. 2.5). A diode between prevents current from ringing back into the coils. The capacitor discharges through a $100\ \Omega$ resistor.

Evaporative cooling works by eliminating the hottest atoms from the trap, in our case by a microwave transition that transfers them from the trapped $F = 1, m_F = -1$ state to the untrapped $F = 2, m_F = -2$ state. Hotter atoms are selectively removed by detuning the microwaves from the magnetic-field-free resonance, so that only atoms with enough energy to reach a critical radius away from the trap zero are Zeeman shifted into resonance. Once the hotter atoms are removed, the remaining atoms collide and rethermalize at a lower temperature. This process is repeated, with the critical radius being decreased as the atoms are cooled. After the initial ‘snap up’, we ramp up the quadrupole current to 250 A in order to increase the collision rate and hence the thermalization rate, which allows the evaporative cooling process to proceed more quickly. After 4.5 s, we decrease the current to ~ 100 A in order to lower the atomic density, which increases as the atoms are cooled. We do so in order to avoid three-body losses that occur at high density.

A general concern for evaporation in a quadrupole trap is that once the atoms become cold enough, they will be trapped near the magnetic-field zero, making them

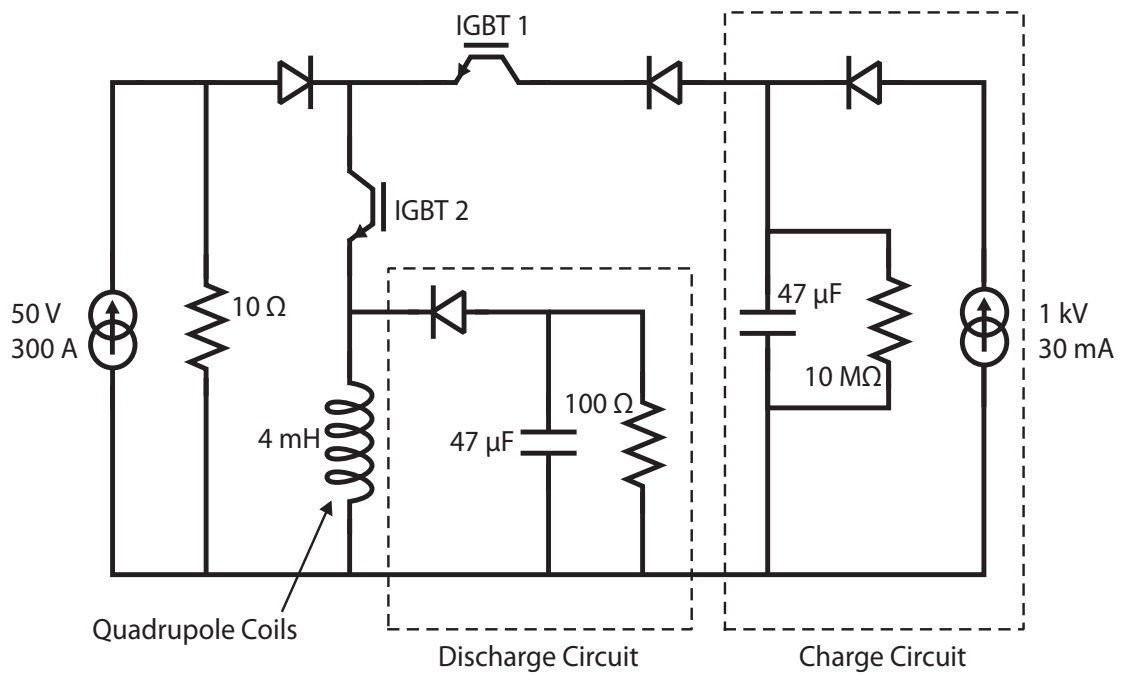


Figure 2.5: Circuit for quickly ‘snapping’ on and off current through the inductive quadrupole coils. IGBT 1 is typically kept open, while IGBT 2 is typically kept closed. To ‘snap up’ the current, we close IGBT 1, allowing energy from the capacitor in the charge circuit to ring into the coils. To ‘snap off’ the current, we open IGBT 2, and the current rings into the capacitor in the discharge circuit. Updated from [11].

more likely to undergo spin flips into untrapped magnetic sublevels (Majorana losses). A common way to solve this problem is to turn on a rotating radial bias field of magnitude B_0 . Where ∇B denotes the radial quadrupole gradient, the new magnetic field zero moves in a circle at radius $r_c = B_0/\nabla B$. As long as the rotation rate is fast enough so that the atoms do not move significantly during a single cycle, the atoms couple to the rotating field through its time-averaged influence on the trapping potential. This time-orbiting potential (TOP) trap has the desirable feature of having a nonzero magnetic field offset at the trapping potential minimum. Additionally, atoms with enough energy to reach the field zero at radius r_c will undergo Majorana losses (the circular trajectory of the field zero is therefore commonly referred to as the ‘circle of death’). By this mechanism, the TOP trap can also contribute to the evaporation, with r_c being decreased as the atoms become colder.

In our apparatus, the rotating bias field is generated by two pairs of coils (see Fig. 6.1a) driven at 2.6 kHz and 90° out of phase. The coils are able to provide a maximum bias field of $B_0 = 7$ G. The TOP field is turned on 6 s into the evaporation. The evaporation then continues for another 8 s, ultimately yielding an ensemble of $\sim 10^5$ atoms with 20 nK effective temperature. After a magnetic lensing sequence (see Chapter 6), the effective temperature is reduced to ~ 1 nK. Between the end of evaporation and the magnetic lensing sequence, the quadrupole current is adiabatically lowered to approximately 20 A over the course of 2 s. The lensing sequence begins when the current through the TOP coils is suddenly increased, weakening the overall trap.

2.2.4 Optical Pumping Before Evaporation

During the 1 ms depump pulse, we optically pump atoms that are depumped into $F = 1$ into the $F = 1, m_F = -1$ magnetic sublevel. To do this, we phase modulate the optical pumping path at 4.86 GHz to generate frequency content on resonance with the $F = 1 \rightarrow F' = 1$ transition. For σ^- circular polarization, $F = 1, m_F = -1$ is a dark state for the $F = 1 \rightarrow F' = 1$ transition in which population will accumulate. On the other hand, population from $F = 1, m_F = 0$ and $F = 1, m_F = 1$ will be

excited into $F' = 1, m'_F = -1$ and $F' = 1, m'_F = 0$, respectively. Some of this excited state population will spontaneously decay into the target state $F' = 1, m'_F = -1$. Some will decay into $F = 1, m_F = 0$ and $F = 1, m_F = 1$, where it will once again be excited. And finally, some will decay into $F = 2$ and be depumped back into $F = 1$ (this is why it is important to carry out the optical pumping in the presence of the depump light).

Light from the optical pumping path (~ 2 mW) enters the 3D MOT along a separate horizontal beamline from any of the MOT beams (the same beamline is used for absorption imaging of the MOT). The bias magnetic field that sets the quantization axis with respect to which the polarization is defined is generated by pulsing on the TOP coils. The polarization will only be σ^- for a particular orientation of the rotating bias field. We therefore set the initial phase between the two TOP coils so that the bias field has the proper orientation when the optical pumping light illuminates the atoms. However, because the orientation of the bias field rotates at 2.6 kHz, the polarization remains close to σ^- for only a short time. This leads us to implement the optical pumping through three short (40 μ s) pulses that are spaced by one period of the bias field rotation. The edges of the pulses are set by an rf switch, which turns on and off the rf modulation into the optical pumping phase modulator. Ultimately, the use of optical pumping increases the number of atoms after evaporation by a factor of 1.5-2.

2.2.5 Optical Lattice Launch

After releasing the atoms from the magnetic lens, we let them freely fall for 60 ms to allow for eddy currents arising from the sudden ‘snap off’ of the quadrupole coils to subside. We then adiabatically load the atoms into an optical lattice potential formed by two counter-propagating laser beams. The loading occurs by ramping up the power of the laser beams over 4-10 ms while the lattice is freely falling with the atoms. The velocity of the optical lattice is determined by the frequency difference between the two beams. By ramping this frequency difference, we accelerate the lattice—and the atoms trapped in it—upward to a velocity of 13 m/s. Subsequently,

we adiabatically release the atoms from the lattice by ramping down the power of the laser beams. The lattice has a depth of 40 times the recoil energy and a $1/e^2$ radial waist of 1.5 mm, and the lattice acceleration is 60-100g.

The lattice beams derive from a Vortex ECDL that is 90 GHz blue detuned from resonance. The blue detuning of the lattice reduces atom loss from spontaneous emission [12]. After amplification by a BOA, the lattice path is combined with the branch of the cooling path that is sent via fiber to the z box (see Fig. 2.3). This combination occurs on a polarizing beam splitter just before the final TA before this fiber. Since we never need the lattice light and the cooling light to be on at the same time, we place shutters just before each input to the polarizing beam splitter, allowing us to switch between seeding the TA with cooling or lattice light.

The optics configuration in the z box is shown in Fig. 2.4. The lattice light is split into two paths, each of which goes through a double-passed AOM that allows for frequency shifting over tens of MHz. The AOM frequency for one path is chirped against gravity, while the AOM frequency for the other path provides for the acceleration of the lattice in a freely falling frame. After the AOMs, each lattice path is amplified by a separate TA and independently fiber coupled. The TA current is used to control the intensity of each lattice beam. The two lattice paths are combined on an in-fiber PBS. After being coupled back into free space, the two orthogonally-polarized lattice beams pass through a polarization walk-off crystal, which spatially displaces the two beams while keeping them parallel. The lattice beams are then directed downward into the atomic fountain at a 2 mrad angle from the vertical. The downward going and retroreflected lattice beam pairs form a W-configuration in which the atoms are hit only by the retroreflected beam from one lattice path and the downward going beam from the second lattice path [12, 11]. If the lattice were in a retroreflected configuration without the 2 mrad angle, the atoms would also see a mirror image of the desired lattice potential. When the lattice velocity passes through zero, the lattice and its mirror image would become degenerate, leading to atom loss that we avoid with the W-configuration.

2.2.6 Water Cooling of Quadrupole Coils and Repair of Leaks

While the quadrupole coils run at high current during the evaporation, they dissipate 12.5 kW of power (50 V, 250 A). This high power dissipation requires that the coils be water cooled. The coils are made of copper and have square cross sections with empty space in the middle through which cooling water is run. The upper and lower coils are divided into six segments. The ends of these segments are sequentially electrically connected and have independent connections to hoses. Thus, from the main water line, the quadrupole coils have a total of 12 input hoses and 12 output hoses. At each joint between quadrupole coil and hose, the square coil is attached to a circular hose connector. The gaps between the square and circular cross sections were originally sealed with solder. In the ten years since these joints were made, the solder on some of the joints underwent a noticeable amount of corrosion. Several of the joints began to leak.

In order to repair the leaking joints and other joints that looked significantly corroded, we resealed the connections with JB Weld Marine Epoxy. Before applying the epoxy, we used moist, coarse grained sandpaper to remove corroded material (we moistened the sandpaper so that the corroded dust was not kicked into the air). Additionally, we removed a section of insulation from the coil so that the epoxy could bond directly to the copper. The epoxy takes several hours to set, and a full day to cure. To prevent all the epoxy from flowing to the bottom of joint while it was setting, we used Kapton tape to make a mold for the epoxy. With the mold in place, the full circumference of the joint was well covered by epoxy. Figure 2.6 shows pictures of an example of a joint between the square copper wire and a hose connector. The epoxy seals were applied in September 2015.

2.3 Dual Species $^{87}\text{Rb}/^{85}\text{Rb}$ Cold Atom Source

2.3.1 Upgraded MOT Laser System

The MOT laser system described in Sec. 2.2.2 was able to create dual species MOTs of ^{87}Rb and ^{85}Rb . However, we found that in order to load a sufficient number of

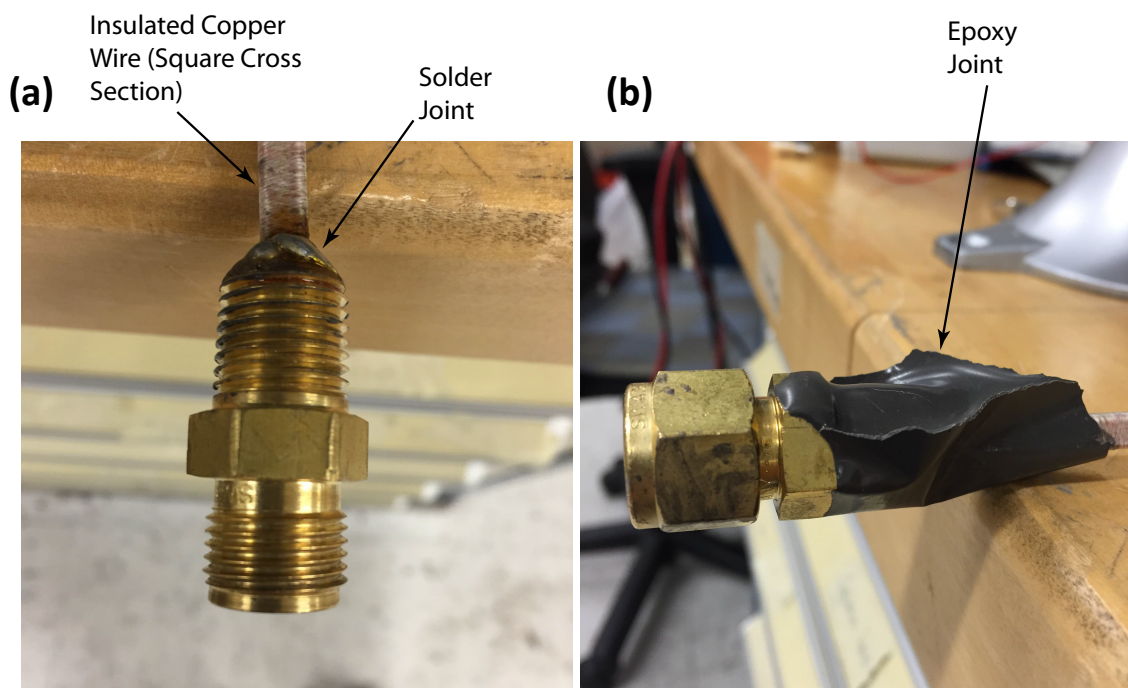


Figure 2.6: Example of a joint between square copper wire like that used for the quadrupole coils and a hose connector. (a) Joint sealed by solder. (b) Epoxy added to improve the seal.

^{85}Rb atoms, the number of ^{87}Rb atoms was necessarily compromised. Moreover, the atom numbers for both species were more unstable from shot to shot than for ^{87}Rb alone. We identified these undesirable behaviors as arising from the fact that the ^{87}Rb cooling, ^{85}Rb cooling, and repump paths were all combined prior to several subsequent amplification stages in TAs. This led to gain competition in the TAs, reducing the available optical power for each path. Moreover, putting so many different frequency components into a sequence of TAs gave rise to a messy spectrum, with a significant fraction of the power ending up in unwanted intermodulation peaks. Ultimately, we decided to redesign the MOT laser system, mostly decoupling the amplification stages for each path. With these improvements, we can now load the desired $10^7\text{-}10^8$ ^{85}Rb atoms into the MOT without decreasing the number of loaded ^{87}Rb atoms (which is now typically 7×10^9). Additionally, the new optical path was made more compact and uses steel mirror mounts in key locations to improve the stability of fiber couples. This reduces the amount of time needed to tweak up alignments in the path each day. A schematic of the updated dual species laser system is shown in Fig. 2.7.

Before the fiber phase modulators, the new MOT laser system is unchanged from the setup described in Sec. 2.2.2. After the phase modulators, instead of immediately combining the ^{87}Rb cooling, ^{85}Rb cooling, and repump paths as before, each of these three paths is independently amplified. For each of the two cooling paths, we use a Thorlabs 2 W TA module. These modules have a fiber-coupled input and a free space ouput. We use a fiber-fiber connector to attach the output of the fiber phase modulator to the input of the Thorlabs TA. The TA output modes are elliptical, so we circularize them with anamorphic prism pairs to improve subsequent fiber coupling efficiency. The repump path is amplified by a BOA and then an Eagleyard TA. We use home designed butterfly mounts for the Thorlabs 2 W TA modules (see Fig. 2.8). The mounts were machined from aluminum blocks and allow for water cooling of the TAs.

After amplification, different combinations of the ^{87}Rb cooling, ^{85}Rb cooling, and repump light are separately sent to the 2D MOT, the 3D MOT x and y paths, and the 3D MOT z path. The ^{87}Rb and ^{85}Rb cooling paths are combined on a nonpolarizing 50:50 beamsplitter cube. One output of this beamsplitter is coupled into a fiber that

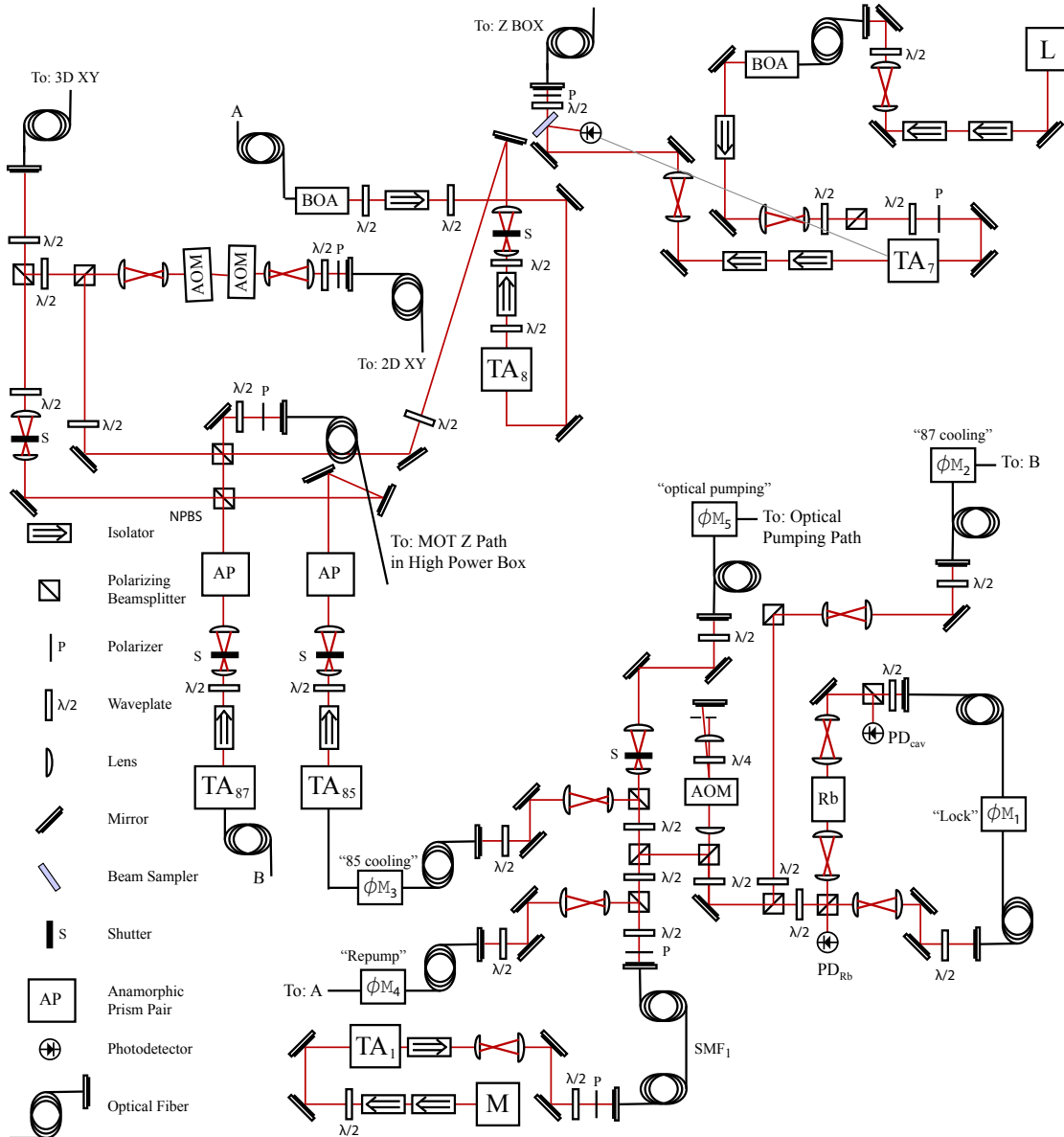


Figure 2.7: Updated MOT laser optics path for the optimized dual species source. The redesigned optical setup performs nearly all amplification before the ^{87}Rb cooling, ^{85}Rb cooling, and repump paths are combined.

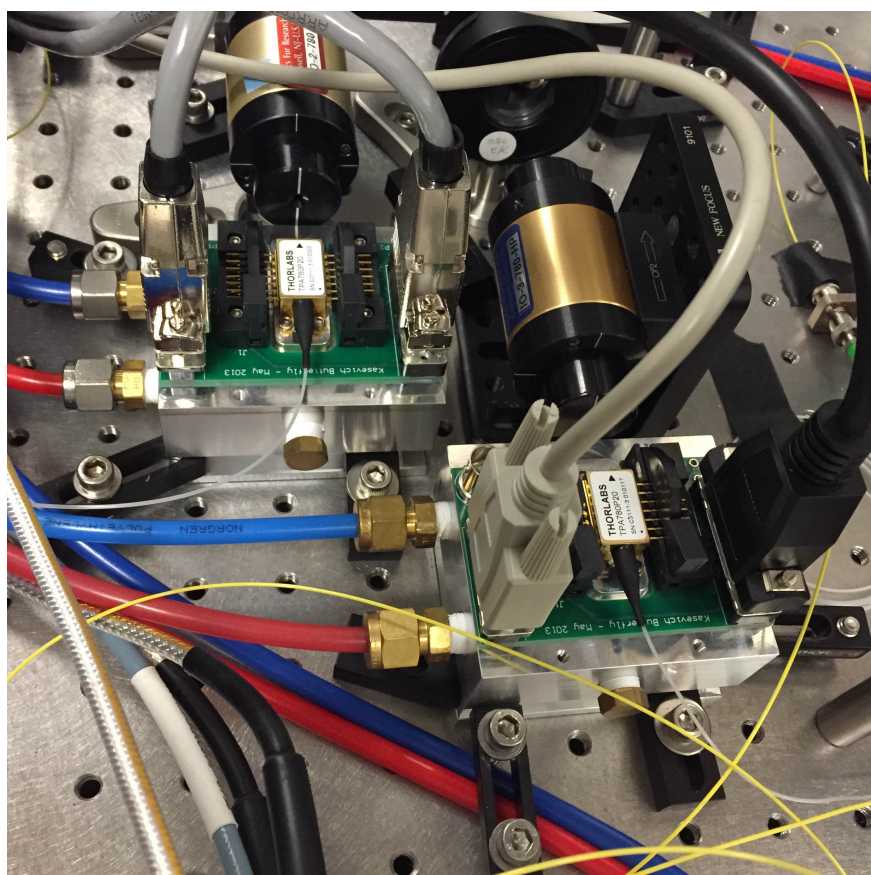


Figure 2.8: Home designed mounts for Thorlabs 2 W TA modules. The mounts hold the TAs in place, provide cable connections for TA current and temperature control, and are connected to hoses for water cooling.

leads to the 3D MOT z path. Enough power is coupled into this fiber so that it is no longer necessary to have an additional TA at the top of the tower to further amplify the 3D MOT z path. Between the nonpolarizing beamsplitter and the fiber, some repump light is inserted into this path using a polarizing beam splitter. A reflective polarizer just before the fiber then fixes the ratio of cooling light to repump light.

The second output of the nonpolarizing 50:50 beamsplitter cube is coupled into a fiber that provides light to the x and y axes of the 3D MOT. Just before this second fiber, a polarizing beam splitter picks off a small fraction of the cooling light and directs it through the push-pull AOM pair (see Sec. 2.2.2). Between this polarizing beam splitter and the AOMs, repump light combines into this path on another polarizing beam splitter. After the AOMs, an absorptive polarizer determines the cooling to repump power ratio, and the path is coupled into a fiber leading to the 2D MOT. The 2D MOT path is the only place in the new MOT laser system where amplification occurs after combining the ^{87}Rb cooling, ^{85}Rb cooling, and repump paths (we still use the Eagleyard TA at the bottom of the pit to amplify the 2D MOT light). This additional amplification stage for the 2D MOT does not appear to negatively affect the MOT performance.

2.3.2 Dual Species Evaporative Cooling

The stages just before evaporation and the evaporation itself proceed in a similar manner as for when we prepare ^{87}Rb alone. While the ^{87}Rb MOT detuning is ramped to 46 MHz, we simultaneously ramp up the ^{85}Rb MOT detuning to 70 MHz. During the depump process, we include light on resonance with the $F = 3 \rightarrow F' = 3$ transition for ^{85}Rb in order to depump the ^{85}Rb atoms into $F = 2$. This depump light is generated by switching the frequency of the DDS that acts as the rf source for the ^{85}Rb cooling path phase modulator.

As before, ^{87}Rb is evaporated in the $F = 1, m_F = -1$ state, and ^{85}Rb is evaporated in the $F = 2, m_F = -2$ state. This pair of states has an acceptably low interspecies inelastic collision rate ($\sim 10^{-15} \text{ cm}^3/\text{s}$) so that losses from inelastic collisions do not prevent effective evaporation. The microwave hyperfine splittings for ^{85}Rb and

^{87}Rb are quite different (3.0 GHz versus 6.8 GHz), so it is not difficult to implement species selective forced microwave evaporation. Direct microwave evaporation of ^{85}Rb is hampered by the comparatively low intraspecies collision cross section. Instead, it is more efficient to perform forced microwave evaporation on ^{87}Rb and use the higher interspecies collision cross section between ^{85}Rb and ^{87}Rb to sympathetically cool ^{85}Rb [11]. The evaporation profile proceeds similarly to the case of ^{87}Rb alone, but the overall evaporation process is less efficient because the ^{87}Rb atoms act as a refrigerant not only for themselves, but also for the ^{85}Rb atoms. We therefore cannot efficiently evaporate dual species sources as far as for ^{87}Rb alone, and we typically stop the dual species evaporation after 13 s (instead of 14 s for the ^{87}Rb only source). After evaporation, we perform a modified lensing sequence to reduce the effective temperatures of the ^{87}Rb and ^{85}Rb clouds. The dual species source places additional constraints on the lensing sequence, since we want both species to be approximately collimated at a simultaneous point in time while also having matched vertical center-of-mass velocities so that they can both be simultaneously launched in the lattice. The optimization of the lensing sequence under these constraints is detailed in Chapter 9.

2.4 Atom Optics: High Power Frequency Doubled Laser System

2.4.1 Why Frequency Doubling?

To be able to efficiently drive Bragg transitions for Rb atoms in the ten meter atomic fountain, we need a pair of atom optics laser beams that each contain multiple Watts of power at 780 nm. This high power requirement stems from a combination of several constraints. First, we need the radial waist of the laser beams to be large enough so that even after several seconds of free expansion, the atom clouds see a nearly uniform transverse laser intensity profile. This leads us to use a relatively large radial waist of 2 cm. Second, the two-photon Rabi frequency of the Bragg transitions is proportional to the laser intensity and inversely proportional to the detuning from resonance. If this Rabi frequency is too low, the Bragg pulses become more Doppler

selective, leading to the loss of a large portion of the atoms to longitudinal velocity selection. The intensity is necessarily reduced by the large radial waist, so one might be tempted to maintain a high Rabi frequency by using a smaller detuning. This, however, brings us to our third constraint. The rate at which atoms are lost from the interferometer due to spontaneous emission scales inversely with the square of the detuning, making smaller detuning an unappealing choice. The only satisfactory option is to use as large a detuning as possible (for us ~ 30 GHz), and to achieve sufficiently high Rabi frequency (~ 20 kHz) by increasing the optical power.

Frequency doubling 1560 nm light is one way to achieve a high power 780 nm source. This method leverages the advanced state of fiber amplifier technology at 1560 nm. We find that passing the 30 W output of an IPG Photonics EAR-30K-C-LP-SF fiber amplifier through a 40 mm long Magnesium-doped periodically poled lithium niobate (PPLN) nonlinear crystal (Covision MSHG1550-1.0-40) yields approximately 10 W at 780 nm. In a separate demonstration, we have shown that coherently combining two of these IPG fiber amplifiers and sending the resulting 60 W through two cascaded PPLN crystals gives 43 W at 780 nm (see Ch. 5). We do not implement this coherently combined configuration at the moment because we need our two IPG fiber amplifiers to generate two independent atom optics paths with different frequencies. Future upgrades might use two coherently combined fiber amplifiers for each atom optics path to dramatically increase the power. In comparison to a frequency doubled source, TAs typically output significantly less power (usually about 1-2 W). An interesting option to explore would be to coherently combine an array of many TAs. A Ti:Sapphire laser can provide > 6 W at 780 nm if pumped with enough power (more than 10 W), but such a setup is substantially more expensive than a frequency doubled fiber amplifier.

2.4.2 Frequency Doubling Optics Setup

The optics for the two frequency doubled atom optics paths are arranged in a compact drawer mounted in a 19 inch rack. We refer to this drawer as the high power laser box. The two fiber amplifiers are mounted above this drawer on the same rack,

making the entire laser system transportable. The 19 inch rack stands adjacent to the optics assembly at the top of the tower (the z box). The two atom optics paths are delivered to the z box over 2 m long optical fibers for subsequent delivery into the atomic fountain, as shown in Fig. 2.4. Photographs showing the 19 inch rack mount setup and the inside of the high power laser box are shown in Fig. 2.10.

One might ask why we do not take a similar approach for the high power laser system as for the cooling lasers. That is, for the sake of convenience, why do we not set up the frequency doubling optics on an optical table in a separate room (what we refer to as the optics area in our lab) and deliver the light to the top of the tower via long optical fibers. The most important reason why we do not do this is because the transport of high optical power in long fibers is impeded by stimulated Brillouin scattering, which leads to light being backscattered in the fiber [58]. For the Thorlabs single mode, polarization maintaining fibers that we use, we found that stimulated Brillouin scattering limited the power transmitted through a 5 m fiber to 3 W. With a 2 m fiber, we did not notice any effects of stimulated Brillouin scattering with 7 W of transmitted power. Because the fiber length is constrained due to stimulated Brillouin scattering, the high power laser system must be close to the z box. Since there is limited space at the top of the tower, it was necessary to make the frequency doubling optics compact. Although it took more time to initially align the optics, the compact setup is highly stable, with alignment tweaks often not needed for several months. We performed the initial alignment with the high power laser system sitting on an optical table in the optics area, a more convenient working space than the top of the tower. To bring the laser system to the top of the tower, we needed to bring it outside the building using an engine hoist and lower it through a hatch in the roof above the tower using a home built winch assembly. Remarkably, the optics in the high power laser box stayed well-aligned throughout this process.

A diagram of the optics in the high power box is shown in Fig. 2.9. The output of each fiber amplifier is emitted through an optical isolator at the end of a 1 m long armored fiber. Each isolator is clamped in a fixed position inside the high power box (the isolators are the two long, grey metal cylinders near the outer corners of the box shown in Fig. 2.10(b)). After the isolator, each atom optics path passes through

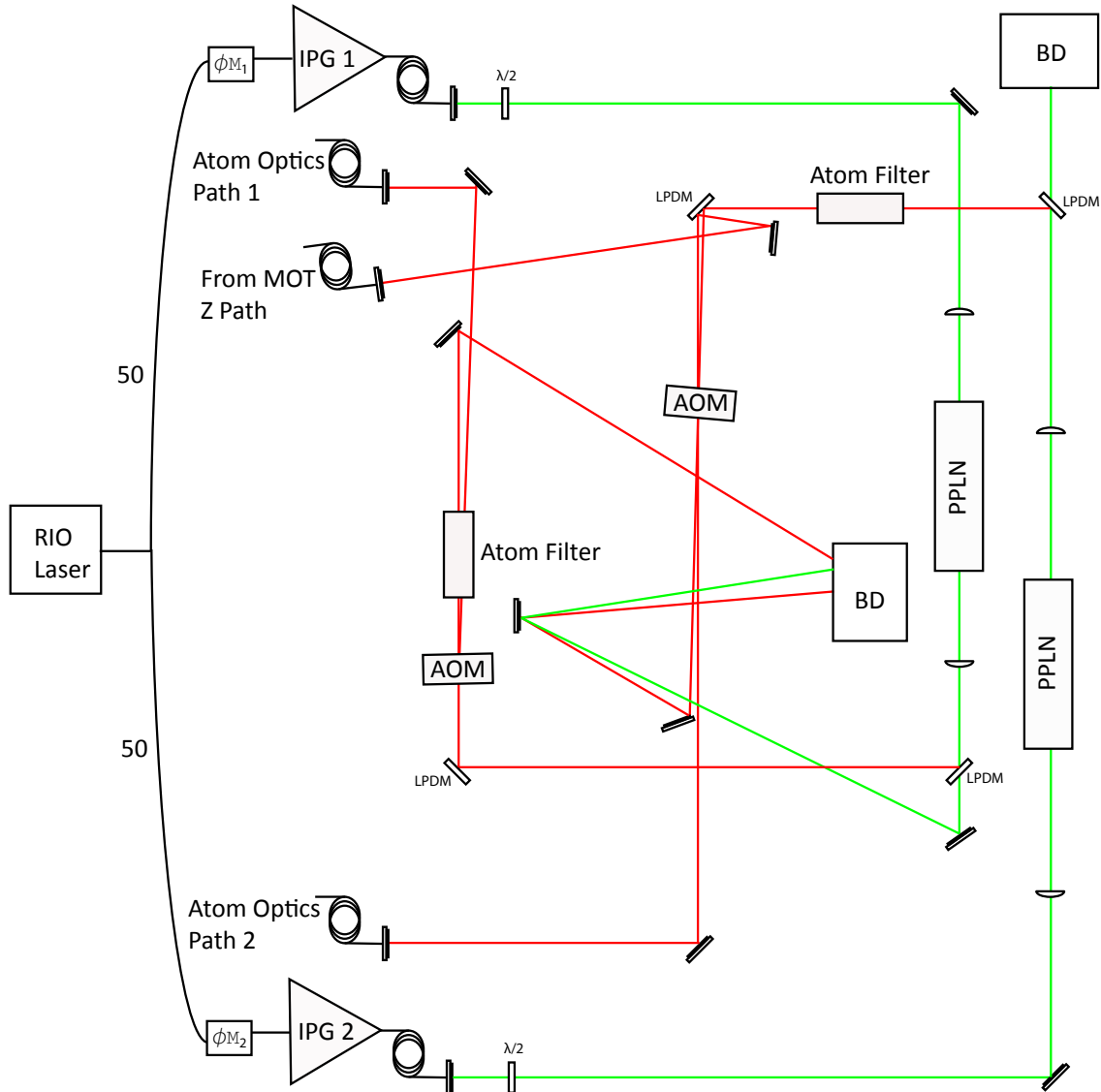


Figure 2.9: High power laser box optics layout. A RIO Orion master laser is split in fiber and seeds the two IPG fiber amplifiers. The seeds of the two fiber amplifiers are independently phase modulated by ϕM_1 and ϕM_2 . In the high power box, the 1560 nm light is doubled by PPLN crystals and directed via fiber into the z box. The z axis MOT path is combined with atom optics path 2 on an AOM. BD: beam dump, LPDM: long pass dichroic mirror, red lines: 780 nm light, green lines: 1560 nm light.

a $\lambda/2$ waveplate and is focused through a PPLN crystal with a 50 mm focal length lens. After the crystal, another 50 mm focal length lens collimates the beam. At this point, the beam contains approximately 10 W of light at 780 nm and 20 W of light at 1560 nm. To remove the 1560 nm light, we make the beam incident on a long-pass dichroic mirror (Thorlabs DMLP1180). The 780 nm light reflects off the mirror, while the 1560 nm light passes through the mirror and is directed into a water-cooled beam dump¹. Subsequently, the 780 nm light passes through an AOM that provides amplitude control and frequency fine-tuning ability. In the steady state condition, the AOM rf drive is switched off so that the AOM does not diffract. When atom optics light is demanded, the AOM is pulsed on, usually with a Gaussian temporal profile for Bragg pulses. A pickoff mirror directs undiffracted light into a beam dump, while the diffracted light is coupled into a fiber and sent to the z box. For a brand new doubling crystal, the power delivered to the z box for a given atom optics path is 5-7 W. As discussed in Sec. 2.4.4, the doubling crystal performance can slowly degrade over many months of use.

As shown in Fig. 2.4, in the z box the two atom optics paths are combined on a PBS and directed to the atoms. The z axis MOT path is directed to the atoms along the same beamline. A convenient way to switch between two beams with the same polarization is to combine them on an AOM. With each beam incident on the AOM at the appropriate angle, the AOM can switch which of the two beams is directed into a given output direction. We combine the z axis MOT path and atom optics path 2 on the path 2 AOM in the high power box in this way. Specifically, the undiffracted z axis MOT beam overlaps with the diffracted path 2 beam, and vice versa. Therefore, when the AOM is diffracting, the path 2 beam couples into the fiber, and when the AOM is not diffracting the z axis MOT beam couples into the fiber. We chose to perform this AOM beam combination in the high power box instead of after path 2 is delivered to the z box so that spatial mode perturbations from the AOM are filtered out by propagation through the optical fiber. This requires that z axis MOT light be fiber coupled into the high power box. For the cooling optics setup described in

¹We initially tried air cooled beam dumps, which would heat up to ~ 100 °C with the fiber amplifiers at full power. The water-cooled beam dumps do not heat up more than several °C.

Sec. 2.2.2, this fiber couple occurs after the z axis MOT TA in the z box, as shown in Fig. 2.4. For the upgraded dual species optics setup described in Sec. 2.3.1, the z axis MOT fiber bypasses the z box and leads directly to the high power box.

In order to reduce spontaneous emission from residual resonant spectral content, which can be present when optical amplifiers are used, the two atom optics paths both pass through atom filters. The atom filters are vapor cells containing ^{87}Rb and heated to 80 °C. For light near resonance, the atom filters are optically thick, so spectral content near resonance is filtered out of the beam. For long sequences of Bragg pulses, we found the atom filters to noticeably reduce atom loss due to spontaneous emission. We have not yet installed atom filters that also contain ^{85}Rb in the high power box—it is likely that we will do this in the future. For path 2, it is necessary that the atom filter is placed before combination with the z axis MOT beam, which would otherwise be dramatically attenuated by the atom filter.

The PPLN doubling crystals are mounted in ovens provided by Coversion and heated to approximately 150 °C. The temperature of a PPLN crystal is tuned to optimize phase matching for doubling a particular frequency. The fact that the phase matching condition for our frequency occurs at a relatively high temperature is advantageous from the point of view of reducing the potential for photorefractive damage from passing high optical power through the crystals². The ovens are heated by computer controlled Arroyo Instruments 5300 temperature controllers. Each oven is mounted on a five axis translation stage to precisely align the crystal relative to the laser beam.

2.4.3 Optical Spectrum of Atom Optics Laser Beams

Bragg transitions can be driven by a standing wave created by a pair of counter-propagating laser beams. An atom will undergo efficient two-photon Bragg diffraction when the relative velocity between the atom and the standing wave is close to $\pm \frac{\hbar k}{m}$ (the sign determines the direction of the two-photon momentum kick from the Bragg diffraction). The frequency difference between the two laser beams controls

²In fact, Coversion has suggested to us that annealing PPLN crystals at 150 – 200 °C might be a way to reverse photorefractive damage

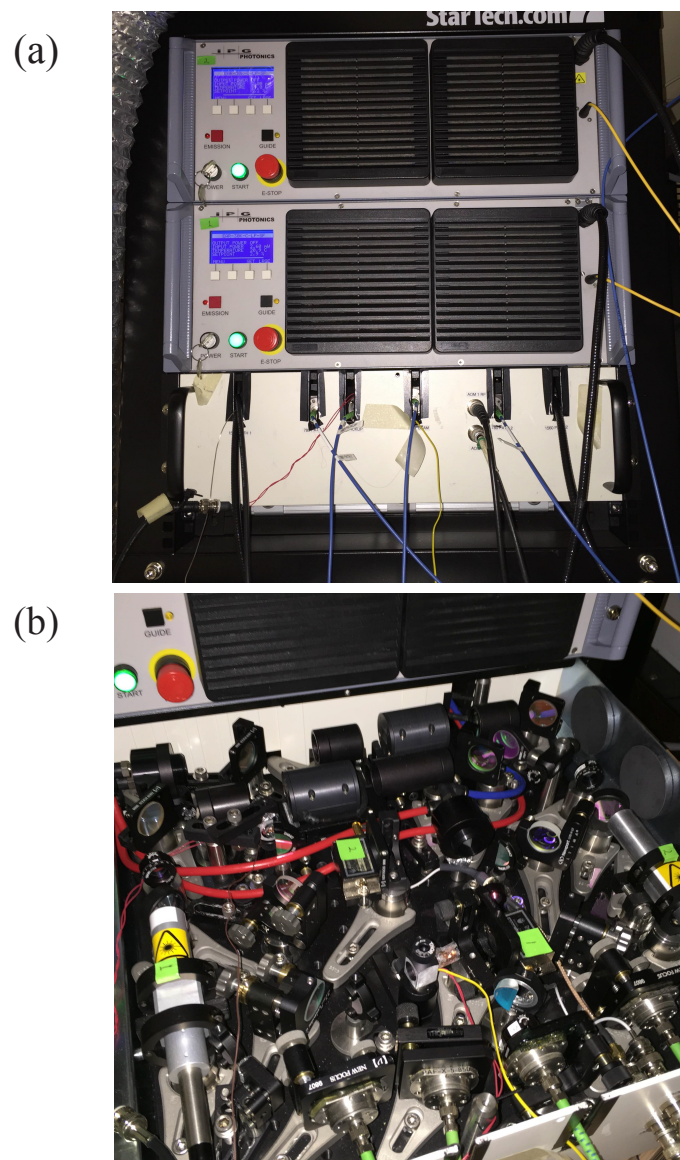


Figure 2.10: Photographs of high power laser system. (a) The two IPG fiber amplifiers and a home built drawer with optics for frequency doubling, beam manipulation, and amplitude and phase control are mounted in a standard, transportable 19 inch rack. (b) Optics layout inside the drawer.

the velocity of the standing wave, and so it is necessary to be able to adjust this frequency difference, in our case by tens of MHz, to keep the Bragg transitions on resonance as the atom velocity changes due to free fall under gravity. In our apparatus, the Bragg standing wave is generated by the interference of a pair of spectral components, one from each atom optics beam, that are ~ 30 GHz blue detuned from resonance. The relevant interference is between the downward-propagating path of one beam and the retroreflected path of the other beam. Because of the retroreflection mirror, the mirror image of this standing wave is also present, but it is highly Doppler detuned from resonance³. Additionally, to compensate unwanted ac Stark shifts (light shifts), we want each atom optics beam to have a spectral component of approximately equal power that is ~ 30 GHz red detuned from resonance, as red and blue detuned spectral components lead to ac Stark shifts of opposite signs. To achieve a suitable spectrum, we phase modulate each atom optics beam at ~ 30 GHz, with the carrier placed midway between the 6.8 GHz separated $F = 1$ and $F = 2$ resonances of the ^{87}Rb D₂ line. The +1 sideband provides the blue detuned sideband used for Bragg transitions, and the -1 sideband provides the red detuned sideband for ac Stark compensation. The carrier is nearly fully suppressed (the ratio of the power in the carrier to the power in one of the sidebands is $\sim 1\%$) and compensates for residual ac Stark shifts arising from the fact that the +1 and -1 sidebands have slightly different detunings from the $F = 2$ (or $F = 1$) transition.

Existing high frequency phase modulation technology is optimal for low power 1560 nm light in fiber. Because of this, we modulate the inputs to the fiber amplifiers. The inputs are derived from a RIO Orion external cavity diode laser. A fiber 50:50 beam splitter divides the RIO's 20 mW fiber coupled output into two paths, each of which is separately phase modulated before seeding a fiber amplifier, as illustrated in Fig. 2.9. It is important to note that frequency doubling of a phase modulated spectrum does not double the effective modulation frequency, but rather the modulation index. To see why this is true, consider a field E_ω at carrier frequency ω that is modulated at frequency ω_m with modulation index h :

³The mirror image standing wave would be problematic if we were to drive Bragg transitions near zero velocity, in which case the desired standing wave and its mirror image would come closer to degeneracy. By design, we never operate in such a regime.

$$E_\omega = A_\omega \exp [i(\omega t + h \sin (\omega_m t))]. \quad (2.1)$$

The frequency doubled field $E_{2\omega}$ is proportional to the square of E_ω , so

$$E_{2\omega} \propto A_\omega^2 \exp [2i(\omega t + h \sin (\omega_m t))] = A_\omega^2 \exp [i(2\omega t + 2h \sin (\omega_m t))], \quad (2.2)$$

which amounts to doubling the carrier frequency and the modulation index while keeping the modulation frequency unchanged.

The high frequency drives for the phase modulators originate from Phase Matrix frequency synthesizers that put out frequencies of approximately 7.6 GHz. The frequency is then quadrupled and amplified by a Marki Microwave AQA-2040 amplifier/quadrupler/amplifier module. Spurious spectral components are then removed by a Marki Microwave FB-3270 bandpass filter (passband 29-37 GHz). The signal next passes through a Millitech VCA-28-SIFS0 voltage-controlled attenuator (VCA) that is used to control the modulation depth. Finally, the signal is amplified by a Millitech AMP-28-01180 power amplifier before entering the phase modulator input.

We keep the Phase Matrix frequencies at fixed values. The frequency agility needed to drive Bragg transitions throughout the interferometer is provided by adding a DDS frequency to the path 2 Phase Matrix frequency through the use of a Hittite HMC-C041 single-sideband mixer. We implement a feedback loop to stabilize the power fed into the frequency quadrupler. The actuator for this loop is a Mini-Circuits ZMX-8GH mixer, which is used as a voltage-controlled attenuator (the control voltage is connected to the IF port of the mixer). After the mixer, the power is measured using a Pasternack PE8016 peak detector (a small fraction of the signal is picked off with a Narda 4245B-10 directional coupler and sent to the peak detector). The output of the peak detector is low-pass filtered at 1.9 MHz and directed to a Stanford Research Systems PID control module, which provides the control voltage for the mixer. A schematic of the 30 GHz frequency chain is shown in Fig. 2.11.

In order to maintain a constant Rabi frequency and to retain an ac Stark shift compensating spectrum, it is necessary to ensure that the total optical power in each

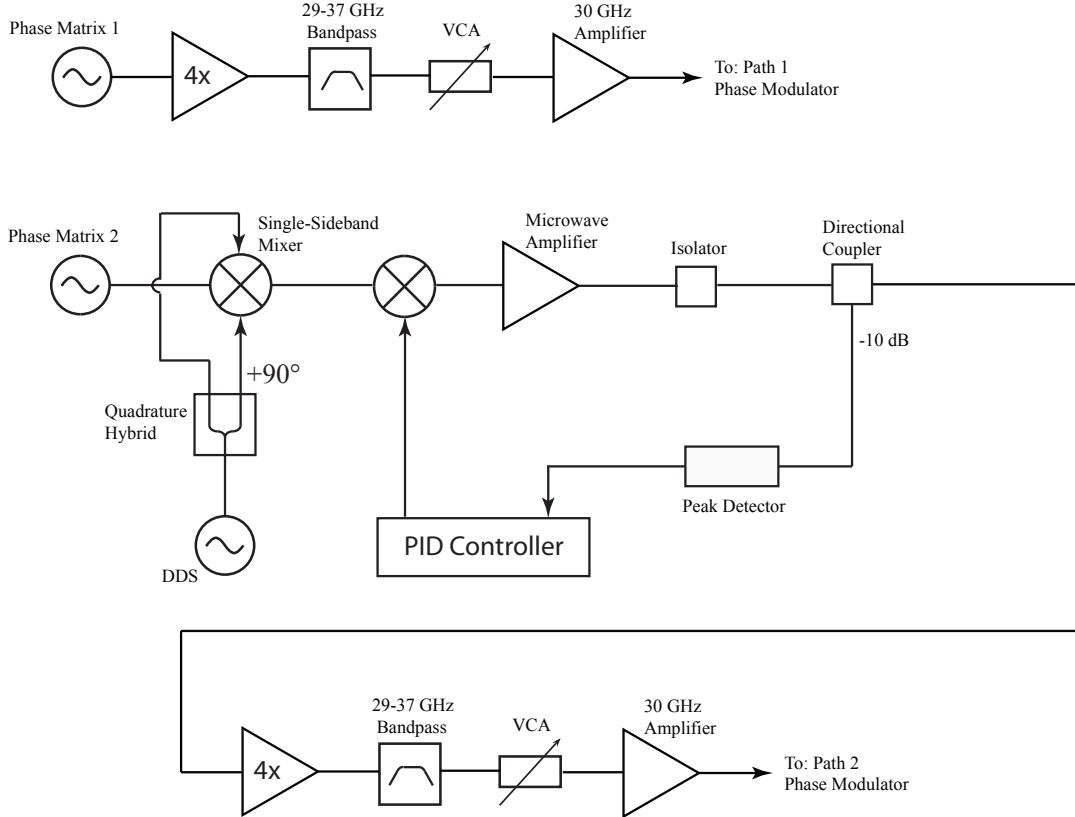


Figure 2.11: 30 GHz frequency chain for atom optics phase modulation. The ~ 30 GHz inputs to the phase modulators are generated from frequency quadrupled Phase Matrix frequency synthesizers. Frequency agility is provided by single-sideband mixing Phase Matrix 2 with a DDS of frequency near 40 MHz. The two quadratures for the single-sideband mixer are provided by a M/A-COM JH-131 quadrature hybrid. The path 2 microwave power into the quadrupler is stabilized using a PID controller that adjusts the microwave power by actuating the the voltage into the IF port of a mixer (in this configuration, the mixer functions as a voltage-controlled attenuator). After this mixer, the path 2 signal is amplified by a Mini-Circuits ZVA-183-S microwave amplifier, which is followed by a Narda 4915 isolator.

path as well as the relative powers of the carrier and ± 1 sidebands remain constant. We observe that over time scales much longer than a single shot (typically a half hour or longer), these quantities drift. We therefore implement slow feedback loops to stabilize them.

To stabilize the overall power in each path, we perform a power measurement for each path at the end of every experimental shot. The measurement is carried out by separately pulsing on path 1 and path 2. During each of the two pulses, the voltage on the intensity monitor photodetector⁴ is recorded by an analog input channel to the timing system that controls the experiment⁵. A software program compares this signal to a reference value and provides feedback using an analog output channel that actuates a voltage-controlled attenuator to adjust the rf power driving the corresponding AOM in the high power box (see Fig. 2.13).

Similarly, we measure and feed back on the spectrum of each path at the end of every experimental shot. The spectrum is measured with a scanning Fabry-Perot spectrometer. As shown in Fig. 2.4, atom optics light in the z box is picked off and directed into a fiber that leads to the Fabry-Perot spectrometer. A separate spectrum measurement for each path is taken by pulsing on that path, scanning the Fabry-Perot spectrometer, and recording the output time trace on a Cleverscope digital oscilloscope after amplification by a Stanford Research Systems SR570 low noise current amplifier. A software program runs a peak finding algorithm on the time trace to identify the relative powers of the carrier, the $+1$ sideband, and the -1 sideband.

To stabilize the spectrum, we simultaneously perform feedback on two quantities. First, we servo any power asymmetry between the $+1$ and -1 sidebands to zero. Sideband asymmetry can arise from drifts in the degree to which the two sidebands are phase matched in the doubling crystal. The doubling crystal has a finite bandwidth over which frequencies are well phase matched and can be effectively doubled. To have symmetric sidebands, we want this doubling envelope to be centered on the carrier, in which case the doubling efficiency for the sidebands is approximately half

⁴A pickoff after path 1 and path 2 are combined in the z box directs light to this photodetector, see Fig. 2.4.

⁵The timing system is described in Sec. 2.6.

of that for the carrier. The phase matching condition for the doubling crystal, and hence the center of the doubling envelope, can be adjusted by changing the crystal temperature. The temperature controller for the oven housing the crystal is therefore the actuator for the sideband asymmetry feedback loop. Second, we stabilize the ratio of the carrier power to the mean of the powers in the +1 and -1 sidebands. The actuator for this feedback loop is the VCA in the 30 GHz chain (see Fig. 2.11), which controls the modulation depth.

Figure 2.12 presents a diagram of the atom optics spectrum. It is important to note that there is a frequency offset between the carriers of path 1 and path 2, which is provided by the AOMs in the high power box. Specifically, the two AOMS are driven at the same frequency (approximately 79.5 MHz), but the path 1 AOM shifts the frequency up, while the path 2 AOM shifts the frequency down. The carrier frequency difference is therefore approximately $f_{\text{AOM}} = 159$ MHz. Having the carrier frequencies be offset in this way is important, because it breaks the degeneracy between the blue detuned (+1) and red detuned (-1) sidebands. Otherwise, the frequency difference f_{Red} between the path 2 and path 1 red detuned sidebands would have the same magnitude and the opposite sign as the frequency difference f_{Bragg} between the path 2 and path 1 blue detuned sidebands that we want to drive the Bragg transitions (i.e., $f_{\text{Red}} = -f_{\text{Bragg}}$). If f_{Bragg} is set to be on resonance with the atoms for a given set of path 1 and path 2 propagation directions (i.e., path 1 downward-propagating, path 2 upward-propagating after retroreflection), f_{Red} would be on resonance with the atoms for the mirror image of this propagation configuration, because reflection of propagation directions implies switching the sign of the Doppler shifts for each path. Therefore, contributions to the Bragg transition Rabi frequency would arise from both the desired blue detuned frequency pair and the red detuned frequency pair. If these two contributions to the Rabi frequency always added constructively, this would actually be beneficial. However, this is not the case. The red detuned and blue detuned sidebands have a frequency difference of ~ 60 GHz, which corresponds to a k -vector difference of $k_{\text{Blue}} - k_{\text{Red}} \sim 1 \text{ mm}^{-1}$. The two contributions to the Rabi frequency would thus oscillate between adding constructively and destructively over millimeter length scales. Such high spatial frequency vertical variations in the Rabi

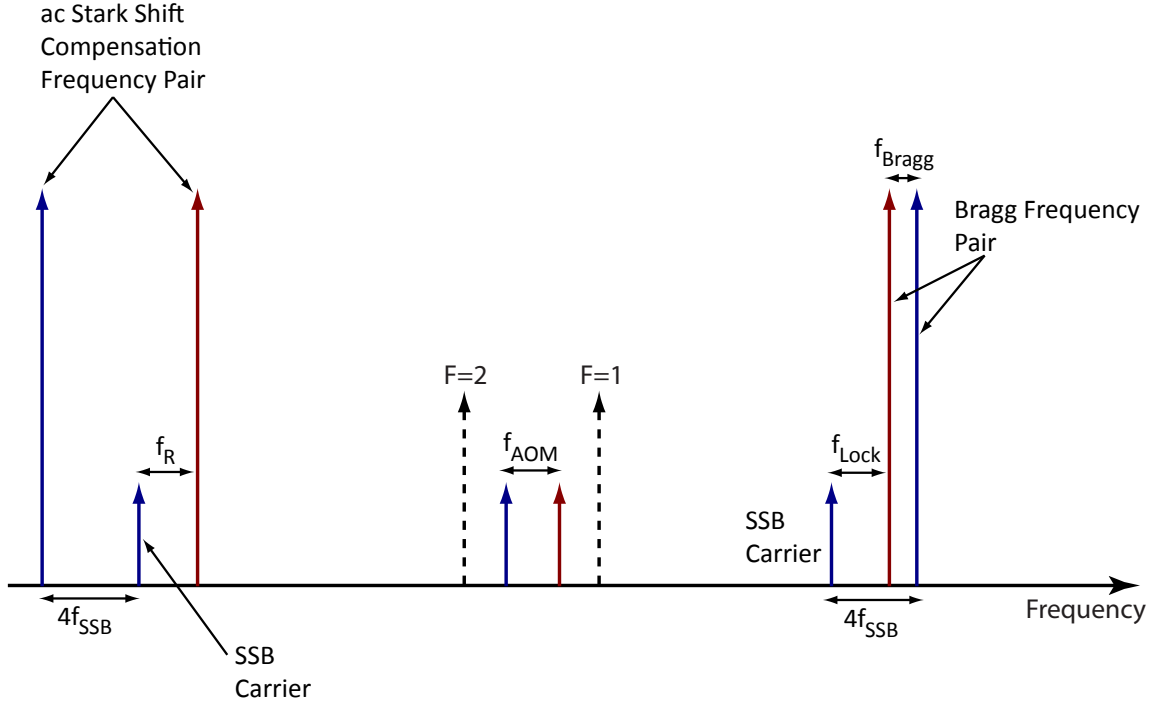


Figure 2.12: Schematic of the atom optics spectrum. The x -axis of the diagram corresponds to optical frequency. The solid red arrows represent spectral components from path 1, and the solid blue arrows represent spectral components from path 2. The dashed black arrows indicate the frequencies of the $F = 1$ and $F = 2$ resonances for ^{87}Rb . The blue detuned sidebands, labeled ‘Bragg Frequency Pair’, are used to drive the Bragg transitions, while the red detuned sidebands are used for ac Stark shift compensation. An AOM shift of $f_{\text{AOM}} \approx 159$ MHz between the path 1 and path 2 carriers breaks the degeneracy between the red and blue sidebands. For path 2, the modulation frequency is the quadrupled sum of the frequency of Phase Matrix 2 (f_{PM2}) and the DDS frequency that is added to it by a single-sideband mixer (f_{SSB}). The main sidebands are thus separated from the carrier by $4(f_{\text{PM2}} + f_{\text{SSB}})$. Due to imperfections of the single-sideband mixing, small residual ‘SSB carrier’ sidebands remain that are separated from the carrier by $4f_{\text{PM2}}$. The beatnote between the blue detuned ‘SSB carrier’ sideband and path 1 sideband is locked to a reference at $f_{\text{Lock}} = 160$ MHz in order to stabilize the relative phase between path 1 and path 2. The frequency difference between the red detuned ‘SSB carrier’ sideband and path 1 sideband is $f_R = 158$ MHz. For clarity of presentation, the frequency spacings of the spectral components are not to scale, and the amplitudes of the carriers and the ‘SSB carrier’ sidebands are exaggerated.

frequency would be highly problematic, and the carrier frequency offset allows us to avoid this issue.

Phase Matrix 1 puts out a frequency of $f_{PM1} = 7635.25$ MHz, and Phase Matrix 2 puts out a frequency of $f_{PM2} = 7635$ MHz. Where we let f_{SSB} denote the DDS frequency added to f_{PM2} by the single-sideband mixer (SSB), the path 2 frequency before the quadrupler is $f_{PM2} + f_{SSB}$. Therefore, f_{Bragg} , defined above and illustrated schematically in Fig. 2.12, is given by

$$f_{Bragg} = 4(f_{PM2} + f_{SSB}) - 4f_{PM1} - f_{AOM} = 4f_{SSB} - f_{AOM} - 1 \text{ MHz}. \quad (2.3)$$

If we express f_{SSB} and f_{AOM} in terms of deviations from their central values, $f_{SSB} = 40$ MHz + δ_{SSB} and $f_{AOM} = 159$ MHz + δ_{AOM} , we can write f_{Bragg} as

$$f_{Bragg} = 4\delta_{SSB} - \delta_{AOM}. \quad (2.4)$$

We therefore see that the frequencies are chosen so that $\delta_{SSB} = \delta_{AOM} = 0$ corresponds to a stationary Bragg standing wave. As mentioned above, we use δ_{SSB} to keep the Bragg transitions on resonance as the atom Doppler shifts change throughout the interferometer. We use small adjustments of δ_{AOM} to stabilize the phase difference between path 1 and path 2 after they are combined in the z box, compensating for the effect of differential path length fluctuations.

To implement this phase lock between the two paths, we use the beatnote between the blue sideband of path 1 and a small residual ‘SSB carrier’ sideband on path 2 that results from imperfections in the single-sideband mixing and is split from the path 2 carrier by $4f_{PM2}$ (see Fig. 2.12). Neglecting differential path length fluctuations, the beatnote frequency between these two spectral components is

$$f_{Beat} = 159 \text{ MHz} + \delta_{AOM} + 4(f_{PM1} - f_{PM2}) = 160 \text{ MHz} + \delta_{AOM}. \quad (2.5)$$

We therefore lock the beatnote to a reference at 160 MHz, using δ_{AOM} as an actuator. The choice to use this specific sideband pair for the beatnote was motivated by two

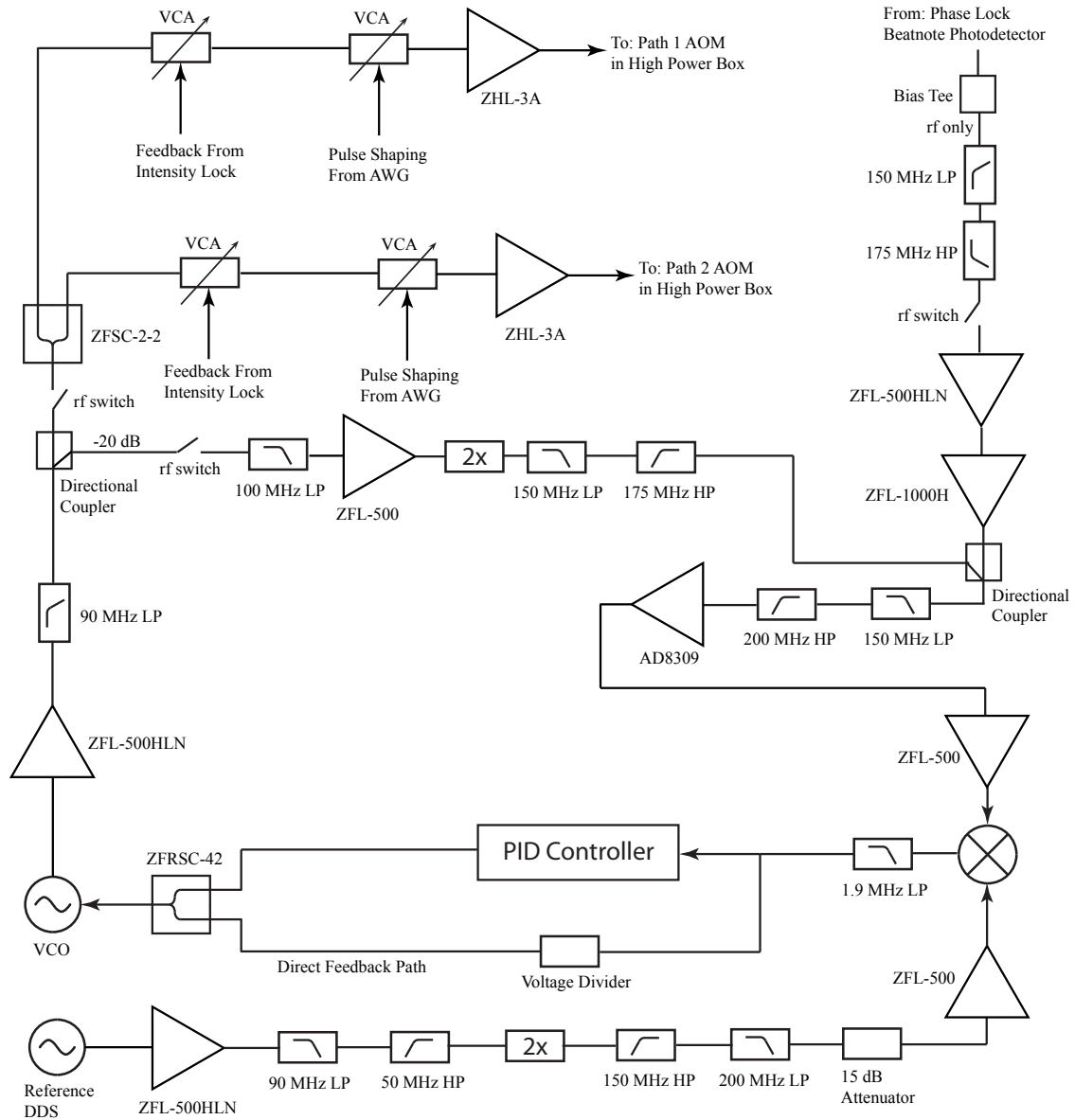


Figure 2.13: Atom optics lasers amplitude and phase control. A phase stabilized VCO serves as the master oscillator for the atom optics AOMs in the high power laser box. When atom optics light is pulsed on, feedback to the VCO frequency is used to lock the phase between atom optics path 1 and path 2. Signals in the depicted rf circuit pass through amplifiers (large triangles, labeled by part number), low pass (LP) and high pass (HP) filters, and frequency doublers (Mini-Circuits FD-2, rectangles labeled '2x').

factors. First, their frequency difference remains constant throughout the interferometer (unlike, for instance, f_{Bragg}), making the task of filtering the signal simpler. Second, we verified that stabilizing the phase between these sidebands stabilizes the phase between the Bragg sideband pair. By contrast, we found that there was still significant residual phase noise between the Bragg pair if we stabilized the phase between the path 1 and path 2 carriers.

Figure 2.13 presents a diagram of the electronics for implementing the phase lock, and also for controlling and shaping the pulse amplitudes of the atom optics lasers. The frequency source for the AOMs is a Mini-Circuits ZX95-78 voltage-controlled oscillator (VCO). The output of this VCO is split into two paths with a power splitter/combiner, amplified, and used to drive the two AOMs. When no atom optics light is demanded, an rf switch in front of the power splitter/combiner is kept open so that the AOMs do not diffract. When atom optics light is pulsed on, the signal from the phase lock beatnote photodetector in the z box, to which combined path 1 and path 2 light is directed after a pickoff (see Fig. 2.4), is bandpass filtered around 160 MHz, amplified, and mixed with a 160 MHz reference. The reference is generated by frequency doubling an 80 MHz DDS channel. The output of the mixer is the error signal for the phase lock. We split the error signal into two paths. The first path provides direct proportional feedback, with a tunable voltage divider setting the gain. The second path passes through a Stanford Research Systems PID controller, which allows for integral gain as well. These two paths are ultimately combined on a power splitter/combiner and connected to the frequency tuning input port of the VCO. The phase lock stabilizes the phase difference between path 1 and path 2 at the ~ 10 mrad level.

For most of the experimental sequence, the atom optics light is not pulsed on, so there is no signal on the phase lock beatnote photodetector. In this steady state condition, we want to keep f_{AOM} at its central value of 159 MHz so that the phase lock only has to make minimal adjustments when the atom optics light does turn on. Thus, in the absence of atom optics light, the VCO frequency should be stabilized to 79.5 MHz. A small fraction of the VCO output is picked off by a directional coupler, amplified, frequency doubled, and combined (using a second directional coupler) with

the optical beatnote rf path, leading to the mixer. In this configuration, the reference sent into the mixer is set to 159 MHz. When atom optics light is turned on, the reference frequency is hopped to 160 MHz, and an rf switch after the first directional coupler opens to cut off the VCO pickoff signal. Likewise, in the absence of atom optics light, an rf switch opens to cut off the optical beatnote photodetector output from the mixer.

To optimize Bragg pulse transfer efficiency, the atom optics pulses have a Gaussian temporal profile. In order to ensure that the phase lock functions in the tails of the Gaussian, when the intensity is low, we include a logarithmic amplifier (Analog Devices AD8309) in the optical beatnote rf path. The use of Gaussian pulses has the additional benefit that any phase transients during the initial lock acquisition occur at low intensity and thus have a minimal effect on the Bragg pulse performance.

For each of the two atom optics paths, the VCO signal passes through a pair of VCAs before being amplified and sent to the AOMs in the high power laser box. One of these VCAs is the actuator for the intensity stabilization loop described above. The second VCA is used for temporal shaping of the pulses. The control voltage for this pulse shaping VCA is provided by a Tektronix AFG3102 arbitrary waveform generator (AWG) or by a slow analog out channel from the timing system controlling the experiment.

2.4.4 Doubling Crystal Aging

We observe that over many months of use, the efficiency of the doubling crystals for high 1560 nm power can significantly degrade. A comparison of the doubling performances of a new versus an aged crystal is shown in Fig. 2.14. The aged crystal had been regularly used for approximately one year. The exact mechanism that causes this aging is currently uncertain. One possibility is photorefractive damage to the crystal. In an attempt to undo potential photorefractive damage, we annealed the crystals overnight at 200 °C, which did not lead to any noticeable improvement (this was perhaps unsurprising, since we already operate the crystals at a relatively high temperature of 150 °C). It is interesting to note that the new and aged crystals

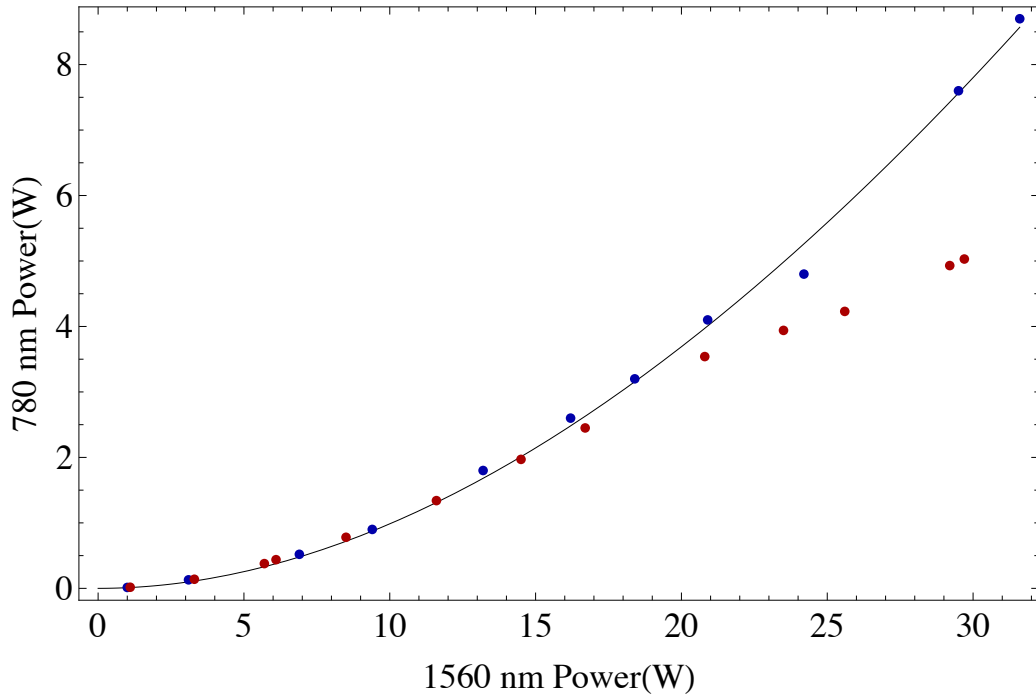


Figure 2.14: Doubling crystal aging. The blue markers show output 780 nm power versus 1560 nm pump power for a previously unused doubling crystal. The red markers correspond to the aged doubling crystal. The curve indicates the expected scaling of the output power with pump power. In the limit of small pump depletion, this scaling should be approximately quadratic. The new and aged crystals perform similarly for up to 20 W of pump power. For higher pump power, the aged crystal performs significantly worse.

perform similarly for 1560 nm pump power up to 20 W. For more than 20 W of pump power, the scaling of the doubling efficiency of the aged crystal with power dramatically falls off from the expected behavior.

2.5 Imaging

We use fluorescence detection to image the atoms after they are launched and fall back to the bottom of the fountain. The fluorescence imaging occurs in a region vertically

between the 3D MOT and the magnetic shield. This region has four separate 4 inch windows, providing a significant amount of optical access. We make the atoms fluoresce by pulsing on cooling and repump light along the z axis of the MOT. The detuning of the cooling light is typically set to be smaller than that used for the MOT (2 MHz red detuned for ^{87}Rb , 3.2 MHz red detuned for ^{85}Rb). When an atom absorbs a photon, it soon thereafter spontaneously emits a photon into 4π solid angle. Depending on the particular experimental sequence we are running, we illuminate the atoms for anywhere from 1 to 11 ms. Longer fluorescence times allow for more collected signal at the cost of spatial resolution, because the atoms heat and diffuse as they undergo repeated spontaneous emission events. We use a series of lenses to collect the photons that exit the vacuum chamber through a particular window and image them onto a CCD camera (Photometrics Quantix), allowing us to obtain spatially resolved images of the atom ensemble. To gain maximal information about the atom ensemble, we image it using two separate CCD cameras along orthogonal axes.

Figure 2.15 shows two different imaging lens assemblies that we have used in our experiments. The lens configuration in Fig. 2.15(a) was used for primary data collection in Ch. 6 and for general purpose atom source optimization and tweaking. This configuration demagnifies by a factor of approximately 2.5, allowing the CCD to image a larger field of view. Spherical aberration causes the point spread function to have a broad, low amplitude pedestal, as can be seen from the spread of rays in the CCD plane in Fig. 2.15(a). Characterizing and accounting for the point spread function was important for the data analysis in Ch. 6. The lens configuration in Fig. 2.15(b) was used for primary data collection in Ch. 7. It does not demagnify and is designed to minimize spherical aberration, allowing for improved spatial resolution. Both lens configurations include a 10 nm wide bandpass interference filter centered at 780 nm (Edmund Optics NT65-239) to reduce the amount of stray light that reaches the CCD camera.

We notice that, depending on the magnetic field gradient in the fluorescence imaging region, the vertical center of mass position of the atom ensemble can undergo a drift during fluorescence imaging [11]. Such a drift is undesirable, because it causes

the fluorescence image to be blurred vertically. We experimentally determined that we could eliminate this drift by adjusting the magnetic field gradient and the offset field that is present while the fluorescence imaging occurs. This was achieved by temporarily changing the current flowing through the upper z axis MOT trim coil during fluorescence imaging. This current is controlled by an analog input to the supply and is changed 200 ms before detection. We found that it was necessary to change the direction as well as the magnitude of the current, and we implement this direction change with a voltage controlled mechanical relay switch. At the end of detection, the current and the relay switch are set back to their steady state configurations. We suspect that the vertical motion of the cloud without the current change comes about from position dependent forces like those experienced in a MOT. As discussed in Sec. 2.2.2, these forces arise from the interplay of counter-propagating laser beams with circular polarizations of opposite helicity and a magnetic field gradient, and they tend to push the atom cloud toward a magnetic field zero (or away from a magnetic field zero in the case of an anti-MOT, for which the orientation of the polarizations is flipped with respect to that of a MOT). It therefore makes sense that adjusting the vertical magnetic field gradient and the field offset affects the vertical motion of the cloud.

It is often useful to characterize the atom source before it is launched. For this purpose, we use absorption imaging. A separate absorption imaging beam passes through the center of the 3D MOT chamber. We image the shadow that the atom cloud casts onto this beam using an Andor iXon CCD camera. The optical depth imaged by a particular pixel is determined by comparing an image when the atoms are present with an image of the absorption imaging beam alone, once the atoms have left the beam. Knowledge of the optical depth, the detuning of the absorption imaging beam, and the properties of the atomic transition allows the number of atoms with transverse position corresponding to a given pixel to be determined. The light for the absorption imaging beam originates from a separate Vortex external cavity diode laser with frequency locked by saturation absorption spectroscopy a fixed detuning from either the ^{87}Rb or the ^{85}Rb cooling transition [11]. When an AOM is pulsed on, approximately 2 mW of light is sent via fiber to the absorption imaging beam line

at the bottom of the tower. The absorption imaging pulses typically have $\sim 30 \mu\text{s}$ durations. Just before absorption imaging, we typically apply repump light to the atoms to pump them into the upper hyperfine ground state. Atoms in the lower hyperfine ground state are not resonant with light at the cooling frequency and would therefore not contribute significantly to the absorption image signal.

2.6 Timing System

In order to run the experiment, many control voltages and frequencies have to be adjusted with precise timing. This functionality is provided by a pair of custom-designed timing systems. Most of these voltages and frequencies are set by the first of these timing systems (Timing System 1), which is based around a Xilinx Spartan 3 FPGA [54]. Timing System 1 has 40 slow analog out ($\sim 1 \mu\text{s}$ rise time) channels, 4 fast analog out channels, 8 DDS channels, 24 digital out channels, and 2 analog input channels⁶.

For the work described in Ch. 7, we performed sequences of more than 100 sequential Bragg transitions, each of which required an overall DDS frequency change and a DDS frequency sweep to compensate the time-dependent Doppler shift from gravitational free fall. Timing System 1 did not have enough memory for all of these new DDS events in addition to its other functions. We therefore used the second timing system (Timing System 2) for the atom optics DDS events. Timing System 2 is based around a Xilinx Spartan 6 FPGA. At the beginning of each experimental sequence, Timing System 1 triggers Timing System 2. Timing System 1 is itself triggered by the AC line⁷. The clocks for both timing systems are externally referenced to a 100 MHz source, and the DDS channels are separately referenced to a 25 MHz source. These 100 MHz and 25 MHz references, as well as all other important frequencies in the experiment, are ultimately referenced to a stable master oscillator (Oscilloquartz OCXO 8607-BGE).

⁶As described in Sec. 2.4.3, the analog input channels are used to record photodetector signals for the atom optics power stabilization feedback loops.

⁷Specifically, the trigger output channel of an Agilent 54621A oscilloscope that is triggered by the AC line provides the TTL signal to trigger Timing System 1.

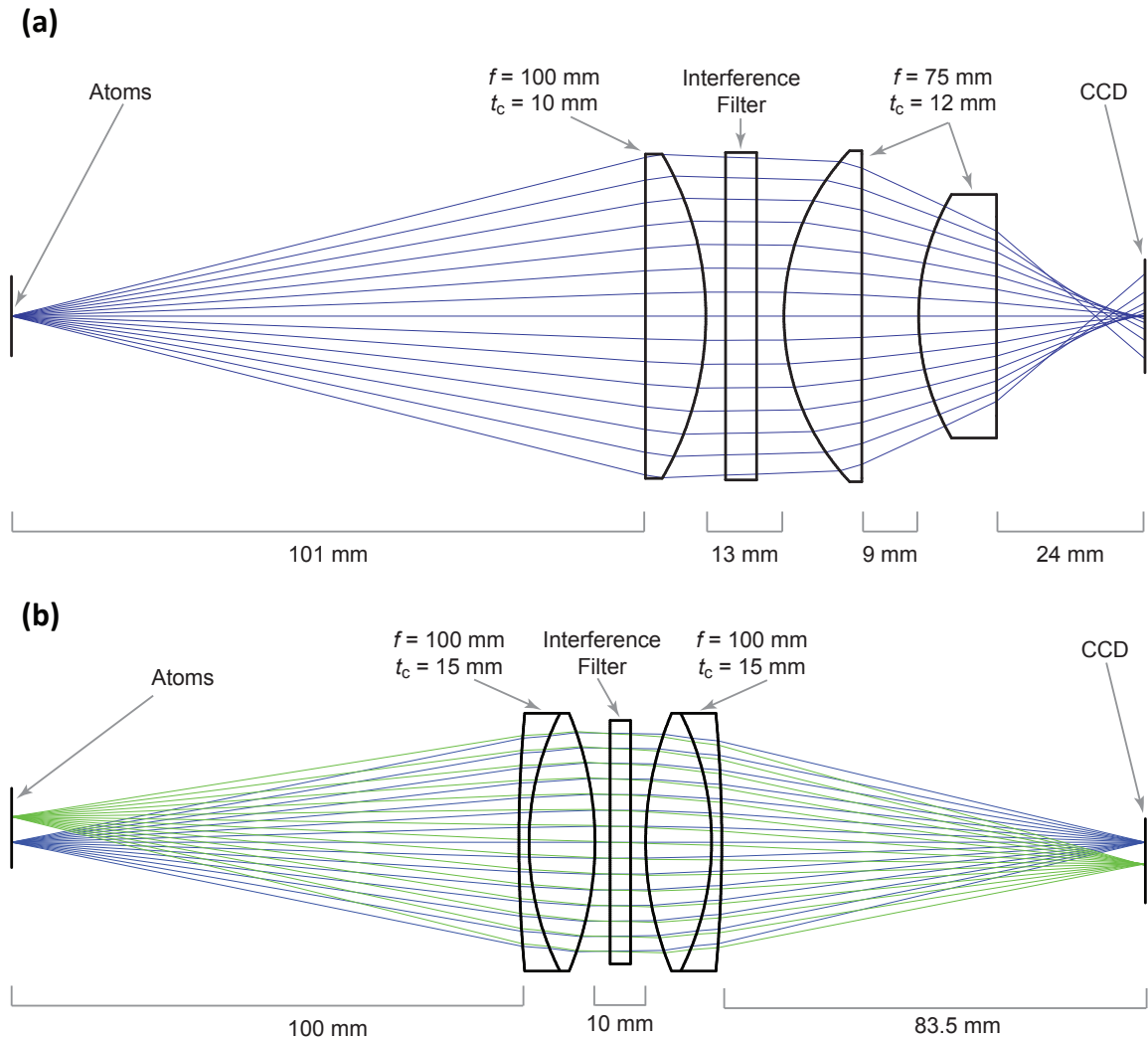


Figure 2.15: Two different imaging lens setups that we have used in our apparatus. (a) Lens configuration with $2.5\times$ demagnification. The leftmost lens has model number Thorlabs LA1050-B. The other two lenses have model number Thorlabs LA1145-B. (b) Lens configuration with no demagnification and reduced spherical aberration. Both lenses are Thorlabs AC508-100-B. In this figure, f denotes the focal length of a lens, and t_c denotes the thickness of a lens at its center. Part (a) of this figure is adapted from [12].

2.7 Magnetic Shielding

This section describes the magnetic shield for the 10 m atomic fountain. We published a detailed account of the magnetic shield in [59] (collaboration with Susannah Dickerson, Jason M. Hogan, David M. S. Johnson, Alex Sugarbaker, Sheng-wey Chiow, and Mark A. Kasevich). Figures from this section are from or modified from [59] and an earlier unpublished writeup (the work in the unpublished writeup was performed in collaboration with Jason M. Hogan, David M. S. Johnson, and Mark A. Kasevich).

2.7.1 Importance of Magnetic Shielding

We use a three layer, high magnetic permeability mu-metal magnetic shield to reduce magnetic field inhomogeneities in the interferometer region. It is important that the atoms experience a uniform magnetic field in the interferometer, because magnetic field gradients lead to unwanted forces on the atoms. Independently of any magnetic shielding considerations, to mitigate the effects of magnetic fields on the interferometer, we use microwave pulses to prepare the atoms in the magnetic field insensitive Zeeman sublevel ($m_F = 0$). For $m_F \neq 0$, the atomic energy has a linear response to magnetic fields, with a sensitivity on the order of $2\pi\hbar \times 1 \text{ MHz/G}$ for Rb. For $m_F = 0$, there is no linear response. Instead, the energy changes quadratically with the magnetic field \vec{B} . Where α is the second order Zeeman coefficient, this energy shift has magnitude $\frac{1}{2}\hbar\alpha |\vec{B}|^2$. The magnitude of the z axis force on the atoms, for bias field B_0 oriented along the z axis and vertical magnetic field gradient $\frac{\partial B_z}{\partial z}$, is then given by $\hbar\alpha B_0 \frac{\partial B_z}{\partial z}$. It is important to note that α differs by approximately a factor of two for ^{85}Rb and ^{87}Rb ($\alpha_{85} = 2\pi \times 1.3 \text{ kHz/G}^2$, $\alpha_{87} = 2\pi \times 0.58 \text{ kHz/G}^2$) [60, 61]. Therefore, the influence of magnetic field gradients will not cancel as a common mode in a dual species interferometer for tests of the equivalence principle.

2.7.2 Challenges of Building a Tall Magnetic Shield

Due to the geometry of our apparatus, it was necessary to construct a magnetic shield of unusual dimensions. The shield needed to be tall with a comparatively narrow

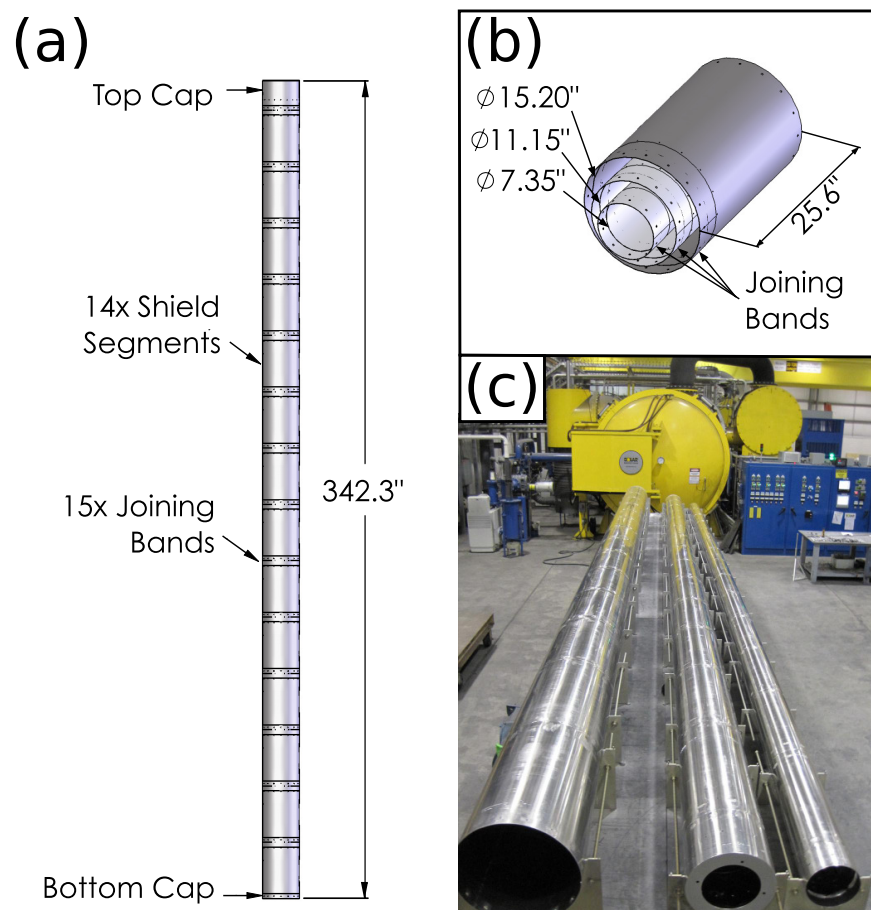


Figure 2.16: Initial magnetic shield design. (a) The initial shield design consisted of 14 mu-metal segments connected by joining bands. (b) Schematic of segments from the three layers of the shield. (c) Ultimately, we found it necessary to weld the shield segments together and anneal them in a large furnace. This photograph shows the three shield layers in front of the annealing furnace.

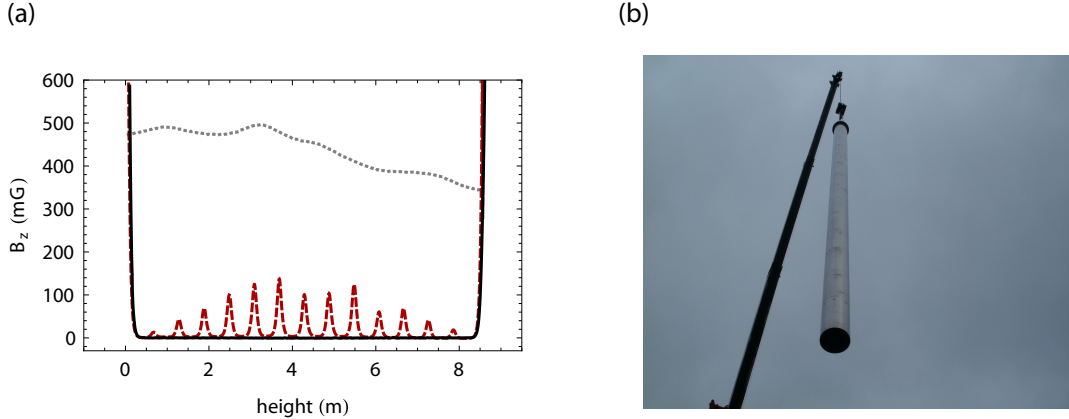


Figure 2.17: Comparison of the initial segmented shield and the welded shield. (a) The vertical component of the magnetic field is plotted as a function of height for the initial shield (dashed red) and the welded shield (black). For reference, the background field before the shield was installed is also plotted (dotted gray). (b) Photograph of the outer layer of the welded shield being installed. Each layer of the welded shield was lowered by crane through a hatch in the roof above the pit in our lab.

radius. An important consideration was to make the shield as continuous as possible, to give magnetic flux a nearly continuous path through the high-permeability mu-metal so that it would not leak out into the interferometer region. Ideally, then, each layer of the shield would have been a monolithic cylinder of mu-metal. However, this was not possible at the time when the shield was initially designed. The mu-metal used in the shield must undergo an annealing procedure in a specialized furnace, and no 10 m long furnace was available at the time. Instead, as shown in Fig. 2.16, each layer of the shield was constructed from a stack of 14 segments. Consecutive segments were connected with a mu-metal joining band with the aim of improving the continuity of the high permeability material.

After the shield was installed, measurements of the magnetic field inside the shield revealed a sequence of 100 mG magnetic field spikes along the vertical axis, as shown in Fig. 2.17(a). The amplitude of these spikes was not much smaller than the unshielded magnetic field of the Earth (about 500 mG). We proceeded to perform finite element

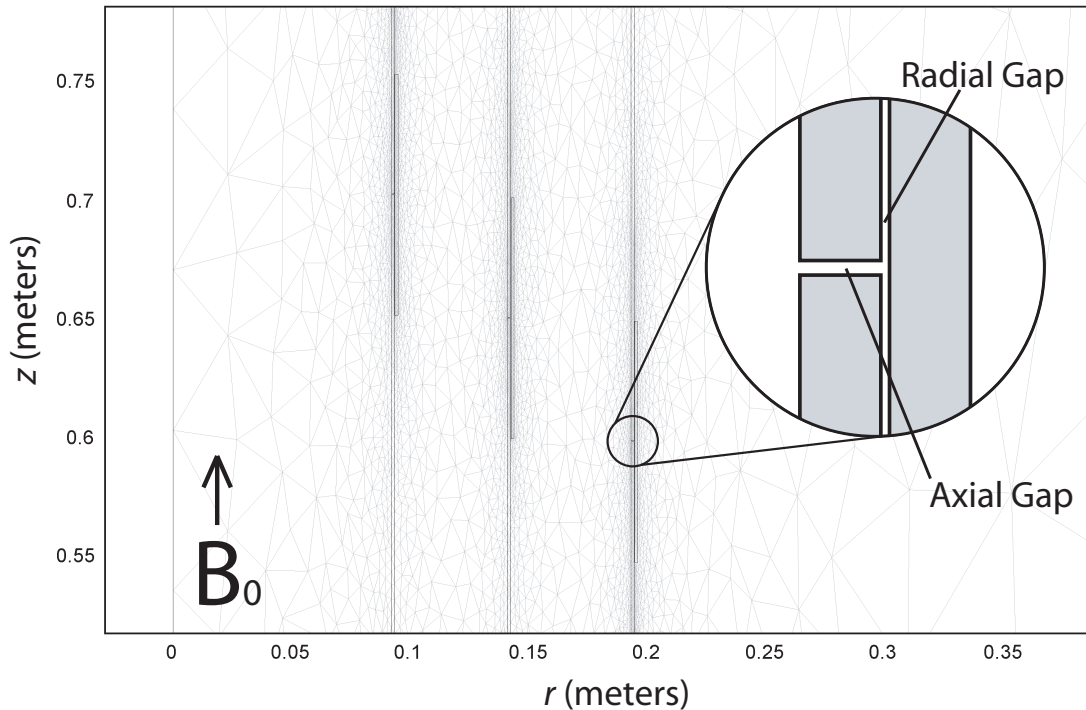


Figure 2.18: Finite element simulation of the initial segmented three layer magnetic shield, performed using COMSOL Multiphysics software. This figure shows a zoomed in view of a small vertical portion of the shield. Gaps between consecutive shield segments and between the shield segments and joining bands were included in the simulation. The gray triangles indicate the adaptive mesh for the simulation, with finer mesh used to model the smaller spatial features arising from the gaps. In the simulation, Earth's field was modeled by applying a background vertical field of 500 mG. Based on examination of the shield components, we used an axial gap size of 0.010 inches and a radial gap size of 0.006 inches for the simulation. The simulation assumed cylindrical symmetry.

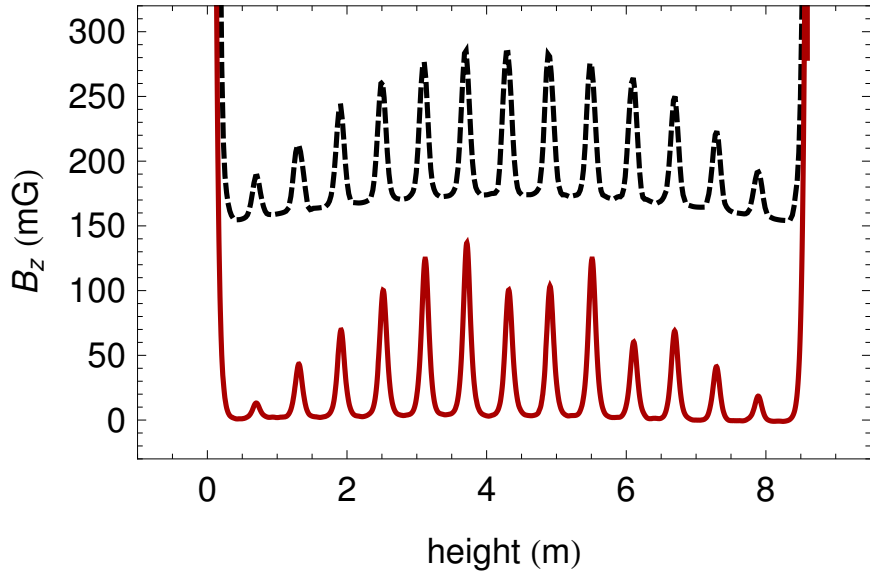


Figure 2.19: Comparison of the measured (solid red) and simulated (dashed black) magnetic fields inside the segmented shield. The simulated field plot is vertically offset by 150 mG for clarity. The heights and positions of the simulated magnetic field spikes show good quantitative agreement with measurements. The simulation predicts a curved baseline field that is largest at the center of the shield. A zoomed in view of the measured data shows the same qualitative behavior, although it is a smaller effect (the baseline field is about 4 mG higher at the center of the shield than at the edges for the measured data). It is possible that the quantitative disagreement regarding the magnitude of baseline curvature is related to the specific assumptions made in the simulation about the magnetic permeability of the mu-metal (10^5) and the gap size.

simulations on a realistic model of the shield to develop a quantitative understanding of the origin of the spikes (see Fig. 2.18). The simulations were able to reproduce the spikes with a high degree of quantitative agreement (see Fig. 2.19), making clear that the spikes arose from small (millimeter scale) gaps between consecutive segments and the corresponding joining bands. A photograph of a typical gap, with a ruler shown for reference, is shown in Fig. 2.20.

At a conceptual level, one can think of the shield as working by redirecting nearby magnetic flux through the high permeability mu-metal. The tall height of our shield gives it a larger surface area over which to intake flux. The magnetic flux density

inside the mu-metal is therefore very high. The data and the simulations both indicate that even a small spatial disruption of the continuity of the mu-metal is sufficient for enough flux to leak out of the mu-metal to cause a significant magnetic field spike inside the shield—at the same vertical position as the discontinuity. The simulations revealed that gaps in the shield’s inner layer were most harmful in terms of leading to large spikes.

The magnetic field as a function of vertical position along the center of the shield was measured by performing a sequence of measurements with an Applied Physics Systems 540 fluxgate magnetometer. The magnetometer was housed in a shuttle suspended from a computer-controlled stepper motor by four cables made from fishing line (see Fig. 2.21). The field was measured at approximately 2300 stepper motor positions. We converted each recorded stepper motor position to a physical height of the magnetometer, accounting for nonlinearities from cable stretching⁸ and from changes in the radius of the cable spool as the spool was unwound (these were $\sim 2\%$ corrections).

2.7.3 Eliminating the Magnetic Field Spikes: The Welded Shield

The analysis of the segmented magnetic shield described above signified that it was necessary to improve the uniformity of the shield by reducing the size of the gaps. Several attempts to do this, including increasing the torque on the joining band fasteners and performing thermal interference fits between consecutive shield segments, yielded only modest reductions of the magnetic field spikes [59]. Fortunately, by this time, a new option had become available. A company called Solar Atmospheres had built an annealing furnace large enough to accommodate the full shield. The shield segments were welded together by the mu-metal provider (Amuneal Manufacturing) and subsequently annealed. After installing and degaussing [59] the welded shield, we observed dramatic improvement in the shielding performance (see Fig. 2.17(a)).

⁸We determined the elastic modulus of the fishing line by measuring the amount it stretched when using it to suspend various weights of water in a bucket.



Figure 2.20: Photograph of the millimeter-sized gap between a shield segment and a joining band. Gaps of this size were typical for the initial magnetic shield design.

Figure 2.22 shows detailed plots of the vertical and transverse magnetic fields inside the welded shield as a function of height. Notably, there are no longer any visible magnetic field spikes. The residual vertical field is below 1 mG, and the residual transverse field oscillates around zero with a peak-to-peak amplitude of several mG.

2.8 State Preparation

As discussed in Sec. 2.7.1, it is important to prepare the atoms in a magnetic field insensitive Zeeman sublevel ($m_F = 0$) to reduce unwanted forces from stray magnetic field gradients. Recall from Sec. 2.3.2 that we evaporate ^{87}Rb in the $F = 1, m_F = -1$

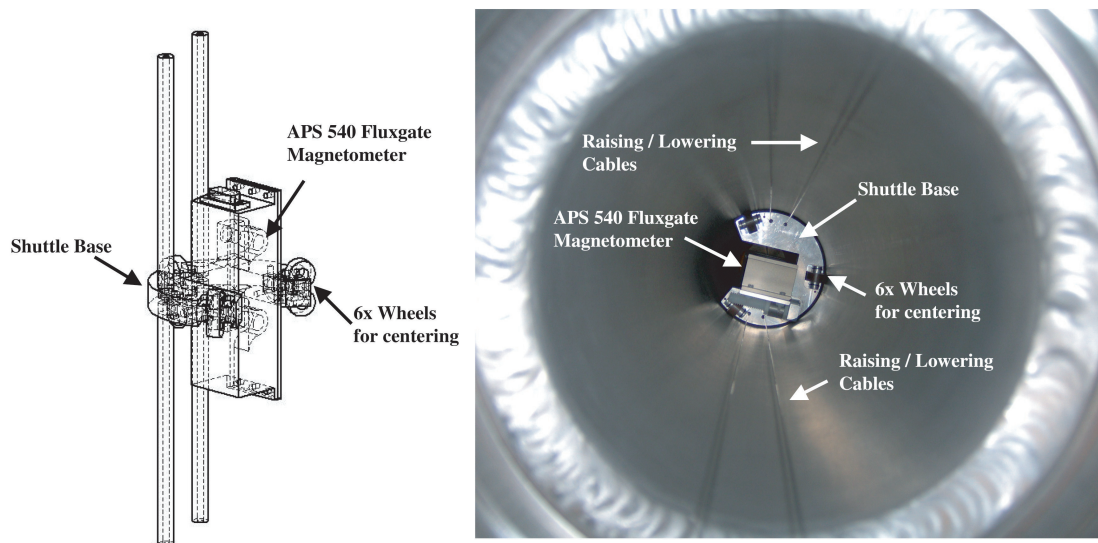


Figure 2.21: Apparatus for controllably lowering a fluxgate magnetometer down the center of the magnetically shielded region. The magnetometer was held by a shuttle suspended by four cables from a stepper motor. The shuttle was guided by the vacuum tube into which the atoms are now launched (we had not yet installed the 3D MOT chamber at the bottom of this tube, and the tube was not yet under vacuum). Wheels around the circumference of the shuttle ensured that the shuttle moved smoothly through the center of the tube.

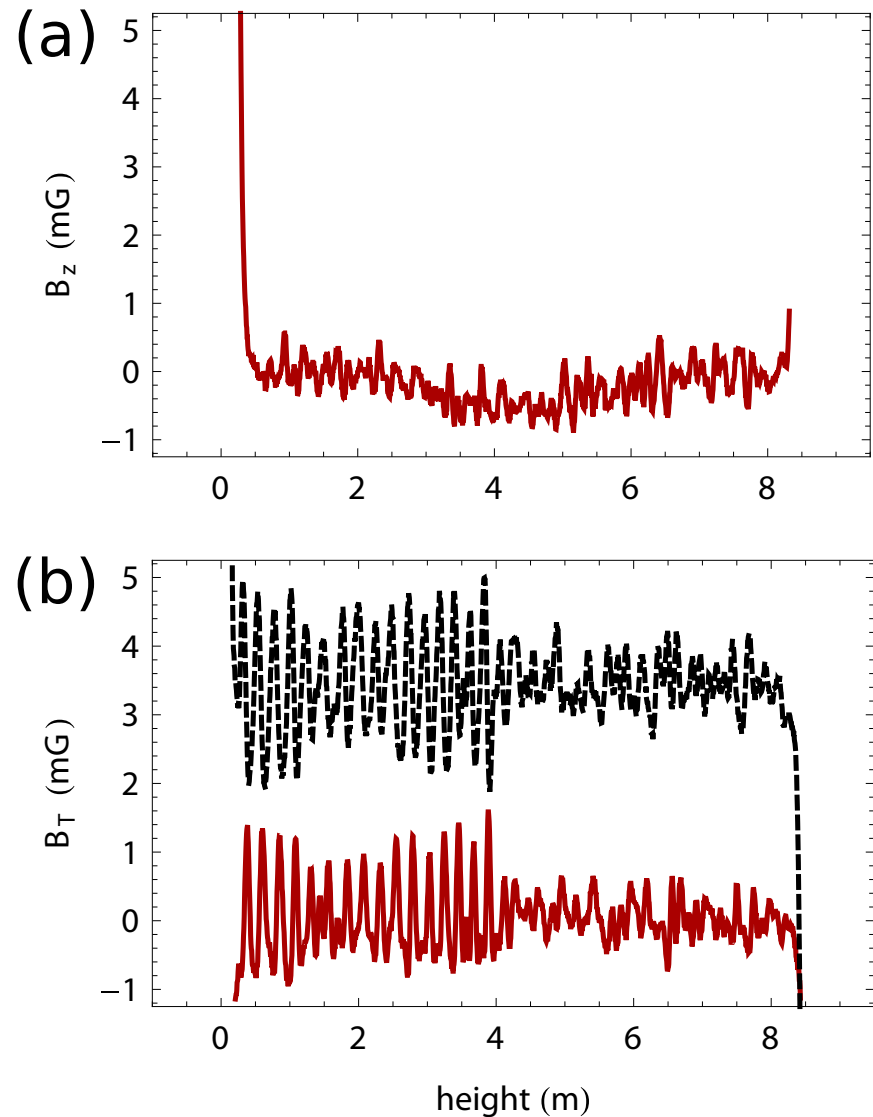


Figure 2.22: Welded shield magnetic fields. (a) The vertical field as a function of height. (b) The magnetic field along the two transverse axes (solid red and dashed black, respectively) as a function of height. The dashed black trace is offset by 3.5 mG for clarity.

state and ^{85}Rb in the $F = 2, m_F = -2$ state. After the evaporation and the magnetic lensing sequence, we use microwave pulses to transfer the ^{87}Rb atoms into the $F = 2, m_F = 0$ state and the ^{85}Rb atoms into the $F = 3, m_F = 0$ state.

State preparation for ^{87}Rb is simpler than for ^{85}Rb because it only requires a single microwave transition. For ^{87}Rb , the σ^+ component of the microwave field drives the $F = 1, m_F = -1 \longrightarrow F = 2, m_F = 0$ transition. State preparation for ^{87}Rb is performed in the 3D MOT chamber, 60 ms after the atoms have been released from the magnetic lens. The 60 ms delay time allows eddy currents arising from the ‘snap off’ of the magnetic trap to reduce in amplitude. Eddy currents can cause magnetic field gradients that would lead to spatially dependent resonances of the microwave transition across the cloud. To ensure that the quantization axis for the transition is well defined by a bias field, we adjust the current through the z axis MOT trim coils 50 ms before the microwave pulse, leading to a bias field of magnitude 0.7 G. We find that we can make the transfer efficiency nearly perfect by implementing an adiabatic rapid passage (ARP) transition with appropriate parameters. The ARP transfer efficiency is robust against inhomogeneous broadening from residual Zeeman shift gradients across the cloud. The microwave pulse has a duration of 3.5 ms with smoothed temporal edges. During the pulse, the microwave frequency is linearly swept over 40 kHz. The microwaves for the ^{87}Rb state preparation are generated by the same microwave chain that is used for the forced microwave evaporation discussed in Sec. 2.2.3. Microwaves are directed into the 3D MOT chamber by a pair of horns located near windows. A detailed diagram of the ^{87}Rb microwave chain can be found in [11].

State preparation for ^{85}Rb requires a sequence of three microwave transitions: $F = 2, m_F = -2 \longrightarrow F = 3, m_F = -1$ (driven by σ^+ polarization), $F = 3, m_F = -1 \longrightarrow F = 2, m_F = 0$ (driven by σ^- polarization), and $F = 2, m_F = 0 \longrightarrow F = 3, m_F = 0$ (driven by π polarization). For a weak bias field B_0 , the energy shift of sublevel m_F for $F = 2$ is $(-0.47 \frac{\text{MHz}}{\text{G}})m_F B_0$, and the energy shift of sublevel m_F for $F = 3$ is $(+0.47 \frac{\text{MHz}}{\text{G}})m_F B_0$ [60]. Thus, the first order Zeeman shifts of the three microwave transitions from the magnetic-field-free resonance are $-3 \times (0.47 \frac{\text{MHz}}{\text{G}})B_0$,

$-1 \times (0.47 \frac{\text{MHz}}{\text{G}})B_0$, and zero, respectively. A diagram of these three microwave transitions and their corresponding Zeeman shifts is shown in Fig. 2.23. The microwaves for ^{85}Rb have a longer wavelength (10 cm) than those for ^{87}Rb due to their lower frequency (3 GHz vs. 6.8 GHz). We therefore couple the ^{85}Rb microwaves into the vacuum chamber with a microwave horn placed near one of the larger windows in the fluorescence imaging detection region. We found that there was not enough microwave intensity to efficiently drive the transitions in the 3D MOT region, so we perform state preparation for ^{85}Rb 50 cm into the magnetic shield after the atoms have been launched. The microwave intensity is higher inside the shield, and the magnetic field is more uniform, reducing inhomogeneous broadening. Inside the shield, a 130 mG bias field is provided by the solenoid wrapped around the vacuum chamber.

The first microwave transition ($F = 2, m_F = -2 \rightarrow F = 3, m_F = -1$) is driven by a 1.2 ms ARP pulse, with a linear frequency sweep over 22 kHz. The second transition ($F = 3, m_F = -1 \rightarrow F = 2, m_F = 0$) is driven by another ARP pulse with the same parameters but a shifted overall frequency. We find that the Rabi frequency for the third transition ($F = 2, m_F = 0 \rightarrow F = 3, m_F = 0$) is significantly lower than that for the first two transitions, indicating that π polarization is not as effectively coupled into the vacuum tube inside the shield. We optimized transfer for the third transition with an 800 μs square pulse with no frequency sweep. The ^{85}Rb state preparation efficiency is $\sim 75\%$, with imperfect transfer predominantly arising from the third transition.

The microwave chain for ^{85}Rb is shown in Fig. 2.24. The microwave frequency is generated by subtracting the amplified (MITEQ AM-1607-2000 amplifier) output frequency of a DDS from the 3.135732439 GHz output of a Hewlett Packard 83711B frequency generator using an IQ mixer (Marki Microwave IQ0255LMP). The frequencies are chosen so that a DDS frequency of 100 MHz corresponds to the magnetic-field-free resonance of the microwave transition. The DDS is used for frequency adjustments between the pulses and for frequency sweeps. The ARP pulses are shaped by a VCA (Mini-Circuits ZX73-2500M-S) in the DDS path. When no microwaves are demanded, a mechanical switch (Teledyne Microwave CS33S1C) after the IQ mixer provides additional extinction. The microwaves pass through a high power (16 W)

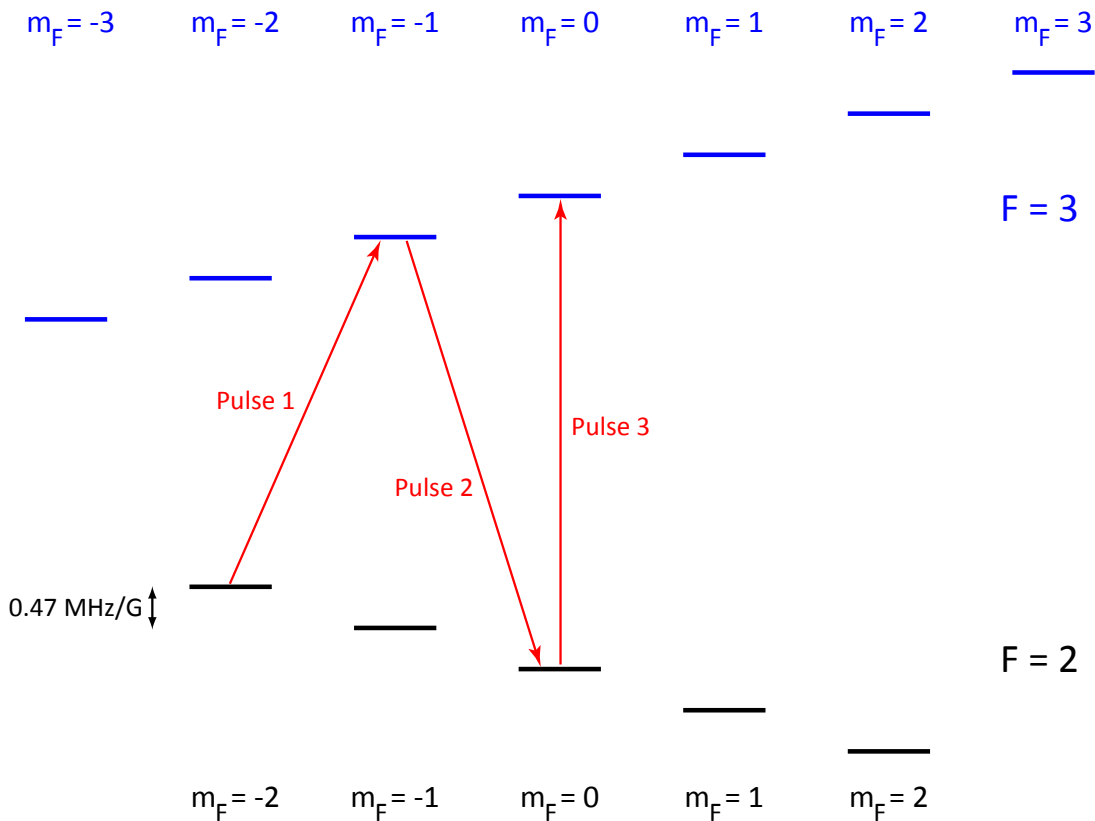


Figure 2.23: Diagram of state preparation microwave transitions for ^{85}Rb . A sequence of three microwave pulses transfers population from $F = 2, m_F = -2$ to $F = 3, m_F = 0$. The frequencies of the individual transitions that we drive are resolvable due to Zeeman shifts from the 130 mG bias field. For ease of visualization, the energy splittings between adjacent Zeeman sublevels (different m_F values) within a given hyperfine level ($F = 2$ or $F = 3$) are exaggerated in comparison to the 3 GHz energy difference between $F = 2$ and $F = 3$.

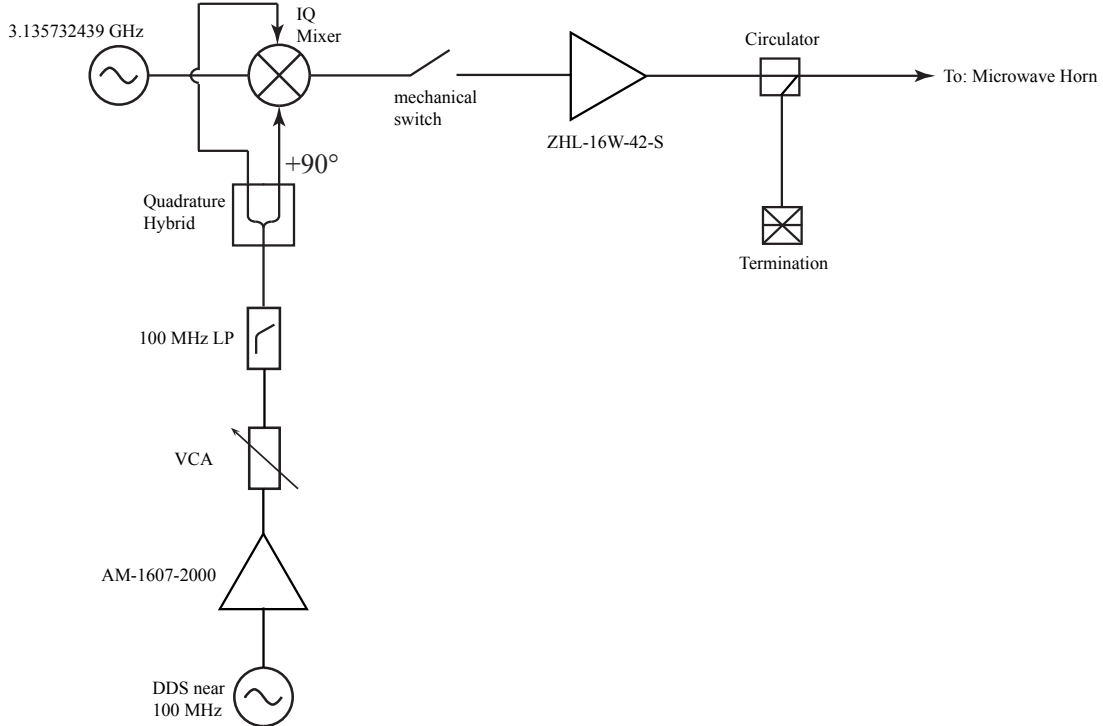


Figure 2.24: Microwave chain for ^{85}Rb . A DDS frequency is subtracted from the 3.135732439 GHz output of a frequency generator using an IQ mixer. The signal is amplified and coupled into the vacuum chamber with a microwave horn placed near a window in the fluorescence imaging detection region. Amplifiers in this schematic (large triangles) are labeled by part number.

amplifier (Mini-Circuits ZHL-16W-42-S) and are then directed to the horn. The amplifier is protected from reflected power by a Narda 4923 circulator, whose return path is directed into a Narda 4378BM termination.

Following state preparation, residual population remaining in $F = 1$ for ^{87}Rb or $F = 2$ for ^{85}Rb is blown away by a $250 \mu\text{s}$ pulse of light from the repump path along the z axis. For this blowaway pulse, an rf switch changes the frequency drive for the repump path phase modulator from the usual 2.526 GHz source used for repump to a separate source at 2.4215 GHz. With the modulation at 2.4215 GHz, the +1 phase modulation sideband is near the $F = 2 \rightarrow F' = 1$ resonance for ^{85}Rb , and the +2

phase modulation sideband is near the $F = 1 \longrightarrow F' = 0$ resonance for ^{87}Rb . The use of these transitions maximizes the number of photons scattered from the atoms that we want to blow away, as the chosen excited state hyperfine levels ($F' = 0$ for ^{87}Rb , $F' = 1$ for ^{85}Rb) are forbidden from decaying to the upper ground state hyperfine levels ($F = 2$ for ^{87}Rb , $F = 3$ for ^{85}Rb).

2.9 Time Orbiting Potential (TOP) Trap Current Stabilization

As discussed in Sec. 2.2, we use a time orbiting potential (TOP) trap for evaporation and magnetic lensing. The TOP trap arises from the magnetic field from the quadrupole coils combined with the rotating bias field from the TOP coils (see Fig. 6.1). For the magnetic lens, the TOP trap is suddenly weakened, and the atoms undergo breathing mode oscillations (see Fig. 6.5(b)). Additionally, because of gravity, weakening the TOP trap corresponds to vertically lowering the trap minimum. As a consequence of the trap minimum being suddenly lowered, the atoms undergo sizable vertical center of mass oscillations during the magnetic lens, as shown in Fig. 6.5(a). The corresponding amplitude of oscillation for the vertical center of mass velocity is ~ 100 mm/s. Shot-to-shot variations in the vertical velocity at the level of several mm/s can affect the launch efficiency and the Bragg transition resonances. Through these effects, we noticed that the TOP coil current for the magnetic lens underwent a thermalization process when we ran sequences of experimental shots. The thermalization process takes about 5 experimental shots. As the coils heated over multiple sequential shots, the coil resistance increased, causing the current to drop. This decrease in current reduced the magnitude B_0 of the rotating bias field, affecting the strength of the lensing potential and hence the center of mass velocity after a given oscillation time (the radial and axial trap frequencies of the lens both scale as $1/\sqrt{B_0}$).

In order to stabilize the TOP coil current against such thermal effects, we implement a feedback loop. The two quadratures (i.e., sine and cosine) for driving the two

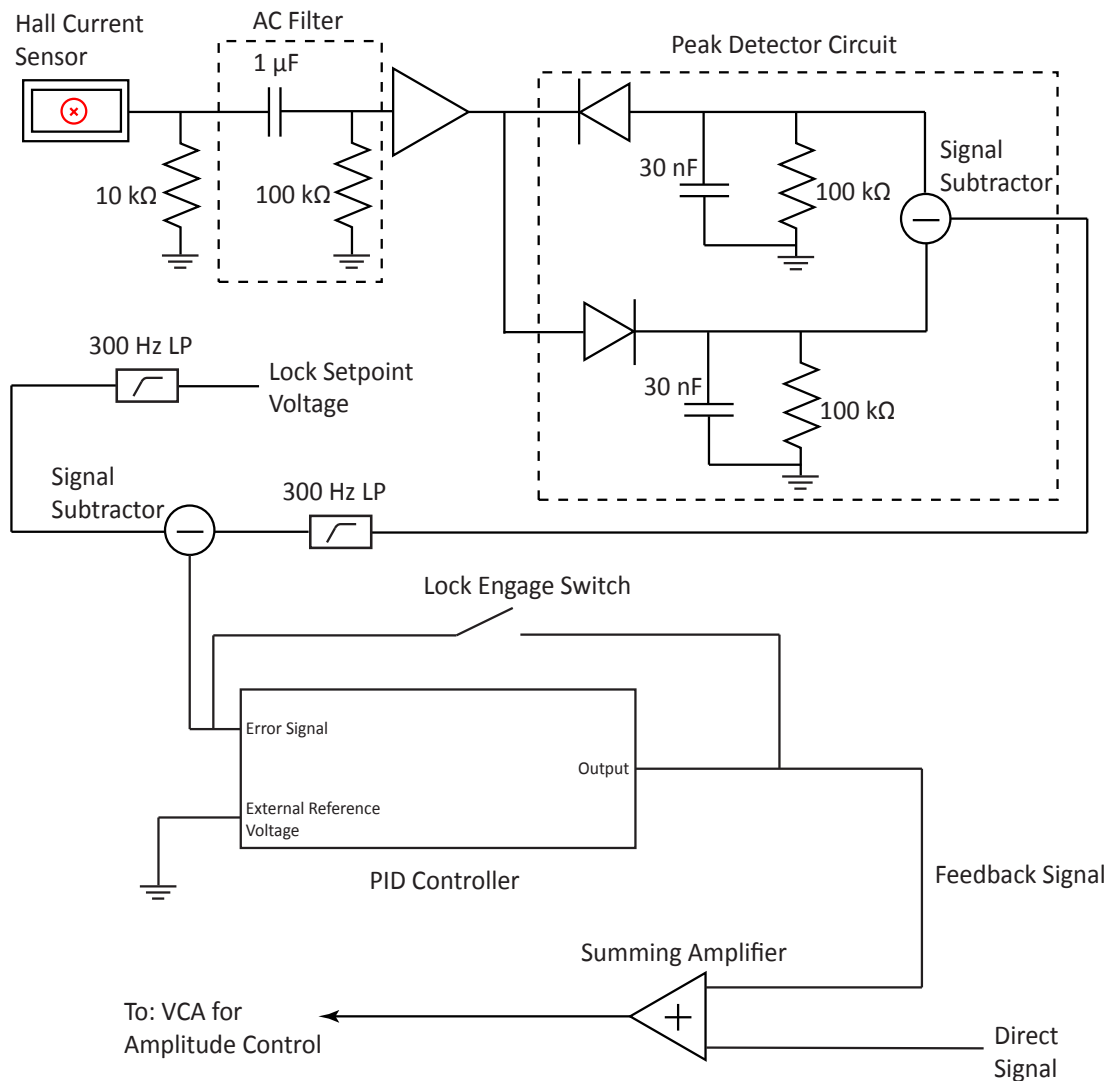


Figure 2.25: TOP coil current stabilization circuit diagram. A Hall effect current sensor measures the AC TOP coil current, and the signal is converted to a DC voltage via a peak detector circuit. This DC voltage is compared to a reference lock setpoint voltage, and feedback is applied to a VCA that actuates the TOP coil current.

TOP coil pairs are independently amplified by a dual channel Hafler P1000 audio amplifier and then a dual channel Lab Gruppen FP13000 audio amplifier⁹. A common VCA before the independent quadratures are generated actuates the current through both coil pairs [12]. A pair of Hall effect current sensors measures the currents of the two coil pairs. We use one of these current sensors to generate the error signal for the current stabilization loop¹⁰. Figure 2.25 shows a circuit diagram of this feedback loop. The voltage output of the Hall effect current sensor, which oscillates at the 2.6 kHz frequency of the TOP field, is amplified after passing through an AC filter. A peak detector circuit then generates a DC voltage equal to the peak-to-peak voltage of the AC signal. The peak detector circuit consists of two diodes with opposite orientation, each connected to ground via a capacitor. The voltage on the capacitor attached to the first diode (lower diode in Fig. 2.25) charges up to the peak positive voltage of the AC signal. The capacitor discharges sufficiently slowly through the 100 kΩ resistor across it that the AC signal will undergo a full period and recharge the capacitor before the voltage has significantly decreased. Similarly, the voltage on the capacitor attached to the second diode (upper diode in Fig. 2.25) charges up to the peak negative voltage of the AC signal. A signal subtractor (Stanford Research Systems SIM980) subtracts the peak negative voltage from the peak positive voltage, yielding the peak-to-peak voltage.

Another signal subtractor generates the error signal for the lock by taking the difference of the peak detector voltage and a lock setpoint voltage provided by an analog output channel from the timing system. Before the signal subtractor, both the peak detector voltage and the lock setpoint voltage are lowpass filtered at 300 Hz to avoid fast transient responses. A Stanford Research Systems PID Controller with

⁹The maximum output voltage of the Lab Gruppen FP13000 has degraded over time. Recently, the amplifier reached a point where it could no longer drive the desired amount of current for the magnetic lensing sequence through both TOP coil pairs. We then installed a separate Lab Gruppen FP9000 amplifier, using the FP13000 to drive one TOP coil pair and the FP9000 to drive the other. Both amplifiers are now operated in bridged mode to provide more voltage overhead.

¹⁰Up until this point, we have found it sufficient to measure the current through one coil pair and apply the corresponding feedback to both coil pairs, indicating that the thermalization effect is largely common to the two coil pairs. For the equivalence principle test, where slight vertical velocity mismatches between ^{85}Rb and ^{87}Rb could be a potentially significant source of noise, it may be beneficial to independently stabilize the current through each coil pair.

a grounded external reference voltage is used to provide the feedback. The output of the PID controller is added to a direct signal using a summing amplifier. The summed signal is used to control the VCA. The feedback is only active during the magnetic lensing sequence. During the evaporation process, the TOP current runs open loop. When feedback is not enabled, a switch is closed to short the output of the PID controller to the error signal input, forcing the PID controller output voltage to zero.

Chapter 3

102 Photon Large Momentum Beam Splitters

We demonstrate atom interferometers utilizing a novel beam splitter based on sequential multi-photon Bragg diffractions. With this sequential Bragg large momentum transfer (SB-LMT) beam splitter, we achieve high contrast atom interferometers with momentum splittings of up to 102 photon recoil momenta ($102\hbar k$). To our knowledge, this is the highest momentum splitting achieved in any atom interferometer, advancing the state-of-the-art by an order of magnitude. We also demonstrate strong noise correlation between two simultaneous SB-LMT interferometers, which alleviates the need for ultra-low noise lasers in some future applications. Our method is intrinsically scalable and can be used to dramatically increase the sensitivity of atom interferometers in a wide range of applications, including inertial sensing, measuring the fine structure constant, and detecting gravitational waves.

This chapter also appeared as Ref. [62] and was written with collaborators Sheng-wey Chiow, Hui-Chun Chien, and Mark A. Kasevich.

3.1 Overview

Atom interferometry has proven to be a powerful tool for precision metrology [1]. Light-pulse atom interferometers [63, 8], which use two-photon Raman transitions as

beam splitters ($\pi/2$ -pulses) and mirrors (π -pulses) for the atoms, have demonstrated the capability to be precise inertial sensors [13, 30, 42, 28] and to precisely measure the fine structure constant [31]. Additionally, atom interferometry is a promising means to test general relativity [37] and to detect gravitational waves [39, 40].

The full potential of atom interferometric sensors has yet to be realized due to the relatively modest performance of the existing atom optics: the sensitivity of an atom interferometer typically scales linearly with the space-time area enclosed by the interferometer [1], whereas two-photon Raman transitions provide momentum separation of only 2 photon recoils of momentum ($2\hbar k$, where k is the wavenumber of the light). A long-standing goal has been to increase the interferometer area through the use of beam splitters that transfer many photon recoils. Such beam splitters have been achieved by applying sequential two-photon Raman transitions [10] and alternatively by applying a single multi-photon Bragg diffraction [17]. However, the degree to which these methods are scalable has been limited by population loss for a large number of two-photon Raman pulses and by the prohibitive intensity requirements for higher order Bragg pulses [16]. Another promising method for achieving scalable beam splitters involves transferring momentum to the atoms through Bloch oscillations in an optical lattice [23, 24, 25, 64]. This approach, however, currently reaches $24\hbar k$ and is limited mainly by the spatial extent of the atomic cloud and the wavefront distortion of the beams.

In this work, we demonstrate that appropriately configured sequences of optical pulses used in conjunction with evaporatively cooled ensembles of atoms can be used to realize very large momentum transfer atom optics. In particular, we demonstrate coherent atom optics capable of delivering nearly 1 m/s velocity kicks to atomic wavepackets, corresponding to a momentum transfer of $102\hbar k$.

3.2 Experimental Results

We operate a Mach-Zehnder interferometer consisting of an initial beam splitter sequence to split a cold cloud from a Bose-Einstein Condensate (BEC) into two

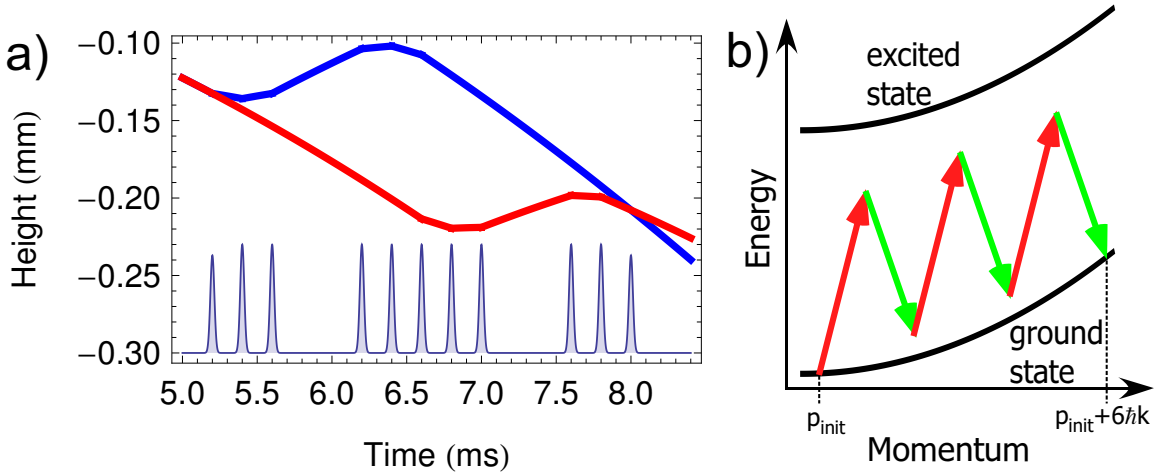


Figure 3.1: Panel a) depicts a sample pulse sequence and the corresponding trajectories of the interfering wavepackets. The thick lines illustrate the wavepacket trajectories, while the thin line in the bottom portion of the figure represents the temporal intensity profile of the pulse sequence. This particular sequence has SB-LMT beam splitters consisting of three $6\hbar k$ pulses ($j = 3, n = 6$ as defined in text), corresponding to a total momentum splitting of $18\hbar k$. The first and final pulses of the sequence are $\pi/2$ -pulses, and the middle nine pulses are π -pulses. Each pulse has a Gaussian temporal profile. Panel b) shows the energy-momentum diagram of $6\hbar k$ Bragg transition driven by two counter-propagating beams (green and red).

wavepackets with different momenta, a mirror sequence to redirect the wavepackets toward each other, and a final beam splitter sequence to interfere the wavepackets (Fig. 3.1 a.). The use of a BEC atom source mitigates interference contrast loss from transverse and longitudinal atom source velocity spread. Each beam splitter and mirror sequence is a composite of a number of multi-photon Bragg pulses (sequential Bragg large momentum transfer, SB-LMT). An n th order multi-photon Bragg pulse can be understood as a $2n$ -photon process that couples two momentum states separated by $2n\hbar k$, creating an effective two-level system (Fig. 3.1 b.) [6]. Where j is a positive integer, the initial beam splitter sequence consists of a single $\pi/2$ -pulse followed by $j - 1$ π -pulses. The $\pi/2$ -pulse splits the cloud into two wavepackets, while the π -pulses accelerate the diffracted wavepacket upward. The mirror sequence consists of $2j - 1$ π -pulses, the first half of which decelerate the upper wavepacket and the latter half of which accelerate the lower wavepacket. The final beam splitter sequence consists of $j - 1$ π -pulses to decelerate the lower wavepacket followed by a single $\pi/2$ -pulse to recombine and interfere the two wavepackets. If each Bragg pulse transfers n photon recoils ($n\hbar k$), then the total momentum splitting between the arms is $N\hbar k$, where $N = j \times n$. Figure 3.2 shows an image of the two wavepackets after a $30\hbar k$ SB-LMT beam splitter and an image of a single wavepacket given a $30\hbar k$ momentum kick.

To produce the BECs, we use the apparatus described in [67, 68, 69]. Approximately 10^8 ^{87}Rb atoms are loaded into a time-orbiting potential (TOP) trap. Evaporative cooling yields a BEC of ~ 3000 atoms in the $|F = 2, m_F = 2\rangle$ state with temperature ~ 4 nK. The atoms are detected using absorption imaging with a CCD camera. The spatial resolution of the imaging system is $2.5 \mu\text{m}$, allowing us to clearly resolve populations in different momentum states using time-of-flight imaging. To minimize the effect of stray magnetic fields on the atoms, we transfer the population into the $|F = 2, m_F = 0\rangle$ state with 50% efficiency with a $3.8 \mu\text{s}$, 1.35 MHz rf pulse in the adiabatically relaxed TOP trap. After switching off the TOP trap, the population in other Zeeman states is pulled away from the interferometer interrogation region by magnetic dipole forces by a short current pulse in the quadrupole magnetic coils. At the beginning of the interferometer sequence, the cloud has $1/e$ radius $\sim 8 \mu\text{m}$. (Note

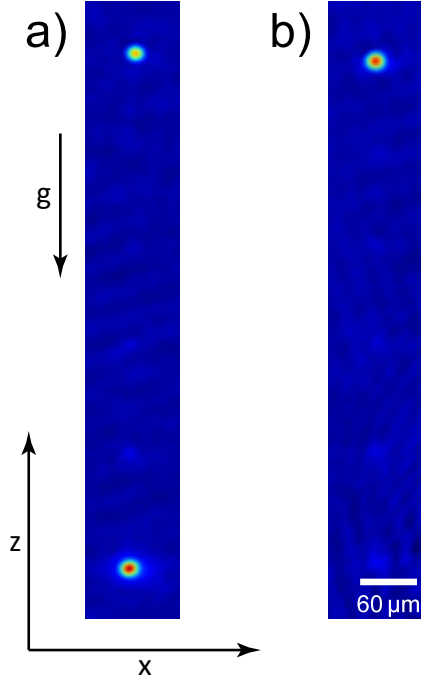


Figure 3.2: Panel a) shows an image of the cloud after the application of a $30\hbar k$ SB-LMT beam splitter. The beam splitter consists of five sequential $6\hbar k$ pulses (one $\pi/2$ -pulse, four π -pulses). The image is taken after 4 ms time-of-flight from the application of the first pulse, corresponding to a wavepacket separation of $600 \mu\text{m}$. The faint spots between the two main wavepackets arise from pulse inefficiency due to imperfections. Panel b) shows an image of the cloud after the application of five consecutive $6\hbar k \pi$ -pulses, effectively forming a $30\hbar k$ SB-LMT π -pulse. Each $6\hbar k \pi$ -pulse has an efficiency of 94%, corresponding to a total efficiency of $\sim 73\%$ for the five pulse sequence. In both panels, the z axis represents the vertical direction and the x axis represents the transverse direction resolved by the camera (the y axis points into the page). The Earth's gravity g points downward (the negative z direction). False color red corresponds to a higher atom density. To remove some of the imaging noise (due to, for example, stray light and vibration of the imaging optics), images are passed through a Principal Component Analysis filter [65, 66]. Subsequently, we smooth the images by convoluting them with a 4 pixel by 4 pixel square kernel.

that the $30\hbar k$ and $102\hbar k$ interferometer sequences do not start at identical delays from the cloud generation).

To generate the laser beams for the atoms optics, we use the fiber-coupled output of a tunable Titanium-sapphire laser having ~ 300 mW output power. The laser beam is split evenly into two paths, each of which passes through an acousto-optic modulator (AOM) to adjust the frequency offset and amplitude. The two paths are directed so as to respectively form the downward (top beam) and upward (bottom beam) propagating atom optics beams. The offset frequencies of the top beam (f_1) and the bottom beam (f_2) are controlled by an FPGA-controlled direct digital synthesizer (DDS) system.

The atom optics beams have Gaussian spatial profiles with Gaussian waist sizes of 1.5 mm in the transverse x and y dimensions (the Gaussian waist size is the transverse distance away from the center of the Gaussian beam profile at which the intensity falls to $1/e^2$ of its value at the center). The divergence of the beams as they propagate through the apparatus in the z direction is negligible. The beams have a lin||lin polarization configuration. We adjust the power coupled through the fiber so that the top (bottom) beam contains approximately 100 mW of power before being diffracted by the AOM. The laser frequency is tuned between 27 GHz and 200 GHz below the 780 nm D₂ ($F = 2 \rightarrow F' = 3$) transition. We use closer detunings for higher order Bragg pulses, which require larger two-photon Rabi frequencies [14, 15, 16].

We shape the Bragg pulses to have Gaussian temporal profiles by shaping the amplitude at which we drive the AOMs with an AFG3102 Tektronix arbitrary function generator (AFG). A variable attenuator (Mini-Circuits ZAS-3) allows us to separately control the AOM frequencies and amplitudes with inputs from the DDS and the AFG, respectively. The use of Gaussian pulses instead of square pulses allows for a significantly improved transfer efficiency [17, 16].

The sequences we implement use individual Bragg pulses that transfer 6-20 $\hbar k$ of momentum, with sequential pulses spaced by 200 μ s. The full width half maximum (FWHM) of each pulse is $\sim 100 \mu$ s. To specify whether a particular pulse is a π -pulse or a $\pi/2$ -pulse, we set its amplitude appropriately. We chirp f_1 to compensate for gravity, and we use piecewise adjustments of f_2 to set each pulse to be on resonance

with the targeted wavepacket.

Using SB-LMT beam splitters and mirrors consisting of $6\hbar k$ pulses, we realize interferometers with momentum splittings of up to $102\hbar k$, an order of magnitude increase over previous atom interferometers [17, 25]. For the $102\hbar k$ interferometer, each SB-LMT beam splitter consists of 17 pulses, and the mirror sequence consists of 33 pulses, i.e., f_2 is changed every $200 \mu\text{s}$ for 67 times while f_1 is chirped at a constant rate. Mainly due to the vibration of the folding mirror $\sim 1\text{m}$ above the optical table, laser phase noise is too large to allow us to scan an interference fringe, which in the absence of such noise could be achieved by systematically varying the chirp rate of f_1 and observing the corresponding oscillations in the difference between the populations in the two output ports ($6\hbar k$ and $0\hbar k$ momentum states) of the interferometer. In our case, laser phase noise is large enough to drive full amplitude fluctuations of this population difference with the chirp rate of f_1 held constant. By observing the amplitude of these fluctuations, we can estimate the contrast of the interferometer, which is the maximum observed value of the normalized population difference between the two output ports. Panels a)–d) of Fig. 3.3 show images illustrating the population fluctuating between the two interferometer output ports for $30\hbar k$ and $102\hbar k$ interferometers, respectively. Panel e) shows the $\sim 5\%$ diffraction efficiency fluctuation of a $\pi/2$ pulse. In a full interferometer, this leads to an inferred $\sim 1\%$ fluctuation in the normalized population difference between the outputs¹, which is a small effect compared to the observed $\sim 20\%$ fluctuation for a $102\hbar k$ interferometer. A histogram depicting the distribution of this $\sim 20\%$ fluctuation is included in panel f). As expected, this distribution is consistent with a sinusoidal fringe with randomly varying phase from shot to shot. The respective maximum wavepacket separations for the $30\hbar k$ and $102\hbar k$ interferometers are $200 \mu\text{m}$ and 2 mm .

The contrast of our SB-LMT interferometers is typically above 15%. With $30\hbar k$ beam splitters we observe 70% contrast. Even with $102\hbar k$ beam splitters, we observe

¹Where the first $\pi/2$ -pulse has efficiency P_1 and the second $\pi/2$ -pulse has efficiency P_2 , the normalized population difference between the two output ports (in the absence of interference) is $(1 - 2P_1)(1 - 2P_2)$. For the pulse efficiencies P_1 and P_2 nominally equal to 50%, 5% fluctuations in the pulse efficiencies lead to fluctuations in the normalized population difference of $0.1 \times 0.1 = 1\%$.

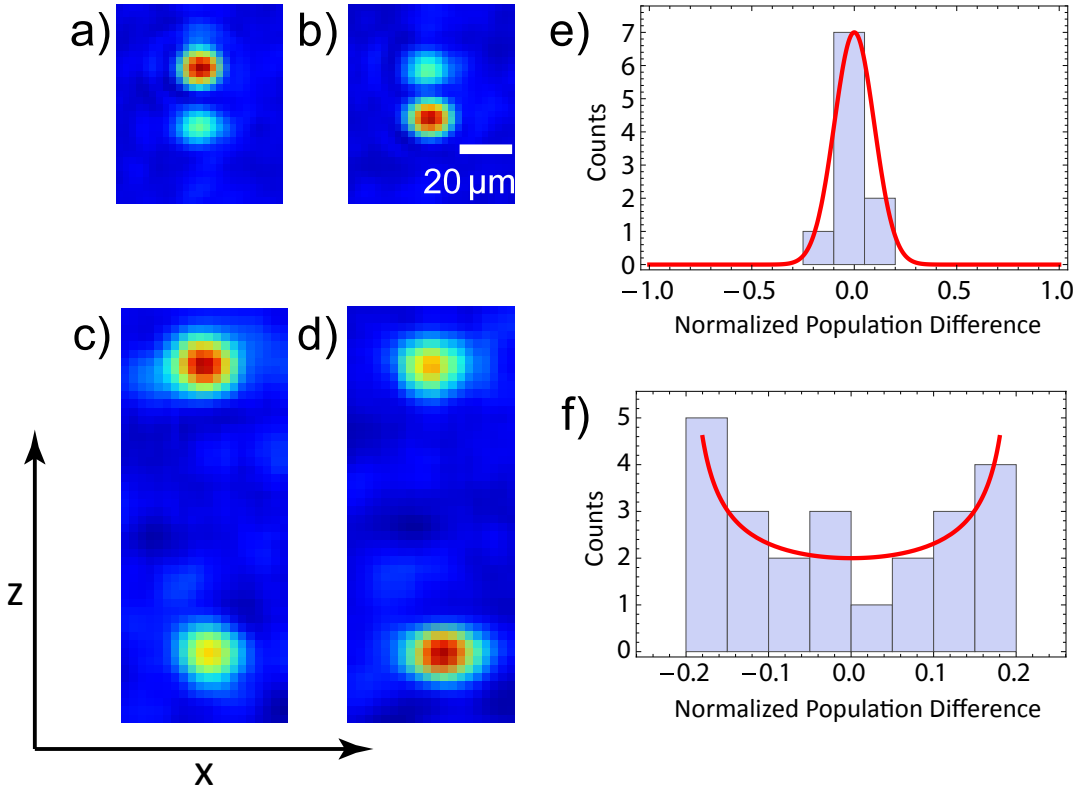


Figure 3.3: Panels a)—d) are examples of typical data showing images of the two interferometer output ports. a) and b) correspond to an interferometer with $30\hbar k$ SB-LMT beam splitters, while c) and d) correspond to an interferometer with $102\hbar k$ SB-LMT beam splitters. The fact that the atom clouds for the $102\hbar k$ interferometer are slightly larger than the clouds for the $30\hbar k$ interferometer is due to the fact that the detection time was later for the $102\hbar k$ interferometer than for the $30\hbar k$ interferometer (respectively 21 ms and 12 ms after the production of the cold cloud), so that in each case the atoms would return to our imaging region at the time of detection), which gives the clouds more time to thermally expand. Panel e) shows a histogram of normalized population difference of a single $\pi/2$ -pulse and a normal distribution with 5% diffraction efficiency variation (standard deviation). Panel f) shows a histogram of normalized population difference of a $102\hbar k$ interferometer, and a synthesized distribution of an interferometer output with 18% contrast and randomly varying phase from shot to shot (red curve). Note that $30\hbar k$ interferometer output has similar distribution with respective 70% contrast. Where N_1 is the number of atoms detected in output port 1 and N_2 is the number of atoms detected in output port 2, the normalized population difference between the output ports is defined to be $(N_1 - N_2) / (N_1 + N_2)$.

a contrast of 18%, which is significantly better than previous work with $24\hbar k$ beam splitters [17]. The increase in contrast is due to the narrow velocity distribution of our cloud, which results in high transfer efficiency, and to the small cloud size, which reduces influences from wavefront distortions. Nevertheless, wavefront distortions are likely responsible for the fact that we see less than full contrast with $102\hbar k$ SB-LMT beam splitters. As discussed in detail in [40], wavefront distortions can lead to a spatially dependent interferometer phase shift across the cloud. For instance, for $102\hbar k$ beam splitters, a wavefront distortion across the atom cloud of magnitude $\sim \lambda/100$ leads to a spatially dependent phase of magnitude $\sim 2\pi$. Note that the contribution of wavefront distortions to the interferometer phase shift is coupled to the transverse motion of the atoms, since in the absence of any transverse motion the phase imparted by wavefront distortions would cancel as a common mode between the two arms of the interferometer. The effects of wavefront distortions are proportional to the number N of photon recoils transferred to the atoms, which is consistent with the fact that the observed contrast is lower for $102\hbar k$ SB-LMT beam splitters. A top view of the cloud would allow us to resolve the resulting spatially dependent interference pattern—however, since we image the cloud from the side, we see an apparent decrease in contrast.

For this work, the momentum separation we can achieve in an interferometer is not limited by the degradation of contrast, but rather by population loss. We observe that the maximum efficiency per photon recoil transferred is achieved by using $6\hbar k$ pulses. Each $6\hbar k$ π -pulse has an efficiency of 94% (which is $\sim 99\%$ per $\hbar k$), leaving us with $0.94^{34} \sim 10\%$ of the original atom number after a $102\hbar k$ interferometer, since each arm of the interferometer undergoes 34 pulses. We believe that the inefficiency is due to the instability of the two-photon Rabi frequency. We expect that in future experiments, the diffraction efficiency can be improved by implementing robust laser frequency and intensity stabilization feedback loops, and by individually optimizing the parameters of each pulse. Such improvement is important since the atom shot noise limited sensitivity of an interferometer increases as the square root of the number of atoms remaining at the end of the interferometer sequence. We do not observe significant diffraction efficiency change over this range of population difference, which indicates

that the mean field shift [70] is not a concern in our case. Note also that fluctuations in the mean field shift from shot to shot can cause noise in the output phase of an interferometer or in the differential phase between two conjugate interferometers. Given our estimated mean field of ~ 10 Hz and our interferometer interrogation times of ~ 10 ms, this does not currently limit us (see discussion below). The use of dense samples in this work is dictated by our detection scheme, and in future work, dilute ensembles can be used to mitigate mean field effects (including phase diffusion [69, 71]).

Common mode noise cancellation between simultaneous interferometers is used to take advantage of the extraordinary sensitivity of LMT atom optics while providing immunity from vibration-induced phase noise [30, 72]. Here, we implement simultaneous interferometers with $30\hbar k$ SB-LMT beam splitters to demonstrate the noise cancellation capability of SB-LMT. For the $30\hbar k$ SB-LMT interferometer, in addition to the previously mentioned nearly full contrast, enough atoms remain after the interferometer sequence to allow us to divide the initial population into two simultaneous, topologically identical interferometers separated vertically by ~ 70 μm : a single $6\hbar k \pi/2$ -pulse splits the sample into two clouds, which subsequently spatially separate during a drift time of 2 ms. After this drift time, we apply the interferometer pulse sequence. Since the two interferometers are addressed by the same laser beams, the contributions from laser phase noise and from accelerations (e.g., gravity) to the difference $\Delta\phi_{\text{upper}} - \Delta\phi_{\text{lower}}$ between the phase shifts of the two interferometers cancel as a common mode. (Here each readout phase $\Delta\phi$ is defined so that the normalized population difference of the corresponding $6\hbar k$ and $0\hbar k$ output ports varies as $C \sin \Delta\phi$, where C is the contrast.) The difference $\Delta\phi_{\text{upper}} - \Delta\phi_{\text{lower}}$ is sensitive to the local gravity gradient [30, 42], but in our case this contribution is too small to be resolved due to the short baseline separating the two interferometers. Thus, the lone non-negligible contribution to $\Delta\phi_{\text{upper}} - \Delta\phi_{\text{lower}}$ arises from the fact that initial populations for the two interferometers occupy two different input ports. Namely, the population in the upper interferometer is initially in state $|6\hbar k\rangle$, while the population in the lower interferometer is initially in state $|0\hbar k\rangle$, so that $\Delta\phi_{\text{upper}} - \Delta\phi_{\text{lower}} = \pi$. Our data are consistent with this result—that is, we observe

the respective population differences of the $6\hbar k$ and $0\hbar k$ output ports of the two interferometers fluctuating out of phase, as shown in Fig. 3.4. This demonstrates that the common mode cancellation of laser phase noise works as expected for SB-LMT beam splitters. This common mode cancellation is crucial to future experiments with large-area atom interferometers, such as those proposed in [39, 40]. As indicated in Fig. 3.4, the common mode noise cancellation works well enough so that fluctuations in $\Delta\phi_{\text{upper}} - \Delta\phi_{\text{lower}}$ occur at the level of atom shot noise. Future work will explore the limitations and requirements of the common mode noise cancellation [42, 39, 40].

3.3 Outlook

To put our results into perspective, we consider their implications for several future experiments. The 10 m atomic fountain at Stanford will allow for pulse spacings of ~ 1 s [8], which with $\sim 100\hbar k$ beam splitters corresponds to meter-scale wavepacket separations (we describe the realization of this experiment in Chapter 7). With a flux of 10^6 atoms/s, the shot-noise-limited acceleration sensitivity of such an interferometer is $\sim 10^{-13}\text{g}/\sqrt{\text{Hz}}$, surpassing the current state-of-the-art by multiple orders of magnitude [13, 73]. The $10^{-13}\text{g}/\sqrt{\text{Hz}}$ number implies that for a measurement time of 1 s, the resolution is 10^{-13}g , assuming that gravity is constant over this time. For a 1 s repetition rate, the instrument could operate as a seismometer for periods greater than 1 s. It would be possible to gain sensitivity at lower periods by interleaving many such interferometers. Current state-of-the-art, highly accurate gravimeters based on atom interferometers or falling corner cubes have sensitivities of $\sim 10^{-8}\text{g}/\sqrt{\text{Hz}}$ and can integrate to $\sim 10^{-9}\text{g}$ resolution after minutes of measurement [13, 73]. Moreover, $\sim 100\hbar k$ beam splitters can allow for highly sensitive inertial sensors that can fit in a spatially compact interrogation region, making them readily transportable outside of the laboratory. For instance, with ~ 30 ms pulse spacings, a signal to noise ratio of 100:1 per shot, and one shot per second, an accelerometer with sensitivity $\sim 10^{-9}\text{g}/\sqrt{\text{Hz}}$ could be achieved with a ~ 1 cm interrogation region. Also, by using an interferometer geometry analogous to that described in [72] with $\sim 100\hbar k$ beam

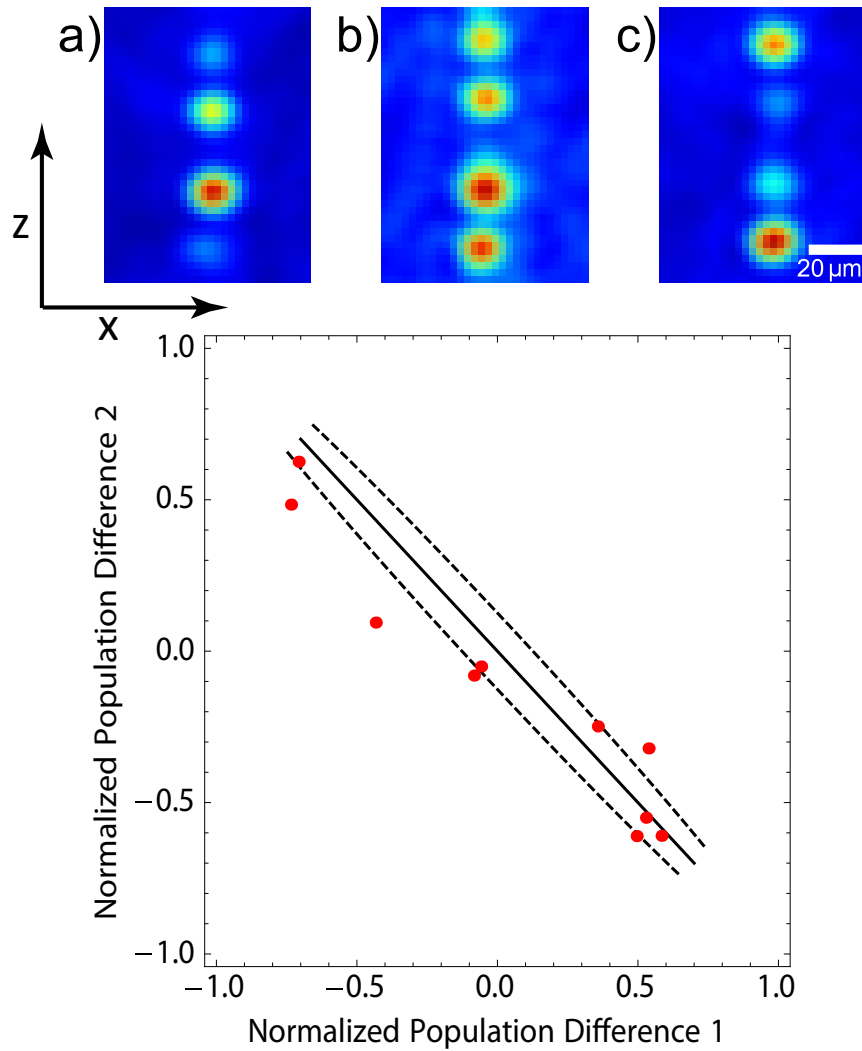


Figure 3.4: Parametric plot of simultaneous $30\hbar k$ interferometer outputs. The upper interferometer output is plotted on the x-axis while the lower interferometer is plotted on the y-axis. The off-diagonal line shows the expected correlation between two simultaneous interferometers having phase difference π with 70% contrast, and the dashed curves show the atom shot noise (there are 250 atoms per interferometer at the time of detection). Panels a)—c) are typical images at various points. The lower spots correspond to the two output ports of the lower interferometer, while the upper spots correspond to the two output ports of the upper interferometer.

splitters, ~ 1 s pulse spacings, and a flux of 10^6 atoms/s, a shot-noise-limited measurement of h/m_{Rb} would have a sensitivity of $\sim 10^{-12}h/m_{\text{Rb}}/\sqrt{\text{Hz}}$, allowing for a greatly improved determination of the fine structure constant [31, 72]. In addition, the proposed AGIS-LEO mission, which will use satellite-based atom interferometers in low-Earth orbit to detect gravitational waves, requires $\sim 100\hbar k$ beam splitters to reach its design sensitivity [40]. Our realization of such beam splitters in the laboratory is thus an important milestone in this effort. Finally, with technical improvements such as better wavefront quality, brighter atom sources, and higher pulse efficiency, we see no impediments to scaling this method to larger momentum transfer, perhaps in excess of $1000\hbar k$.

Chapter 4

Adiabatic-rapid-passage Bragg diffraction

The combination of adiabatic rapid passage and multiphoton Bragg diffraction (ARPMB pulses) to efficiently transfer many photon recoils of momentum ($\hbar k$) to cold atom clouds is theoretically and experimentally investigated. This method is insensitive to perturbations of the pulse intensity or detuning. In particular, the theoretically calculated velocity acceptance can be up to 80% of one recoil velocity v_r , the theoretical maximum in Bragg diffraction. We experimentally demonstrate ARPMB pulses with transfer efficiency of 99.7% per $\hbar k$ using $10\hbar k$ pulses, limited by spontaneous emission losses, and Mach-Zehnder interferometers with 80% contrast.

This chapter also appeared as Ref. [74] and was written with collaborators Sheng-wey Chiow and Mark A. Kasevich.

4.1 Overview

Quantum control provides a powerful framework for optimizing the transfer of population between multiple quantum states in a variety of physical systems [75, 76, 77, 78, 79, 80, 81, 82, 83, 84, 85]. A particularly valuable technique that is widely-used in quantum control problems is adiabatic rapid passage (ARP), which allows for high-fidelity population transfer that is robust against variations in experimental

parameters [19, 20, 21]. In this work, we approach the problem of optimizing the performance of large momentum transfer (LMT) beam splitters ($\pi/2$ -pulses) and mirrors (π -pulses) for atom interferometers from the point of view of quantum control, demonstrating a novel combination of ARP and multiphoton Bragg diffraction [6, 14, 15]. While typical uses of quantum control involve the dynamics of a particle’s internal state, an interesting feature of our work is that it applies analogous methods to an atom’s external momentum state, leaving the atom’s internal state unchanged.

Atom interferometers with beam splitters and mirrors derived from optical pulses [63, 8] have pushed the frontiers in many areas of precision metrology [1], such as inertial sensing [13, 30, 42, 28, 86] and tests of quantum electrodynamics [31]. A key technique to increase the sensitivity of atom interferometers is the use of LMT atom optics that transfer many photon recoils of momentum ($\hbar k$) to the atoms [10, 17, 16, 23, 24, 25, 64, 62, 87, 18, 88]. Many implementations of LMT atom optics rely on multiphoton Bragg diffraction of the atoms from a pulsed-on optical standing wave [6, 14, 15]. A $2n$ -photon Bragg pulse creates an effective two-level system consisting of two momentum states separated by $2n\hbar k$ [6], allowing it to be naturally understood from the point of view of quantum control. Specifically, the goal is to design a pulse that minimizes the dependence of the population transfer and phase on the multiphoton detuning (which corresponds to the velocity spread of the atom source) and laser intensity [89]. For standard multiphoton Bragg pulses, this dependence is quite strong (in particular, the pulses are highly velocity-selective) [18]. An additional constraint for atom optics is that the pulse area should be used efficiently in order to avoid excessive spontaneous emission losses.

Here, we show that by combining ARP with multiphoton Bragg pulses (adiabatic rapid passage multiphoton Bragg pulses, ARPMB) as mirrors and as beam splitters, we can significantly ease the requirements on the velocity spread of the atom source, allowing for increased atom flux through an interferometer. ARPMB pulses with momentum transfer $\geq 10\hbar k$ have the additional benefit of allowing for the clean extraction of a momentum class from a polarization gradient cooled ensemble.

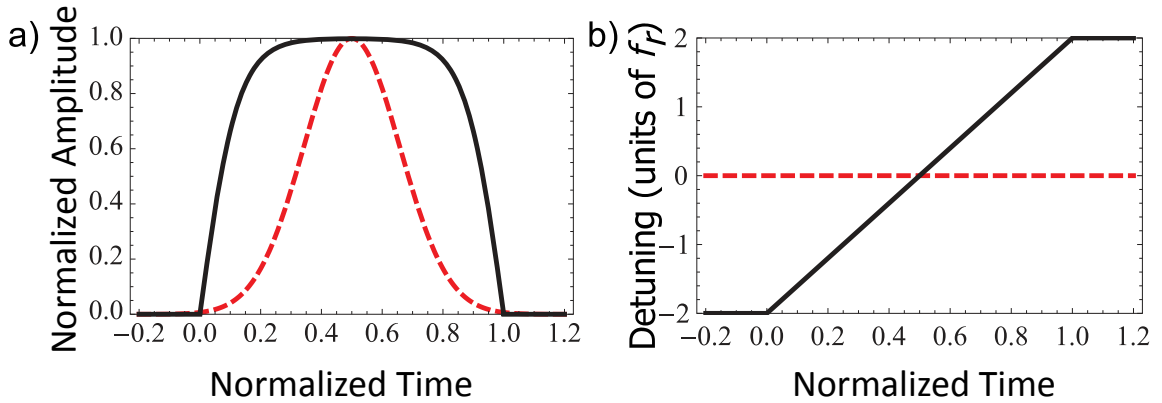


Figure 4.1: Panel a) depicts an ARPMB tanh pulse (black) and a standard gaussian pulse $\exp[-20(t-0.5)^2]$ (red, dashed) of equal length. The normalized pulse amplitude (the amplitude at a given time normalized to the maximum amplitude reached) is plotted versus the normalized time (normalized so that the ARPMB tanh pulse begins at time 0 and ends at time 1). The absolute (not normalized) values of the duration of the pulse and of the maximum pulse amplitude are free parameters that can be tuned. Panel b) shows the two-photon detuning $\delta(t)$ during the pulses when they are on resonance ($\delta_0 = 0$).

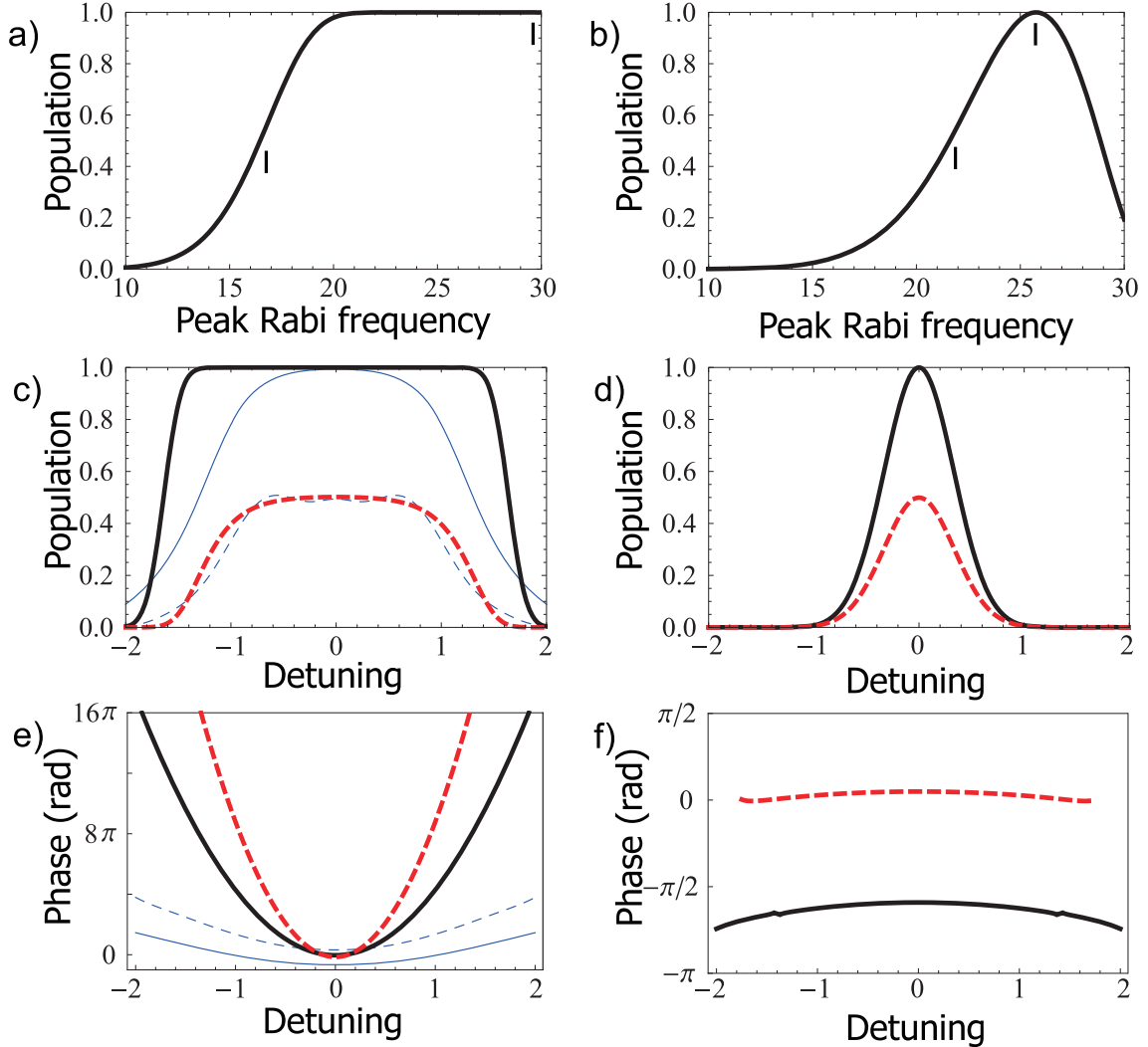


Figure 4.2: Simulations of Bragg diffraction from $|0\hbar k\rangle$ to $|10\hbar k\rangle$ using tanh pulses of length $8/f_r$ (panels a,c,e) and standard gaussian pulses of length $1/f_r$ (panels b,d,f). Rabi frequency and detuning are in units of f_r . Panels a) and b) show diffracted population in $|10\hbar k\rangle$ versus peak two-photon Rabi frequency. Short vertical bars indicate the π and $\pi/2$ intensities used in calculations shown in c), d), e), and f). Panels c) and d) show π -pulse (solid curve) and $\pi/2$ -pulse (dashed curve) diffraction efficiencies versus detuning δ_0 of the pulses. Results using tanh pulse of length $1/f_r$ are also shown for comparison (thin curves), with respective π and $\pi/2$ amplitude $29.2f_r$ and $20.8f_r$. Panels e) and f) show the phase shift versus detuning of state $|10\hbar k\rangle$ after a π -pulse (solid curve) or after a $\pi/2$ -pulse (dashed curve). Linear phase shifts proportional to the pulse length and to the energy difference between initial and final states are removed for clarity.

4.2 Experimental Results

A $2n\hbar k$ ARPMB pulse works as follows. The atoms are initially in the momentum state $|0\hbar k\rangle$. The two-photon Rabi frequency $\Omega(t)$ of two counter-propagating Bragg beams then undergoes an enveloped pulse, with the two-photon detuning $\delta(t)$ from the $2n$ -photon resonance linearly swept across zero during the pulse, as depicted in Fig. 4.1. For an appropriate choice of parameters, the atoms are transferred to the state $|2n\hbar k\rangle$ with nearly perfect efficiency.

Numerical simulations are used to compare standard gaussian Bragg pulses and ARPMB pulses. For the ARPMB method, we have found that “tanh” pulses are especially effective, corresponding to the intensity profile (Fig. 4.1a)

$$\Omega(t) = \tanh(8t) \tanh(8(1-t)), \text{ for } 0 < t < 1.$$

During the ARPMB pulses, $\delta(t)$ is linearly swept from $-2f_r + \delta_0$ to $+2f_r + \delta_0$, where $2\pi f_r = \hbar k^2 / 2m \simeq 2\pi \times 3.77$ kHz (for ^{87}Rb , used in this work) is the photon recoil frequency and δ_0 is the mean detuning of the pulse (Fig. 4.1b). Figure 4.2 shows the results of numerical simulations comparing the efficiencies and sensitivities to variations in pulse amplitude and detuning of an ARPMB tanh pulse and a standard gaussian pulse as implemented in previous work [62]. In the simulations, the Schrödinger equation is numerically integrated for a $|0\hbar k\rangle$ to $|10\hbar k\rangle$ process in the basis of 41 discrete momentum states ($|-40\hbar k\rangle, |-38\hbar k\rangle, \dots$), with the adjacent state coupling strength $\Omega(t)$ shaped appropriately [64, 16, 17]. Frequency sweeping and two-photon detuning are implemented as differential energy level changes between momentum states, as seen in a proper rotating frame of reference.

Figures 4.2a, 4.2b show the diffracted population in $|10\hbar k\rangle$ with different pulse amplitude for a tanh pulse of length $8/f_r$ and a gaussian pulse of length $1/f_r$, respectively. With the tanh pulse, the diffraction efficiency remains high as the pulse amplitude increases, which is a signature of adiabatic rapid passage. In Figs. 4.2c, 4.2d the diffraction efficiency is plotted against the detuning δ_0 of the pulse. The velocity acceptance of a π -pulse and a $\pi/2$ -pulse can be inferred via the Doppler shifts δ of resonance frequencies of atoms with velocity v : $\delta = 4f_r v / v_r$, where $v_r = \hbar k / m$

is the recoil velocity. The tanh π -pulse has a full width half maximum (FWHM) velocity acceptance of $0.83v_r$ ($3.3f_r$) (black curve, Fig. 4.2c), which corresponds to the FWHM velocity of a thermal cloud with temperature $0.12T_r$ ($T_r = mv_r^2/k_B$ is the recoil temperature). This is close to theoretical maximum velocity acceptance of $\sim 1v_r$ of standard Bragg diffractions (for velocities outside this maximum theoretical acceptance range, the atoms will be closer to Bragg resonances of different orders $2v_r$ away). Similarly, the tanh $\pi/2$ -pulse has a much larger velocity acceptance than the standard gaussian pulse (dashed red curves in Figs. 4.2c and 4.2d). These simulation results suggest that atom interferometers using tanh pulses as beam splitters can benefit not only in atom number due to the large velocity acceptance during π -pulses, but also in contrast due to the wide $\pi/2$ -condition validity range.

ARPMB pulses are implemented on cold atom clouds of various temperatures. The cold atom clouds are generated by the apparatus described in [67, 68, 69, 62]. Approximately 10^8 ^{87}Rb atoms are loaded into a time-orbiting potential (TOP) trap in the $|F = 2, m_F = 2\rangle$ state. After evaporative cooling, a cloud with velocity spread tunable from $\lesssim 0.1v_r$ (henceforth referred to as cold cloud) to $\sim 0.7v_r$ (henceforth referred to as thermal cloud) set by the rf cut of the evaporation is obtained. To minimize the effect of stray magnetic fields on the atoms, the population is transferred into the $|F = 2, m_F = 0\rangle$ state with 50% efficiency with a short rf pulse in the adiabatically relaxed TOP trap. After switching off the TOP trap, the population in other Zeeman states is pulled away from the interrogation region by magnetic dipole forces from a short current pulse in the quadrupole magnetic coils. Time-of-flight imaging is used to determine the populations in different momentum states, and the atoms are imaged using spatially resolved fluorescence detection with a CCD camera and $100\mu\text{s}$ retro-reflected detection pulses.

The atom optics beams are generated from the fiber-coupled output of a Ti:sapphire laser operating near the 780 nm D_2 ($F = 2 \rightarrow F' = 3$) transition. The laser power after the fiber is actively stabilized to within 0.1% of the designated set point via an acousto-optic modulator (AOM) before the fiber. After passing through a mechanical shutter, the power-stabilized beam is then split evenly into two paths, each of which passes through an AOM to adjust the frequency offset and amplitude. The two paths

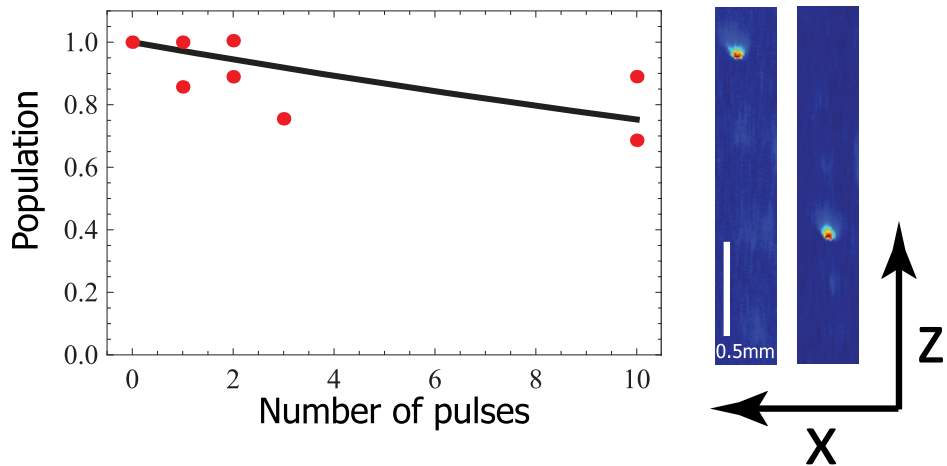


Figure 4.3: Plot showing the remaining population after a number of $10\hbar k$ tanh pulses. The scattering of data points is due to atom number fluctuation from shot to shot (the population is normalized globally). The black curve shows the fit with $97.2 \pm 0.9\%$ efficiency per pulse, which corresponds to an efficiency of 99.7% per $\hbar k$. Images to the right are falling clouds 12 ms after sequential $10\hbar k$ ARPMB π -pulses. The left image shows the population after 3 π -pulses against gravity, overall $30\hbar k$ transferred to the cloud. The right image shows the population after 5 π -pulses against gravity followed by 5 π -pulses along gravity, with no net momentum transferred after these 10 pulses. Note that remnants of early pulses may arrive at the same final velocity ($0\hbar k$) due to the following pulses, but they would be spatially resolved so that the estimate of diffraction efficiency is not affected. The tails in the images are caused by an intensity imbalance of the counter-propagating detection beams.

are directed in a race-track setup [42] with a rigid two-mirror assembly above the vacuum chamber, so as to respectively form the downward (top beam) and upward (bottom beam) propagating atom optics beams. The offset frequencies of the top beam (f_1) and the bottom beam (f_2) are controlled by an FPGA-controlled direct digital synthesizer (DDS) system.

The atom optics beams have gaussian spatial profiles with waists of 1.5 mm, and with lin||lin polarization configuration. By adjusting the set point of the power stabilization servo, each beam contains 50–200 mW of power before being diffracted by the AOM. The laser frequency is typically tuned 110 GHz below or above the D₂ transition.

The temporal profiles of the ARPMB pulses are controlled by shaping the amplitude at which the AOMs are driven with an AFG3102 Tektronix arbitrary function generator (AFG). A variable attenuator (Mini-Circuits ZAS-3) allows for separate control of the AOM frequency and amplitude with inputs from the DDS and the AFG, respectively.

The sequences that are implemented use individual ARPMB pulses that transfer $10\hbar k$ of momentum, each of which is about 300 μ s long ($\sim 1/f_r$) with 40 μ s between pulses. Each pulse amplitude is set to serve as a beam splitter or a mirror on demand. f_1 is chirped to compensate for gravity, and phase-continuous frequency sweeps of f_2 of the same range with adjustable center frequency are used to address atoms in different velocity groups; f_2 is set to a constant frequency between pulses. The diffraction efficiency of the $10\hbar k$ pulse is demonstrated in Fig. 4.3, where multiple pulses are applied sequentially to a cold cloud. The efficiency reaches 99.7% per $\hbar k$, estimated by fitting the remaining fraction after a various number of such pulses using the data shown in Fig. 4.3. This is consistent with spontaneous emission losses, which we calculate to be 0.2% per $\hbar k$. Figure 4.4 shows experimental data illustrating the detuning dependence of the π - and $\pi/2$ -pulse efficiencies on cold clouds. The detuning is varied from shot to shot via f_2 by the DDS. The simulation results shown in Fig. 4.4 (black curves) are for $1/f_r$ tanh pulses with no free parameter to fit data.

In addition to transfer efficiency, it is crucial to understand the phase imprinted

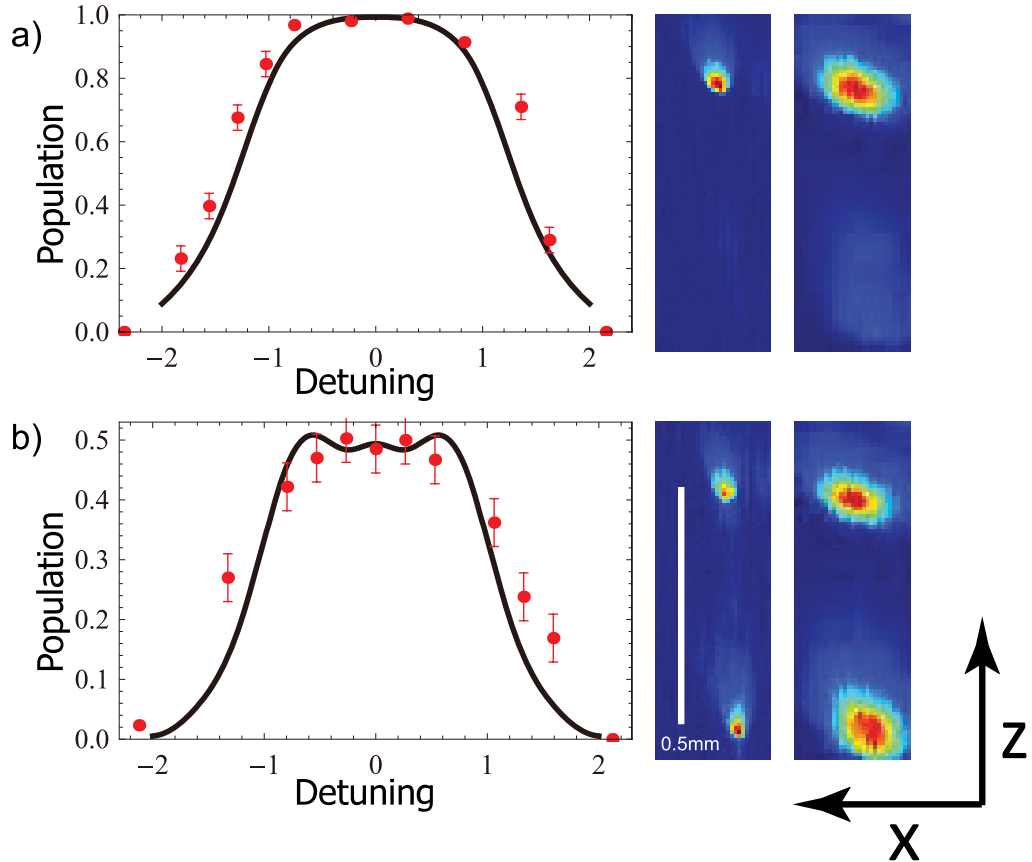


Figure 4.4: $10\hbar k$ tanh pulse diffraction efficiency versus detuning (in units of f_r) of a π -pulse (a) and a $\pi/2$ -pulse (b). Error bars indicate typical fluctuations when the populations in $|0\hbar k\rangle$ and $|10\hbar k\rangle$ are comparable. Since the fluctuations are largest when these populations are comparable, the error bars shown on other points illustrate a conservative bound on the fluctuations at these points. For points with no error bars shown (where the efficiency is close to zero or to unity), the error bars are smaller than the point size. Simulation results of a $1/f_r$ tanh pulse are presented as black curves. Images show near zero detuning with cold (left) and thermal (right) clouds. An image of the atoms that resolved the y axis instead of the x axis would look similar. When we carried out this experiment, we only had one camera, which resolved the x axis and not the y axis.

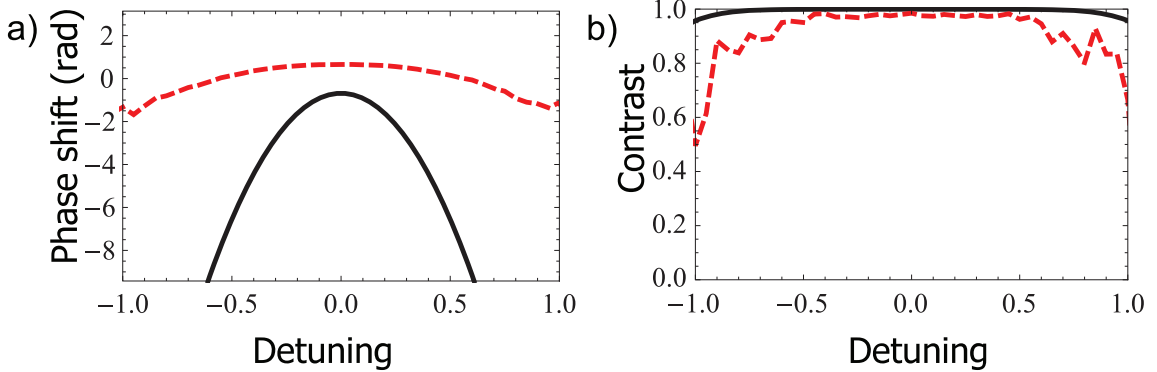


Figure 4.5: Simulations of ARPMB Mach-Zehnder interferometers. The fringe phase and contrast versus detuning (in units of f_r) of Mach-Zehnder interferometers using tanh pulses of length $8/f_r$ (black) and of length $1/f_r$ (dashed red) are shown in a) and b), respectively. Each interferometer is composed of three tanh pulses of equal length with amplitudes satisfying the π - or $\pi/2$ -pulse condition.

to the atomic wavefunction during ARPMB pulses for applying them to atom interferometry. This is because an interferometer would have no contrast if the phases of participating velocity components vary over 2π rad. Figures 4.2e, 4.2f show the detuning dependence of the phase change of state $|10\hbar k\rangle$ after a $10\hbar k \pi$ -pulse (black curves) or $\pi/2$ -pulse (dashed red curves) using a tanh pulse and a gaussian pulse, respectively. With standard gaussian pulses, the phase shift has negligible dependence on δ_0 , apart from a linear shift due to the rotating frame of reference and the duration of the process. With ARPMB pulses, the phase shift depends strongly on δ_0 and on the details of the pulse shapes. However, this detuning dependence does not necessarily prevent us from having atom interferometers with large velocity acceptance. For instance, in a symmetric Mach-Zehnder interferometer, the output phase is the phase difference of its π -pulse and $\pi/2$ -pulses. As shown in Figs. 4.5a and 4.5b, with properly chosen pulse lengths and amplitudes, the phase shifts of each velocity component largely cancel out so that the phase variation is well within one cycle and that the contrast of the interferometer is preserved.

To demonstrate the coherence of our ARPMB pulse, a $\pi/2-\pi-\pi/2$ Mach-Zehnder

atom interferometer using $10\hbar k$ ARPMB tanh pulses is implemented. A fringe from this interferometer is displayed in Fig. 4.6a, where a sinusoidal fit is also presented. To map out a fringe, the DDS is used to vary the phase of the final pulse of the interferometer from shot to shot by changing the constant frequency of f_2 during the $40 \mu\text{s}$ between the second and the final pulses. For a cold cloud, we observe 80% contrast. For a thermal cloud, we still observe a relatively high contrast of 25%. We experimentally verify that blue-detuned beams work equally well as red-detuned beams, and that the direction of frequency sweeps of f_2 is irrelevant (as expected).

Additionally, the detuning dependence of the interferometer phase is experimentally studied. We confirm that while the interferometer phase for ARPMB pulses does depend on detuning, this dependence can be made relatively flat (~ 1 rad over a range of $2f_r$ ($0.5v_r$)), as shown in Fig. 4.6b. To obtain each data point in Fig. 4.6b, a fringe is mapped out for a cold cloud at a specific detuning (same for all three pulses) set by the DDS, and a fit is performed to extract the fringe's phase. Both the velocity acceptance and the interferometer phase shift agree well with simulations using comparable pulse length ($1/f_r$), the black curves in Fig. 4.4 and Fig. 4.6. The slight mismatch of the data and simulations is due to distortion of the pulse temporal profile caused by the nonlinearity of the variable attenuators and the AOMs.

4.3 Outlook

To conclude, we have theoretically and experimentally studied the combination of ARP and multiphoton Bragg diffraction and have demonstrated dramatically improved velocity acceptance when compared to standard multiphoton Bragg pulses. We anticipate that this improvement will be especially valuable for LMT atom optics sequences that involve many successive multiphoton Bragg pulses [62], as a result of the fact that the application of repeated pulses amplifies velocity selection. For instance, by exponentiating the simulation results shown in Fig. 4.2 by 100, the velocity acceptance of $1000\hbar k$ LMT is $2.6f_r$ by using tanh pulses, while merely $0.08f_r$ by using standard gaussian pulses. Moreover, ARPMB beam splitters can be combined with Bloch oscillations, whose velocity acceptance is Brillouin-zone limited, to achieve the

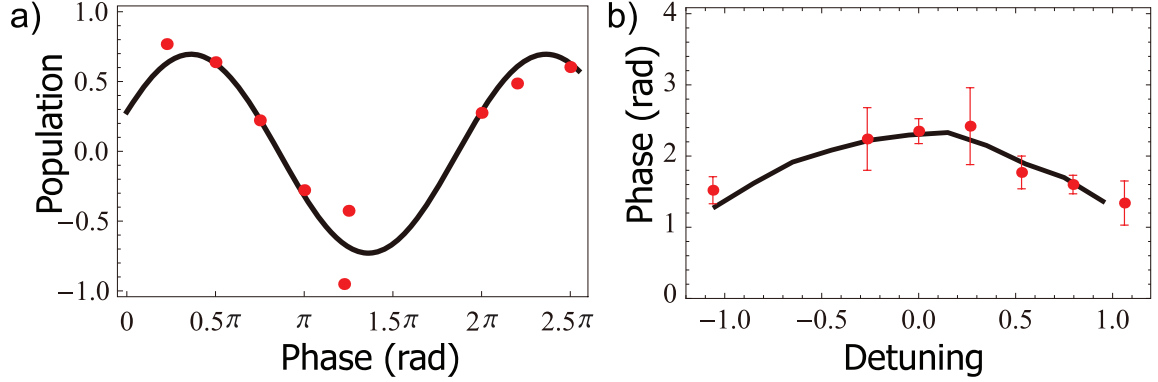


Figure 4.6: $10\hbar k$ Mach-Zehnder interferometer results. Panel a) shows normalized population difference of interferometer output using tanh pulses with zero detuning on cold clouds. The fringe is taken by scanning the phase of the last pulse. Panel b) shows the fitted fringe phase versus detuning (in units of f_r) (error bars indicate the uncertainty in the fitted phase, predominantly due to vibration-induced laser phase noise); the black curve shows the best fit of the simulation result of such an interferometer with the π -pulse amplitude as the only free parameter.

largest possible overall velocity acceptance for this kind of interferometer [23, 24, 25].

Chapter 5

43 W Quasi-Continuous Laser Source at 780 nm

We demonstrate high-efficiency frequency doubling of the combined output of two 1560 nm 30 W fiber amplifiers via single pass through periodically poled lithium niobate (PPLN) crystals. The temporal profile of the 780 nm output is controlled by adjusting the relative phase between the seeds of the amplifiers. We obtain a peak power of 34 W of 780 nm light by passing the combined output through one PPLN crystal, and a peak power of 43 W by passing through two cascading PPLN crystals. This source provides high optical power, excellent beam quality and spectral purity, and agile frequency and amplitude control in a simple and compact setup, which is ideal for applications such as atom optics using Rb atoms.

This chapter also appeared as Ref. [90] and was written with collaborators Sheng-wey Chiow, Jason M. Hogan, and Mark A. Kasevich.

5.1 Overview

High-power, high-quality laser sources in the near infrared region are of great interest in a variety of fields, including atomic, molecular, and optical physics. Diode pumped alkali vapor lasers generated up to 48 W at 894 nm [91] and up to 28 W at 780 nm [92, 93]. Another approach is to use the frequency doubled output of an infrared

laser [94, 95]. Frequency doubling of 900 mW at 1550 nm in a periodically poled lithium niobate (PPLN) waveguide yielded over 400 mW output at 775 nm [96], and >50 W at 589 nm was generated from >60 W at 1178 nm through the use of a doubling cavity [97]. In the efforts of developing simple, compact, and robust laser systems for laser cooling and trapping, efficient frequency doubling of 1560 nm light via PPLN crystals in free space has been explored and 11 W at 780 nm was demonstrated [98, 99, 100, 101].

In addition to high optical power, light sources with high spectral purity, dynamic frequency agility, and temporal profile control are also demanded in applications such as atom interferometry using large momentum transfer beam splitters [62, 40, 72]. These features are typically obtained by passing high power beams through additional modulators. For instance, acousto-optic modulators are commonly used for generating complex patterns in frequency and amplitude [62]. However, the delivered optical power is severely reduced due to the modulators' limited diffraction efficiency and modulation bandwidth, material damage threshold, and wavefront distortions.

In this work, we demonstrate a high power laser system at 780 nm based on frequency doubling of the combined output of two fiber amplifiers via a single pass through PPLN crystals. We achieve 34 W at 780 nm with a total of 65 W at 1560 nm with a single crystal (52% efficiency), and 43 W at 780 nm with two cascading crystals (66% efficiency). A key benefit of this scheme is its relative simplicity—for instance, high efficiency frequency doubling at high power is achieved without the need for resonant enhancement using an optical cavity. In addition to high power and high efficiency, we also demonstrate that the 780 nm output exhibits a controlled temporal profile. With the use of a narrow linewidth seed laser and wideband phase modulators, this 43 W of 780 nm light is thus ready to be delivered (e.g., to Rb atoms as matter wave beam splitters) without further modulation. Although in this work we focus on the generation of 780 nm light, we expect our method to be extendable to a broad range of wavelengths.

5.2 Experimental Results

In the ideal case of perfect phase matching and a lossless device, the doubling efficiency η of optical frequency ω after a doubling crystal of length l is

$$\eta = P_{2\omega}/P_\omega = \tanh^2 \left(l \sqrt{\eta_0 P_\omega} \right), \quad (5.1)$$

where $P_{\omega(2\omega)}$ is the power of frequency component $\omega(2\omega)$ and η_0 is a constant [96]. We exploit the dependence of η on P_ω to achieve high doubling efficiency. By coherently combining at a beam splitter the outputs of two fiber amplifiers seeded by the same laser, up to two times higher power is available than that attainable using a single amplifier. We also cascade two doubling crystals to extend the effective crystal length l in order to achieve even larger η . The coherent combination scheme allows for convenient control of P_ω by changing the relative phase ϕ between the outputs of the amplifiers: $P_\omega = P_0 (1 + \cos \phi)$, where P_0 is the power of each amplifier. $P_{2\omega}$ is thus enveloped by properly adjusting ϕ as a function of time.

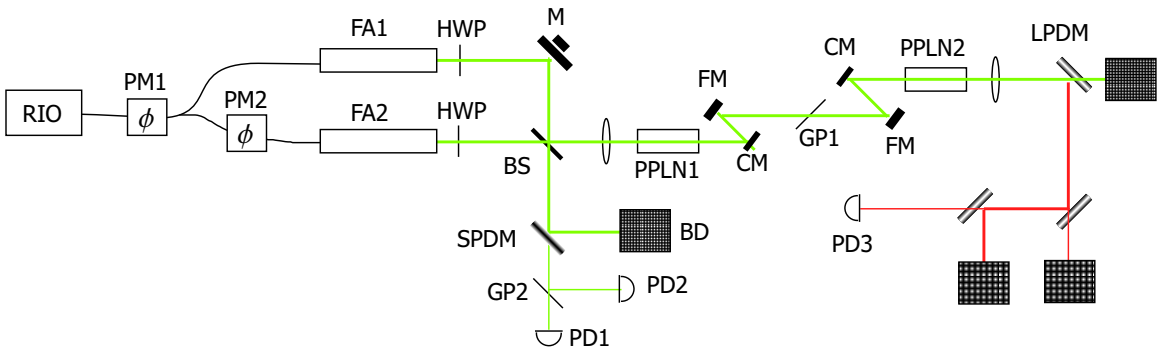


Figure 5.1: Schematic of the setup. FA: fiber amplifier, HWP: half-wave plate, M: mirror on a PZT stack, PPLN: PPLN crystal, BS: beam splitter, SPDM: short pass dichroic mirror, LPDM: long pass dichroic mirror, BD: beam dump, GP: glass plate, RIO: the RIO laser, PM: phase modulator, PD: photo diode, CM: dual wavelength concave mirror, FM: dual wavelength flat mirror.

Each of the fiber amplifiers we use (IPG Photonics EAR-30K-C-LP-SF) provides more than 30 W of light at 1560 nm with specified beam quality factor $M^2 \leq 1.1$. A compact laser module (RIO ORION) at 1560 nm serves as the common master

laser, which has a linewidth of 8 kHz and 20 mW fiber coupled output. As shown in Fig. 5.1, the RIO output is evenly split into two paths after passing through a fiber coupled phase modulator, PM1 (Covega Mach-10, $V_\pi = 4V$). Fiber amplifier 2 (FA2) is seeded with light that is phase modulated by PM2, while FA1 is seeded directly without modulation. After the combining beam splitter (BS), one path goes to the doubling crystals as the main output (the dark port), while the other path (the bright port) is directed to a beam dump via a short pass dichroic mirror (SPDM), which reflects more than 99% of 1560 nm light. The leakage is detected by a photo diode (Thorlabs D400FC, PD1 in Fig. 5.1) for locking the path length difference from RIO to BS. Several percent of the leakage light is picked up by a glass plate (GP2) and detected by PD2 as an intensity monitor. PM2 is weakly driven at 100 MHz (-10 dBm), and the signal from PD1 is demodulated as the error signal for the path length difference servo. The servo output is applied to both PM2 and the piezo-actuated mirror M. When locked, most of the power is steered away from the crystals, and PM2 is kept at 2 V_{DC} .

When output is demanded, the error signal fed to the servo and the 100 MHz modulation to PM2 are switched off; instead, a shaped phase excursion is applied to PM2 in addition to the 2 V_{DC} offset. We typically apply a gaussian waveform of -3.5 V_p with a duration of 1 ms, provided by an arbitrary function generator (Tektronix AFG3102). The shaped pulse at the main output of BS is focused into a 40 mm doubling crystal (Covesion MSHG1550-1.0-40, PPLN1 in Fig. 5.1) with a lens of focal length 50 mm. After PPLN1, the beam is collimated to a waist of ~ 1.1 mm with a concave mirror (CM) high-reflection (HR) coated for 780 nm and 1560 nm with a radius of curvature of 10 cm. A pair of flat mirrors (FM) HR-coated for both wavelengths direct the collimated beam into PPLN2 after it is focused by another CM. This arrangement largely maintains the mode-match condition between the injecting 1560 nm light and the generated 780 nm light by eliminating refractive elements such as lenses. To account for the differential phase shift between these wavelengths, a glass plate oriented at the Brewster angle is inserted in the beam (GP1), allowing independent optimization of each crystal in contrast to [95]. After passing through PPLN2, the beam is collimated and reflected by several long pass dichroic mirrors

(LPDM), which pass 1560 nm light but reflect 780 nm light. PD3 detects the 780 nm light behind a LPDM for proper attenuation. The PPLN crystals are housed inside temperature controlled ovens provided by Covision. They are kept at about 150°C for maximum doubling efficiency, and are kept at 200°C to turn off the doubling for diagnosis purposes.

As shown in Fig. 5.1, PD2 measures the power of 1560 nm in the bright port, which is complementary to the power in the dark port before the crystals. The W/V scaling of PD2 is calibrated with a Newport 818T power meter and is consistent with the power meters built into the fiber amplifiers, while the scaling for PD3 is calibrated with a Coherent FieldMaster power meter. We observe that the extinction ratio of 1560 nm is about 40:1, while there is no detectable 780 nm power at its minimum. By comparing the signal traces of PD2 and PD3, we plot the doubling efficiency as a function of injection power. Figure 5.2a shows a pair of signal traces when applying a gaussian phase excursion. Figure 5.2b shows the parametric plot of 780 nm and 1560 nm power using one or two crystals. With both crystals on, and with GP1 properly adjusted, the 780 nm output reaches 43 W when the 1560 nm input is 65 W, an efficiency of 66%. With a single crystal on, the 780 nm output reaches 34 W, an efficiency of 52%. The data do not fit well with Eq. (5.1); however, an excellent fit can be obtained with an additional scaling factor of ~ 0.7 (red curves in Fig. 5.2). We believe that the need for this scaling factor arises due to a slight mode mismatch of the beams to the crystals and between the beams. We do not observe thermal effects in the crystals [94, 95] with our experimental parameters, which would otherwise deviate the data from the fit in Fig. 5.2 at high powers. Future work will explore the role of thermal effects for longer pulses.

By examining the open loop beatnote on PD2, we infer the degree to which the linewidth of the combined beams is broadened due to phase noise introduced by the fiber amplifiers and the frequency doubling setup. We observe phase excursions of $\lesssim \pi$ rad over ~ 1 ms, corresponding to a linewidth broadening of ~ 300 Hz assuming that the noise from the two paths is uncorrelated. The phase noise arises primarily from vibrations of the mirror mounts and optical fibers. Differential phase noise between the two paths also leads to amplitude fluctuations during the pulse, during which the

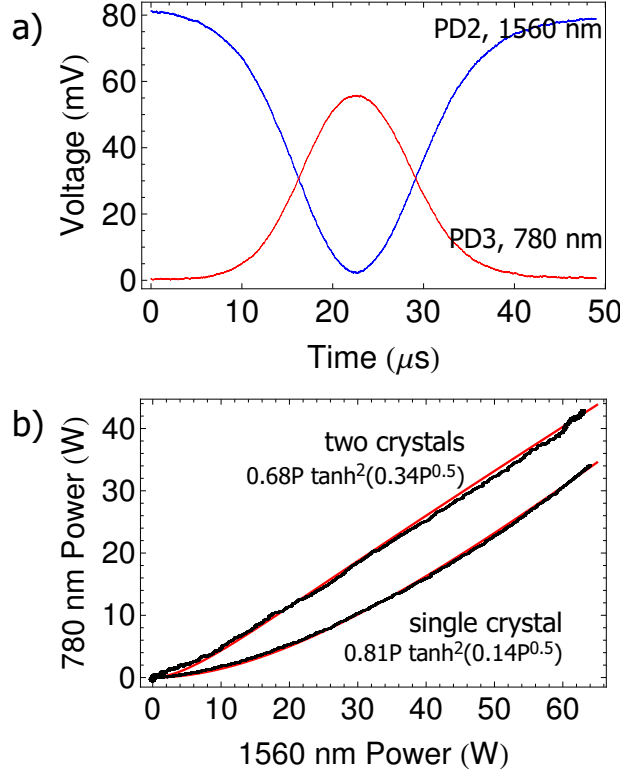


Figure 5.2: Experimental result. Panel a) Scope trace of PD2 (blue) and PD3 (red). Panel b) Parametric plot of 780 nm power versus 1560 nm power using one or two crystals. The black curves show the measured power and the red curves are the fits. Note that the fitted coefficient inside the \tanh^2 increases by a factor of ~ 2 when using two crystals, which is consistent with the doubling of the interaction length.

servo is switched off in our present scheme. In future work, PM2 can be used as an actuator to servo the pulse to a desired temporal profile.

Additionally, we characterize the spatial beam quality of the 780 nm light. Figure 5.3a shows the beam profile and an image of shear interference. The shear interference reveals no low frequency wavefront disturbance, which is critical in applications such as [40]. Figure 5.3b shows the beam width ($1/e^2$ radius) σ versus axial position z after a 1-inch achromatic lens with a focal length of 10 cm. M^2 is estimated to be 1.15 ± 0.2 by fitting the data to the equation $\sigma^2 = \sigma_0^2 + M^4(\lambda/\pi\sigma_0)^2(z - z_0)^2$, where σ_0 is the width at focus z_0 , and $\lambda = 780$ nm is the wavelength.

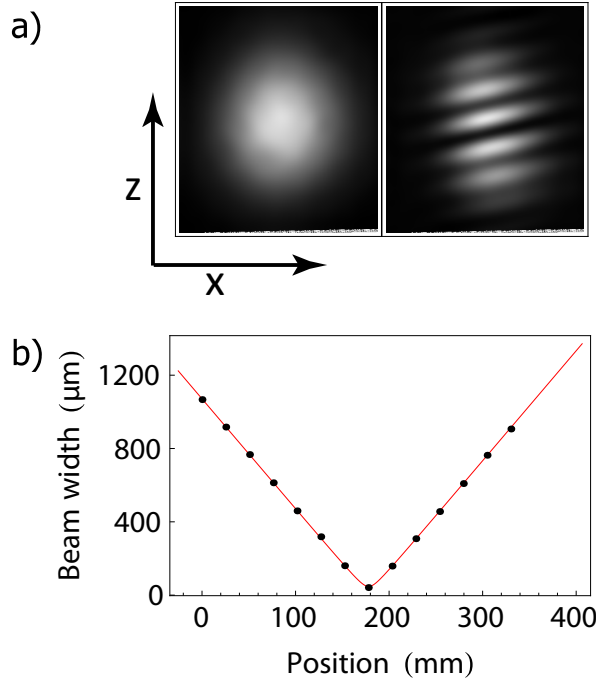


Figure 5.3: Beam quality measurement. Panel a) Beam profile and shear interference. The beam propagates parallel to the optical table on which the measurements are performed (in the y direction, into the page). Panel b) Beam width versus position.

5.3 Outlook

We demonstrate a novel scheme for achieving a power of 43 W at 780 nm by high-efficiency, single-pass frequency doubling of combined fiber amplifiers in two cascading PPLN crystals. The output has an excellent spatial mode and a narrow linewidth, and can be amplitude modulated on demand without additional modulators. This compact and simple laser system is ideal for applications such as atom optics for large area atom interferometers [62, 40, 72]. Moreover, by coherently combining a larger number of fiber amplifiers, we anticipate even higher output power and better conversion efficiency, perhaps enabling >100 W power levels. Furthermore, this technique can be extended to second harmonic generation in the visible or even in the uv region. For instance, passing the coherent combination of 780 nm light from two such systems through a doubling crystal would generate appreciable power at 390

nm, with full amplitude modulation capability.

Chapter 6

Atom Lensing to Picokelvin Temperatures

Using a matter wave lens and a long time-of-flight, we cool an ensemble of ^{87}Rb atoms in two dimensions to an effective temperature of less than 50_{-30}^{+50} pK. A short pulse of red-detuned light generates an optical dipole force that collimates the ensemble. We also report a three-dimensional magnetic lens that substantially reduces the chemical potential of evaporatively cooled ensembles with high atom number. By observing such low temperatures, we set limits on proposed modifications to quantum mechanics in the macroscopic regime. These cooling techniques yield bright, collimated sources for precision atom interferometry.

This chapter also appeared as Ref. [102] and was written with collaborators Jason M. Hogan, Alex Sugarbaker, Susannah M. Dickerson, Christine A. Donnelly, Chris Overstreet, and Mark A. Kasevich.

6.1 Overview

The observation of low-temperature phenomena has historically enabled new discoveries [50, 51, 52]. Accordingly, significant experimental effort has been dedicated to reaching increasingly cold temperatures. In this work, we report the demonstration of a cooling protocol to prepare ensembles of ^{87}Rb atoms with effective temperatures of

tens of pK, which is to our knowledge the lowest kinetic temperature ever measured. We present a new approach to atomic thermometry that allows us to resolve such low temperatures.

Atomic thermometry with kinetic temperatures in the pK range tests quantum mechanics at macroscopic scales [103, 104]. Our results place bounds on proposed modifications to quantum mechanics that predict the breakdown of quantum superpositions in the macroscopic regime [103].

Additionally, the ability to reach lower temperatures has driven numerous advances in precision measurement [1, 29, 105], quantum information [106], and quantum simulation [107]. Our realization of a cooling protocol to achieve effective temperatures of tens of pK meets a critical need for a new generation of atomic sensors with dramatically increased sensitivity [40]. These sensors are expected to have a broad scientific reach, with applications including gravitational wave detection [40, 3], tests of general relativity [37, 73, 9], and precision geodesy [40].

Evaporative cooling offers one route to low kinetic temperatures [108]. An alternative cooling method¹, often called delta-kick cooling, is to freely expand an atom cloud and then reduce its velocity spread with a collimating lens [53, 109, 110, 111, 112, 113, 114, 115]. Compared to evaporation, lensing typically requires less time and avoids intrinsic atom loss, but does not increase phase space density. The lens is implemented by a transient harmonic potential, realized magnetically [116, 110, 117], electrostatically [118], or optically [53]. In previous work, lensing has yielded effective temperatures as low as ~ 1 nK [9, 26].

In this work, we use a sequence of lenses to continuously manipulate the RMS velocity of ensembles of ^{87}Rb atoms through a minimum value of $\Delta v < 70 \mu\text{m/s}$, corresponding to effective temperature $T = m\Delta v^2/k_{\text{B}} < 50 \text{ pK}$ for atomic mass m [2]. The dipole lensing potential [53, 2] is generated from the transverse intensity profile of a vertically-propagating Gaussian beam, providing cooling in two dimensions.

This cooling performance is facilitated by several advances. We use a long expansion time $> 1 \text{ s}$ before the application of the dipole lens, which greatly improves its cooling capability. Additionally, we realize a cooling protocol that minimizes the

¹Here ‘cooling’ is understood to mean kinetic temperature reduction.

influence of imperfections of the lensing potential on the ensemble temperature. For instance, we implement a dual-stage sequence in which a magnetic lens provides initial cooling, reducing the heating from aberrations in the second-stage dipole lens.

6.2 Experimental Results

The potential cooling performance of the dipole lens depends on the available expansion time. Consider an initial atom ensemble (condensate or thermal state) with RMS size Δx_o and velocity spread Δv_o , allowed to expand for an object time t_o before application of the lens potential. After the lens is applied, the RMS velocity is Δv_ℓ and the temperature ratio is $\eta \equiv (\Delta v_\ell / \Delta v_o)^2$. For an ideal harmonic potential that has been tuned to minimize Δv_ℓ (the collimation condition), η is bounded by $\eta_c = (\Delta x_o / \Delta x_\ell)^2 \equiv \gamma^2$, where Δx_ℓ is the RMS size of the ensemble when the lens is applied and γ is the size ratio [53]. Correlations between position and velocity in the initial ensemble (e.g, arising from mean field interactions during expansion) can lead to temperatures that are lower than this bound². To achieve low temperatures, it is beneficial to have a long expansion time so that $\Delta x_\ell \approx \Delta v_o t_o \gg \Delta x_o$.

An ideal harmonic lens (frequency ω) exerts a force $F_H = -m\omega^2 x$, where x is the transverse position. For the dipole potential lens, the lens duration δt is short (delta-kick limit, $\omega\delta t \ll 1$), so we may approximate its effect as an impulse that changes the atom's velocity by $\delta v(x) = -\omega^2 \delta t x$. The lens focal time is defined by $1/f \equiv \omega^2 \delta t$ so that a point source of atoms expanding for time f would be perfectly collimated.

In order to measure these very low temperatures, we use a new method of atomic thermometry. At pK temperatures, the time necessary for the ensemble size to noticeably increase can be very long (> 10 s), making time-of-flight expansion an ineffective probe of temperature. To circumvent this, we extend the duration of the dipole-potential lens interaction beyond the collimation condition to refocus the ensemble. As in optics, the minimum achievable image size after refocusing is a measure of the degree of collimation. Thus, we can infer the collimated temperature of the

²An initially correlated ensemble corresponds to a virtual source with an effective initial size smaller than Δx_o .

atom ensemble from the refocused cloud size. An analogous method has been used to measure the temperature of electron beams [119].

To formalize this relationship, we solve the quantum Liouville equation for the evolution of an arbitrary initial state during the lensing sequence. In the delta-kick limit, this reduces to solving the classical Liouville equation [120, 121] (see Sec. 6.4). To account for aberration in the lens, we assume a general lens force $F(x)$. We find that the minimum refocused size $(\Delta x_i)_{\min}$ sets a bound on the minimum velocity spread Δv_ℓ achievable at collimation. By this metric, the minimum velocity variance for the lens (including aberrations) can be inferred by:

$$(\Delta v_\ell)_{\text{bound}}^2 \equiv \frac{(\Delta x_i)_{\min}^2}{t_i^2} = \Delta v_\ell^2 + \delta A \gtrsim \Delta v_\ell^2 \quad (6.1)$$

where t_i is the time between the lens and detection ('image time'), and δA arises from lens aberrations present during refocusing. For a wide class of aberrations (including those encountered in this work), δA is positive, so $(\Delta v_\ell)_{\text{bound}}^2$ provides an upper bound on the collimated temperature³.

The cooling performance demonstrated here depends critically on an optics configuration that reduces spatial intensity perturbations on the dipole lensing beam. Perturbations with spatial frequency κ produce forces $\propto \kappa$, so high spatial frequency perturbations ($\kappa\sigma > 1$ for radial waist σ) are particularly detrimental (see Sec. 6.5). For example, for our beam waist $\sigma = 3.4$ mm, a 1% perturbation with $\kappa \sim (100 \mu\text{m})^{-1}$ can result in a spurious force comparable in magnitude to the lensing force, substantially heating the cloud. To avoid this, the beam propagates for 16 m or more from the collimation lens (retroreflected after 10.6 m) before interacting with the atoms [Fig. 6.1(b)], allowing high spatial frequencies to diffract from the beam (Fig. 6.2). With $\delta t = 30$ ms and $t_o = 1.1$ s, the lens substantially refocuses the atoms at a time $t_i = 1.8$ s later [Fig. 6.1(d)].

The atom source is a cloud of 10^5 ^{87}Rb atoms with initial RMS size $\Delta x_o = 56 \mu\text{m}$ ⁴ and an effective temperature of 1.6 ± 0.1 nK [Fig. 6.1(c)]. To prepare this ultracold

³Correlations between lens aberrations and the initial atom distribution can yield $\delta A < 0$, but even in the worst case the correction to $(\Delta v_\ell)_{\text{bound}}$ is within our stated uncertainty.

⁴Determined by Gaussian fits to absorption images.

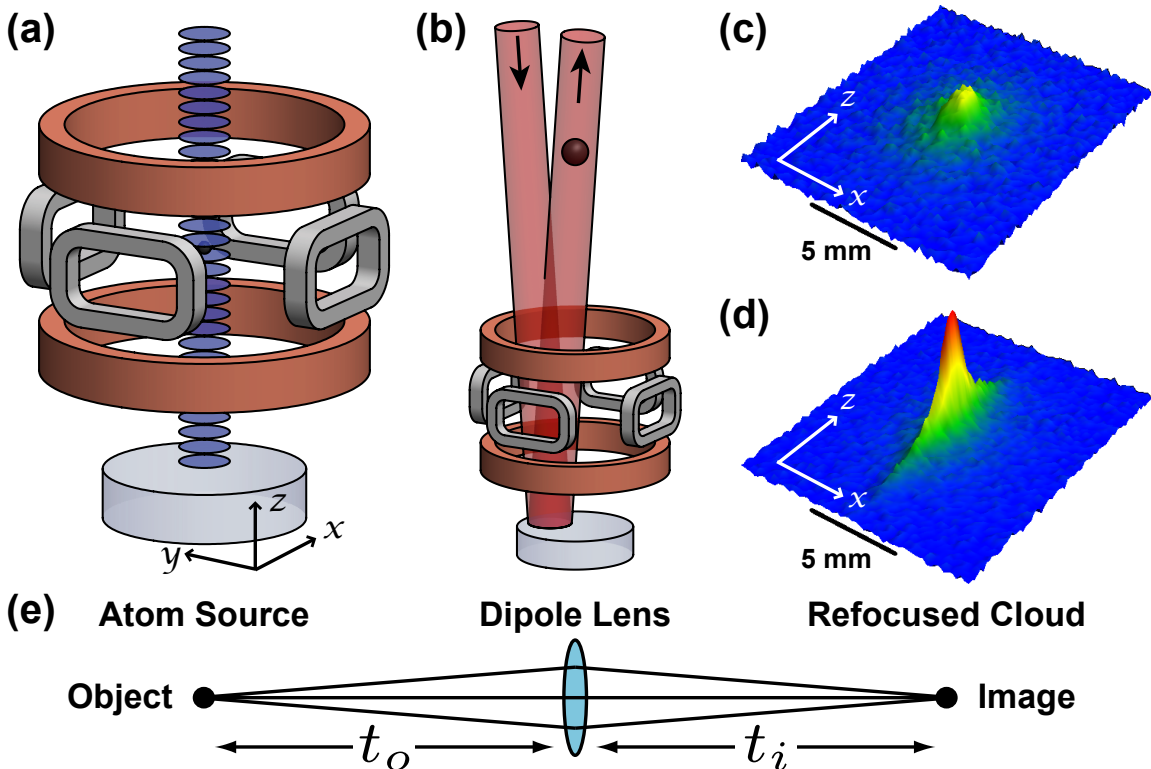


Figure 6.1: (a) Schematic of the apparatus (including vertically-oriented quadrupole trap, horizontal TOP coil pairs, and blue-detuned launching lattice). (b) A 3 W laser, $1/e^2$ radial waist $\sigma = 3.4$ mm, 1.0 THz red-detuned from the $^{87}\text{Rb } D_2$ line, acts on the atom cloud as a dipole lens (the ~ 1 mrad beam angle is exaggerated for clarity). (c) Fluorescence image of a 1.6 nK cloud after 2.8 s of free-fall. (d) The distribution in (c) refocused using the dipole lens. There is no observed axial heating. (e) Optical analogy showing the object, lens, and image, with object distance t_o and image distance t_i .

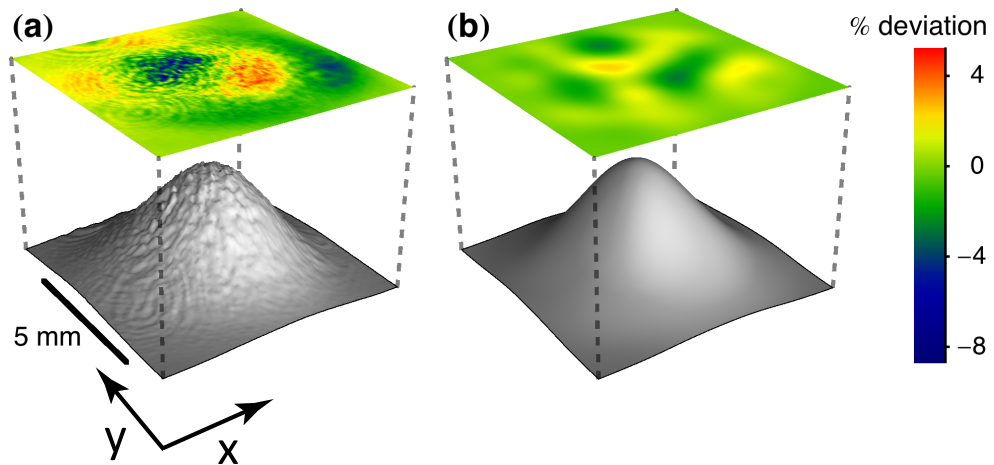


Figure 6.2: Comparison of the dipole lens beam intensity profile after numerical paraxial wave propagation of the measured profile by (a) 0.25 m and (b) 16.25 m. The residuals of fitting a 2D Gaussian are shown above each beam profile. The beam is initially spatially filtered by propagation through an optical fiber. Deviations from Gaussian are important to consider because the action of the lens for an exact Gaussian can be straightforwardly calculated analytically (see Fig. 6.4 and Sec. 6.5), and because high spatial frequency perturbations on top of an exact Gaussian can be shown to produce large amounts of heating (see Sec. 6.5). As shown here, the propagation of the dipole lens beam over 16.25 m allows high spatial frequency perturbations to be removed due to diffraction.

source, we evaporate in a time-orbiting potential (TOP) trap [Fig. 6.1(a)]. The atoms are further cooled with a magnetic lens (details follow) and prepared in a magnetically insensitive state. We then launch them upwards into a 10 m vacuum tube with a chirped optical lattice⁵ [29]. After 2.8 s (⁶), the atoms fall back down, and we image them with a vertical fluorescence beam onto two CCD cameras (the y -axis camera images the x - z plane, and x -axis camera images the y - z plane).

To evaluate the performance of the optical lens, we vary the lens duration and measure the width of the lensed cloud. As the lens acts only transversely, we bin the corresponding images in the vertical dimension and analyze in 1D. Extracting cloud widths requires accounting for the point spread function (PSF) of the imaging system. We fit all imaged clouds to a Gaussian profile convolved with a smooth representation of the PSF (see Sec. 6.6).

To characterize the PSF, we fit a cloud with a known, small size; this fixes the PSF parameters for subsequent analysis. We use a cloud imaged after a short drift time (100 ms; the time needed to reach the fluorescence imaging region) as the small source [Fig. 6.3(b)]. To directly measure this cloud's size, we image it with a low-aberration imaging system⁷. The measured width of $90 \pm 10 \mu\text{m}$ is consistent with an extrapolation from the known cloud parameters at the end of the TOP sequence.

Figure 6.3(a) shows the fitted transverse cloud size Δx_i versus lens duration δt for the two camera axes, demonstrating the continuous variation of the atom cloud through collimation and refocus. For this data, the lens is applied $t_i = 1.8$ s before detection. We fit the data with the predicted cloud size (see Sec. 6.5),

$$\Delta x_i^2 = (\Delta x_{i\min})^2 + \frac{1}{m^2} \Delta F^2 t_i^2 (\delta t - \delta t_{\min})^2 \quad (6.2)$$

where ΔF^2 is a fitting parameter characterizing the variance of the lensing force (including any aberrations), and δt_{\min} is the lens duration to refocus the cloud. Even for the smallest refocused cloud size, the chemical potential is negligibly small (\sim

⁵The lattice's depth is 40 times the recoil energy and its $1/e^2$ radial waist is 1.5 mm.

⁶The release from the magnetic trap occurs 100 ms before the end of the lattice launch.

⁷This imaging system was not used for primary data collection because of its comparatively poor photon collection efficiency.

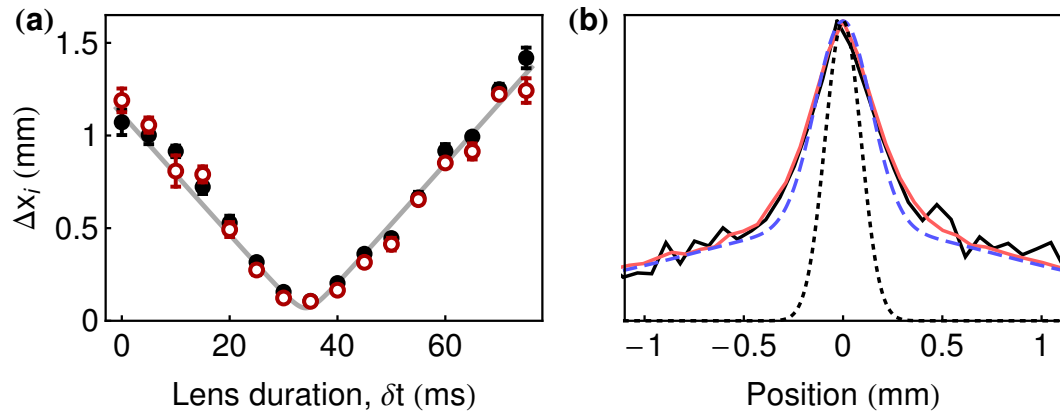


Figure 6.3: (a) Filled black (open red) points denote measured RMS cloud widths on the x -axis (y -axis) camera. Each point is the weighted mean of Gaussian fits to 6 experimental shots. The dashed gray curve is a simultaneous fit to the measurements from both cameras and reports a minimum size of $70 \mu\text{m}$ at a lens duration of 34 ms. (b) Vertically-binned images comparing the transverse size of a $90 \pm 10 \mu\text{m}$ cloud used to characterize the PSF (solid red/gray) to a cloud refocused 2.8 s later (solid black). The good overlap indicates high-fidelity refocusing. Dotted black: Gaussian profile extracted from a fit of the refocused cloud. The fit accounts for the broadening and distorting effects of the PSF (dashed blue).

0.2 pK), so chemical potential does not limit our ability to refocus (the chemical potential corresponds to collisions in the gas, so this statement implies that the effect of collisions is negligibly small). In fact, since the cloud expands vertically during the drift time, chemical potential would not prevent the cloud from being refocused to smaller than its initial transverse size.

The point at $\delta t = 35$ ms is nearest to the fitted refocusing time and sets the best bound on the achievable collimation temperature T . From Eq. 6.1, we find that $(\Delta v_\ell)_{\text{bound}} \equiv (\Delta x_i)_{\text{min}}/t_i = 65 \pm 20 \mu\text{m/s}$ for the x -axis and $70 \pm 25 \mu\text{m/s}$ for the y -axis. These bound the effective temperature at collimation to below $T_{\text{bound}} \equiv m(\Delta v_\ell)_{\text{bound}}^2/k_B = 40_{-20}^{+40}$ pK and 50_{-30}^{+50} pK for the x and y axes, respectively. This T_{bound} estimate includes extra heating δA that arises between collimation time δt_c and refocus δt_{min} . Since heating from aberrations scales as δt^2 , we can estimate T by multiplying the aberration contribution $((\Delta v_\ell)_{\text{bound}}^2 - \gamma^2 \Delta v_o^2)$ by $(\delta t_c/\delta t_{\text{min}})^2 \approx (0.6)^2$, yielding effective temperatures of 30_{-10}^{+10} pK and 35_{-10}^{+15} pK for the x and y axes, respectively (see Sec. 6.5). The temperature uncertainties result primarily from the standard deviation of the measured cloud sizes, likely caused by shot-to-shot fluctuations in the strength of the lens (e.g., due to fluctuations in optical power or alignment). Uncertainties in the measured PSF do not contribute significantly. It is interesting to note that if the atoms had too low of a temperature, their self-gravity would cause them to collapse. For our system, this would correspond to a much lower temperature of $\sim 10^{-23}$ K.

These kinetic temperature measurements are a sensitive probe of quantum mechanics at the macroscale. For a wide class of proposed modifications to quantum mechanics, the mechanism that leads to decoherence of macroscopic quantum superpositions also causes a free gas to undergo a small amount of spontaneous heating [103, 104]. For example, in the theory discussed in [103], the heating results from spontaneous momentum kicks that also lead to spontaneous wavefunction localization. These theories can therefore be bounded using precise heating rate measurements of ensembles of ultracold atoms. In our experiment, spontaneous heating would lead to diffusion of the atom cloud during the long drift time, limiting our ability to refocus the cloud. The measured refocused cloud size $(\Delta x_i)_{\text{min}}$ constrains the heating

rate for ^{87}Rb to 20 ± 30 pK/s (see Sec. 6.7).

Our ability to transversely cool an atom cloud to low effective temperatures and to refocus the cloud after long drift times has many applications [9, 29], including terrestrial atom interferometers with interrogation times previously thought to require microgravity. Refocusing the atom cloud to its original size allows us to relaunch the ensemble, extending the effective free-fall time to 5.1 s. One or more of these relaunches could be integrated into an atom interferometer, possibly leading to > 10 s interrogation times on Earth. Similarly, a series of relay lenses (or an initial collimation lens) could be integrated with light-pulse atom interferometry to maintain a small transverse cloud size at the beamsplitter pulses, even for very long interrogation times. This would ensure a homogeneous atom optics beam intensity across the cloud, which is critical for large momentum transfer atom interferometry [62].

To characterize imperfections in the dipole lensing potential and the corresponding deviations from ideal lens behavior, we measure the refocused cloud size $(\Delta x_i)_{\min}$ and corresponding lens duration δt_{\min} for various object times t_o , with the total atom drift time held constant (Fig. 6.4). Each point is the result of a fit of Eq. 6.2 to a scan of the lens duration [like Fig. 6.3(a)] at one of four fractional object times: $t_o/(t_o+t_i) = 0.32$, 0.39, 0.60, and 0.71. Also shown is the ideal harmonic lens scaling for $(\Delta x_i)_{\min}$ and δt_{\min} . Neglecting x - v correlations, the focal time $f_{\min} \equiv (\omega^2 \delta t_{\min})^{-1}$ satisfies the thin lens formula from geometric optics $\frac{1}{f_{\min}} = \frac{1}{t_i} + \frac{1-\gamma^2}{t_o}$ (the γ correction results from finite velocity spread and vanishes in the point source limit $\gamma \ll 1$ ⁸) and the image size $(\Delta x_i)_{\min} = \Delta x_o \frac{t_i}{t_o} \sqrt{1 - \gamma^2}$ scales as the magnification of the lens $\frac{t_i}{t_o}$.

The deviation of the data in Fig. 6.4 from the harmonic lens theory results primarily from large-scale aberrations due to the Gaussian profile of the optical potential. Modeling the lens potential as a 2D Gaussian, we calculate $(\Delta x_i)_{\min}$ and δt_{\min} assuming Gaussian initial ensemble velocity and position distributions (Fig. 6.4, see also Sec. 6.5). Although the cooling performance of the lens is partially limited by the finite expansion time t_o , further extending t_o would not improve cooling performance, since a larger Δx_ℓ would increase the effect of Gaussian aberration.

⁸An identical correction arises in optics with a finite source divergence (e.g., a Gaussian laser beam).

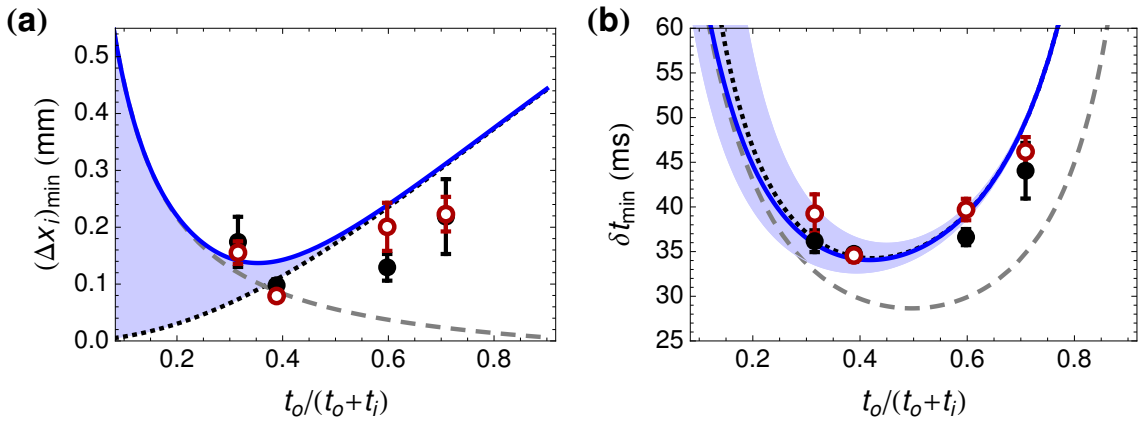


Figure 6.4: (a) Minimum RMS width of the cloud as a function of the fractional object time. (b) The lens duration required to refocus the atom cloud (δt_{\min}) as a function of the fractional object time. The filled black (open red) points represent measurements on the x -axis (y -axis) camera. Solid blue: expected behavior for a cloud of finite initial size (56 μ m) and no initial x - v correlations in an optical beam with a Gaussian profile. The blue shaded regions represent the corresponding ranges possible with correlations. The curve in (a) has no free parameters. For (b), the optical power is a free parameter that fits to 2.8 W. Dashed gray: expected behavior for an ideal harmonic potential of the same strength as at the center of the beam (see Sec. 6.5). Dotted black: expected behavior for a cloud with zero initial size subject to Gaussian aberrations.

To reach the lowest temperatures, it is necessary to minimize the impact of anharmonicities of the dipole lensing beam. To do this, we implement a dual-stage lensing sequence, pre-cooling the atoms with an initial magnetic lens. This increases the effective $f/\#$ of the dipole lens by reducing the duration δt required for collimation. It has the added benefit of cooling along the third axis not addressed by the dipole lens.

The magnetic lens is performed by abruptly releasing tightly-confined atoms into a shallow harmonic TOP trap potential [Fig. 6.1(a)] [122]. Subsequently turning off the shallow trap when the ensemble has reached its maximum size yields a colder cloud [116]. Synchronizing the radial (ρ) and vertical (z) oscillations to optimize 3D cooling requires a trap frequency ratio of $\omega_z/\omega_\rho = (n_z + 1/2) / (n_\rho + 1/2)$ for integers n_z and n_ρ (we use $n_z = 3$, $n_\rho = 2$). In the absence of gravity, the irrational ratio $\omega_z/\omega_\rho = 2\sqrt{2}$ of the TOP trap makes perfect synchronization impossible, but with gravity the ratio is tunable by selecting the appropriate quadrupole gradient [123].

Figure 6.5 shows the evolution of a cloud while in the lens (widths are from 2D Gaussian fits). The center of mass oscillates vertically because the atoms start above the minimum of the shallow trap. The initial evaporated source used here has a release temperature of $1.4 \mu\text{K}$ (dominated by chemical potential). The optimized lens duration of 162 ms gives a minimum effective temperature of $(T_\rho, T_z) = (50, 40) \text{ nK}$ and reduced chemical potential. The 1.6 nK source used as input to the dipole lens is derived from an identical magnetic lens sequence, but with a deeper initial evaporation cut.

Our combined magnetic/dipole lensing sequence has the potential to reach even colder temperatures. Fundamentally, the diffraction-limited collimation temperature for a wavepacket with size Δx_e at the lens is determined by the minimum velocity width allowed by the uncertainty principle, in this work $\sim 10 \text{ fK}$ (for the $\sim 400 \mu\text{m}$ clouds). Future work will seek to achieve these limits.

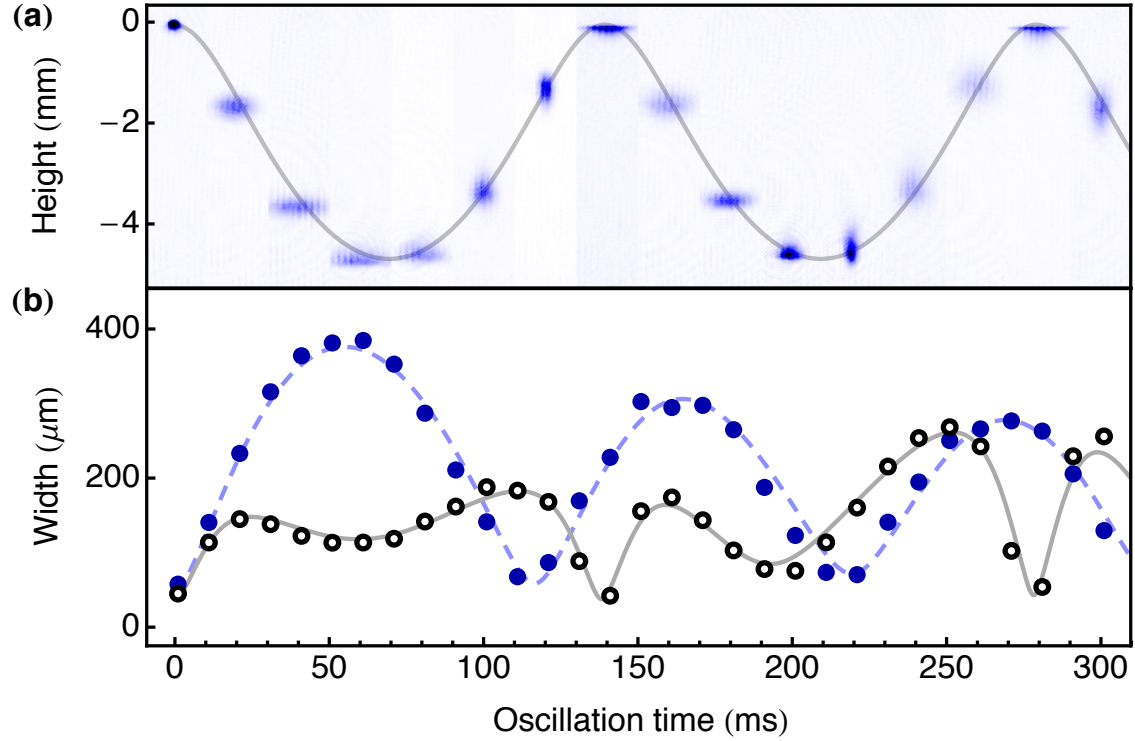


Figure 6.5: Magnetic lensing in the TOP trap. (a) Absorption images of the ensemble oscillating in the trap. (b) Radial (filled blue circles) and vertical (open black circles) RMS cloud widths. Theory curves are based on numerical solutions for trajectories of non-interacting particles in the exact TOP potential. The solid grey curves are simultaneous fits to the center-of-mass trajectory and the vertical width, with free parameters for the TOP potential (radial quadrupole gradient ∇B , spinning bias field B_0 , and vertical position) as well as initial first and second moments of the vertical distribution. The dashed blue curve results from a 2D Monte Carlo simulation of the atom distribution using the fitted parameters (including $\nabla B = 20.9 \pm 0.1 \text{ G/cm}$, $B_0 = 6.9 \pm 0.3 \text{ G}$) but no free parameters. The initial radial size is scaled from the fitted vertical size by the ratio of the measured initial cloud widths.

6.3 Overview of theoretical background and analysis details

Below we present additional analysis that is relevant to our lensing experiment and to other lensing experiments in the future. Section 6.4 uses a Wigner function approach to delta-kick cooling to rigorously justify the analysis of our lensing sequence in a geometric optics framework. Section 6.5 presents calculational details regarding the effect of aberrations in the lensing potential. Section 6.6 discusses specifics of our smooth representation of the PSF. Section 6.7 provides the calculational details of the relationship between our temperature measurement and our heating rate bound.

6.4 Time evolution of the Wigner function in a delta-kick cooling sequence

We analyze the delta-kick cooling sequence using the phase space representation of the density matrix. This allows the treatment to be valid in both the quantum and classical cases. The results we derive here are therefore applicable to the case of a pure (non-interacting) Bose-Einstein condensate and also to a classical thermal distribution of atoms. The Wigner phase-space distribution function provides a convenient description of the dynamics because it naturally supports both the classical and quantum treatment. In the classical limit, the Wigner function time evolution equation approaches the classical Liouville equation, and so the evolution of the Wigner function in this limit is the same as the evolution of a classical thermal ensemble of particles.

6.4.1 Free space evolution

The Wigner function for the density matrix is defined as [121]

$$W(\mathbf{r}, \mathbf{p}; t) = \frac{1}{(2\pi\hbar)^3} \int d^3\xi e^{-i\mathbf{p}\cdot\xi/\hbar} \langle \mathbf{r} + \frac{1}{2}\xi | \hat{\rho}(t) | \mathbf{r} - \frac{1}{2}\xi \rangle \quad (6.3)$$

The time evolution of the density matrix is governed by the von Neumann equation: $i\hbar\partial_t\hat{\rho} = [\hat{H}, \hat{\rho}]$, where $\hat{H} = \frac{\hat{\mathbf{p}}^2}{2m} + V(\hat{\mathbf{r}})$ is the Hamiltonian with potential energy $V(\hat{\mathbf{r}})$. For Hamiltonians that are at most second order in \mathbf{r} and \mathbf{p} , the Wigner function evolves according to the classical Liouville equation [120]. In particular, for free space evolution $\hat{H} = \frac{\hat{\mathbf{p}}^2}{2m}$, and the quantum Liouville equation for the Wigner function is reduced to

$$\frac{\partial W(\mathbf{r}, \mathbf{p}; t)}{\partial t} + \frac{\mathbf{p}}{m} \cdot \nabla_{\mathbf{r}} W(\mathbf{r}, \mathbf{p}; t) = 0 \quad (\text{free space}) \quad (6.4)$$

The solution at time t can then be expressed in terms of the Wigner function at some earlier time t_0 [120]:

$$W(\mathbf{r}, \mathbf{p}; t) = W(\mathbf{r} - \frac{\mathbf{p}}{m}(t - t_0), \mathbf{p}; t_0) \quad (\text{free space}) \quad (6.5)$$

as can be verified by inspection.

In the lens sequence, we take $t = 0$ to correspond to the object plane of the lens. We assume the initial phase-space distribution function at the object plane (at $t = 0$) is $W_o(\mathbf{r}, \mathbf{p})$. From Eq. 6.5, the Wigner function after a time t of free space evolution is then

$$W_{\text{free}}(\mathbf{r}, \mathbf{p}; t) = W_o(\mathbf{r} - \frac{\mathbf{p}}{m}t, \mathbf{p}). \quad (6.6)$$

6.4.2 Time evolution during the delta kick

During the time that the lens is applied to the ensemble, the Hamiltonian is $\hat{H} = \frac{\hat{\mathbf{p}}^2}{2m} + V(\hat{\mathbf{r}})$, where $V(\hat{\mathbf{r}})$ is the lens potential. For an ideal lens, the lens potential should be harmonic. However, the real lens potential will contain anharmonicities that correspond to aberrations in the lens. To model these lens imperfections, we treat the lens potential as an arbitrary function $V(\hat{\mathbf{r}})$. Without loss of generality, we note that $V(\hat{\mathbf{r}})$ is roughly harmonic along the lens axes (assumed to be x and y) plus some small aberration terms:

$$V(\hat{\mathbf{r}}) = \frac{1}{2}m\omega^2(\hat{x}^2 + \hat{y}^2) + \delta V(\hat{\mathbf{r}}) \quad (6.7)$$

where ω is the nominal harmonic oscillator frequency of the lens and $\delta V(\hat{\mathbf{r}})$ is an arbitrary function that describes the aberrations.

The lens potential is assumed to turn on at time $t_o - \delta t$ and is then turned off a duration δt later at time t_o . We can formally solve the von Neumann equation for the density matrix time evolution from the beginning to the end of the lens pulse:

$$\hat{\rho}(t_o) = e^{-i\hat{H}\delta t/\hbar} \hat{\rho}(t_o - \delta t) e^{i\hat{H}\delta t/\hbar} \quad (6.8)$$

Since the lens potential is off for times $t < t_o - \delta t$, the solution for $\hat{\rho}$ before the lens is the free space solution described in the previous section. Therefore we have as a boundary condition between the two time regions $\hat{\rho}(t_o - \delta t) = \hat{\rho}_{\text{free}}(t_o - \delta t)$, where $\hat{\rho}_{\text{free}}$ corresponds to W_{free} from Eq. 6.6 using the definition in Eq. 6.3.

Next we solve for the evolution during the lens, taking advantage of the delta-kick limit. Since δt is small, we can approximate the time evolution in Eq. 6.8 by splitting the Hamiltonian into a kinetic and a potential evolution operator and then evaluating the evolution from the kinetic and potential terms separately. To see this, we can formally rewrite the time evolution operator using the Zassenhaus identity

$$e^{\lambda(\hat{A} + \hat{B})} = e^{\lambda\hat{A}} e^{\lambda\hat{B}} e^{-\frac{\lambda^2}{2!} [\hat{A}, \hat{B}]} e^{\frac{\lambda^3}{3!} (2[\hat{B}, [\hat{A}, \hat{B}]] + [\hat{A}, [\hat{A}, \hat{B}]])} \dots \quad (6.9)$$

for operators \hat{A} and \hat{B} . In order to rewrite $e^{i\hat{H}\delta t/\hbar}$, we choose $\hat{A} = i\frac{\hat{\mathbf{p}}^2/2m}{\hbar\omega}$, $\hat{B} = i\frac{V(\hat{\mathbf{r}})}{\hbar\omega}$, and $\lambda = \omega\delta t$. Here we have explicitly factored out an ω from the Hamiltonian to help indicate the size of the various terms in the expansion. This choice is motivated by the fact that the scale of the Hamiltonian is set by $|H| \sim \hbar\omega$. We now use the fact that in the delta-kick limit $\omega\delta t \ll 1$, and so we have using Eq. 6.9

$$e^{i\left(\frac{\hat{\mathbf{p}}^2}{2m} + V(\hat{\mathbf{r}})\right)\delta t/\hbar} \approx e^{i\frac{\hat{\mathbf{p}}^2}{2m}\delta t/\hbar} e^{iV(\hat{\mathbf{r}})\delta t/\hbar} + \mathcal{O}(\omega\delta t)^2 \quad (6.10)$$

where we can neglect terms quadratic and higher in $\omega\delta t$. Combining this with Eq. 6.8,

the Wigner function after application of the lens is

$$\begin{aligned} W(\mathbf{r}, \mathbf{p}; t_o) = & \\ \frac{1}{(2\pi\hbar)^3} \int d^3\xi e^{-i\mathbf{p}\cdot\xi/\hbar} \langle \mathbf{r} + \frac{1}{2}\xi | e^{-\frac{i}{\hbar}V(\hat{\mathbf{r}})\delta t} & \left(e^{-\frac{i}{\hbar}2m\delta t} \hat{\rho}_{\text{free}}(t_o - \delta t) e^{\frac{i}{\hbar}2m\delta t} \right) e^{\frac{i}{\hbar}V(\hat{\mathbf{r}})\delta t} | \mathbf{r} - \frac{1}{2}\xi \rangle \end{aligned} \quad (6.11)$$

where we also have applied the previously mentioned boundary condition for $\hat{\rho}$ at time $t_o - \delta t$. The term in parenthesis simply represents additional free space time evolution by time δt , so we have

$$W(\mathbf{r}, \mathbf{p}; t_o) = \frac{1}{(2\pi\hbar)^3} \int d^3\xi e^{-i\mathbf{p}\cdot\xi/\hbar} e^{\frac{i}{\hbar}(V(\mathbf{r} - \frac{1}{2}\xi) - V(\mathbf{r} + \frac{1}{2}\xi))\delta t} \langle \mathbf{r} + \frac{1}{2}\xi | \hat{\rho}_{\text{free}}(t_o) | \mathbf{r} - \frac{1}{2}\xi \rangle \quad (6.12)$$

where the $V(\hat{\mathbf{r}})$ operators were applied to the adjacent position bra and ket. We now expand the potential as a Taylor series in ξ

$$V(\mathbf{r} \pm \frac{1}{2}\xi) = \sum_{n=0}^{\infty} \frac{1}{n!} \left(\frac{\pm\xi}{2} \cdot \nabla_{\mathbf{r}'} \right)^n V(\mathbf{r}') \Big|_{\mathbf{r}'=\mathbf{r}} \quad (6.13)$$

which allows the potential terms to be combined as

$$V(\mathbf{r} - \frac{1}{2}\xi) - V(\mathbf{r} + \frac{1}{2}\xi) = \sum_{n=0}^{\infty} \frac{1}{n!2^{n-1}} \left(\frac{(-1)^n - 1}{2} \right) (\xi \cdot \nabla_{\mathbf{r}'})^n V(\mathbf{r}') \Big|_{\mathbf{r}'=\mathbf{r}}. \quad (6.14)$$

Only the odd terms are non-zero, so we re-index the sum $n \rightarrow (2n+1)$

$$V(\mathbf{r} - \frac{1}{2}\xi) - V(\mathbf{r} + \frac{1}{2}\xi) = -\nabla V(\mathbf{r}) \cdot \xi - \sum_{n=1}^{\infty} \frac{1}{(2n+1)!2^{2n}} (\xi \cdot \nabla_{\mathbf{r}'})^{(2n+1)} V(\mathbf{r}') \Big|_{\mathbf{r}'=\mathbf{r}} \quad (6.15)$$

where we have explicitly pulled the linear term out of the sum. Additionally, from the Fourier transform of Eq. 6.3 we have

$$\langle \mathbf{r} + \frac{1}{2}\xi | \hat{\rho}_{\text{free}}(t_o) | \mathbf{r} - \frac{1}{2}\xi \rangle = \int d^3p' e^{i\mathbf{p}'\cdot\xi/\hbar} W_{\text{free}}(\mathbf{r}, \mathbf{p}'; t_o). \quad (6.16)$$

Combining Eq. 6.15 and Eq. 6.16 with Eq. 6.12 yields

$$W(\mathbf{r}, \mathbf{p}; t_o) = \frac{1}{(2\pi\hbar)^3} \int d^3\xi \int d^3p' e^{i(\mathbf{p}' - \mathbf{p} - \nabla V(\mathbf{r})\delta t) \cdot \xi / \hbar} e^{-\frac{i}{\hbar}V_3(\xi)\delta t} W_{\text{free}}(\mathbf{r}, \mathbf{p}'; t_o) \quad (6.17)$$

where we have defined

$$V_3(\xi) \equiv \sum_{n=1}^{\infty} \frac{1}{(2n+1)!2^{2n}} (\xi \cdot \nabla_{\mathbf{r}'})^{(2n+1)} V(\mathbf{r}') \Big|_{\mathbf{r}'=\mathbf{r}} \quad (6.18)$$

as a collection of terms with third order and higher odd derivatives of V . In the delta kick limit, we can expand the $V_3(\xi)$ exponential as

$$e^{-\frac{i}{\hbar}V_3(\xi)\delta t} \approx 1 - \frac{i}{\hbar\omega} V_3(\xi) \omega \delta t + \mathcal{O}(\omega \delta t)^2 \quad (6.19)$$

Next, we perform the ξ integrals in Eq. 6.17 using the following representation of the Dirac delta function

$$\delta(\mathbf{p}) = \frac{1}{(2\pi\hbar)^3} \int d^3\xi e^{i\mathbf{p}\cdot\xi/\hbar} \quad (6.20)$$

from which it follows that

$$\nabla_{\mathbf{p}} \delta(\mathbf{p}) = \frac{i/\hbar}{(2\pi\hbar)^3} \int d^3\xi \xi e^{i\mathbf{p}\cdot\xi/\hbar}. \quad (6.21)$$

The Fourier transforms of higher order terms in ξ then correspond to higher derivatives of delta functions. The result of the integration is

$$\begin{aligned} W(\mathbf{r}, \mathbf{p}; t_o) &= \\ &\int d^3p' \left(\delta(\delta\mathbf{p}) \frac{i}{\hbar\omega} (\omega \delta t) \sum_{n=1}^{\infty} \frac{(\hbar/i)^{2n+1}}{(2n+1)!2^{2n}} (\nabla_{\mathbf{p}'} \cdot \nabla_{\mathbf{r}'})^{2n+1} \delta(\delta\mathbf{p}) V(\mathbf{r}') \Big|_{\mathbf{r}'=\mathbf{r}} \right) W_{\text{free}}(\mathbf{r}, \mathbf{p}'; t_o) \end{aligned} \quad (6.22)$$

where $\delta\mathbf{p} \equiv \mathbf{p}' - \mathbf{p} - \nabla V \delta t$. Performing the p' integrals gives the final result:

$$\begin{aligned} W(\mathbf{r}, \mathbf{p}; t_o) = & \\ W_{\text{free}}(\mathbf{r}, \mathbf{p} - \Delta p(\mathbf{r}); t_o) + \delta t \sum_{n=1}^{\infty} \frac{(-1)^n (\hbar/2)^{2n}}{(2n+1)!} & (\nabla_{\mathbf{p}'} \cdot \nabla_{\mathbf{r}'})^{2n+1} V(\mathbf{r}') W_{\text{free}}(\mathbf{r}, \mathbf{p}'; t_o) \Big|_{\mathbf{r}'=\mathbf{r}, \mathbf{p}'=\mathbf{p}-\Delta p} \end{aligned} \quad (6.23)$$

where the momentum impulse of the lens is defined as $\Delta p(\mathbf{r}) \equiv -\nabla V(\mathbf{r}) \delta t$. The result is of the form

$$W(\mathbf{r}, \mathbf{p}; t_o) = W_{\text{free}}(\mathbf{r}, \mathbf{p} - \Delta p(\mathbf{r}); t_o) + Q \quad (6.24)$$

where we refer to Q as the quantum term. Ignoring Q for a moment, the action of the delta kick lens is to shift the momentum of the distribution by the classical momentum impulse. This is equivalent to the classical evolution of an ensemble. In this sense we may say that throughout the lens sequence the Wigner function evolves according to the classical Liouville equation. As a result, to a good approximation we may analyze the evolution of the distribution using classical physics.

The quantum term Q in Eq. 6.24 is negligible in many relevant situations. In the delta-kick limit, a sufficiently small ($\omega \delta t$) will ensure that Q can be ignored. Additionally, since Q depends only on derivatives of the potential that are third order and higher, $Q = 0$ in the case that the potential contains only terms that are second order or less in position. Even when this condition is not exactly met, we expect these higher order terms to be small compared to the second derivative terms ($\sim \omega^2$) for an approximately harmonic lens. Nevertheless, Q also depends on higher order derivatives of the Wigner function, so if the initial distribution varies sufficiently rapidly with \mathbf{p} then it is possible for the corrections from Q to be non-negligible. To account for this possibility, we do not ignore Q when using the Wigner function to calculate the experimentally observed moments of the distribution. As shown below, we find that Q has no effect on these moments.

6.4.3 Time evolution from the lens to detection

Combining Eq. 6.6 and Eq. 6.24, we can write the Wigner function immediately after the lens in terms of the initial Wigner function:

$$W(\mathbf{r}, \mathbf{p}; t_o) = W_o(\mathbf{r} - \frac{\mathbf{p} - \Delta p(\mathbf{r})}{m} t_o, \mathbf{p} - \Delta p(\mathbf{r})) \quad (6.25)$$

where we have ignored the quantum term Q . Using Eq. 6.5, the propagation from the lens to detection (i.e., the image plane of the lens) is given by

$$W(\mathbf{r}, \mathbf{p}; t_o + t_i) = W(\mathbf{r} - \frac{\mathbf{p}}{m} t_i, \mathbf{p}; t_o) \quad (6.26)$$

and so the final result for the Wigner function $W_i(\mathbf{r}, \mathbf{p}) \equiv W(\mathbf{r}, \mathbf{p}; t_o + t_i)$ at the image plane is

$$W_i(\mathbf{r}, \mathbf{p}) = W_o\left(\mathbf{r} - \frac{\mathbf{p} - \Delta p(\mathbf{r} - \frac{\mathbf{p}}{m} t_i)}{m} (t_o + t_i) - \frac{\Delta p(\mathbf{r} - \frac{\mathbf{p}}{m} t_i)}{m} t_i, \mathbf{p} - \Delta p(\mathbf{r} - \frac{\mathbf{p}}{m} t_i)\right) \quad (6.27)$$

which is the same as what is obtained using the classical Liouville equation.

6.4.4 Classical correspondence of observables calculated using the Wigner function

Next we compute the expectation values for the position and momentum widths of the ensemble at various points in the delta-kick sequence using the Wigner function derived in the previous sections. These expectation values are our experimental observables. In this section we show that the expectation values of the experimentally relevant moments computed using the Wigner function are all of the form

$$\langle g(\hat{x}, \hat{p}_x) \rangle = \int d^3r \int d^3p \, g(x, p_x) W_o(\mathbf{r}, \mathbf{p}) \quad (6.28)$$

which takes the form of a classical expectation value if $W_o(\mathbf{r}, \mathbf{p})$ is identified as the classical probability distribution. Furthermore, we show explicitly that the quantum correction term Q discussed in Sec. 6.4.2 does not affect the moments.

The final result will depend on the initial spread of the quantum state in both x and p , as well as cross moments between x and p that quantify position-momentum correlations in the cloud. However, unlike \hat{x} and \hat{p} , we note that $\hat{x}\hat{p}$ is not a Hermitian operator, so its expectation value does not correspond to an observable. With this in mind, it is convenient to define the symmetrized operator expectation value

$$\langle A \rangle \equiv \left\langle \frac{\hat{A} + \hat{A}^\dagger}{2} \right\rangle \quad (6.29)$$

for a general operator \hat{A} that need not be Hermitian. The symmetrized operator is guaranteed to be Hermitian, and when \hat{A} itself is Hermitian we recover the normal result: $\langle A \rangle = \langle \hat{A} \rangle$. We show in Sec. 6.4.5 that this symmetrized form naturally arises when computing the cross moments using the Wigner function.

Expectation values immediately after the lens

The first set of observables we calculate are the position and momentum widths at the time just after the lens application:

$$\Delta x_\ell^2 = \langle x_\ell^2 \rangle - \langle x_\ell \rangle^2 \quad (6.30)$$

$$\Delta v_\ell^2 = \langle v_\ell^2 \rangle - \langle v_\ell \rangle^2 \quad (6.31)$$

where the ℓ subscript indicates that the moments are evaluated at the time the lens is applied ($t = t_o$):

$$\langle x_\ell^n \rangle \equiv \langle x^n \rangle_{t=t_o} = \langle \hat{x}^n \rangle_{t=t_o} \quad (6.32)$$

$$\langle v_\ell^n \rangle \equiv \langle (\frac{p_x}{m})^n \rangle_{t=t_o} = \langle (\hat{p}_x/m)^n \rangle_{t=t_o} \quad (6.33)$$

for integer n . The Wigner-Weyl transform of \hat{x} is x , so we can write the x moments as

$$\langle \hat{x}^n \rangle_{t=t_o} = \int d^3r \int d^3p \ x^n W(\mathbf{r}, \mathbf{p}; t_o) \quad (6.34)$$

Using Eq. 6.17 combined with Eq. 6.6,

$$\langle \hat{x}^n \rangle_{t=t_o} = \frac{1}{(2\pi\hbar)^3} \int d^3\xi \int d^3p' \int d^3r \int d^3p x^n e^{i(\mathbf{p}' - \mathbf{p} + \Delta p(\mathbf{r})) \cdot \xi / \hbar} e^{-\frac{i}{\hbar} V_3(\xi) \delta t} W_o(\mathbf{r} - \frac{\mathbf{p}'}{m} t_o, \mathbf{p}') \quad (6.35)$$

which we note includes all the quantum terms arising from $V_3(\xi)$ discussed previously. Performing the \mathbf{p} integrals results in a delta function in ξ :

$$\langle \hat{x}^n \rangle_{t=t_o} = \int d^3\xi \int d^3p' \int d^3r x^n \delta(\xi) e^{i(\mathbf{p}' + \Delta p(\mathbf{r})) \cdot \xi / \hbar} e^{-\frac{i}{\hbar} V_3(\xi) \delta t} W_o(\mathbf{r} - \frac{\mathbf{p}'}{m} t_o, \mathbf{p}') \quad (6.36)$$

Evaluating the ξ integral eliminates the quantum terms:

$$\langle \hat{x}^n \rangle_{t=t_o} = \int d^3p' \int d^3r x^n W_o(\mathbf{r} - \frac{\mathbf{p}'}{m} t_o, \mathbf{p}'). \quad (6.37)$$

Finally, we perform a change of variables $\mathbf{r} \rightarrow \mathbf{r} + \frac{\mathbf{p}'}{m} t_o$ and $\mathbf{p}' \rightarrow \mathbf{p}$, yielding the final result in the form of Eq. 6.28:

$$\langle \hat{x}^n \rangle_{t=t_o} = \int d^3p \int d^3r (x + \frac{p_x}{m} t_o)^n W_o(\mathbf{r}, \mathbf{p}). \quad (6.38)$$

The moments of position are therefore equivalent to the expectation values of the appropriate power of the classical position of an atom at the time of the lens.

We also calculate the momentum expectation values at the time of the lens. Once again, since the Wigner-Weyl transform of \hat{p}_x is p_x we can write the p_x moments as

$$\langle \hat{p}_x^n \rangle_{t=t_o} = \int d^3r \int d^3p p_x^n W(\mathbf{r}, \mathbf{p}; t_o) \quad (6.39)$$

Proceeding along the same lines as for the position moments,

$$\begin{aligned} \langle \hat{p}_x^n \rangle_{t=t_o} &= \frac{1}{(2\pi\hbar)^3} \int d^3\xi \int d^3p' \int d^3r \int d^3p p_x^n e^{i(\mathbf{p}' - \mathbf{p} + \Delta p(\mathbf{r})) \cdot \xi / \hbar} e^{-\frac{i}{\hbar} V_3(\xi) \delta t} W_o(\mathbf{r} - \frac{\mathbf{p}'}{m} t_o, \mathbf{p}') \\ &= \int d^3\xi \int d^3p' \int d^3r \frac{\hbar^n}{(-i)^n} \frac{\partial^n \delta(\xi)}{\partial \xi_x^n} e^{i(\mathbf{p}' + \Delta p(\mathbf{r})) \cdot \xi / \hbar} e^{-\frac{i}{\hbar} V_3(\xi) \delta t} W_o(\mathbf{r} - \frac{\mathbf{p}'}{m} t_o, \mathbf{p}') \end{aligned} \quad (6.40)$$

$$\begin{aligned} &= \int d^3\xi \int d^3p' \int d^3r \frac{\hbar^n}{(-i)^n} \frac{\partial^n \delta(\xi)}{\partial \xi_x^n} e^{i(\mathbf{p}' + \Delta p(\mathbf{r})) \cdot \xi / \hbar} e^{-\frac{i}{\hbar} V_3(\xi) \delta t} W_o(\mathbf{r} - \frac{\mathbf{p}'}{m} t_o, \mathbf{p}') \end{aligned} \quad (6.41)$$

where the p integral results in the n th derivative of the Dirac delta function with respect to ξ_x . Next, for the $\boldsymbol{\xi}$ integral we have that

$$\int d^3\xi \frac{\partial^n \delta(\boldsymbol{\xi})}{\partial \xi_x^n} h(\boldsymbol{\xi}) = (-1)^n \frac{\partial^n h(\boldsymbol{\xi})}{\partial \xi_x^n} \Big|_{\boldsymbol{\xi}=0} \quad (6.42)$$

for any function $h(\boldsymbol{\xi})$. For the case at hand, $h(\boldsymbol{\xi}) = e^{\frac{i}{\hbar}(\mathbf{p}' + \Delta p(\mathbf{r})) \cdot \boldsymbol{\xi} - V_3(\boldsymbol{\xi}) \delta t}$. As a result of the $\boldsymbol{\xi}$ -dependence of V_3 , the lowest two derivative have a particularly simple form:

$$\frac{\partial h(\boldsymbol{\xi})}{\partial \xi_x} \Big|_{\boldsymbol{\xi}=0} = \frac{i}{\hbar} (p'_x + \Delta p_x(\mathbf{r})) \quad (6.43)$$

$$\frac{\partial^2 h(\boldsymbol{\xi})}{\partial \xi_x^2} \Big|_{\boldsymbol{\xi}=0} = \left(\frac{i}{\hbar}\right)^2 (p'_x + \Delta p_x(\mathbf{r}))^2 \quad (6.44)$$

Note that higher derivatives will give quantum corrections arising from V_3 , but for $n \leq 2$ these do not contribute. Thus after computing the $\boldsymbol{\xi}$ integrals we have for $n \leq 2$

$$\begin{aligned} \langle \hat{p}_x^n \rangle_{t=t_o} &= \int d^3p' \int d^3r \frac{\hbar^n}{(-i)^n} (-1)^n \left(\frac{i}{\hbar}\right)^n (p'_x + \Delta p_x(\mathbf{r}))^n W_o(\mathbf{r} - \frac{\mathbf{p}'}{m} t_o, \mathbf{p}') \quad (n \leq 2) \\ &= \int d^3p' \int d^3r (p'_x + \Delta p_x(\mathbf{r}))^n W_o(\mathbf{r} - \frac{\mathbf{p}'}{m} t_o, \mathbf{p}') \end{aligned} \quad (6.45)$$

As before, we perform a change of variables $\mathbf{r} \rightarrow \mathbf{r} + \frac{\mathbf{p}'}{m} t_o$ and $\mathbf{p}' \rightarrow \mathbf{p}$ yielding the final result:

$$\langle \hat{p}_x^n \rangle_{t=t_o} = \int d^3p \int d^3r (p_x + \Delta p_x(\mathbf{r} + \frac{\mathbf{p}}{m} t_o))^n W_o(\mathbf{r}, \mathbf{p}) \quad (n \leq 2). \quad (6.46)$$

Just like the moments of position, the moments of momentum are therefore equivalent to the expectation values of the appropriate power of the classical momentum of an atom immediately after the lens, where the second term (Δp_x) accounts for the classical momentum kick imparted by the lens.

Expectation values at the image plane

Next we calculate the width of the ensemble at the image plane:

$$\langle \Delta x_i^2 \rangle = \langle x_i^2 \rangle - \langle x_i \rangle^2 \quad (6.47)$$

This corresponds to the experimentally observed cloud width at detection. Here the i subscript indicates that the moments are evaluated at the image plane of the lens ($t = t_o + t_i$):

$$\langle x_i^n \rangle \equiv \langle x^n \rangle_{t=t_o+t_i} = \langle \hat{x}^n \rangle_{t=t_o+t_i} \quad (6.48)$$

Using the Wigner function at the image plane, the x moments can be written

$$\langle \hat{x}^n \rangle_{t=t_o+t_i} = \int d^3r \int d^3p \ x^n W(\mathbf{r}, \mathbf{p}; t_o + t_i) \quad (6.49)$$

$$= \int d^3r \int d^3p \ x^n W(\mathbf{r} - \frac{\mathbf{p}}{m} t_i, \mathbf{p}; t_o) \quad (6.50)$$

$$= \int d^3r \int d^3p \ (x + \frac{p_x}{m} t_i)^n W(\mathbf{r}, \mathbf{p}; t_o) \quad (6.51)$$

where we took advantage of Eq. 6.26 in the second line and did a change of variable in the third line. Using Eq. 6.17,

$$\langle \hat{x}^n \rangle_{t=t_o+t_i} = \frac{1}{(2\pi\hbar)^3} \int d^3\xi \int d^3p' \int d^3r \int d^3p \ (x + \frac{p_x}{m} t_i)^n e^{i(\mathbf{p}' - \mathbf{p} + \Delta p(\mathbf{r})) \cdot \xi / \hbar} e^{-\frac{i}{\hbar} V_3(\xi) \delta t} W_o(\mathbf{r} - \frac{\mathbf{p}'}{m} t_o, \mathbf{p}') \quad (6.52)$$

It is now convenient to use the change of variables $\mathbf{r}'' \equiv \mathbf{r}$ and $\mathbf{p}'' \equiv \frac{m}{t_i} \mathbf{r} + \mathbf{p}$ so that

$$\begin{aligned} & \langle \hat{x}^n \rangle_{t=t_o+t_i} = \\ & \frac{1}{(2\pi\hbar)^3} \int d^3\xi \int d^3p' \int d^3r'' \int d^3p'' \ (\frac{p''_x}{m} t_i)^n e^{i(\mathbf{p}' - \mathbf{p}'' + \frac{m}{t_i} \mathbf{r}'' + \Delta p(\mathbf{r}'')) \cdot \xi / \hbar} e^{-\frac{i}{\hbar} V_3(\xi) \delta t} W_o(\mathbf{r}'' - \frac{\mathbf{p}'}{m} t_o, \mathbf{p}') \end{aligned} \quad (6.53)$$

Next we formally define a shifted momentum impulse $\overline{\Delta p}(\mathbf{r}'') \equiv \Delta p(\mathbf{r}'') + \frac{m}{t_i} \mathbf{r}''$. With this identification, we can use the fact that Eq. 6.53 is of the same form as Eq. 6.40

with $\Delta p \rightarrow \overline{\Delta p}$. Therefore we have

$$\begin{aligned}\langle \hat{x}^n \rangle_{t=t_o+t_i} &= \left(\frac{t_i}{m}\right)^n \langle \hat{p}^n \rangle_{t=t_o} \Big|_{\Delta p \rightarrow \overline{\Delta p}} \\ &= \left(\frac{t_i}{m}\right)^n \int d^3p \int d^3r \left(p_x + \Delta p_x(\mathbf{r} + \frac{\mathbf{p}}{m}t_o) + \frac{m}{t_i}(x + \frac{p_x}{m}t_o)\right)^n W_o(\mathbf{r}, \mathbf{p}) \quad (n \leq 2).\end{aligned}\quad (6.54)$$

where we used the result from Eq. 6.46. Thus we arrive at the final result

$$\langle \hat{x}^n \rangle_{t=t_o+t_i} = \int d^3p \int d^3r \left(x + \frac{p_x}{m}(t_o + t_i) + \frac{1}{m}\Delta p_x(\mathbf{r} + \frac{\mathbf{p}}{m}t_o)t_i\right)^n W_o(\mathbf{r}, \mathbf{p}) \quad (n \leq 2). \quad (6.55)$$

which is of the form of the expectation value of moments of the classical position at detection.

Results in terms of initial moments

It is possible to write the results for each of the measured moments explicitly in terms of expectation values of the initial moments of the distribution:

$$\Delta x_o^2 = \langle x_o^2 \rangle - \langle x_o \rangle^2 \quad (6.56)$$

$$\Delta v_o^2 = \langle v_o^2 \rangle - \langle v_o \rangle^2 \quad (6.57)$$

$$\langle \Delta x_o \Delta v_o \rangle = \langle x_o v_o \rangle - \langle x_o \rangle \langle v_o \rangle \quad (6.58)$$

where the cross moments are defined using Eq. 6.29. This is desirable because the initial moments are the experimentally defined quantities. The conversion requires performing an inverse Wigner-Weyl transform on the arguments of the integral in Eq. 6.55 (and equivalent for the other moments). This process will result in expectation values of symmetrized operators. Since we only consider first and second order moments, the only terms that we must consider are of the form x^2 , p_x^2 , $\Delta p_x^2(\mathbf{r} + \frac{\mathbf{p}}{m}t_o)$, xp , $p_x \Delta p_x(\mathbf{r} + \frac{\mathbf{p}}{m}t_o)$, and $x \Delta p_x(\mathbf{r} + \frac{\mathbf{p}}{m}t_o)$. The inverse Wigner-Weyl transforms of x^2 and p_x^2 are trivial, and the transform of xp is $(\hat{x}\hat{p} + \hat{p}\hat{x})/2$, but the transforms of $p_x \Delta p_x$, $x \Delta p_x$, and Δp_x^2 are less obvious. In the following section we prove that the latter three terms can be written as symmetrized expectation values, even for arbitrary functions

$$\Delta p_x(\mathbf{r}).$$

6.4.5 Evaluation of position-momentum cross moments

In calculating the effect of the lens on the atom distribution, it will be necessary to convert terms of the form

$$C_f \equiv \int d^3x d^3p \ p_x f \left(\mathbf{r} + \frac{\mathbf{p}}{m} t_o \right) W_o(\mathbf{r}, \mathbf{p}) \quad (6.59)$$

into expectation values of appropriate operators. We assume that f is real-valued and that it can be Taylor expanded in its arguments. Using Eq. 6.6 and a change of variables, we can alternatively write

$$C_f = \int d^3x d^3p \ p_x f(\mathbf{r}) W_{\text{free}}(\mathbf{r}, \mathbf{p}; t_o) = \int d^3x d^3p \ p_x \left(\sum_{i,j,k} f_{i,j,k} x^i y^j z^k \right) W_{\text{free}}(\mathbf{r}, \mathbf{p}; t_o) \quad (6.60)$$

$$= \sum_{i,j,k} f_{i,j,k} \int d^3x d^3p \ p_x x^i y^j z^k W_{\text{free}}(\mathbf{r}, \mathbf{p}; t_o) \quad (6.61)$$

where $f_{i,j,k}$ are the appropriate Taylor series coefficients for $f(\mathbf{r})$. Since the Wigner-Weyl transform of the symmetrized operator $(\hat{p}_x \hat{x}^i \hat{y}^j \hat{z}^k + \hat{x}^i \hat{y}^j \hat{z}^k \hat{p}_x)/2$ gives $p_x x^i y^j z^k$, we can write this series as

$$C_f = \sum_{i,j,k} f_{i,j,k} \left\langle \frac{\hat{p}_x \hat{x}^i \hat{y}^j \hat{z}^k + \hat{x}^i \hat{y}^j \hat{z}^k \hat{p}_x}{2} \right\rangle_{t=t_o} \quad (6.62)$$

$$= \left\langle \frac{\hat{p}_x \left(\sum_{i,j,k} f_{i,j,k} \hat{x}^i \hat{y}^j \hat{z}^k \right) + \left(\sum_{i,j,k} f_{i,j,k} \hat{x}^i \hat{y}^j \hat{z}^k \right) \hat{p}_x}{2} \right\rangle_{t=t_o} \quad (6.63)$$

$$= \left\langle \frac{\hat{p}_x f(\hat{\mathbf{r}}) + f(\hat{\mathbf{r}}) \hat{p}_x}{2} \right\rangle_{t=t_o}. \quad (6.64)$$

We will now express C_f as an expectation value evaluated at $t = 0$. In the Heisenberg

picture, we can write Eq. 6.64 as

$$C_f = \left\langle \frac{\hat{p}_x(t_o)f(\hat{\mathbf{r}}(t_o)) + f(\hat{\mathbf{r}}(t_o))\hat{p}_x(t_o)}{2} \right\rangle_{t=0} \quad (6.65)$$

where the subscript indicates that the expectation value is evaluated using the state at $t = 0$. The operators at $t = t_o$ are related to the operators at $t = 0$ by

$$\hat{\mathbf{r}}(t_o) = \hat{\mathbf{r}}(0) + \frac{\hat{\mathbf{p}}(0)}{m}t_o \quad (6.66)$$

$$\hat{\mathbf{p}}(t_o) = \hat{\mathbf{p}}(0), \quad (6.67)$$

so

$$C_f = \left\langle \frac{\hat{p}_x(0)f\left(\hat{\mathbf{r}}(0) + \frac{\hat{\mathbf{p}}(0)}{m}t_o\right) + f\left(\hat{\mathbf{r}}(0) + \frac{\hat{\mathbf{p}}(0)}{m}t_o\right)\hat{p}_x(0)}{2} \right\rangle_{t=0}. \quad (6.68)$$

In Schrödinger picture notation, this is simply

$$C_f = \left\langle \frac{\hat{p}_x f\left(\hat{\mathbf{r}} + \frac{\hat{\mathbf{p}}}{m}t_o\right) + f\left(\hat{\mathbf{r}} + \frac{\hat{\mathbf{p}}}{m}t_o\right)\hat{p}_x}{2} \right\rangle_{t=0} \equiv \left\langle p_x f\left(\mathbf{r} + \frac{\mathbf{p}}{m}t_o\right) \right\rangle, \quad (6.69)$$

using the symmetrized operator expectation value notation defined in Eq. 6.29 for the final equality. A similar argument demonstrates that the $x\Delta p_x$ term can be written as

$$\left\langle \frac{\hat{x}\Delta p_x\left(\hat{\mathbf{r}} + \frac{\hat{\mathbf{p}}}{m}t_o\right) + \Delta p_x\left(\hat{\mathbf{r}} + \frac{\hat{\mathbf{p}}}{m}t_o\right)\hat{x}}{2} \right\rangle_{t=0} \equiv \left\langle x\Delta p_x\left(\mathbf{r} + \frac{\mathbf{p}}{m}t_o\right) \right\rangle \quad (6.70)$$

and that the Δp_x^2 term can be written as

$$\left\langle \Delta p_x^2(\hat{\mathbf{r}} + \frac{\hat{\mathbf{p}}}{m}t_o) \right\rangle_{t=0} \equiv \left\langle \Delta p_x^2(\mathbf{r} + \frac{\mathbf{p}}{m}t_o) \right\rangle. \quad (6.71)$$

6.4.6 Modified Cauchy-Schwarz inequality for symmetrized operators

We now derive a modified Cauchy-Schwarz inequality for symmetrized operators that is needed to prove our claims in the following section. This inequality states that for Hermitian operators \hat{A} and \hat{B} ,

$$\langle A^2 \rangle \langle B^2 \rangle - \langle AB \rangle^2 \equiv \langle \hat{A}^2 \rangle \langle \hat{B}^2 \rangle - \left\langle \frac{\hat{A}\hat{B} + \hat{B}\hat{A}}{2} \right\rangle^2 \geq 0, \quad (6.72)$$

where once again we use the symmetrized operator expectation value notation. The lefthand side of this inequality can be written as a sum of two terms which are independently ≥ 0 :

$$\langle A^2 \rangle \langle B^2 \rangle - \langle AB \rangle^2 = \Gamma_1 + \Gamma_2 \quad (6.73)$$

where

$$\Gamma_1 = \langle \hat{A}^2 \rangle \langle \hat{B}^2 \rangle - \langle \hat{A}\hat{B} \rangle \langle \hat{B}\hat{A} \rangle = \langle \hat{A}^2 \rangle \langle \hat{B}^2 \rangle - |\langle \hat{A}\hat{B} \rangle|^2 \quad (6.74)$$

$$\Gamma_2 = -\frac{1}{4} \left[\langle \hat{A}\hat{B} \rangle^2 + \langle \hat{B}\hat{A} \rangle^2 - 2 \langle \hat{A}\hat{B} \rangle \langle \hat{B}\hat{A} \rangle \right] = -\frac{1}{4} [\langle \hat{A}\hat{B} \rangle - \langle \hat{B}\hat{A} \rangle]^2 = -\frac{1}{4} \langle [\hat{A}, \hat{B}] \rangle^2. \quad (6.75)$$

The fact that $\Gamma_1 \geq 0$ follows directly from the standard Cauchy-Schwarz inequality for Hermitian operators. Because \hat{A} and \hat{B} are Hermitian, the expectation value of their commutator is purely imaginary, giving us $\Gamma_2 \geq 0$.

6.5 Aberrations

Here we analyze the effect that aberrations in the lens potential have on the ability to collimate and refocus atoms in a delta kick cooling procedure. The lens potential can deviate from the ideal harmonic form for a variety of reasons. For the optical dipole

lens like the one used in this work, these include deviations due to the Gaussian profile of the laser beam as well as higher spatial frequency intensity variations arising from imperfections in the delivery optics. Other types of lens potentials (e.g., magnetic fields) can suffer from analogous aberrations. We also use a lens based on a TOP trap where aberrations result from the fact that the magnetic trap is effectively harmonic only over a limited spatial extent.

To model the lens aberrations, we consider an arbitrary position-dependent lens force $F(x)$ acting on the atoms during the brief lens operation. In the harmonic limit, this force reduces to the simple case discussed in the paper, $F(x) \rightarrow -m\omega^2x$, but for now we allow $F(x)$ to remain completely general. For this analysis we consider the delta-kick (thin lens) limit discussed in Sec. 6.4, where we may treat the action of the lens as delivering a position-dependent momentum impulse $F(x)\delta t$. This approximation holds as long as the atom does not move much during the lens pulse so that the force is roughly constant.

As established in Sec. 6.4, we can calculate the experimentally relevant moments in terms of symmetrized operator expectation values (discussed in Sec. 6.4.4) by considering the evolution of classical trajectories in phase space. Immediately after the lens is applied, a given classical trajectory with initial x -position x_o and initial velocity v_o in the x -direction has the form

$$x_\ell = x_o + v_o t_o \quad (6.76)$$

$$v_\ell = v_o + a(x_\ell, y_\ell)\delta t, \quad (6.77)$$

where we have defined the lens induced acceleration in the x -direction as $a(x, y) = F(x, y)/m$ and where y is the orthogonal transverse direction. As discussed above, when calculating moments, we integrate over the y -dependence of the trajectories. To emphasize this, we suppress the y -dependence of a in subsequent equations.

At the image plane, the trajectory has final position

$$x_i = x_o + v_o(t_o + t_i) + a(x_\ell)t_i\delta t. \quad (6.78)$$

We are interested in evaluating the collimation performance of the lens – that is, how cold are the atoms immediately after applying the lens. Computing expectation values using Eq. 6.77, the second moment of the velocity after the lens is

$$\langle v_\ell^2 \rangle = \langle v_o^2 \rangle + 2\delta t \langle v_o a \rangle + \delta t^2 \langle a^2 \rangle \quad (6.79)$$

and the square of the mean velocity is

$$\langle v_\ell \rangle^2 = \langle v_o \rangle^2 + 2 \langle v_o \rangle \langle a \rangle \delta t + \langle a \rangle^2 \delta t^2 \quad (6.80)$$

where $a \equiv a(x_\ell) = a(x_o + v_o t_o)$. The velocity variance after the lens is $\Delta v_\ell^2 \equiv \langle v_\ell^2 \rangle - \langle v_\ell \rangle^2$. Choosing the lens duration δt_c to minimize the velocity variance, we obtain

$$\delta t_c = -\frac{\langle \Delta v_o \Delta a \rangle}{\Delta a^2}, \quad (6.81)$$

and the minimum (collimated) velocity variance after the lens is given by

$$\Delta v_\ell^2 = \frac{\Delta v_o^2 \Delta a^2 - \langle \Delta v_o \Delta a \rangle^2}{\Delta a^2} \quad (6.82)$$

where $\langle \Delta x \Delta y \rangle \equiv \langle (x - \langle x \rangle)(y - \langle y \rangle) \rangle = \langle xy \rangle - \langle x \rangle \langle y \rangle$ and $\Delta a^2 \equiv \langle a^2 \rangle - \langle a \rangle^2$. This velocity width corresponds to the coldest temperatures that can be produced by the lens.

In Sec. 6.2, we characterize the performance of the lens by observing the RMS size of the ensemble at detection. From Eq. 6.78, the second moment of the position at detection is

$$\langle x_i^2 \rangle = \langle (x_o + v_o(t_o + t_i))^2 \rangle + 2 \langle x_o a \rangle t_i \delta t + 2 \langle v_o a \rangle (t_o + t_i) t_i \delta t + \langle a^2 \rangle t_i^2 \delta t^2 \quad (6.83)$$

and the square of the mean position is

$$\langle x_i \rangle^2 = \langle x_o \rangle^2 + 2 \langle x_o \rangle \langle v_o \rangle (t_o + t_i) + \langle v_o \rangle^2 (t_o + t_i)^2 + 2 (\langle x_o \rangle + \langle v_o \rangle (t_o + t_i)) \langle a \rangle t_i \delta t + \langle a \rangle^2 t_i^2 \delta t^2. \quad (6.84)$$

The ensemble width at detection is $\Delta x_i^2 \equiv \langle x_i^2 \rangle - \langle x_i \rangle^2$ and may be written in the

form that appears in Eq. 6.2 in Sec. 6.2:

$$\Delta x_i^2 = (\Delta x_i)_{\min}^2 + \Delta a^2 t_i^2 (\delta t - \delta t_{\min})^2 \quad (6.85)$$

where $(\Delta x_i)_{\min}$ is the minimum width, $\Delta a^2 = \Delta F^2/m$, and δt_{\min} is the lens duration that minimizes Eq. 6.83. We find that

$$\delta t_{\min} = - \frac{\langle \Delta x_\ell \Delta a \rangle}{\Delta a^2} \left(\frac{1}{t_i} + \frac{1}{t_o} \left(1 - \frac{\langle \Delta x_o \Delta a \rangle}{\langle \Delta x_\ell \Delta a \rangle} \right) \right) \quad (6.86)$$

and

$$\begin{aligned} (\Delta x_i)_{\min}^2 &= t_i^2 \left(\frac{\Delta v_o^2 \Delta a^2 - \langle \Delta v_o \Delta a \rangle^2}{\Delta a^2} \right) \\ &\quad + \left(1 + 2 \frac{t_i}{t_o} \right) \left(\frac{\Delta x_\ell^2 \Delta a^2 - \langle \Delta x_\ell \Delta a \rangle^2}{\Delta a^2} \right) - 2 \frac{t_i}{t_o} \left(\frac{\langle \Delta x_o \Delta x_\ell \rangle \Delta a^2 - \langle \Delta x_\ell \Delta a \rangle \langle \Delta x_o \Delta a \rangle}{\Delta a^2} \right). \end{aligned} \quad (6.87)$$

We define the measured ensemble RMS velocity as $(\Delta v_\ell)_{\text{bound}}^2 \equiv (\Delta x_i)_{\min}^2 / t_i^2$. Combining Eqs. 6.82 and 6.87, we arrive at Eq. 6.1, namely

$$(\Delta v_\ell)_{\text{bound}}^2 = \Delta v_\ell^2 + \delta A \quad (6.88)$$

where we define the aberration during refocusing δA as

$$\delta A \equiv \frac{1}{t_i^2} \left[\left(1 + 2 \frac{t_i}{t_o} \right) \left(\frac{\Delta x_\ell^2 \Delta a^2 - \langle \Delta x_\ell \Delta a \rangle^2}{\Delta a^2} \right) - 2 \frac{t_i}{t_o} \left(\frac{\langle \Delta x_o \Delta x_\ell \rangle \Delta a^2 - \langle \Delta x_\ell \Delta a \rangle \langle \Delta x_o \Delta a \rangle}{\Delta a^2} \right) \right]. \quad (6.89)$$

It is important to note that Δv_ℓ in Eq. 6.88 includes effects from aberrations during collimation and is therefore the physical minimum RMS velocity that can be reached with this particular lens. We can therefore use $(\Delta v_\ell)_{\text{bound}}$ to set an upper bound on the coldest possible ensemble that can be produced with this lens, accounting for aberration in both Δv_ℓ and the observed $(\Delta x_i)_{\min}$.

In order for the experimentally inferred $(\Delta v_\ell)_{\text{bound}}$ to be an upper bound for the minimum RMS velocity Δv_ℓ , we must have $\delta A \geq 0$. Using the fact that $x_\ell = x_o + v_o t_o$,

we may rewrite δA as

$$\begin{aligned} \delta A = & \frac{1}{t_i^2} \left(1 + \frac{t_i}{t_o} \right) \left(\frac{\Delta x_\ell^2 \Delta a^2 - \langle \Delta x_\ell \Delta a \rangle^2}{\Delta a^2} \right) + \frac{t_o}{t_i} \left(\frac{\Delta v_o^2 \Delta a^2 - \langle \Delta v_o \Delta a \rangle^2}{\Delta a^2} \right) \\ & - \frac{1}{t_i t_o} \left(\frac{\Delta x_o^2 \Delta a^2 - \langle \Delta x_o \Delta a \rangle^2}{\Delta a^2} \right). \end{aligned} \quad (6.90)$$

The first two terms in this expression are non-negative by the Cauchy-Schwarz inequality, and the magnitude of the third term is bounded by the Cauchy-Schwarz inequality (here, we are using the Cauchy-Schwarz inequality for symmetrized operators derived in Sec. 6.4.6). Allowing the third term to be as negative as possible, and taking the first two terms to be zero, we arrive at a lower bound on δA :

$$\delta A \geq -\frac{\Delta x_o^2}{t_i t_o}. \quad (6.91)$$

Thus, even though δA is not strictly positive for arbitrary potentials and intial phase space distributions, δA can provide only a small negative contribution to $(\Delta v_\ell)_{\text{bound}}$ even in the worst case. For our parameters, this worst-case contribution is still smaller than the stated uncertainty in the temperature bound reported in Sec. 6.2 and can be neglected.

A potentially stronger lower bound on δA can be obtained by writing the lens acceleration $a(x_\ell)$ as the sum of harmonic and aberration terms:

$$a(x_\ell) = -\omega^2 x_\ell + \delta a(x_\ell). \quad (6.92)$$

Here the linear effect of the aberrations has been incorporated into the definition of ω , so

$$\omega^2 = -\frac{\langle \Delta x_\ell \Delta a \rangle}{\Delta x_\ell^2} \quad (6.93)$$

and $\langle \Delta x_\ell \Delta \delta a \rangle = 0$. Substituting $a = -\omega^2 x_\ell + \delta a$ into Eq. 6.90, we obtain

$$\delta A = \frac{\Delta x_\ell^2}{t_i^2 \Delta a^2} \left(\left(1 + \frac{t_i}{t_o} + \frac{\Delta v_o^2 t_o^2 - \Delta x_o^2}{\Delta x_\ell^2} \right) \Delta \delta a^2 - 2 \frac{t_i}{t_o} \omega^2 \langle \Delta x_o \Delta \delta a \rangle \right). \quad (6.94)$$

From this expression, we see that if the lens is harmonic (i.e. if $\delta a = 0$), then $\delta A = 0$. In addition, we have $\delta A \geq 0$ as long as

$$\Delta\delta a^2 \geq \frac{2\frac{t_i}{t_o}}{1 + \frac{t_i}{t_o} + \frac{\Delta v_o^2 t_o^2 - \Delta x_o^2}{\Delta x_\ell^2}} \omega^2 \langle \Delta x_o \Delta \delta a \rangle. \quad (6.95)$$

In the worst case, $\langle \Delta x_o \Delta \delta a \rangle = \sqrt{\Delta x_o^2 \Delta \delta a^2} = \Delta x_o \Delta \delta a$ by the Cauchy-Schwarz inequality, and $\delta A \geq 0$ if

$$\Delta \delta a \geq \frac{2\frac{t_i}{t_o}}{1 + \frac{t_i}{t_o} + \frac{\Delta v_o^2 t_o^2 - \Delta x_o^2}{\Delta x_\ell^2}} \omega^2 \Delta x_o \sim \omega^2 \Delta x_o. \quad (6.96)$$

Thus, lens aberrations are guaranteed to contribute positively to the image size as long as the aberration-induced acceleration is larger than the scale set by $\omega^2 \Delta x_o$. We also show explicitly that $\delta A > 0$ for a lensing potential with Gaussian aberrations (see section 6.5.2), which are the dominant source of aberrations in our experiment. Thus $\delta A \geq 0$ for the results stated in this paper, and $(\Delta v_\ell)_{\text{bound}}$ is an upper bound on the minimum velocity width Δv_ℓ .

6.5.1 Harmonic lens

With no aberrations, $a(x) = -\omega^2 x$. Then from Eq. 6.81, the lensing time required to collimate the cloud is

$$\delta t_c = \frac{1}{\omega^2} \frac{\langle \Delta v_o \Delta x_o \rangle + t_o \Delta v_o^2}{\Delta x_\ell^2}. \quad (6.97)$$

If there are no correlations between x_o and v_o in the initial cloud, we can rewrite the expression for δt_c to obtain

$$\delta t_c = \frac{1}{\omega^2} \frac{t_o \Delta v_o^2}{\Delta x_\ell^2} = \frac{1}{\omega^2 t_o} \frac{\Delta x_\ell^2 - \Delta x_o^2}{\Delta x_\ell^2} = \frac{1}{\omega^2 t_o} (1 - \gamma^2) \quad (6.98)$$

which implies a focal time of

$$f_c \equiv \frac{1}{\omega^2 \delta t_c} = \frac{t_o}{1 - \gamma^2}. \quad (6.99)$$

Here $\gamma \equiv \frac{\Delta x_o}{\Delta x_\ell}$ is the ratio of the initial cloud width to the cloud width at the lens. The minimum achievable velocity width is calculated from Eq. 6.82 to be

$$\Delta v_\ell^2 = \Delta v_o^2 \gamma^2 - \frac{\langle \Delta v_o \Delta x_o \rangle^2}{\Delta x_\ell^2} \quad (6.100)$$

In the absence of correlations between x_o and v_o , the lens reduces the effective temperature of the cloud by a factor of

$$\eta_c \equiv \frac{\Delta v_\ell^2}{\Delta v_o^2} = \gamma^2 \quad (6.101)$$

at collimation.

From Eq. 6.85, the RMS position width at the imaging time is

$$\Delta x_i^2 = (\Delta x_i)_{\min}^2 + \omega^4 \Delta x_\ell^2 t_i^2 (\delta t - \delta t_{\min})^2. \quad (6.102)$$

The lens time required to achieve the minimum RMS position width is given by Eq. 6.86,

$$\delta t_{\min} = \frac{1}{\omega^2} \left(\frac{1}{t_i} + \frac{1}{t_o} \left(1 - \frac{\langle \Delta x_o \Delta x_\ell \rangle}{\Delta x_\ell^2} \right) \right) = \frac{1}{\omega^2} \left(\frac{1}{t_i} + \frac{1}{t_o} (1 - \gamma^2) - \frac{\langle \Delta x_o \Delta v_o \rangle}{\Delta x_\ell^2} \right) \quad (6.103)$$

and the minimum RMS position width is given by Eq. 6.87,

$$(\Delta x_i)_{\min}^2 = \frac{t_i^2}{\Delta x_\ell^2} (\Delta v_o^2 \Delta x_o^2 - \langle \Delta v_o \Delta x_o \rangle^2) = t_i^2 \Delta v_o^2 \gamma^2 - \frac{t_i^2 \langle \Delta v_o \Delta x_o \rangle^2}{\Delta x_\ell^2}. \quad (6.104)$$

If x_o and v_o are uncorrelated, we can rewrite this expression for $(\Delta x_i)_{\min}^2$ as

$$(\Delta x_i)_{\min}^2 = \frac{t_i^2}{t_o^2} t_o^2 \Delta v_o^2 \gamma^2 = \frac{t_i^2}{t_o^2} \Delta x_o^2 (1 - \gamma^2). \quad (6.105)$$

Note that for a harmonic lens, $\delta A = 0$, and

$$(\Delta v_\ell)^2_{\text{bound}} \equiv \frac{(\Delta x_i)^2_{\min}}{t_i^2} = \Delta v_\ell^2 \quad (6.106)$$

so the refocused cloud size is an unbiased estimator of the collimated temperature.

6.5.2 Gaussian aberrations

A Gaussian potential has the form $V(x, y) = -m\Phi e^{-2(x^2+y^2)/\sigma^2}$, where σ is the $1/e^2$ radial waist of the beam. The acceleration in the x -direction induced by this potential is

$$a_x(x, y) = -\frac{4\Phi}{\sigma^2} xe^{-2(x^2+y^2)/\sigma^2} \equiv -\omega^2 xe^{-2(x^2+y^2)/\sigma^2} \quad (6.107)$$

In this section, we assume the initial position and velocity distributions of the ensemble to be 2D Gaussians given by

$$\begin{aligned} W(x, y, v_x, v_y) &= \frac{1}{2\pi\Delta x_o\Delta v_{ox}\sqrt{1-\beta_x^2}} \exp\left[-\frac{1}{2(1-\beta_x^2)}\left(\frac{x^2}{\Delta x_o^2} + \frac{v_x^2}{\Delta v_{ox}^2} - 2\frac{\beta_x x v_x}{\Delta x_o \Delta v_{ox}}\right)\right] \\ &\times \frac{1}{2\pi\Delta y_o\Delta v_{oy}\sqrt{1-\beta_y^2}} \exp\left[-\frac{1}{2(1-\beta_y^2)}\left(\frac{y^2}{\Delta y_o^2} + \frac{v_y^2}{\Delta v_{oy}^2} - 2\frac{\beta_y y v_y}{\Delta y_o \Delta v_{oy}}\right)\right] \end{aligned} \quad (6.108)$$

where

$$\beta_x \equiv \frac{\langle \Delta v_{ox} \Delta x_o \rangle}{\Delta x_o \Delta v_{ox}} \quad \text{and} \quad \beta_y \equiv \frac{\langle \Delta v_{oy} \Delta y_o \rangle}{\Delta y_o \Delta v_{oy}} \quad (6.109)$$

are parameters that characterize the position-velocity correlation in the initial distribution, and we have $|\beta_x| \leq 1$ and $|\beta_y| \leq 1$.

We compute the minimum velocity width Δv_ℓ^2 in the x -direction and the collimation lensing time δt_c by performing the integrals in Eq. 6.79 and minimizing with

respect to δt :

$$\Delta v_\ell^2 = \Delta v_{ox}^2 \left(1 - (1 - \gamma^2 + \beta_x^2 \gamma^2) \frac{(1 + 8\alpha_x^2)^{3/2}}{(1 + 4\alpha_x^2)^3} \frac{(1 + 8\alpha_y^2)^{1/2}}{(1 + 4\alpha_y^2)} \right) \quad (6.110)$$

$$\delta t_c = \frac{1}{\omega^2 t_o} \left(1 - \gamma^2 - \frac{\langle \Delta v_{ox} \Delta x_o \rangle t_o}{\Delta x_\ell^2} \right) \left(\frac{1 + 8\alpha_x^2}{1 + 4\alpha_x^2} \right)^{3/2} \left(\frac{1 + 8\alpha_y^2}{1 + 4\alpha_y^2} \right)^{1/2} \quad (6.111)$$

where $\alpha_x^2 \equiv \Delta x_\ell^2/\sigma^2$ and $\alpha_y^2 \equiv \Delta y_\ell^2/\sigma^2$ parameterize the width of the cloud at the lensing plane with respect to the width of the beam.

Similarly, we compute $(\Delta x_i)^2_{\min}$ and δt_{\min} by performing the integrals in Eq. 6.83 and minimizing with respect to δt , which yields

$$\begin{aligned} (\Delta x_i)^2_{\min} &= \Delta x_o^2 + 2 \langle \Delta v_{ox} \Delta x_o \rangle (t_i + t_o) + \Delta v_{ox}^2 (t_i + t_o)^2 \\ &\quad - \Delta x_\ell^2 \left(1 + \frac{t_i}{t_o} \left(1 - \gamma^2 - \frac{\langle \Delta v_{ox} \Delta x_o \rangle t_o}{\Delta x_\ell^2} \right) \right)^2 \frac{(1 + 8\alpha_x^2)^{3/2}}{(1 + 4\alpha_x^2)^3} \frac{(1 + 8\alpha_y^2)^{1/2}}{(1 + 4\alpha_y^2)} \end{aligned} \quad (6.112)$$

and

$$\delta t_{\min} = \frac{1}{\omega^2} \left(\frac{1}{t_i} + \frac{1}{t_o} \left(1 - \gamma^2 - \frac{\langle \Delta v_{ox} \Delta x_o \rangle t_o}{\Delta x_\ell^2} \right) \right) \left(\frac{1 + 8\alpha_x^2}{1 + 4\alpha_x^2} \right)^{3/2} \left(\frac{1 + 8\alpha_y^2}{1 + 4\alpha_y^2} \right)^{1/2} \quad (6.113)$$

Note that when the size of the cloud at the lens is much less than the size of the beam, $\Delta x_\ell \ll \sigma$ and $\Delta y_\ell \ll \sigma$, then $\alpha_x, \alpha_y \rightarrow 0$ and we recover the harmonic case. In addition, the difference between $(\Delta x_i)^2_{\min}/t_i^2$ and Δv_ℓ^2 is the aberration during refocus δA :

$$\delta A = \frac{\Delta x_\ell^2}{t_i^2} \left(1 + 2 \frac{t_i}{t_o} \left(1 - \gamma^2 - \frac{\langle \Delta v_{ox} \Delta x_o \rangle t_o}{\Delta x_\ell^2} \right) \right) \left(1 - \frac{(1 + 8\alpha_x^2)^{3/2}}{(1 + 4\alpha_x^2)^3} \frac{(1 + 8\alpha_y^2)^{1/2}}{(1 + 4\alpha_y^2)} \right) \quad (6.114)$$

Since we have $|\langle \Delta v_{ox} \Delta x_o \rangle t_o / \Delta x_\ell^2| \leq (\Delta v_{ox} t_o) \Delta x_o / \Delta x_\ell^2 \approx \gamma \ll 1$, it is clear by inspection that $\delta A > 0$, so $(\Delta v_\ell)_{\text{bound}}$ is an upper bound on the collimated temperature.

6.5.3 High spatial frequency aberrations

In this section, we consider potentials of the form

$$V(x_\ell) = \frac{m\omega^2}{2}x_\ell^2 - m\delta\Phi \sin(kx_\ell + \phi) \quad (6.115)$$

which induce accelerations of the form

$$a(x_\ell) = -\omega^2 x_\ell + \delta\Phi k \cos(kx_\ell + \phi). \quad (6.116)$$

We assume that the aberration has a high spatial frequency, so its wavelength $2\pi/k$ is much smaller than any size scale associated with the initial phase space distribution $W(x_o, v_o)$. In addition, we assume that the aberrations are weak compared to the harmonic potential, so

$$\delta\Phi^2 k^2 \ll \omega^4 \Delta x_\ell^2. \quad (6.117)$$

From Eq. 6.82, the minimum achievable velocity width is

$$\Delta v_\ell^2 = \frac{\omega^4 (\Delta v_o^2 \Delta x_o^2 - \langle \Delta x_o \Delta v_o \rangle^2) + \delta\Phi^2 k^2 \Delta v_o^2 \langle \cos^2(kx_\ell + \phi) \rangle}{\Delta a^2} + \frac{C}{\Delta a^2} \quad (6.118)$$

where we have used the fact that $x_\ell = x_o + v_o t_o$, and where

$$\begin{aligned} C = & 2\omega^2 \delta\Phi k (-\Delta v_o^2 \langle \Delta x_o \cos(kx_\ell + \phi) \rangle + \langle \Delta x_o \Delta v_o \rangle \langle \Delta v_o \cos(kx_\ell + \phi) \rangle) \\ & - \delta\Phi^2 k^2 \langle \Delta v_o \cos(kx_\ell + \phi) \rangle^2. \end{aligned} \quad (6.119)$$

Since the aberrations oscillate rapidly with respect to the initial phase space distribution, $\langle \Delta x_o \cos(kx_\ell + \phi) \rangle = \langle \Delta v_o \cos(kx_\ell + \phi) \rangle = 0$, so $C = 0$, and we have

$$\Delta v_\ell^2 = \frac{\omega^4 (\Delta v_o^2 \Delta x_o^2 - \langle \Delta x_o \Delta v_o \rangle^2) + \delta\Phi^2 k^2 \Delta v_o^2 \langle \cos^2(kx_\ell + \phi) \rangle}{\omega^4 \Delta x_\ell^2 + \delta\Phi^2 k^2 \langle \cos^2(kx_\ell + \phi) \rangle}. \quad (6.120)$$

Dividing the numerator and denominator by $\omega^4 \Delta x_\ell^2$ and re-writing Δv_ℓ^2 in terms of the small parameter

$$\epsilon \equiv \frac{\delta\Phi^2 k^2}{\omega^4 \Delta x_\ell^2} \langle \cos^2(kx_\ell + \phi) \rangle \quad (6.121)$$

we obtain

$$\Delta v_\ell^2 = \frac{1}{1 + \epsilon} ((\Delta v_\ell^H)^2 + \epsilon \Delta v_o^2) \quad (6.122)$$

where Δv_ℓ^H is the minimum velocity width achieved by an ideal harmonic lens. To first order in ϵ , we have

$$\Delta v_\ell^2 \approx (\Delta v_\ell^H)^2 + \epsilon (\Delta v_o^2 - (\Delta v_\ell^H)^2). \quad (6.123)$$

If $\langle \Delta x_o \Delta v_o \rangle = 0$, we may re-write this expression as

$$\Delta v_\ell^2 \approx (\Delta v_\ell^H)^2 + \epsilon \Delta v_o^2 (1 - \gamma^2). \quad (6.124)$$

Thus, for high spatial frequency aberrations in the lensing potential with amplitude $\delta\Phi$ and wavelength $2\pi/k$, the heating due to the aberrations scales as $\delta\Phi^2 k^2 (\delta t_c^H)^2$, where δt_c^H is the lens duration required to collimate the cloud with an ideal harmonic lens. Note that ϵ can also be expressed using the expression for ω for a Gaussian beam from the previous section as

$$\epsilon = \frac{1}{32} (k\sigma)^2 \left(\frac{\delta\Phi}{\Phi} \right)^2 \left(\frac{\sigma}{\Delta x_\ell} \right)^2 \quad (6.125)$$

where we have taken $\langle \cos^2(kx_\ell + \phi) \rangle = \frac{1}{2}$. For a Gaussian beam with intensity aberrations, the term $(\delta\Phi/\Phi)$ is the fractional intensity perturbation amplitude at frequency k . Aberrations cause significant heating when ϵ is not negligible compared to γ^2 . For high spatial frequency perturbations ($k\sigma > 1$), the fractional size of the intensity perturbation ($\delta\Phi/\Phi$) must be made sufficiently small to avoid this source of heating.

6.5.4 Scaling of aberration contributions to cloud size with lens duration

Here we show that in our experiment, the imaged cloud size is the sum in quadrature of the relay image size (i.e. the cloud size produced by a perfect harmonic lens) and an aberration term that scales with the lens application time δt . We begin by writing the acceleration induced by a general lens potential as $a(x_\ell) = -\omega^2 x_\ell + \delta a(x_\ell)$. Furthermore, we are free to incorporate the linear effect of the aberrations into the definition of ω , so

$$\omega^2 = -\frac{\langle \Delta x_\ell \Delta a \rangle}{\Delta x_\ell^2} \quad (6.126)$$

and $\langle \Delta x_\ell \Delta \delta a \rangle = 0$.

Combining Eq. 6.83 and Eq. 6.84, the imaged cloud size as a function of δt is

$$\Delta x_i^2 = \langle (\Delta x_o + \Delta v_o(t_o + t_i))^2 \rangle + 2 \langle \Delta x_o \Delta a \rangle t_i \delta t + 2 \langle \Delta v_o \Delta a \rangle (t_o + t_i) t_i \delta t + \Delta a^2 t_i^2 \delta t^2 \quad (6.127)$$

Substituting $a = -\omega^2 x_\ell + \delta a$, we have

$$\Delta x_i^2 = (\Delta x_i^H)^2 + \delta X^2 \quad (6.128)$$

where

$$(\Delta x_i^H)^2 \equiv \langle (\Delta x_o + \Delta v_o(t_o + t_i))^2 \rangle - 2 \langle \Delta x_o \Delta x_\ell \rangle \omega^2 t_i \delta t - 2 \langle \Delta v_o \Delta x_\ell \rangle \omega^2 (t_o + t_i) t_i \delta t + \Delta x_\ell^2 \omega^4 t_i^2 \delta t^2 \quad (6.129)$$

is the relay image size, and

$$\delta X^2 \equiv 2 \langle \Delta x_o \Delta \delta a \rangle t_i \delta t + 2 \langle \Delta v_o \Delta \delta a \rangle (t_o + t_i) t_i \delta t + \Delta \delta a^2 t_i^2 \delta t^2 \quad (6.130)$$

is the contribution from aberrations. Recalling that $x_\ell = x_o + v_o t_o$ and using the fact that $\langle \Delta x_\ell \Delta \delta a \rangle = 0$, we can rewrite δX^2 as

$$\delta X^2 = -2 \langle \Delta x_o \Delta \delta a \rangle \frac{t_i}{t_o} t_i \delta t + \Delta \delta a^2 t_i^2 \delta t^2. \quad (6.131)$$

Defining the velocity kick due to the aberrations as $\delta v(x_\ell) \equiv \delta a(x_\ell)\delta t$, we have

$$\delta X^2 = -\frac{2}{t_o} \langle \Delta x_o \Delta \delta v \rangle t_i^2 + \Delta \delta v^2 t_i^2. \quad (6.132)$$

To establish that the first term in δX^2 is a small correction, we make three assumptions. First, we assume that the aberrations do not vary significantly with x_o over the region where W has support. That is,

$$\left\langle \left(\frac{\partial \delta v}{\partial x_o} \right)^2 \right\rangle \Delta x_o^2 \ll \Delta \delta v^2. \quad (6.133)$$

This claim is physically motivated by the fact that $\Delta x_o \approx 50 \mu\text{m}$; variations in the laser intensity with this length scale diffract out of the beam before it reaches the atoms. Second, we assume that t_o is long enough that

$$\Delta x_o^2 / t_o^2 \lesssim \Delta \delta v^2. \quad (6.134)$$

Finally, we choose coordinates so that $\langle x_o \rangle = 0$ and assume that δv and x_o are uncorrelated at zeroth order in x_o , so

$$\langle \Delta x_o \Delta \delta v(v_o t_o) \rangle = 0. \quad (6.135)$$

With these assumptions, we can Taylor expand $\delta v(x_o + v_o t_o)$ around $x_o = 0$,

$$\delta v(x_o + v_o t_o) \approx \delta v(v_o t_o) + x_o \frac{\partial \delta v}{\partial x_o} + \dots \quad (6.136)$$

and substitute for δv in the first term in δX^2 , which yields

$$\frac{1}{t_o} \langle \Delta x_o \Delta \delta v \rangle = \frac{1}{t_o} \iint x_o \delta v(x_o + v_o t_o) W(x_o, v_o) dx_o dv_o \quad (6.137)$$

$$\approx \frac{1}{t_o} \iint x_o \left(\delta v(v_o t_o) + \frac{\partial \delta v}{\partial x_o} x_o \right) W(x_o, v_o) dx_o dv_o. \quad (6.138)$$

The first term in this integral evaluates to zero by Eq. 6.135. The remaining term is

$$\frac{1}{t_o} \langle \Delta x_o \Delta \delta v \rangle = \frac{1}{t_o} \iint x_o^2 \frac{\partial \delta v}{\partial x_o} W(x_o, v_o) dx_o dv_o = \frac{1}{t_o} \left\langle x_o^2 \frac{\partial \delta v}{\partial x_o} \right\rangle. \quad (6.139)$$

Using the Cauchy-Schwarz inequality, we see that the magnitude of term is less than

$$\frac{1}{t_o} \langle \Delta x_o \Delta \delta v \rangle \leq \frac{1}{t_o} \left(\langle x_o^4 \rangle \left\langle \left(\frac{\partial \delta v}{\partial x_o} \right)^2 \right\rangle \right)^{1/2} \quad (6.140)$$

$$\sim \frac{1}{t_o} \left((\Delta x_o^2)^2 \left\langle \left(\frac{\partial \delta v}{\partial x_o} \right)^2 \right\rangle \right)^{1/2} = \frac{\Delta x_o^2}{t_o} \left\langle \left(\frac{\partial \delta v}{\partial x_o} \right)^2 \right\rangle^{1/2} \quad (6.141)$$

But by assumption,

$$\left\langle \left(\frac{\partial \delta v}{\partial x_o} \right)^2 \right\rangle \Delta x_o^2 \ll \Delta \delta v^2 \quad \text{and} \quad \Delta x_o^2 / t_o^2 \lesssim \Delta \delta v^2 \quad (6.142)$$

so

$$\frac{1}{t_o} \langle \Delta x_o \Delta \delta v \rangle \leq \frac{\Delta x_o^2}{t_o} \left\langle \left(\frac{\partial \delta v}{\partial x_o} \right)^2 \right\rangle^{1/2} = \left(\left\langle \left(\frac{\partial \delta v}{\partial x_o} \right)^2 \right\rangle \Delta x_o^2 \right)^{1/2} \left(\frac{\Delta x_o^2}{t_o^2} \right)^{1/2} \ll \Delta \delta v^2 \quad (6.143)$$

and the dominant contribution to δX^2 comes from the $\langle \delta v^2 \rangle$ term:

$$\delta X^2 \approx \Delta \delta v^2 t_i^2 = \Delta \delta a^2 t_i^2 \delta t^2. \quad (6.144)$$

The imaged cloud size is therefore

$$\Delta x_i^2 = (\Delta x_i^H)^2 + \Delta \delta a^2 t_i^2 \delta t^2, \quad (6.145)$$

which is a sum in quadrature of the relay image size and an aberration term that scales with the lens duration δt .

Since collimating the cloud requires a shorter lens application time than refocusing the cloud, we can correct for the aberration δA that occur during refocusing and generate an unbiased estimate of Δv_ℓ^2 by multiplying the aberration contribution by

a factor of

$$(\delta t_c/\delta t_{\min})^2 = \frac{(1 - \gamma^2)^2}{(\frac{t_o}{t_i} + 1 - \gamma^2)^2} \quad (6.146)$$

where aberrations do not change the ratio $\delta t_c/\delta t_{\min}$ significantly for our configuration. Inserting the experimental parameters $t_o = 1.1$ s, $t_i = 1.8$ s, and $\gamma^2 = 0.017$, we find that

$$(\delta t_c/\delta t_{\min})^2 = 0.37. \quad (6.147)$$

The relay image size is given by

$$\Delta x_i^H = \frac{t_i}{t_o} \sqrt{(1 - \gamma^2)} \Delta x_o = 88 \text{ } \mu\text{m}. \quad (6.148)$$

We measure $(\Delta x_i)_{\min} = 110 \pm 30 \text{ } \mu\text{m}$ for the North axis and $120 \pm 40 \text{ } \mu\text{m}$ for the West axis, so $\sqrt{\delta X^2} = 70 \text{ } \mu\text{m}$ for the North axis and $90 \text{ } \mu\text{m}$ for the West axis. Scaling δX^2 for each axis by $(\delta t_c/\delta t_{\min})^2$, we obtain collimated velocity estimates $(\Delta v_\ell)_{\text{est}} = 55 \text{ } \mu\text{m/s}$ for the North axis and $58 \text{ } \mu\text{m/s}$ for the West axis, which correspond to temperature estimates of 30 pK and 35 pK at collimation.

6.6 Point spread function

As stated in Sec. 6.2, in order to perform the convolution of the Gaussian atom cloud profile with the PSF, we use a smooth representation of the PSF. We find that a sum of three Gaussians, with parameters fixed as described in the text, provides an accurate representation of the PSF. The choice of the triple Gaussian model is purely phenomenological, and the model's exact functional form is unimportant. For instance, a model consisting of a Gaussian convolved with the sum of two exponential decays can also be used to closely represent the PSF, and the choice of this model vs. the triple Gaussian model does not substantially affect the extracted widths of the lensed clouds.

Explicitly, the triple Gaussian model for the PSF has the form

$$\text{PSF}(x) = \frac{c_1}{w_1\sqrt{2\pi}}e^{-x^2/(2w_1^2)} + \frac{c_2}{w_2\sqrt{2\pi}}e^{-x^2/(2w_2^2)} + \frac{c_3}{w_3\sqrt{2\pi}}e^{-x^2/(2w_3^2)}. \quad (6.149)$$

Images are fit by the convolution $\phi(x) \otimes \text{PSF}(x)$ of a Gaussian profile $\phi(x) = (\sigma_x\sqrt{2\pi})^{-1}e^{-x^2/(2\sigma_x^2)}$ with the PSF. The parameters $\vec{\alpha} \equiv (c_1, c_2, c_3, w_1, w_2, w_3)$ of the PSF are fixed by fitting $\phi(x) \otimes \text{PSF}(x)$ to a cloud with known, small size σ_x .

6.7 Spontaneous heating rate limit

The dipole lensing results in Sec. 6.2 constrain possible spontaneous heating rates for a free gas of Rb atoms. In particular, many proposed classicalizing modifications to quantum mechanics predict such fundamental heating [103, 104]. Our results therefore restrict the parameter space of these theories. In the following sections, we first outline some similarities between a classical stochastic heating model and the heating that arises from the classicalizing modification to quantum mechanics presented in [103]. We then analyze the effect that this heating would have on the atom refocusing sequence and find that the refocusing data constrain the heating rate for ^{87}Rb to 20 ± 30 pK/s.

6.7.1 Heating from a classicalizing modification to quantum mechanics

In [103] and [124], the authors present a general classicalizing modification to quantum mechanics and show that it leads to fundamental heating. We summarize the relevant results here to motivate the form of the heating rate that we analyze in subsequent sections. A linear modification of the quantum Liouville equation is considered, such that

$$\frac{\partial\rho}{\partial t} = -\frac{i}{\hbar}[H, \rho] + \mathcal{L}\rho, \quad (6.150)$$

where ρ is the density matrix and \mathcal{L} is a Lindblad operator corresponding to the classicalizing modification. This causes off-diagonal terms in the density matrix to decay over time, such that the state evolves into a classical mixture. For the form of \mathcal{L} considered in [103], interference effects beyond a critical length scale \hbar/σ_q or a critical momentum scale \hbar/σ_s decay in a characteristic time τ .

The time evolution of the expectation value of an observable \hat{A} under the classicalizing modification is [124]

$$\partial_t \langle \hat{A} \rangle = \frac{i}{\hbar} \langle [\hat{H}, \hat{A}] \rangle + \langle \mathcal{L}^\dagger \hat{A} \rangle. \quad (6.151)$$

This corresponds to the Ehrenfest theorem, but with an additional term. For the form of \mathcal{L} considered in [103], the additional term affects the time evolution of expectation values of the position and momentum operators only at second order and above. Specifically, for the free space evolution and harmonic lens of the delta-kick cooling sequence, the time evolution of the relevant operators is [124]

$$\partial_t \langle \hat{\mathbf{r}} \rangle = \frac{\langle \hat{\mathbf{p}} \rangle}{m} \quad (6.152)$$

$$\partial_t \langle \hat{\mathbf{p}} \rangle = -m\omega^2 \langle \hat{\mathbf{r}} \rangle \quad (6.153)$$

$$\partial_t \langle \hat{\mathbf{r}}^2 \rangle = \frac{1}{m} (\langle \hat{\mathbf{p}} \cdot \hat{\mathbf{r}} + \hat{\mathbf{r}} \cdot \hat{\mathbf{p}} \rangle) + \frac{\sigma_s^2}{\tau} \quad (6.154)$$

$$\partial_t \langle \hat{\mathbf{p}} \cdot \hat{\mathbf{r}} \rangle = \partial_t \langle \hat{\mathbf{r}} \cdot \hat{\mathbf{p}} \rangle = \frac{1}{m} \langle \hat{\mathbf{p}}^2 \rangle - m\omega^2 \langle \hat{\mathbf{r}}^2 \rangle \quad (6.155)$$

$$\partial_t \langle \hat{\mathbf{p}}^2 \rangle = -m\omega^2 \langle \hat{\mathbf{p}} \cdot \hat{\mathbf{r}} + \hat{\mathbf{r}} \cdot \hat{\mathbf{p}} \rangle + \frac{\sigma_q^2}{\tau} \quad (6.156)$$

The terms with ω are nonzero only during the lens application time. The classicalizing modification causes deviation from the original equations of motion by introducing an additional diffusion in both momentum and position space, characterized by a constant heating rate $\frac{\sigma_q^2}{2m\tau}$ ($\frac{J}{s}$) and a spreading rate $\frac{\sigma_s^2}{\tau}$ ($\frac{m^2}{s}$).

6.7.2 Analogous classical model: Fokker-Planck equation with a stochastic force

In parallel to the results of Sec. 6.7.1, the classical Fokker-Planck model produces unmodified equations of motion for first moments of a phase space distribution, and an additional constant rate of increase in second moments. This model describes the altered evolution of an otherwise deterministic system due to stochastic white noise forces.

We work in terms of the one-dimensional variables x and v for a single particle's parameter space. Under the Fokker-Planck model, a set of generalized stochastic forces η_x and η_v continuously alter deterministic phase space trajectories via

$$\frac{d}{dt} \begin{bmatrix} x(t) \\ v(t) \end{bmatrix} = \begin{bmatrix} v(t) \\ -\frac{1}{m}\partial_x V \end{bmatrix} + \begin{bmatrix} \eta_x(t) \\ \eta_v(t) \end{bmatrix} \quad (6.157)$$

The curly bracket notation $\{g(\eta(t))\}$ will be used to define the noise-averaged value of a stochastic variable, where “stochastic variable” is defined as the variable $\eta(t)$ itself or any function g which depends on the stochastic term. The angle bracket notation retains its meaning as an expectation value over the phase space distribution.

As Gaussian white noise terms, the forces η have the following properties:

1. The distributions $\eta_x(t)$ and $\eta_v(t)$ at a given time t each have a mean value of zero: $\{\eta_v(t)\} = \{\eta_x(t)\} = 0$.
2. The distribution η_v is delta-correlated in time: $\{\eta_v(t_1)\eta_v(t_2)\} = D_v\delta(t_2 - t_1)$.
3. The distribution η_x is also delta-correlated: $\{\eta_x(t_1)\eta_x(t_2)\} = D_x\delta(t_2 - t_1)$.
4. The separate distributions are uncorrelated: $\{\eta_v(t_1)\eta_x(t_2)\} = 0$.

Here D_x and D_v are constants characterizing the strengths of the stochastic forces. Due to the stochastic forces, the first moments of a noise-averaged trajectory evolve according to the original equations of motion given by Hamilton's equations, and a modifying term is added to the time evolution of the second moments. Taking first the

phase-space ensemble average and next the noise average of Eq. 6.157 for a harmonic potential, and applying the noise-average properties of η :

$$\{\partial_t \langle x \rangle\} = \{\langle v \rangle\} \quad (6.158)$$

$$\{\partial_t \langle v \rangle\} = -\omega^2 \{\langle x \rangle\} \quad (6.159)$$

$$\{\partial_t \langle x^2 \rangle\} = 2 \{\langle x \cdot v \rangle\} + D_x \quad (6.160)$$

$$\{\partial_t \langle x \cdot v \rangle\} = \{\langle v^2 \rangle\} - \omega^2 \{\langle x^2 \rangle\} \quad (6.161)$$

$$\{\partial_t \langle v^2 \rangle\} = -2\omega^2 \{\langle x \cdot v \rangle\} + D_v \quad (6.162)$$

Again, the terms with ω are only nonzero during the lens application time. Eqs. 6.152 through 6.156 (for the effect of the Lindblad operator), and Eqs. 6.158 through 6.162 (for the classical Fokker-Planck model model of diffusion) therefore form an analogous set of differential equations for moments up to second order of a distribution. The connection is made concrete by setting $D_x = \frac{1}{3} \frac{\sigma_s^2}{\tau}$, and $D_v = \frac{1}{3} \frac{\sigma_g^2}{m^2 \tau}$ (the factor of 1/3 arises because we are now considering a 1D problem).

An expression can now be derived for final width of the cloud in terms of D_v and D_x by considering evolution of classical trajectories. Given a particular initial value of both Δx_o and Δv_o , we can compare the modeled minimized final width $(\Delta x_i)_{\min}$ under a perfect harmonic lens to the measured value. If the error between the two values is ascribed fully to the modifications introduced by stochastic diffusive terms, then a maximum heating rate is set.

6.7.3 Stochastic modifications of the trajectories

Terms that couple to η_v and η_x will be expressed in terms of their noise averages. The total change in the trajectory from its deterministic $(x(t), v(t))$ at a time t due to η_v is labeled $(\delta x_{\eta_v}(t), \delta v_{\eta_v}(t))$, and the change due to η_x is $\delta x_{\eta_x}(t)$. Due to the form of Hamilton's equations of motion, η_x does not directly couple to the variable $v(t)$. The

changes are given in integral form by

$$\delta v_{\eta_v}(t_1, t_2) = \int_{t_1}^{t_2} \eta_v(t') dt' \quad (6.163)$$

$$\delta x_{\eta_v}(t_1, t_2) = \int_{t_1}^{t_2} \int_{t_1}^{t'} \eta_v(t'') dt'' dt' \quad (6.164)$$

$$\delta x_{\eta_x}(t_1, t_2) = \int_{t_1}^{t_2} \eta_x(t') dt' \quad (6.165)$$

Using these definitions, the results of Table 6.1 follow from the fact that the stochastic force is independent of phase space trajectory. The results of Table 6.2 can be shown from repeated integration of Eq. 6.157.

Table 6.1: Stochastic variable correlations with initial distribution.

$\{\langle \delta x_{\eta_{v,x}}(t_1, t_2)x_o \rangle\} = 0$	$\{\langle \delta v_{\eta_v}(t_1, t_2)x_o \rangle\} = 0$
$\{\langle \delta x_{\eta_{v,x}}(t_1, t_2)v_o \rangle\} = 0$	$\{\langle \delta v_{\eta_v}(t_1, t_2)v_o \rangle\} = 0$

Table 6.2: Noise averages of stochastic variable correlations.

$\{\langle \delta v_{\eta_v}(t_1, t_2)\delta v_{\eta_v}(t_1, t_2) \rangle\} = D_v(t_2 - t_1)$	$\{\langle \delta x_{\eta_x}(t_1, t_2)\delta x_{\eta_x}(t_1, t_2) \rangle\} = D_x(t_2 - t_1)$
$\{\langle \delta x_{\eta_v}(t_1, t_2)\delta x_{\eta_v}(t_1, t_2) \rangle\} = \frac{1}{3}D_v(t_2 - t_1)^3$	$\{\langle \delta v_{\eta_v}(t_1, t_2)\delta x_{\eta_v}(t_1, t_2) \rangle\} = \frac{1}{2}D_v(t_2 - t_1)^2$

Table 6.2 lists results for fully overlapping time intervals; for nonoverlapping time intervals, the noise-average product of all stochastic terms in the table is zero.

6.7.4 Delta-kick sequence with stochastic modification

In the following sections, we assume $\langle v_o x_o \rangle = 0$ and that the lens provides a perfect harmonic potential.

Object to lens

Directly before the lens (ℓ^-) and immediately after (ℓ^+), the noise average position and velocity of a trajectory in phase space are

$$x_{\ell^-} = x_{\ell^+} = x_o + v_o t_o + \delta x_{\eta_v}(0, t_o) + \delta x_{\eta_x}(0, t_o) \quad (6.166)$$

$$v_{\ell^-} = v_o + \delta v_{\eta_v}(0, t_o) \quad (6.167)$$

$$v_{\ell^+} = v_o + \delta v_{\eta_v}(0, t_o) - \omega^2 \delta t x_{\ell^-} \quad (6.168)$$

It is assumed that the cooling rate during the lens application is much larger than the heating rate due to diffusion, $\langle v_{\ell^+}^2 \rangle - \langle v_{\ell^-}^2 \rangle \gg D_v \delta t$, so that the effect of the stochastic modification can be neglected during the time that the atom spends in the harmonic potential. The noise-averaged and ensemble-averaged position and velocity variance after the lens become

$$\{\langle \Delta x_{\ell^+}^2 \rangle\} = \Delta x_o^2 + \Delta v_o^2 t_o^2 + \frac{D_v t_o^3}{3} + D_x t_o \quad (6.169)$$

$$\{\langle \Delta v_{\ell^+}^2 \rangle\} = \Delta v_o^2 + D_v t_o - 2\omega^2 \delta t \left(\Delta v_o^2 t_o + \frac{D_v t_o^2}{2} \right) + \omega^4 \delta t^2 \left(\Delta v_o^2 t_o^2 + \Delta x_o^2 + \frac{D_v t_o^3}{3} + D_x t_o \right) \quad (6.170)$$

The results from Table 6.1 and Table 6.2 have been applied to eliminate or reduce relevant terms.

Lens to image

The single-particle position and velocities at the image are

$$v_i = v_{\ell^+} + \delta v_{\eta_v}(t_o, t_o + t_i) \quad (6.171)$$

$$x_i = t_i v_{\ell^+} + x_{\ell^+} + \delta x_{\eta_v}(t_o, t_o + t_i) + \delta x_{\eta_x}(t_o, t_o + t_i) \quad (6.172)$$

After neglecting terms with an average value of zero, the noise-averaged, ensemble-averaged position variance at the image takes the form

$$\{\langle \Delta x_i^2 \rangle\} = t_i^2 \{\langle \Delta v_{\ell^+}^2 \rangle\} + \{\langle \Delta x_{\ell^+}^2 \rangle\} + 2t_i \{\langle \Delta x_{\ell^+} \Delta v_{\ell^+} \rangle\} + \frac{D_v t_i^3}{3} + D_x t_i \quad (6.173)$$

Next, the expressions from Eqs. 6.169 and 6.170 are substituted into 6.173. The cross-correlation term between position and velocity directly after the lens takes the form

$$\{\langle \Delta x_{\ell+} \Delta v_{\ell+} \rangle\} = \Delta v_o^2 t_o + \frac{D_v t_o^2}{2} - \omega^2 \delta t \left(\Delta v_o^2 t_o^2 + \Delta x_o^2 + \frac{D_v t_o^3}{3} + D_x t_o \right). \quad (6.174)$$

Constraining the heating rate with refocusing data

Next, we assume that in an experiment, the lens application time will be chosen to minimize the final cloud width. This time is found symbolically as the solution to

$$\frac{\partial \{\langle \Delta x_i^2 \rangle\}}{\partial (\delta t)} = 0. \quad (6.175)$$

In an ideal deterministic case with an uncorrelated position-velocity distribution, the cloud size at the lens is $\Delta x_{\ell}^2 = \Delta x_o^2 + t_o^2 \Delta v_o^2$, and the minimum cloud width after refocusing is given by

$$(\Delta x_i)_{\min} = \frac{t_i^2 \Delta v_o^2 \Delta x_o^2}{\Delta x_{\ell}^2} \quad (6.176)$$

The minimized cloud size at the image plane using the expression for δt from Eqn. 6.175 becomes

$$(\Delta x_i)_{\min} = \frac{t_i^2 \Delta v_o^2 \Delta x_o^2 + a D_x + b D_v + c D_x D_v + d D_x^2 + e D_v^2}{\Delta x_{\ell}^2 + \frac{D_v t_o^3}{3} + D_x t_o} \quad (6.177)$$

where

$$\begin{aligned} a &= t_i \Delta x_\ell^2 \left(1 + \frac{t_i}{t_o} (1 - \gamma^2) \right) \\ b &= \frac{1}{3} t_i^2 t_o \Delta x_\ell^2 \left(1 + \frac{t_i}{t_o} + 2\gamma^2 \right) \\ c &= \frac{1}{3} t_i t_o (t_i^2 + 3t_i t_o + t_o^2) \\ d &= t_i t_o \\ e &= \frac{1}{36} t_i^2 t_o^3 (4t_i + 3t_o) \end{aligned} \quad (6.178)$$

Given experimentally measured distributions Δx_o^2 , and Δv_o^2 , and parameters t_o and t_i , there is in general a discrepancy between the ideal Δx_i^2 given in Eq. 6.176 for a lens application time that minimizes the width, and the experimentally measured final cloud width. Here we consider spontaneous heating attributed solely to D_v and set $D_x = 0$ (this is the case for spontaneous localization theories) [103]. In this case, the larger solution to the quadratic equation defined by Eq. 6.177 for D_v is given by $D_v = \frac{-B+\sqrt{B^2-4AC}}{2A}$, where

$$\begin{aligned} A &= t_i^2 t_o^3 (4t_i + 3t_o) \\ B &= 12 \left(t_i^3 \Delta x_\ell^2 \left(1 + \frac{t_o}{t_i} (1 + 2\gamma^2) \right) - t_o^3 (\Delta x_i)^2_{\min} \right) \\ C &= 36(t_i^2 \Delta v_o^2 \Delta x_o^2 - (\Delta x_i)^2_{\min} \Delta x_\ell^2) \end{aligned} \quad (6.179)$$

In the present experiment, the evolution times were $t_o = 1.1$ s and $t_i = 1.8$ s. The initial cloud effective temperature was 1.6 ± 0.1 nK (corresponding to $\Delta v_o = 0.39$ mm/sec). The initial cloud width is $\Delta x_o = 56 \mu\text{m}$ and the final refocused cloud width is $(\Delta x_i)_{\min} = 120 \pm 40 \mu\text{m}$. Based on these parameters, we set a bound on the spontaneous heating rate of $mD_v/k_B = 20 \pm 30$ pK/s. As discussed in [103], this limit on a fundamental heating rate can be compared to other experiments that test quantum mechanics in the macroscopic regime using the relation $D_v = \frac{1}{3} \frac{\sigma_q^2}{m^2 \tau}$. In general, atomic systems are able to place strong bounds on the model presented in

[103], because they can be probed at low energy scales. The momentum transfer unit σ_q is an undetermined parameter for this model, and various bounds can be evaluated for a range of possible values of σ_q . For σ_q between $\sim \hbar/(10 \mu\text{m})$ and $\sim \hbar/(1 \mu\text{m})$, the bound presented in this work is stronger than the other bounds calculated in [103] (the next strongest bound is from atom interferometry experiments). For σ_q below $\sim \hbar/(10 \mu\text{m})$, the atom interferometry bounds become the strongest [103]. If the momentum transfer unit σ_q becomes significantly larger than $\hbar/(1 \mu\text{m})$, an atom that receives a momentum kick will recoil at a velocity large enough to remove it from the atom cloud so that is not detected, while the remaining atoms are left unaffected. We therefore do not place strong bounds in this region of parameter space (naturally, we only can measure the heating of the atoms that are actually detected).

Chapter 7

Atom Interferometry at the Macroscale

The quantum superposition principle allows massive particles to be delocalized over distant positions. Though quantum mechanics has proven adept at describing the microscopic world, quantum superposition runs counter to intuitive conceptions of reality and locality when extended to the macroscopic scale [38], as exemplified by the thought experiment of Schrödinger's cat [125]. Matter wave interferometers [1], which split and recombine wave packets in order to observe interference, provide a way to probe the superposition principle on macroscopic scales [103] and explore the transition to classical physics [104]. In such experiments, large wave packet separation is impeded by the need for long interaction times and large momentum beam splitters, which cause susceptibility to dephasing and decoherence [38]. Here we use light-pulse atom interferometry [63, 5] to realize quantum interference with wave packets separated by up to 54 cm on the time scale of 1 s. These results push quantum superposition into a new macroscopic regime, demonstrating that quantum superposition remains possible at the distance and time scales of everyday life. The sub-nanokelvin temperatures of the atoms and a compensation of transverse optical forces enable a large separation while maintaining an interference contrast of 28%. In addition to testing the superposition principle in a new regime, large quantum superposition states are vital to exploring gravity with atom interferometers in greater detail. We

anticipate that these states could be used to increase sensitivity in tests of the equivalence principle [33, 34, 35, 36, 37], measure the gravitational Aharonov-Bohm effect [126], and eventually detect gravitational waves [39] and phase shifts associated with general relativity [37].

This chapter also appeared as Ref. [127] and was written with collaborators Peter Asenbaum, Chris Overstreet, Christine A. Donnelly, Susannah M. Dickerson, Alex Sugarbaker, Jason M. Hogan, and Mark A. Kasevich.

7.1 Overview

Progress in the ability to manipulate quantum systems has enabled experimental tests of the foundations of quantum mechanics. These include studies of entanglement [128], tests of local realism with Bell experiments [129, 130], and exploration of wave-particle duality in delayed choice experiments with photons [131] and atoms [132]. The quantum superposition principle is a central axiom of quantum mechanics, and efforts to test its universal validity have drawn much interest [38]. A breakdown of quantum superposition at large scales could arise from fundamental modifications to quantum dynamics [104, 103], interaction with a field of cosmological origin [104], or quantum gravitational effects [104, 38]. Currently, the best bounds on such decoherence mechanisms at large length scales come from matter wave interference experiments [103, 38]. No violations of the quantum superposition principle have yet been detected. To bound or discover such violations at macroscopic scales requires a well-controlled system that limits dephasing and decoherence from conventional and technical sources.

Atom interferometry offers a way to create and characterize atomic superpositions. The field of atom interferometry has developed as a long series of experiments originating from Bordé’s realization of the importance of recoil effects in precision Ramsey laser spectroscopy [133, 63], which led to the Bordé-Ramsey technique [133, 63]. Other important developments include the demonstration of atom interferometers using mechanical gratings [134] and two-photon transitions [5].

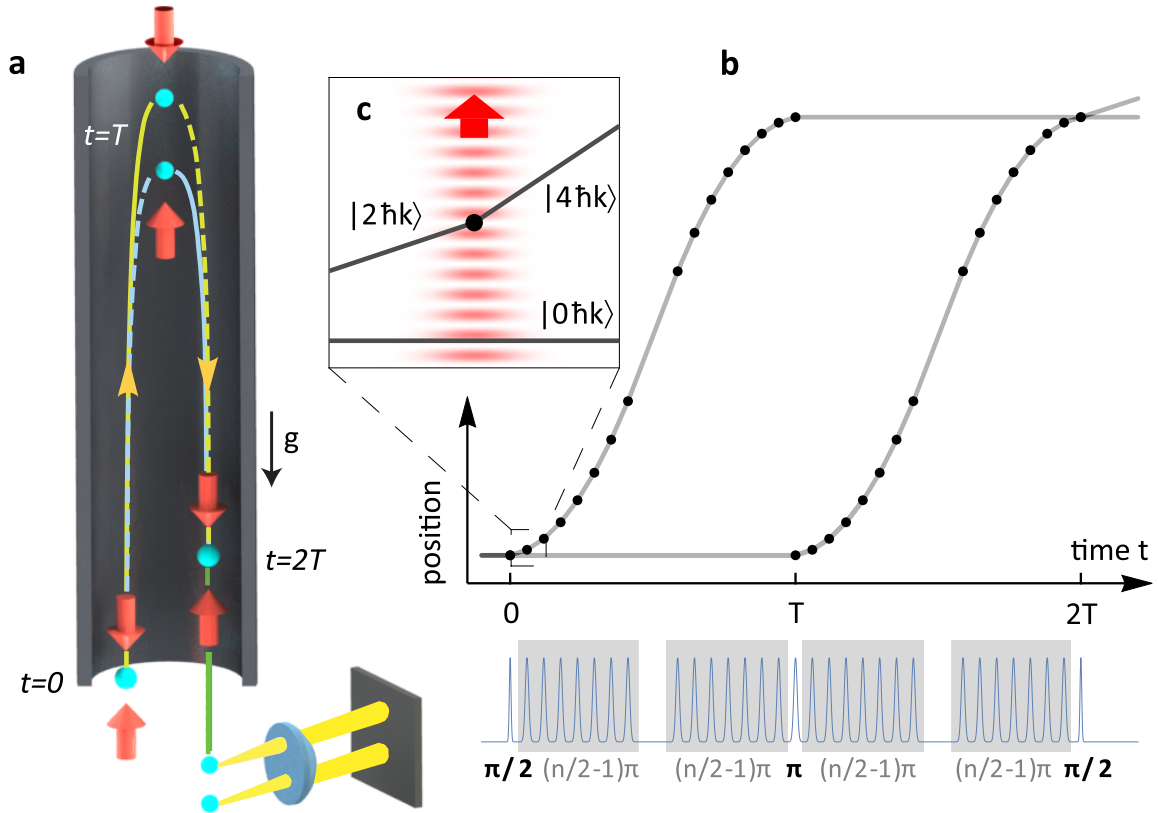


Figure 7.1: Fountain interferometer. **a**, After evaporative cooling and a magnetic lensing sequence (see Sec. 7.3), the ultra-cold atom cloud is launched vertically from below the cylindrical magnetic shield using an optical lattice. ($t = 0$) The first beam splitter sequence splits the cloud into a superposition of momentum states separated by $n\hbar k$. ($t = T$) The wave packet is fully separated, and a mirror sequence reverses the momentum states of the two halves of the cloud. ($t = 2T$) The clouds spatially overlap, and a final beam splitter sequence is applied. After a short drift time, the output ports spatially separate by 6 mm due to their differing momenta, and the two complementary ports are imaged. This diagram is not to scale, and the upward- and downward-going clouds are shown horizontally displaced for clarity. **b**, Pulse sequence of a $16\hbar k$ interferometer, see also Sec. 7.3. **c**, A moving standing wave induces a Bragg transition of one specific velocity class and changes its momentum by $2\hbar k$, e.g. from $2\hbar k$ to $4\hbar k$.

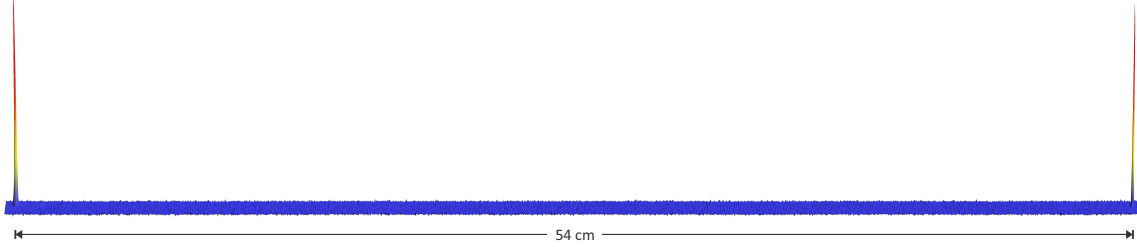


Figure 7.2: Wave packets separated by 54 cm. We adjust the launch height of the millimeter-sized atom cloud so that it passes the detector when the wave packets are maximally separated. In order to visualize the full extent of the wave function, we take 36 snapshots of different slices of the distribution. The images are taken at slightly different times between the atom launch and the fluorescence imaging and are stitched together according to the velocity of the atoms.

To create large atomic quantum superpositions, a significant challenge is to combine large momentum transfer (LMT) atomic beam splitters [17, 62] with long-time (>2 s) atom interferometry [29, 9]. Interferometers with LMT beam splitters are susceptible to dephasing from laser intensity inhomogeneity and wavefront perturbations across the atom cloud. These dephasing mechanisms are coupled to the transverse expansion of the atom cloud and are therefore exacerbated by long interferometer durations.

7.2 Experimental Results

We achieve long free fall times by launching a Bose-Einstein condensed cloud of $\sim 10^5$ ultracold ^{87}Rb atoms into a 10 m atomic fountain using a chirped optical lattice [29]. After the lattice launch, we use a sequence of optical pulses to apply a beam splitter that places each atom into a superposition of two wave packets with different momenta, corresponding to the two arms of a Mach-Zehnder interferometer [5]. We then allow the two wave packets to spatially separate vertically during a drift time $T = 1.04$ s. Subsequently, we redirect the two wave packets back toward each other with additional optical pulses (the mirror sequence) and interfere them with a final beam splitter when they once again spatially overlap after another $T = 1.04$ s drift

interval. Finally, we image the two interferometer output ports onto a CCD camera (see Fig. 7.1).

The maximum spatial separation reached in the interferometer is $\Delta z = n(\hbar k/m)T$, where k is the laser wave number, n is the number of photon recoils ($\hbar k$) transferred by the beam splitter, and m is the atomic mass ($\hbar k/m$ is the velocity associated with a single photon momentum recoil). Our LMT beam splitters transfer up to $90\hbar k$, yielding superpositions with much larger spatial separation than is possible with conventional $2\hbar k$ atom optics (54 cm for $90\hbar k$, as shown in Fig. 7.2). We realize the beam splitters with sequential $2\hbar k$ Bragg transitions [62] (see Sec. 7.3). The laser beams that drive the Bragg transitions are sent into the atomic fountain from the top and retroreflected by a mirror at the bottom.

To quantify the coherence of the macroscopic superposition states, we measure the contrast of the interferometer. To determine the contrast, we record the amount of variation in the normalized population in one of the output ports as it varies between constructive and destructive interference. The normalized population in output port i is $P_i \equiv N_i/(N_1 + N_2)$, where N_i is the measured atom number in output port i . Due to interference between the two arms of the interferometer, the population oscillates between the two output ports [29]. Example fluorescence images showing this population modulation are shown in Fig. 7.3.

Due to the large enclosed spacetime area $\Delta z T$, the interferometer is highly sensitive to acceleration. Specifically, the sensitivity of the interferometer phase ϕ to an acceleration a can be expressed as [5] $\Delta\phi = ma\Delta z T/\hbar$. This leads to an acceleration response for our interferometer of 2×10^8 rad/g for $2\hbar k$ beam splitters and 8×10^9 rad/g for $90\hbar k$ beam splitters (g is the acceleration due to gravity). Consequently, the interferometer phase fluctuates by much more than 2π from shot to shot due to vibration of the retroreflection mirror, causing the output ports to vary randomly between constructive and destructive interference. Therefore, we see significant contrast, but the large acceleration sensitivity prevents the observation of a stable fringe as the phase is scanned. Since the contrast quantifies the coherence of the macroscopic superposition states, the contrast is the relevant metric for this work (as in photon recoil measurements with contrast interferometry [140]). In many future

experiments to explore gravitational physics, differential measurement schemes [141] (e.g., gravity gradiometry) will be used to exploit the increased sensitivity offered by large superposition states while cancelling the vibration-induced phase noise as a common mode [37, 39, 126]. In the work presented here, common-mode cancellation of the vibration-induced phase noise between different parts of the atom cloud allows us to observe contrast and additionally to see spatial interference fringes across the atom cloud (see Fig. 7.5).

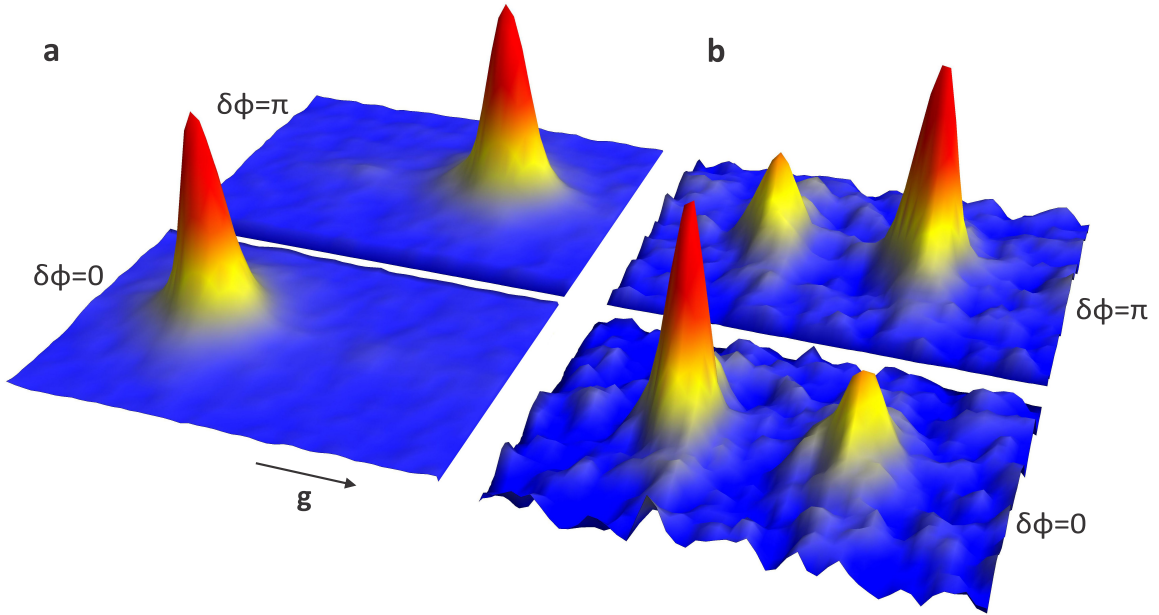


Figure 7.3: Fluorescence images of output ports. The two atom clouds resulting from the final beam splitter constitute the output ports of the interferometer. A single fluorescence image allows us to extract the atom number in each port. **a**, The $2\hbar k$ interferometer shows high contrast with nearly full population oscillation between the upper port (front image) and the lower port (back image). **b**, For the $90\hbar k$ interferometer the population oscillates by over 40%. Due to spontaneous emission and velocity selectivity, the detected atom number is more than ten times smaller than for $2\hbar k$. All displayed images are normalized to have the same peak height and are labeled with $\delta\phi$ corresponding to the interferometer phase modulo 2π . The image size is 13.8 x 9.7 mm, and the data is smoothed with a Gaussian filter with radius 0.5 mm.

To further demonstrate interference, we measure the contrast envelope, i.e. the

variation of P_1 as a function of a timing delay δT before the final beam recombining pulse sequence. At suitably large delays, contrast is suppressed, thus allowing characterization of technical noise sources which might be conflated with contrast at shorter delays. The timing asymmetry leads to a phase shift $nkv_z\delta T$ that depends on the vertical velocity v_z [29, 9]. Integrating over the vertical velocity distribution of the atom cloud after the interferometer (rms width Δv_z), the contrast is expected to decay with δT as [142] $\Gamma(\delta T) \equiv \exp[-n^2k^2\Delta v_z^2\delta T^2/2] = \exp[-\delta T^2/2\delta T_c^2]$ with the coherence time $\delta T_c \equiv 1/(nk\Delta v_z)$. Figure 7.4a displays the contrast envelopes and comparison to theory for $30\hbar k$, $60\hbar k$, and $90\hbar k$ beam splitters. We plot $\sigma(P_1)$, the standard deviation of the set of observed P_1 values after a sequence of 20 shots at the specified δT (see also Fig. 7.7). Note that $2\sqrt{2}\sigma(P_1)$ is approximately equal to the contrast [73]. The data closely match the expected decay dependence $\Gamma(\delta T)$ for the known values of n , k , and Δv_z . Given that the atom cloud has a known time $t_e = 2.6$ s to expand, the vertical size of the interferometer output ports provides us with an independent measurement of $\Delta v_z = 0.20 \pm 0.04$ mm s⁻¹. The measured coherence times, as determined by fits of the contrast envelope widths, show quantitative agreement with their theoretically predicted values (see Fig. 7.4a).

Figure 7.4b shows the interference contrast for various values of n . To determine the contrast value for a given n , we use maximum likelihood estimation on the data corresponding to the highest point in the contrast envelope (see Sec. 7.3). The model used to estimate the contrast corrects for the technical noise measured away from the contrast peak (i.e. at large δT). Also, Fig. 7.4b shows the exponential scaling of atom loss with n . Atom loss derives from two factors: spontaneous emission decay with $1/e$ point $n = 75 \pm 10$ and residual velocity selection of the π -pulses.

A complementary demonstration of interference is the observation of spatial interference fringes across the atom cloud for small time offsets δT [9, 41]. The predicted fringe wavelength is $\lambda_z = 2\pi t_e/(nk|\delta T - \delta T_0|)$, where t_e is the cloud expansion time and δT_0 accounts for velocity-dependent phase shifts from force gradients [41] (see Sec. 7.3). Figure 7.5a shows an unsmoothed example of the directly observed fringe from a single shot. The 1σ uncertainty in the phase extracted from fitting the fringe is 0.1 rad, which is near the atom shot noise limit for the observed contrast. For

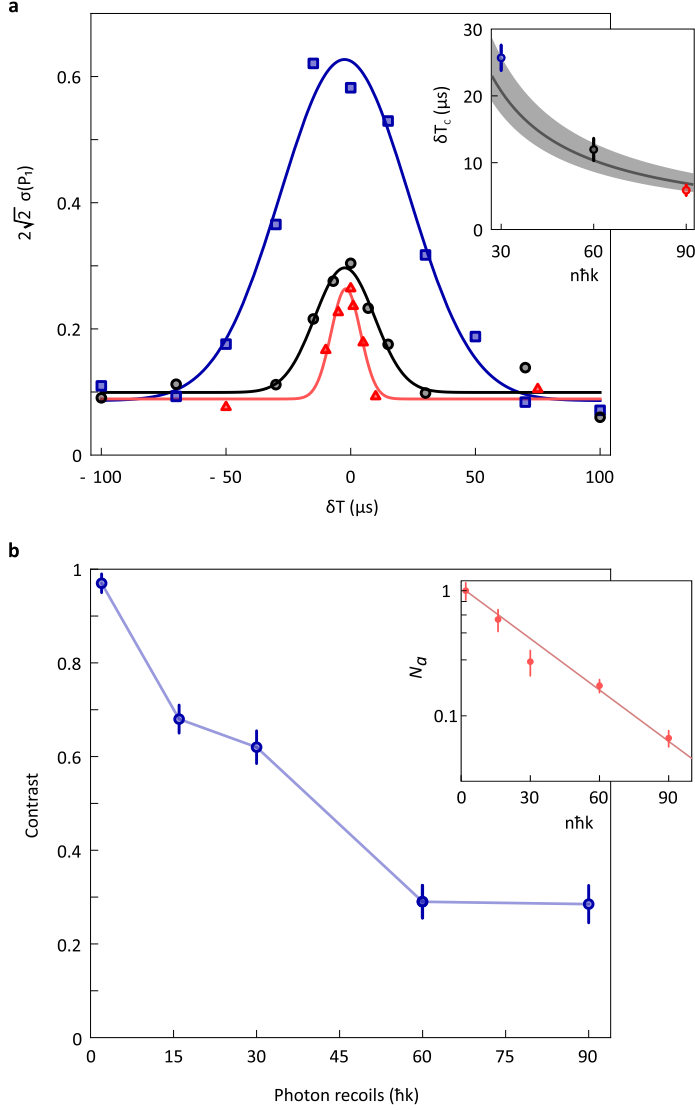


Figure 7.4: Contrast metrics. **a**, The contrast envelopes establish the interference effect. The data points corresponding to the blue squares, black circles, and red triangular marks are for $30\hbar k$, $60\hbar k$, and $90\hbar k$. The solid curves show the theory $A + B \Gamma(\delta T - \delta T_0)$, with coherence time δT_c , offset A , center δT_0 , and amplitude B as fitting parameters. Examples of the traces that lead to the points in the contrast envelopes are shown in Fig. 7.7. Inset: Comparison of fitted coherence times (points, 1σ error bars from fit uncertainty) to theory (gray curve). The gray, shaded region indicates 1σ theoretical uncertainty arising from uncertainty in the measured velocity spread Δv_z . **b**, Trends in maximum observed contrast (blue) and normalized atom number N_a in the output ports (red, inset) with $n\hbar k$. The data points are for $n = 2, 16, 30, 60$, and 90 . The atom number is normalized to the average number of atoms after a $2\hbar k$ interferometer. The thin, red curve shows the predicted atom number based on the measured spontaneous emission loss rate and π -pulse velocity selectivity. Error bars show 1σ uncertainties computed with the analysis discussed in Sec. 7.3.

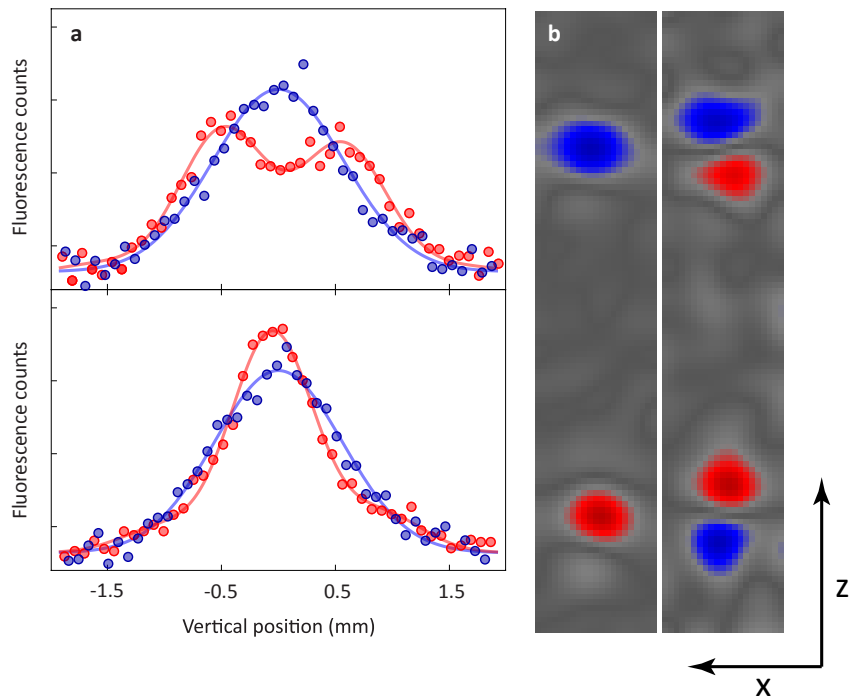


Figure 7.5: Spatial interference fringes. **a**, Horizontally integrated fluorescence images of the two $30\hbar k$ output ports (upper and lower panel) for a single run with $\delta T = -50 \mu\text{s}$ (red). The images are fit to a sinusoidally modulated Gaussian profile (red lines). The fringes across the cloud and their corresponding fits are a usable signal, while the scatter of points around the fits is from detection noise. For comparison, the output ports for $\delta T = 100 \mu\text{s}$ have a Gaussian profile without interference fringes (blue). **b**, Cosine and sine principal components of a set of $30\hbar k$ interferometer runs with $\delta T = -50 \mu\text{s}$, which show the effects of a vertical phase gradient across the cloud. All observed fringes are linear combinations of these basis images. Red and blue regions are anti-correlated.

$\delta T = -50 \mu\text{s}$ the fitted wavelength $\lambda_z = 1.5 \pm 0.1 \text{ mm}$ (1σ error from fit uncertainty) agrees with the theoretical value of $\lambda_z = 1.4 \text{ mm}$ (taking $\delta T_0 = 0$). Assuming a spherical Earth's gravity gradient would shift the prediction to $\lambda_z = 1.5 \text{ mm}$. This is equivalent to $\delta T_0 = -3.5 \mu\text{s}$, which is likely the reason why δT_0 is slightly negative for the contrast envelopes in Fig. 7.4a. While the overall position of the spatial fringes varies from shot to shot, the fringes on the two ports always have complementary phases, as expected. Using principal component analysis on a set of 20 images, we extract the two orthogonal modes describing the spatial fringe [29] (Fig. 7.5b).

Even for the 54 cm delocalization and a total of 180 applied optical Bragg pulses, we observe a contrast of 28%. We attribute the ability to maintain this level of contrast to two factors: the low temperature of the atoms and an absolute light shift compensation technique (see Sec. 7.3). The ultra-cold cloud remains smaller than 1 mm throughout the interferometer. This reduces the contrast loss due to larger scale inhomogeneities in laser intensity and wavefront (e.g., from the 2 cm laser radial waist). The small cloud also minimizes pollution of the output ports by non-interfering atoms originating from spontaneous emission and imperfect transfer efficiency. The importance of absolute light shift compensation is demonstrated by the fact that operating without compensation almost fully eliminates the contrast for a $30\hbar k$ interferometer (see Fig. 7.6). To improve the contrast further at large $n\hbar k$ likely requires reduction of wavefront perturbations, since these are intrinsically imprinted on the cloud at each pulse.

7.3 Methods

7.3.1 Atom source

A 2D magneto optical trap (MOT) loads a 3D MOT in the center of our 10 m vacuum tube for 4 s. We evaporate the ^{87}Rb atoms in a time-orbiting potential (TOP) trap for 14 s and apply a magnetic lensing sequence to further reduce their kinetic energy [102]. The ultra-cold atoms are then launched upwards into the interferometer region with a chirped optical lattice. Overall, we have a cycle time of roughly 22 s.

7.3.2 Atom optics

For the initial beam splitter, a $\pi/2$ -pulse splits the interferometer arms in momentum space by $2\hbar k$, followed by a sequence of $(n/2 - 1)$ π -pulses that selectively accelerate one of the arms to increase the momentum splitting to $n\hbar k$. The mirror sequence consists of $n - 1$ sequential π -pulses that interchange the momenta of the two interferometer arms [10, 62], and the final beam splitter sequence once again contains $(n/2 - 1)$ π -pulses applied to one arm followed by a $\pi/2$ -pulse.

Bragg transitions couple different momentum states of the hyperfine level $F = 2, m_F = 0$. In contrast to Raman transitions [5, 32], a Bragg scheme does not suffer from light-shift-induced variations of the hyperfine splitting between $F = 1$ and $F = 2$. The optical pulses that drive the Bragg transitions have Gaussian temporal profiles with full width at half maximum (FWHM) $60 \mu\text{s}$ for π -pulses and $30 \mu\text{s}$ for $\pi/2$ -pulses. Before the first beam splitter, the vertical velocity width is filtered by a $300 \mu\text{s}$ π -pulse that transfers only a narrow velocity slice. The two atom optics laser beams each contain 3 W of power 30 GHz detuned from the excited state resonance and are generated by frequency doubling the outputs of 1560 nm fiber amplifiers in nonlinear crystals [90]. These beams are combined on a polarizing beam splitter and enter the atomic fountain from the top. They have a radial waist of 2 cm and are retroreflected by a mirror at the bottom of the fountain. The mirror's angle is adjusted between pulse sequences by a piezo-actuated tip-tilt stage to compensate for Coriolis forces from Earth's rotation [29]. Given that the laser intensity is limited by the large beam waist, sequential $2\hbar k$ Bragg transitions offer lower spontaneous emission losses than higher order Bragg transitions [18].

7.3.3 Absolute light shift compensation

We implement a technique to compensate optical dipole forces on the atoms from imperfections in the laser beam profile. Dipole forces arise from gradients in the laser intensity, since the energy of an atomic state is shifted by an amount proportional to the local laser intensity (light shift) [1]. These forces can distort the cloud and cause large differential phase shifts across the cloud. The differential phase shifts

occur because the laser intensity profile varies with vertical position and is therefore not fully common to the two interferometer arms. To perform this compensation, we adjust the laser spectrum so that the absolute light shift from the blue-detuned spectral content, including the frequency components that drive the Bragg transitions, is cancelled by the absolute light shift from the red-detuned spectral content.

We achieve a light-shift-compensating spectrum by phase modulating each of the two atom optics lasers at 30 GHz, with the carrier 3.4 GHz blue-detuned from resonance and nearly fully suppressed. The two atom optics lasers are offset by an AOM shift of 160 MHz so that only one pair of sidebands drives Bragg transitions. The modulation occurs on the 1560 nm light seeding the fiber amplifiers. To tune the asymmetry between the red and blue sidebands, we adjust the temperature of the frequency doubling crystals. We measure the optical spectrum with a scanning Fabry-Perot cavity.

7.3.4 Contrast metrics data analysis

Following similar analysis from previous work [36], we model P_1 as a random variable. Our model for the probability density function (PDF) of P_1 includes additive Gaussian noise [36]. P_1 is related to the phase Φ and contrast c of the interferometer by

$$P_1(\Phi, X; c, w) = \frac{1}{2} + \frac{c}{2} \cos \Phi + X(w). \quad (7.1)$$

We assume that the interferometer phase is uniformly distributed, so the probability density function (PDF) of Φ is given by $f_\Phi(\phi) = \frac{1}{\pi}$ where $\phi \in [0, \pi]$, and that the amplitude noise X is normally distributed with standard deviation w , corresponding to a PDF

$$f_X(x; w) = \frac{1}{w\sqrt{2\pi}} e^{-x^2/2w^2}. \quad (7.2)$$

We also assume that Φ and X are independent, so the PDF of P_1 in the presence of noise X is equal to the convolution of the PDF of P_1 in the absence of noise ($w \rightarrow 0$)

with the PDF of X . In the absence of noise ($w \rightarrow 0$), the PDF of P_1 is given by

$$g_{P_1}(p; c) = \frac{2}{\pi} \frac{1}{\sqrt{c^2 - (2p - 1)^2}}. \quad (7.3)$$

This function is supported on $(\frac{1}{2} - \frac{c}{2}, \frac{1}{2} + \frac{c}{2})$ and has asymptotes at the boundaries. Therefore, the PDF of P_1 for nonzero w is the convolution

$$f_{P_1}(p; c, w) = \int_{1/2-c/2}^{1/2+c/2} g_{P_1}(\tau; c) f_X(p - \tau; w) d\tau. \quad (7.4)$$

Since the contrast approaches zero for large δT , all remaining fluctuations in P_1 at large δT are due to amplitude noise. Therefore, we estimate w by computing the standard deviation of data taken at large values of δT . For the data reported in this work, we typically find $w \approx 0.03 \pm 0.005$. To estimate c , we use maximum likelihood estimation [143] on the data set corresponding to the highest point in each contrast envelope, taking w to be a fixed parameter. The resulting contrast estimates are plotted in Fig. 7.4b. To calculate the uncertainty in the contrast estimates, we use the observed Fisher information for each data set [143]. We also propagate the uncertainty in the measured value of w .

Specifically, for a sequence of shots $\{p_1, \dots, p_m\}$ at fixed δT , we compute the likelihood

$$L(c; w, \{p_1, \dots, p_m\}) = \prod_{i=1}^m f_{P_1}(p_i; c, w) \quad (7.5)$$

taking the data points p_i and the measured value of w to be fixed parameters. The most likely value of c given the data is found by maximizing L as a function of c , or equivalently by solving

$$\frac{\partial}{\partial c} \ln L = 0 \implies \frac{\partial}{\partial c} \sum_{i=1}^m \ln f_{P_1}(p_i; c, w) = 0. \quad (7.6)$$

We maximize L numerically to generate the contrast estimates plotted in Fig. 4b. The standard error $\sigma_c(c)$ of the maximum likelihood method scales as the square root of the inverse of the Fisher information in the limit of a large number of samples m .

The Fisher information $F(c)$ is defined by

$$F(c) = \int \left(\frac{\partial}{\partial c} \ln f_{P_1}(p; c, w) \right)^2 f_{P_1}(p; c, w) dp. \quad (7.7)$$

In the asymptotic limit $m \rightarrow \infty$, we have

$$\sigma_c(c) = \frac{1}{\sqrt{m}} \frac{1}{\sqrt{F(c)}}. \quad (7.8)$$

For $m \geq 20$, the error in the asymptotic approximation does not significantly contribute to the uncertainty. We verify this by computing the observed Fisher information F_o for each data set, where

$$F_o(c; w, \{p_1, \dots, p_m\}) = -\frac{1}{m} \frac{\partial^2}{\partial c^2} \sum_{i=1}^m \ln f_{P_1}(p_i; c, w). \quad (7.9)$$

Error bars for the atom number in Fig. 7.4b are computed from statistical standard deviation. The curve showing the predicted atom number in Fig. 7.4b accounts for atom loss due to spontaneous emission and imperfect π -pulse transfer efficiency. We measure the spontaneous emission loss rate by illuminating the launched cloud with a detuned interferometer pulse sequence. Specifically, all pulses are detuned from their respective two-photon resonances so that there is no transfer. Therefore, the ratio of the number of atoms remaining after such a pulse sequence to the number of atoms remaining after a launch with no pulses allows us to determine the fraction of the atoms lost due to spontaneous emission. To measure the π -pulse transfer efficiency, we apply a $\pi/2$ -pulse followed by 44 π -pulses and compare the number of atoms in the transferred peak ($90\hbar k$ total momentum kick) to the number of atoms in the peak that is left untransferred by the $\pi/2$ -pulse. Spontaneous emission loss is the same for both peaks and therefore does not confound the measurement. We note that the two peaks have the same height, while the transferred peak has a narrower vertical width (e.g., see Fig. 7.2). This indicates that the imperfect transfer efficiency arises from π -pulse velocity selectivity.

7.3.5 Spatial interference fringes

Due to the long expansion time t_e , the launched atom cloud is effectively a point source, meaning that by the time of detection the vertical velocity distribution has been mapped onto the vertical position z through the relation $z \approx v_z t_e$. The velocity dependent phase shift $nkv_z\delta T$ then leads to a position dependent phase shift [41] with corresponding wavelength $\lambda_z = 2\pi t_e/(nk|\delta T - \delta T_0|)$. Here δT_0 accounts for any velocity-dependent phase shifts from force gradients [41]. To observe the fringes, we reduce the fluorescence imaging time to 2.5 ms (see Fig. 7.5). We choose $\delta T = -50 \mu\text{s}$ so that a full wavelength is visible on the atom cloud. For $\delta T = 100 \mu\text{s}$ the smaller fringe period is completely blurred out by imaging heating of the atom cloud. The direct spatial interference contrast for $\delta T = -50 \mu\text{s}$ is lower than the contrast with $\delta T = 0$ reported in Fig. 7.4b due to this blurring.

We use principal component analysis (PCA) to extract spatial fringes from a set of 20 interferometer runs. In addition to the fringe pattern, PCA is sensitive to shot-to-shot variation of the center of mass position of the cloud. To minimize crosstalk between these effects, we correct for the vertical and horizontal motion prior to performing PCA. We find the position of the cloud center of mass for each shot using Gaussian fits and then shift each image appropriately to remove the motion. The data is also smoothed with a $400 \mu\text{m}$ Gaussian filter prior to PCA. We identify the first principal component as the shape of the overall cloud envelope. Principal components two and three correspond to the cosine and sine components of the fringe pattern (Fig. 7.5).

7.4 Outlook

We probe the quantum superposition principle in an unprecedented regime. Table 7.1 compares the wave packet separation, duration, and mass of our superposition states to those of other matter wave interferometers, showing that we occupy a new region of large wave packet separation and long time. In addition, these large superposition

states pave the way for a new generation of fundamental physics tests using ultra-sensitive atom interferometers [37, 39, 126]. The wave packet delocalization and coherence time demonstrated here already meet the requirements for certain proposed atomic gravitational wave detectors [39]. The demonstrated enclosed space-time area combined with optical atomic clock states could also enable the study of decoherence induced by general relativistic proper time [144].

Description	Wave packet separation Δz (m)	Duration T (s)	Mass m (amu)	Acceleration sensitivity factor $m\Delta z T/\hbar$ (m/s^2) $^{-1}$
This work, Rb, 90 $\hbar k$	0.54	1.04	86.9	8×10^8
Cs, 2012	9×10^{-3}	0.25	132.9	5×10^6
Cs, 2009	3×10^{-3}	0.4	132.9	3×10^6
Rb, 2013	4×10^{-3}	0.35	86.9	2×10^6
Cs, 2001	1.1×10^{-3}	0.16	132.9	4×10^5
Na, 1992	3×10^{-3}	0.05	23	5×10^4
$\text{C}_{284}\text{H}_{190}\text{F}_{320}\text{N}_4\text{S}_{12}$, 2013	$\sim 3 \times 10^{-7}$	1.2×10^{-3}	10123	60
Neutrons, 2002	0.07	4×10^{-5}	1.01	40
C_{70} , 2002	$\sim 10^{-6}$	1.9×10^{-3}	840	30

Table 7.1: Comparison of superposition parameters to other matter wave interference experiments. We compare the wave packet separation Δz , the duration T between the beam splitter and mirror sequences, and the mass m to those of a sodium interferometer from 1992 [135], a cesium interferometer from 2001 [13], a neutron interferometer from 2002 [136], a C_{70} molecular interferometer from 2002 [137], a cesium interferometer from 2009 [138], a cesium interferometer from 2012 [88], a $\text{C}_{284}\text{H}_{190}\text{F}_{320}\text{N}_4\text{S}_{12}$ molecular interferometer from 2013 [139], and a rubidium interferometer from 2013 [9]. Additionally, we compare the factor $m\Delta z T/\hbar$, which is directly related to the acceleration sensitivity (see the discussion of acceleration sensitivity in Sec. 7.2). The wave packet separation in our experiment is nearly an order of magnitude larger than the next largest value (from a neutron interferometer), and the duration in our experiment is more than four orders of magnitude longer than in the neutron interferometer with a nearly hundred times larger mass.

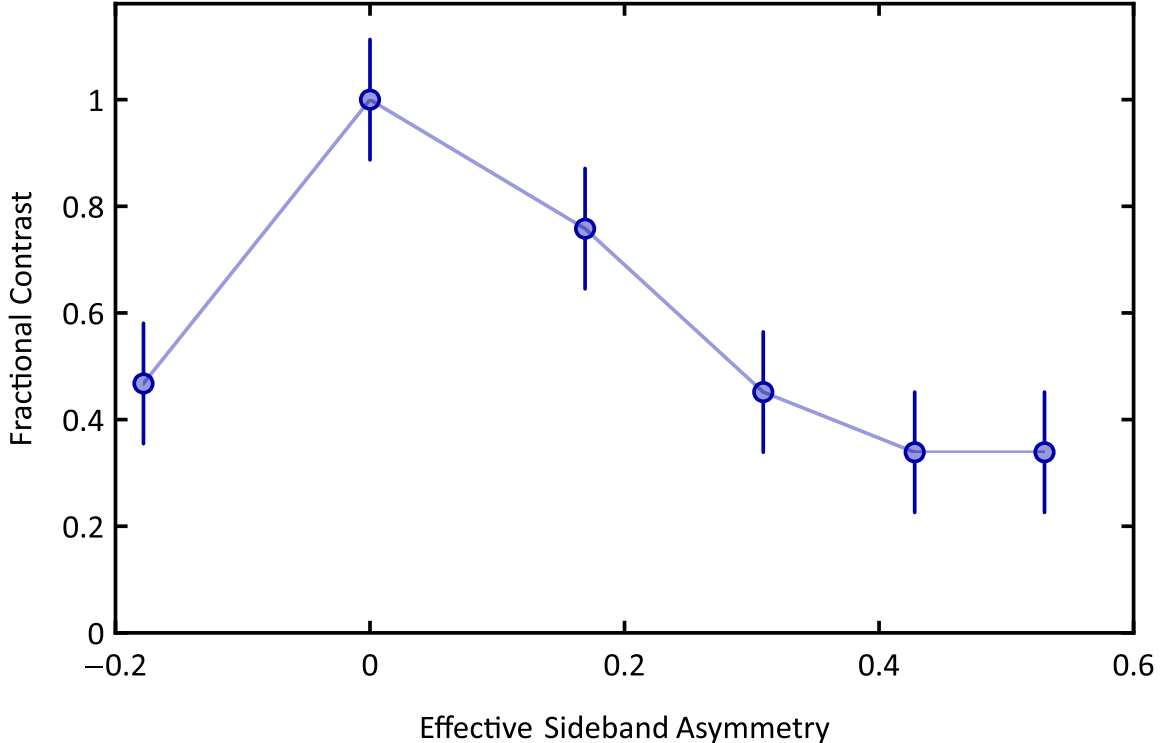


Figure 7.6: Dependence of contrast on absolute light shift compensation. For $30\hbar k$, the contrast as a fraction of its maximum value is plotted as a function of the asymmetry between the red and blue sidebands for one of the atom optics laser beams. To change the sideband asymmetry, we adjust the temperature of one of the frequency doubling crystals while keeping the sidebands of the second atom optics laser beam symmetric. Where P_{red} and P_{blue} are the respective optical powers in the red and blue sidebands, we define an asymmetry parameter $1 - (P_{\text{red}}/P_{\text{blue}})$. Since the blue sideband is used to drive the Bragg transitions, we keep P_{blue} fixed in order to maintain constant Rabi frequency. This prevents us from reaching large negative values of the asymmetry parameter, because there is only enough total optical power available to increase P_{red} slightly without suppressing P_{blue} . In order to achieve a more negative effective value of the asymmetry parameter, we suppress the power in the carrier to half its usual amount for the one negative point in the plot. The carrier is blue detuned, so decreasing its power pulls the absolute light shift in the same direction as decreasing P_{blue} . To account for this, we plot the fractional contrast versus the effective asymmetry parameter that would yield the same light shift as the one that we implement, but at a fixed carrier power. The observed dependence of contrast on the sideband asymmetry indicates the importance of absolute light shift compensation for LMT interferometry. Error bars show 1σ uncertainty.

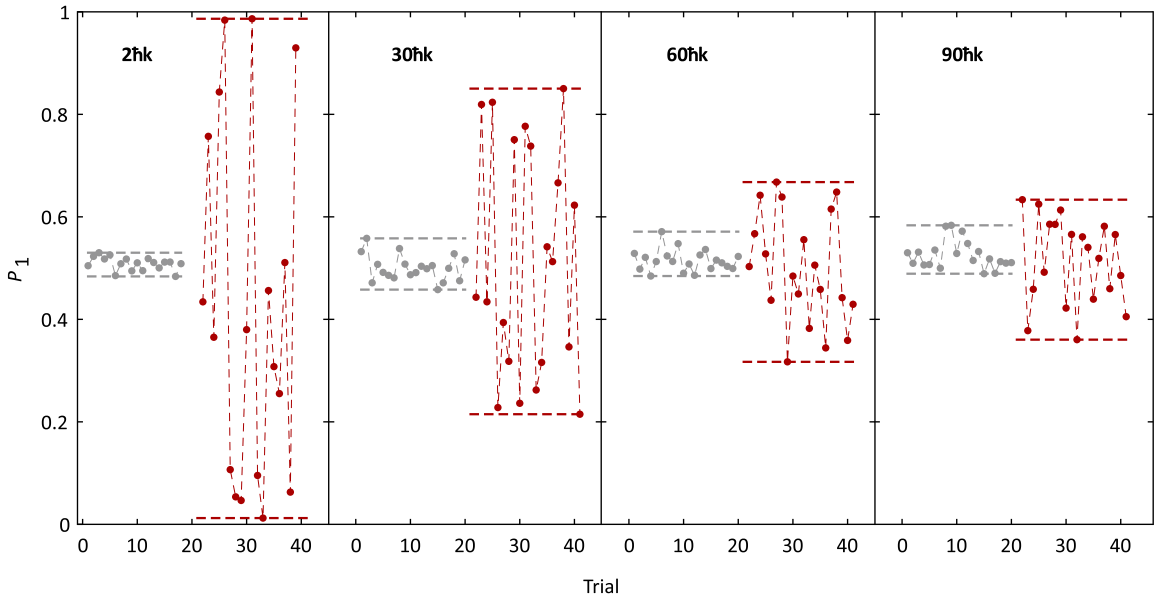


Figure 7.7: Examples of data showing interference contrast. Plots of P_1 versus experimental trial for $2\hbar k$, $30\hbar k$, $60\hbar k$, and $90\hbar k$. The red traces have small values of δT and therefore display interference contrast. As discussed in the Sec. 7.2, we do not observe a stable fringe because of the vibration of the retroreflection mirror. For comparison, the gray traces have large values of δT so that contrast is eliminated, and they therefore show the amount of background amplitude noise in P_1 . **2 $\hbar k$** , Red trace: $\delta T = 0 \mu s$. Gray trace: $\delta T = 2 ms$. **30 $\hbar k$** , Red trace: $\delta T = -15 \mu s$. Gray trace: $\delta T = 100 \mu s$. **60 $\hbar k$** , Red trace: $\delta T = 0 \mu s$. Gray trace: $\delta T = 100 \mu s$. **90 $\hbar k$** , Red trace: $\delta T = 1 \mu s$. Gray trace: $\delta T = -50 \mu s$.

Chapter 8

Theory of Atom Optics with Optical Lattices

We provide an analytical description of the dynamics of an atom in an optical lattice using the method of perturbative adiabatic expansion. A precise understanding of the lattice-atom interaction is essential to taking full advantage of the promising applications that optical lattices offer in the field of atom interferometry. One such application is the implementation of Large Momentum Transfer (LMT) beam splitters that can potentially provide multiple order of magnitude increases in momentum space separations over current technology. We also propose interferometer geometries where optical lattices are used as waveguides for the atoms throughout the duration of the interferometer sequence. Such a technique could simultaneously provide a multiple order of magnitude increase in sensitivity and a multiple order of magnitude decrease in interferometer size for many applications as compared to current state-of-the-art atom interferometers.

This chapter also appeared as Ref. [64] and was written with collaborators Jason M. Hogan, David M. S. Johnson, and Mark A. Kasevich.

8.1 Overview

As discussed in Sec. 1.2.2, adiabatically accelerating atoms in an optical lattice is an example of an adiabatic rapid passage method for LMT atom optics. As such, the transfer efficiency of optical lattice manipulations of the atoms is highly robust against Rabi frequency and detuning inhomogeneities. The excellent transfer efficiency of lattice-based atom optics is illustrated by the fact that the lattice launch for the 10 m atomic fountain transfers momentum $\sim 2000\hbar k$ to the atoms with $\sim 30\%$ overall efficiency [12].

The utility of atom interferometry for precision measurements hinges upon the ability to precisely calculate the phase accumulated along the different arms of an interferometer [145, 120, 146], of which the phase acquired during interactions of the atoms with light is an important component. Indeed, the phase obtained by an atom during a Raman or Bragg pulse is well-understood [8, 16, 147, 148]. Analogously, in order to take full advantage of the potential of lattice beam splitters, we must have a detailed understanding of the phase evolution of an atom in an optical lattice. In this chapter, we provide a rigorous analytical treatment of this problem. To our knowledge, such a treatment has not been previously presented in the literature.

Based on this analysis, we propose atom interferometer geometries in which optical lattices are used to continuously guide the atoms, so that the atomic trajectories are precisely controlled for the duration of the interferometer sequence, with a different lattice guiding each arm of the interferometer. We point out here a distinction in terminology between a lattice waveguide and a lattice beam splitter. Here, a lattice waveguide is the use of a lattice to continuously control the trajectory of an arm of an atom interferometer. We note that two different lattice waveguides can independently control the two arms of an interferometer, or a single lattice waveguide can simultaneously control both arms. In contrast, a lattice beam splitter is an interaction of relatively short time (in comparison to a waveguide) with the primary purpose of splitting the arms of the interferometer in momentum space rather than providing continuous trajectory control. The underlying physics behind lattice waveguides and lattice beam splitters is the same, and they can be treated with a common formalism.

A single lattice waveguide that simultaneously transfers $1600\hbar k$ of momentum to the two arms of a Ramsey-Bordé interferometer has been previously achieved in [149]. However, to our knowledge, our idea of using optical lattice waveguides to create a fully confined atom interferometer has not been previously considered.

Our analysis indicates that these lattice interferometers will offer unprecedented sensitivities for a wide variety of applications and that they will be able to operate effectively over distance scales previously considered too small to be studied by precision atom interferometry. For example, one particularly interesting configuration involves using two optical lattice waveguides to continuously pull the two arms of the interferometer apart, subsequently holding the two arms a fixed distance from each other in a single lattice waveguide that is common to the two arms, and then using two lattice waveguides to recombine the arms. Such a configuration could be used, for instance, as a gravimeter. The sensitivity of lattice interferometers is illustrated by the fact that, given the experimental parameters stated in [8] (10^7 atoms/shot and 10^{-1} shots/s), a shot noise limited lattice gravimeter whose arms are separated by 1 m for an interrogation time of 10 s has a sensitivity of $10^{-14} \text{ g/Hz}^{1/2}$ (this corresponds to a measurement resolution of 10^{-14} g after 10 s, where 10 s is the duration of a single measurement cycle). We perform phase shift calculations for these lattice interferometers using the theoretical groundwork formulated in this chapter, and we discuss how lattice interferometers can both exceed the performance of conventional atom interferometers in many standard applications and expand the types of measurements that can effectively be carried out using atom interferometry.

This chapter is organized as follows. Section 8.2 describes the Hamiltonian for an atom in an optical lattice in the different frames we use in the chapter. Section 8.3 discusses the phase evolution of an atom in an optical lattice under the adiabatic approximation. Section 8.4 introduces the formalism of perturbative adiabatic expansion to calculate corrections to the adiabatic approximation, and Sec. 8.5 applies this formalism to calculate phase corrections to a lattice beam splitter. Section 8.6 proposes a number of interferometer geometries that make use of lattice manipulations of the atoms. The main results of the chapter are Eqs. (8.25) and (8.26), which show how to obtain analytical corrections to the lowest order phase shift estimates.

These corrections are surprisingly large, and understanding them is vital to realizing the full accuracy of the sensor geometries proposed in Sec. 8.6, as well as other geometries utilizing optical lattice manipulations of the atoms. For example, the gravitational wave detector proposed in [39] may make use of lattice beam splitters and/or waveguides. Previously, the phase evolution induced by lattice manipulations was not sufficiently well-understood to allow for a detailed design of the atom optics system or an estimation of the corresponding systematic effects.

8.2 The Hamiltonian in Different Frames

An optical lattice is a periodic potential formed by the superposition of two counter-propagating laser beams. Atoms can be loaded into the ground state of the lattice by ramping up the lattice depth adiabatically, and the lattice can then be used to impart momentum to the atoms and/or to control the atoms' trajectories. Optical lattices are thus a useful tool for atom optics.

We begin our discussion of the lattice-atom interaction by finding a useful form for the Hamiltonian. As is typical for many applications of atom interferometry, to minimize decoherence we assume that we work with atomic gases dilute enough so that the effects of atom-atom interactions are negligible. We first consider the Hamiltonian in the lab frame, where for now we assume a vertical configuration with constant gravitational acceleration g so that we have a gravitational potential given by mgx . We expose the atom to a superposition of an upward propagating beam with phase $\phi_{\text{up}}(t)$ and a downward propagating beam with phase $\phi_{\text{down}}(t)$, which couples an internal ground state $|g\rangle$ to an internal excited state $|e\rangle$. The two-photon Rabi frequency is $\Omega(t) \equiv \frac{\Omega_{\text{up}}(t)\Omega_{\text{down}}(t)}{2\Delta}$, where we let $\Omega_{\text{up}}(t)$ denote the single-photon Rabi frequency of the upward propagating beam, $\Omega_{\text{down}}(t)$ denote the single-photon Rabi frequency of the downward propagating beam, and Δ denote the detuning from the excited state. We depict the physical setup in Fig. 8.1. Making the rotating wave approximation and adiabatically eliminating the excited state as is standard procedure [4], we obtain the following Hamiltonian, where the periodic term in the potential arises from a spatially varying ac Stark shift and where k is the magnitude

of the wave vector of the laser beams [150, 27]:

$$\hat{H}_{\text{Lab}} = \frac{\hat{p}^2}{2m} + 2\hbar\Omega(t) \sin^2 \left[k\hat{x} - \frac{1}{2}(\phi_{\text{up}}(t) - \phi_{\text{down}}(t)) \right] + mg\hat{x} \quad (8.1)$$

Note that where the difference between the frequency of the upward propagating beam and the frequency of the downward propagating beam is denoted by $\Delta\omega(t)$, we will have the relation $\Delta\phi(t) \equiv \phi_{\text{up}}(t) - \phi_{\text{down}}(t) = \int_0^t \Delta\omega(t') dt' + \phi_{\text{up}}(0) - \phi_{\text{down}}(0)$. For a given $\Delta\phi(t)$, the lattice standing wave will be translated by $D_{\text{Lab}}(t) \equiv \frac{\Delta\phi(t)}{2k}$ in the x direction from the origin. Thus, the velocity of the lattice in the lab frame is:

$$v_{\text{Lab}}(t) = \frac{d}{dt} D_{\text{Lab}}(t) = \frac{\Delta\omega(t)}{2k} \quad (8.2)$$

and we rewrite the lab frame Hamiltonian as:

$$\hat{H}_{\text{Lab}} = \frac{\hat{p}^2}{2m} + 2\hbar\Omega(t) \sin^2 [k\hat{x} - kD_{\text{Lab}}(t)] + mg\hat{x} \quad (8.3)$$

In order to most readily describe the dynamics of an atom in an accelerating optical lattice, it is useful to work in momentum space. The $mg\hat{x}$ term that appears in the lab frame Hamiltonian makes such an approach difficult, especially when considering non-adiabatic corrections to the phase shift. However, we can change frames by performing a unitary transformation in order to obtain a Hamiltonian that is easier to handle analytically. In the end, we will see that approaching the problem from the point of view of dressed states provides a convenient Hamiltonian for our purposes. We consider the transformation procedure from the lab frame to the dressed state frame in Sec. 8.8, where we also introduce an intermediate frame that freely falls with gravity (which we call the freely falling frame). We note that the general form of the unitary transformations considered in Sec. 8.8 as well as the specific transformations to the different frames we consider can also be found in the Appendix of [27].

It is convenient to absorb the initial velocity v_0 of the atom in the lab frame into the dressed state frame, so that velocity v_0 in the lab frame corresponds to velocity zero in the dressed state frame. The Hamiltonian in the dressed state frame is, as derived in Sec. 8.8:

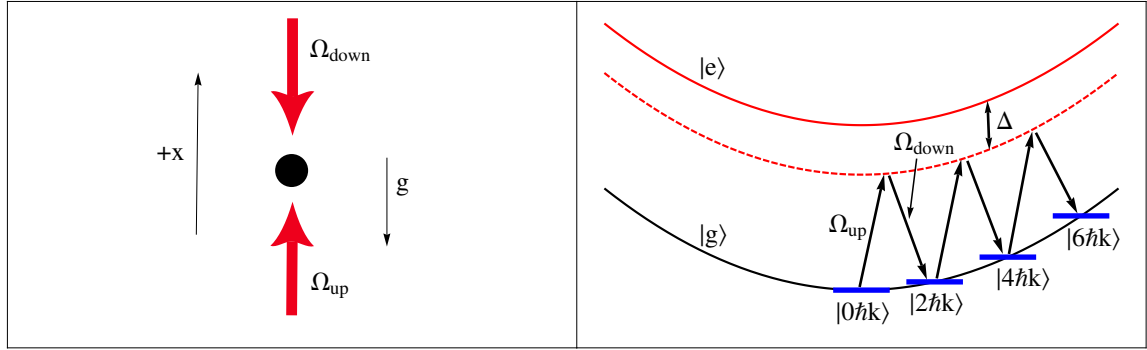


Figure 8.1: The physical setup for applying a periodic potential. We expose atoms to counter-propagating laser beams with respective single-photon Rabi frequencies Ω_{up} and Ω_{down} . The lasers are detuned from the transition between the atom's internal ground state and excited state so that the atom's external momentum states are coupled through two-photon transitions, creating an effective lattice potential.

$$\hat{H}_{\text{DS}} = \frac{\hat{p}^2}{2m} - (v_{\text{Lab}}(t) + gt - v_0)\hat{p} + 2\hbar\Omega(t) \sin^2(k\hat{x}) \quad (8.4)$$

The ability to boost to a frame in which the Hamiltonian contains no position dependent terms outside of the lattice potential is contingent upon the assumption that the external potential in the lab frame (not including the lattice potential) is linear in x . However, real-world potentials such as the potential corresponding to Earth's gravitational field will deviate somewhat from this assumption. Any such deviations would manifest as residual position dependent terms in the dressed state Hamiltonian, which we collectively refer to as V' . Under the semiclassical approximation, we neglect the effects of V' on the time evolution of the atomic wavepacket. This approximation is valid when the energy scale of V' over the spread of the atom's wavefunction (which is on the order of magnitude of the expectation value of V' in the atomic wavepacket) is much smaller than the energy scale of the lattice potential and is small relative to the time scale of the experiment, which is the case for a wide class of experimental parameters. For example, in the case of a Rubidium atom wavepacket with a spatial spread of $\sigma \sim 100\mu\text{m}$ in the gravitational field at the Earth's surface (which has a gradient of $\lambda \sim 10^{-6}\text{ s}^{-2}$), the energy scale of V' will be $\sim \frac{1}{2}m\lambda\sigma^2 \sim h \times (10^{-6}\text{ Hz})$. This energy scale is smaller than that of a lattice of typical experimental depth (\sim

$5E_r$, where E_r is the recoil energy $\frac{\hbar^2 k^2}{2m}$) by a factor of $\sim 10^{10}$ and is small on a time scale of ~ 10 s. The effects of linear gradients and of more general potentials can be accounted for through a straightforward generalization of the results presented in this chapter, as discussed in greater depth in [151].

Now, we will show how working in momentum space allows us to represent \hat{H}_{DS} as an infinite dimensional, discrete matrix. This matrix is discrete because the optical lattice potential term, $V_0 \sin^2(k\hat{x})$, only couples a momentum eigenstate $|p\rangle$ to the eigenstates $|p + 2\hbar k\rangle$ and $|p - 2\hbar k\rangle$ [27]. For the moment, we will examine the evolution of individual eigenstates of the dressed state Hamiltonian \hat{H}_{DS} . These eigenstates reduce to single momentum eigenstates $|p\rangle$ when $\Omega = 0$. The knowledge of how each of these eigenstates evolves under \hat{H}_{DS} will allow us to describe the dynamics of an entire wavepacket. For the moment, we will only consider momentum eigenstates corresponding to an integer multiple of $2\hbar k$, since we have boosted away the initial velocity v_0 of the atom in the lab frame. We note that it is always possible to transform to a particular dressed state frame in which a given momentum eigenstate in the lab frame corresponds to zero momentum in that dressed state frame. The results we derive here can thus be readily generalized to arbitrary momentum eigenstates in a wavepacket, as we discuss in greater detail in Sec. 8.9.

We consider a discrete Hilbert space spanned by the momentum eigenstates $|2n\hbar k\rangle$ for integers n , so that we can express any vector in this Hilbert space as:

$$|\Psi(t)\rangle = \sum_{n=-\infty}^{\infty} c_n(t) |2n\hbar k\rangle \quad (8.5)$$

Since this Hilbert space is discrete, it is natural to adopt the normalization convention that $\langle 2m\hbar k | 2n\hbar k \rangle = \delta_{mn}$. When considered as an operator acting on this discrete Hilbert space, \hat{H}_{DS} can be written as [16, 152]:

$$\begin{aligned}\hat{H}_{\text{DS}}^{\text{discrete}} &= \sum_{n=-\infty}^{\infty} \frac{(2n\hbar k)^2}{2m} |2n\hbar k\rangle \langle 2n\hbar k| - \sum_{n=-\infty}^{\infty} (v_{\text{Lab}}(t) + gt - v_0)(2n\hbar k) |2n\hbar k\rangle \langle 2n\hbar k| \\ &\quad - \sum_{n=-\infty}^{\infty} \hbar \frac{\Omega(t)}{2} (|2n\hbar k\rangle \langle 2(n-1)\hbar k| + |2n\hbar k\rangle \langle 2(n+1)\hbar k|)\end{aligned}\tag{8.6}$$

where we drop the common light shift. Now, it is convenient to introduce the recoil frequency $\omega_r \equiv \frac{E_r}{\hbar} = \frac{\hbar k^2}{2m}$ and the recoil velocity $v_r \equiv \frac{\hbar k}{m}$. In order to make our notation as compact as possible, we will be interested in the quantity $\alpha(t) \equiv \frac{v_{\text{Lab}}(t) + gt - v_0}{v_r}$, which is the velocity of the lattice in the dressed state frame in units of v_r . We can express the second term of $\hat{H}_{\text{DS}}^{\text{discrete}}$ in a useful way by noting that $(v_{\text{Lab}}(t) + gt - v_0)2n\hbar k = 4n\alpha(t)E_r$. Furthermore, we define $\tilde{\Omega}(t) \equiv \frac{\Omega(t)}{8\omega_r}$. We can now write the discrete Hamiltonian in a simplified form:

$$\begin{aligned}\hat{H}_{\text{DS}}^{\text{discrete}} &= 4E_r \sum_{n=-\infty}^{\infty} [n^2 |2n\hbar k\rangle \langle 2n\hbar k| - n\alpha(t) |2n\hbar k\rangle \langle 2n\hbar k| \\ &\quad - \tilde{\Omega}(t) (|2n\hbar k\rangle \langle 2(n-1)\hbar k| + |2n\hbar k\rangle \langle 2(n+1)\hbar k|)]\end{aligned}\tag{8.7}$$

The matrix elements of this Hamiltonian are:

$$H_{mn} \equiv \langle 2m\hbar k | \hat{H}_{\text{DS}}^{\text{discrete}} | 2n\hbar k \rangle = 4E_r \left[(n^2 - n\alpha(t)) \delta_{mn} - \tilde{\Omega}(t) (\delta_{m,n+1} + \delta_{m,n-1}) \right]\tag{8.8}$$

Having derived the above matrix elements, from now on it will be convenient to perform calculations in matrix notation. We define the following notation: we let H be the Hamiltonian matrix whose element in the m th row and n th column is given by H_{mn} and we let $\vec{\Psi}(t)$ be the column vector whose n th entry is $c_n(t)$. Note that that the vector $\vec{\Psi}(t)$ is the matrix representation of the state $|\Psi(t)\rangle$ in the basis of

momentum eigenstates $|2n\hbar k\rangle$ for integers n .

8.3 Phase Evolution Under the Adiabatic Approximation

Now that we have determined the Hamiltonian matrix H , we have the appropriate machinery in place to describe the phase evolution of an atom in an optical lattice. We consider the process in which momentum is transferred to the atom through Bloch oscillations. Reference [27] provides a thorough and insightful description of Bloch oscillations in a number of different pictures. Given our choice of Hamiltonian, we work in the dressed state picture, which is discussed in Sec. IV.B. of [27], making extensive use of Bloch's theorem, the concept of Brillouin zones, and the band structure of the lattice [23]. As in the previous discussion, we consider the evolution of single eigenstates of the dressed state Hamiltonian, noting that we can easily generalize our results to the case of a wave packet of finite width, as we address in Sec. 8.9.

Initially, we consider the system to be in a momentum eigenstate. First, we adiabatically ramp up the lattice depth by increasing the laser power so that we load the system into an eigenstate of the lattice Hamiltonian. For the purposes considered here, we want the system to enter the ground eigenstate (corresponding to the zeroth band of the lattice). In order for this to be achieved, a resonance condition must be met, requiring that the velocity of the lattice must match the velocity of the atom to within v_r . The loading will be adiabatic if the adiabatic condition $|\langle 1 | \dot{H} | 0 \rangle| \ll \frac{(\varepsilon_1 - \varepsilon_0)^2}{\hbar}$ is satisfied, where $|0\rangle$ and $|1\rangle$ respectively denote the ground state and the first excited state of the Hamiltonian [27, 23]. This condition will be easier to meet near the center of the band (where the velocity of the lattice is identical to the velocity of the atom), because the energy gap $\varepsilon_1 - \varepsilon_0$ between the zeroth band and the first band becomes smaller as the velocity difference between the lattice and the atom becomes larger. This corresponds to moving toward the border of the first Brillouin zone. The resonance condition is discussed further in [151].

In the lab frame, the atom accelerates under gravity, increasing the deviation

between its velocity and the lattice velocity during the loading process. In the freely falling and dressed state frames, in which gravity is boosted away, this corresponds to the lattice accelerating upward while the atom remains at rest. This effect can negatively impact the loading efficiency if the loading sequence is sufficiently long so that the accrued velocity difference becomes a significant fraction of v_r . In such a scenario, the effect can be ameliorated by accelerating the lattice in the lab frame to fall with the atom, which corresponds to the lattice velocity remaining constant in the freely falling and dressed state frames.

Furthermore, we note that in the case of a lattice LMT beam splitter, the lattice should only be resonant with one arm of the interferometer, so that negligible population from the other arm is affected. Otherwise, the signal could be distorted by multi-path interference, causing a systematic error in the estimation of the interferometer phase shift. Conditions for when the negative effects of off-resonant lattices can be avoided can be estimated using the Hamiltonian matrix for an off-resonant lattice given in Eq. (8.30). We discuss off-resonant lattices quantitatively and in more detail in Sec. 8.6.

After the adiabatic loading of the atom into the ground state of the Hamiltonian, the frequency difference between the laser beams is swept to accelerate the lattice, periodically imparting momentum to the atom in units of $2\hbar k$. In the dressed state frame, this phenomenon can be understood in terms of avoided line crossings, which occur because the coupling between the atom and the laser beams lifts the degeneracy at the crossing points. We refer the reader to Fig. 10 of [27] for a clear illustration of these avoided crossings. As the frequency difference is swept so that the system passes through the avoided crossings, the system remains in the ground state of the dressed state Hamiltonian as long as the process is adiabatic. Consequently, at each of the avoided crossings, the momentum of the atom increases by $2\hbar k$, which corresponds to a Bloch oscillation. Finally, after the acceleration of the lattice, the frequency difference is held constant while the lattice depth is adiabatically ramped down, delivering the system into the momentum eigenstate $|p_i + 2N\hbar k\rangle$, where p_i is the momentum before the Bloch oscillations and N is the number of Bloch oscillations.

Fig. 8.2 depicts the lattice depth and velocity as functions of time for the process

described above and shows a numerical simulation of a particular instance of this process: the adiabatic loading of the lattice from an initial state $|0\hbar k\rangle$, the transfer of $10\hbar k$ of momentum through five Bloch oscillations, and the ramping down of the lattice to deliver the system into the final state $|10\hbar k\rangle$.

Since under the adiabatic approximation we assume that the atom always stays in the ground state of the Hamiltonian, the phase $\phi(t)$ of the atom evolves as follows:

$$\phi(t) - \phi_0 = -\frac{1}{\hbar} \int_{t_0}^t \varepsilon_0(\alpha, \tilde{\Omega}) dt' \quad (8.9)$$

where $\varepsilon_0(\alpha, \tilde{\Omega})$ is the instantaneous ground state eigenvalue of the Hamiltonian $H(\alpha, \tilde{\Omega})$ (and it is understood that α and $\tilde{\Omega}$ are functions of time) and ϕ_0 is the initial phase of the atom. In addition to Eq. (8.9), there is also a Berry's phase term [153]. However, this term is zero for a linear external potential. Therefore, there is no contribution from the Berry's phase under the semiclassical approximation, as long as the external potential is treated as linear. We discuss the validity and ramifications of this approximation in Sec. 8.2. Note that any such contribution would arise from the residual external potential terms of the dressed state Hamiltonian that are non-linear in x . We collectively denote these terms as V' in Sec. 8.2 and explain why they can often be neglected.

We now consider how the eigenvectors and eigenvalues of $H(\alpha, \tilde{\Omega})$ change with α , the dimensionless velocity of the lattice in the dressed state frame. Say that the eigenvalues of $H(\alpha, \tilde{\Omega})$ are given by $\varepsilon_n(\alpha, \tilde{\Omega})$ with corresponding eigenvectors $\vec{\Psi}_n(\alpha, \tilde{\Omega})$, where the index n runs from 0 to ∞ . We choose to index the eigenvalues so that $\varepsilon_n(\alpha, \tilde{\Omega})$ denotes the the n th eigenvalue labeled in order of increasing value. Moreover, we let $c_j^{(n)}(\alpha, \tilde{\Omega})$ be the j th element of the column vector $\vec{\Psi}_n(\alpha, \tilde{\Omega})$, so that $|\Psi_n(\alpha, \tilde{\Omega})\rangle = \sum_{j=-\infty}^{\infty} c_j^{(n)}(\alpha, \tilde{\Omega}) |2j\hbar k\rangle$. The transformation properties of the eigenvectors and eigenvalues under changes in α can be deduced from Bloch's theorem. It can be shown that when the lattice velocity is increased by $2v_r = \frac{2\hbar k}{m}$, which corresponds to α being increased by two, while $\tilde{\Omega}$ is kept fixed, the new eigenvectors can be obtained through the following relation [151]:

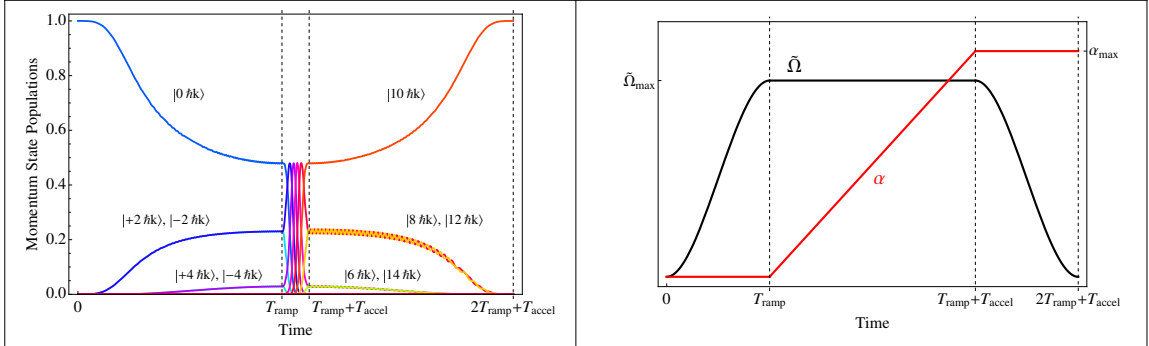


Figure 8.2: The left panel shows a numerical simulation of a lattice acceleration in momentum space that transfers $10\hbar k$ of momentum. The lattice depth and velocity are shown as functions of time in the right panel, where in this particular case the relevant parameters are $T_{\text{ramp}} = 120(4\omega_r)^{-1}$, $T_{\text{accel}} = 16(4\omega_r)^{-1}$, $\tilde{\Omega}_{\text{max}} = \frac{19.5}{8}$, and $\alpha_{\text{max}} = 10$ (corresponding to a final lattice velocity of $10 v_r$). First, we adiabatically ramp up the lattice to a depth of $19.5E_r$ so that the lattice is loaded into the ground state of the dressed state Hamiltonian. Subsequently, we accelerate and ramp down the lattice, leaving the atom in a single momentum eigenstate.

$$c_j^{(n)}(\alpha + 2, \tilde{\Omega}) = c_{j-1}^{(n)}(\alpha, \tilde{\Omega}) \quad (8.10)$$

This simply represents a shift of the wavefunction in momentum space by $2\hbar k$, which is exactly what we expect, since increasing the lattice velocity by $2v_r$ corresponds to undergoing a single Bloch oscillation. The dependence of the eigenvalues on the lattice velocity can be expressed as follows:

$$\varepsilon_n(\alpha, \tilde{\Omega}) = -E_r \alpha^2 + \varepsilon_n(0, \tilde{\Omega}) + p_n(\alpha, \tilde{\Omega}) \quad (8.11)$$

where $p_n(\alpha, \tilde{\Omega})$ is periodic in α such that $p_n(\alpha + 2m, \tilde{\Omega}) = p_n(\alpha, \tilde{\Omega})$ for integer m holds for all α and $p_n(\alpha, \tilde{\Omega})$ vanishes when the condition $\alpha = 2m$ holds. Note that the dependence of the eigenvalues on $\tilde{\Omega}$ can be calculated using the truncated matrix approximation discussed in Sec. 8.4. The relevance of this dependence to the phase shift of an interferometer and how this dependence varies with momentum are discussed in Sec. 8.5. and Sec. 8.9.

The first term in Eq. (8.11) has a simple physical interpretation. Where $v_{\text{Lattice}}(t)$

is the velocity of the lattice in the dressed state frame (so that $v_{\text{Lattice}}(t) = \alpha v_r$), note that:

$$E_r \alpha^2 = \frac{\hbar^2 k^2}{2m} \left(\frac{v_{\text{Lattice}}(t)}{\frac{\hbar k}{m}} \right)^2 = \frac{1}{2} m v_{\text{Lattice}}(t)^2 \quad (8.12)$$

which is simply the kinetic energy of an atom traveling along a classical trajectory defined by the motion of the lattice. The $\varepsilon_n(0, \tilde{\Omega})$ and $p_n(\alpha, \tilde{\Omega})$ terms represent the band structure of the lattice, with the $p_n(\alpha, \tilde{\Omega})$ term accounting for the bands deviating from being flat. For interferometer geometries in which lattices act as waveguides for the atoms, the net contributions to the phase shift from the $\varepsilon_0(0, \tilde{\Omega})$ and $p_0(\alpha, \tilde{\Omega})$ terms in the ground state energy and from corrections to the adiabatic approximation are often negligible, as explained in the following sections. In this case, the phase difference between the two arms of the interferometer is given by the following equation (assuming that the two arms arrive at the same endpoint). During the course of the following calculations, it is convenient to parametrize the Hamiltonian, eigenvalues, and eigenvectors using the single variable t rather than the two variables $\alpha(t)$ and $\tilde{\Omega}(t)$, and we make this switch starting here:

$$\begin{aligned} \phi_1 - \phi_2 &= -\frac{1}{\hbar} \left[\int_0^T \varepsilon_0^{\text{arm1}}(t) dt - \int_0^T \varepsilon_0^{\text{arm2}}(t) dt \right] \\ &= \frac{1}{\hbar} \left[\int_0^T \frac{1}{2} m v_{\text{Lattice}}^{\text{arm1}}(t)^2 dt - \int_0^T \frac{1}{2} m v_{\text{Lattice}}^{\text{arm2}}(t)^2 dt \right] \end{aligned} \quad (8.13)$$

In the above expression, T is the time elapsed during the interferometer sequence.

Observe that this expression for the phase difference can be obtained by assuming that the lattice potential acts as a constraint that forces the atoms in each arm to traverse the classical path traveled by the lattice guiding that arm. In this case the phase shift is just the difference of the respective action integrals over the two classical paths, as we would expect from the Feynman path integral formulation of quantum mechanics [154]. Since the lattice is the only potential in the freely falling and dressed

state frames, the action integrals yield Eq. (8.13) (for an insightful treatment of the applications of path integrals in atom interferometry, we refer the reader to [7]). The terms that we have neglected in Eq. (8.13) embody corrections to the simple picture of the lattice as a force of constraint arising from the quantum nature of the motion (e.g., a small portion of the population leaving the ground state of the lattice), which can sometimes be important. However, our simple picture provides physical intuition into the lattice phase shift and is often sufficient to derive quantitative results.

To summarize, the eigenvalues of the lattice consist of a kinetic energy term, a term that depends only on the lattice depth, and a term that is periodic in α , and the eigenvectors transform under a simple shift operation when α is changed by $2m$ for integer m . These properties are a direct result of Bloch's theorem. The symmetries that we have discussed allow us to conclude that if, for a given $\tilde{\Omega}$, we know the eigenvalues and eigenvectors of the Hamiltonian for all α within any range $[\alpha_0, \alpha_0 + 2]$, we can subsequently determine the eigenvalues and eigenvectors for arbitrary α . This result will prove to be useful from a computational standpoint, since the dynamics of the system are completely described by the solution within a finite range of α .

8.4 Calculating Corrections to the Adiabatic Approximation Using the Method of Perturbative Adiabatic Expansion

We now present the method of perturbative adiabatic expansion [16] to determine corrections of arbitrary order to the adiabatic approximation. We note that the particular adiabatic approximation that we correct here refers to the adiabatic evolution of the ground state of the dressed state Hamiltonian, rather than the adiabatic elimination of the excited state during the Raman process, which is treated in [16]. The corrections we consider will always be present to some extent, since lattice depth and velocity ramps occurring over a finite time can never be perfectly adiabatic. In addition, non-adiabatic corrections can be caused by perturbations arising

from laser frequency noise and amplitude noise. Although our analytical and numerical computations indicate that the contribution of non-adiabatic corrections to the overall phase shift will be highly suppressed for many interferometer geometries, it is important to have a generalized framework with which to treat these corrections in order to determine when they are important and to precisely calculate them when necessary. Note that much of our discussion will follow a similar outline as the proof of the adiabatic theorem in [153]. A more detailed version of the derivation presented here can be found in [151].

For all times t , we can express any state vector $\vec{\Psi}(t)$ in Hilbert space as a linear combination of the instantaneous eigenvectors $\vec{\Psi}_n(t)$ of the dressed state Hamiltonian matrix, where in general the coefficients of each eigenvector can vary in time. The instantaneous eigenvectors satisfy the relation $H(t)\vec{\Psi}_n(t) = \varepsilon_n(t)\vec{\Psi}_n(t)$. Note that the vectors $\vec{\Psi}_n(t)$ do not represent the momentum eigenstates $|2n\hbar k\rangle$, since the momentum eigenstates are not in general eigenstates of the dressed state Hamiltonian. Choosing coefficients with a phase $\varphi_n(t) \equiv -\frac{1}{\hbar} \int_{t_0}^t \varepsilon_n(t') dt'$ factored out, we can write:

$$\vec{\Psi}(t) = \sum_{n=0}^{\infty} b_n(t) e^{i\varphi_n(t)} \vec{\Psi}_n(t) \quad (8.14)$$

To simplify matters further, we choose the phase of the vectors $\vec{\Psi}_n(t)$ so that each element of $\vec{\Psi}_n(t)$ is real for all t and varies continuously with t , which we can do because the particular Hamiltonian matrix $H(t)$ we consider is a real-valued, Hermitian matrix. However, the coefficients $b_n(t)$ will in general be complex.

From here, application of the Schrodinger equation gives:

$$\dot{b}_j(t) = - \sum_{n \neq j} b_n(t) \vec{\Psi}_j^\dagger(t) \frac{\partial \vec{\Psi}_n(t)}{\partial t} e^{i[\varphi_n(t) - \varphi_j(t)]} \quad (8.15)$$

which can equivalently be written as:

$$\dot{b}_j(t) = - \left(\sum_{n \in S_D(t)} b_n(t) \vec{\Psi}_j^\dagger(t) \frac{\partial \vec{\Psi}_n(t)}{\partial t} e^{i[\varphi_n(t) - \varphi_j(t)]} \right) - \left(\sum_{n \in S_{ND}(t)} b_n(t) \frac{\vec{\Psi}_j^\dagger(t) \dot{H}(t) \vec{\Psi}_n(t)}{\varepsilon_n(t) - \varepsilon_j(t)} e^{i[\varphi_n(t) - \varphi_j(t)]} \right) \quad (8.16)$$

where $S_D(t)$ is the set of all n such that $n \neq j$ and $\varepsilon_n(t) = \varepsilon_j(t)$ and $S_{ND}(t)$ is the set of all n such that $\varepsilon_n(t) \neq \varepsilon_j(t)$ [153, 151].

Eq. (8.16) illuminates the rationale behind the adiabatic approximation. Under the adiabatic approximation, we assume that $H(t)$ and hence also its eigenvectors vary slowly enough in time so that the conditions $|\vec{\Psi}_j^\dagger(t) \dot{H}(t) \vec{\Psi}_n(t)| \ll \frac{(\varepsilon_n(t) - \varepsilon_j(t))^2}{\hbar}$ (for $\varepsilon_n(t) \neq \varepsilon_j(t)$) and $|\vec{\Psi}_j^\dagger(t) \frac{\partial \vec{\Psi}_n(t)}{\partial t} \Delta t| \ll 1$ (for $\varepsilon_n(t) = \varepsilon_j(t)$ and where Δt is the time scale of the approximation) hold. The righthand side of Eq. (8.16) can therefore be approximated as zero. Then, all the coefficients $b_j(t)$ are constant in time.

To compute higher order corrections, we employ the method of adiabatic expansion, which mathematically follows in the spirit of the Born approximation [153, 151]. We denote the coefficients correct to p th order as $b_j^{(p)}(t)$, where the zeroth order coefficients correspond to the solution under the adiabatic approximation. Higher order corrections can be obtained recursively through the relation $b_j^{(p)}(t) = b_j^{(p-1)}(t_0) - \sum_{n \neq j} \int_{t_0}^t b_n^{(p-1)}(t') \vec{\Psi}_j^\dagger(t') \frac{\partial \vec{\Psi}_n(t')}{\partial t'} e^{i[\varphi_n(t') - \varphi_j(t')]} dt'$. In the next section, it will prove to be useful to separate the corrections at each order into terms of the following form, as illustrated for the first and second order cases below. For the first order case, we can write:

$$b_j^{(1)}(t) = b_j^{(0)}(t_0) + \sum_{n \neq j} C_{n \rightarrow j}(t) \quad (8.17)$$

where:

$$C_{n \rightarrow j}(t) \equiv - \int_{t_0}^t b_n^{(0)}(t_0) \vec{\Psi}_j^\dagger(t') \frac{\partial \vec{\Psi}_n(t')}{\partial t'} e^{i[\varphi_n(t') - \varphi_j(t')]} dt' \quad (8.18)$$

The second order solution for $b_j(t)$ will then be:

$$\begin{aligned} b_j^{(2)}(t) &= b_j^{(0)}(t_0) - \sum_{n \neq j} \int_{t_0}^t b_n^{(1)}(t') \vec{\Psi}_j^\dagger(t') \frac{\partial \vec{\Psi}_n(t')}{\partial t'} e^{i[\varphi_n(t') - \varphi_j(t')]} dt' \\ &= b_j^{(0)}(t_0) + \sum_{n \neq j} C_{n \rightarrow j}(t) + \sum_{n \neq j} \sum_{m \neq n} C_{m \rightarrow n \rightarrow j}(t) \end{aligned} \quad (8.19)$$

where:

$$C_{m \rightarrow n \rightarrow j}(t) \equiv - \int_{t_0}^t C_{m \rightarrow n}(t') \vec{\Psi}_j^\dagger(t') \frac{\partial \vec{\Psi}_n(t')}{\partial t'} e^{i[\varphi_n(t') - \varphi_j(t')]} dt' \quad (8.20)$$

The calculation of corrections of higher order is discussed in Sec. 8.10.

To find the eigenvectors and eigenvalues that we need to calculate the terms that make a non-negligible contribution to the expansion, we must approximate the infinite dimensional Hamiltonian matrix as a finite dimensional truncated matrix. At the end of Sec. 8.3, we concluded that the problem of determining the eigenvalues and eigenvectors for all α reduces to finding the eigenvalues and eigenvectors for a range $\alpha \in [\alpha_0, \alpha_0 + 2]$ for arbitrary α_0 . In addition, it suffices to calculate the inner products $\vec{\Psi}_j^\dagger(t) \frac{\partial \vec{\Psi}_n(t)}{\partial t}$ just in this range of α , which follows from the symmetry $\vec{\Psi}_j^\dagger(\alpha + 2m, \tilde{\Omega}) \frac{\partial \vec{\Psi}_n(\alpha + 2m, \tilde{\Omega})}{\partial t} = \vec{\Psi}_j^\dagger(\alpha, \tilde{\Omega}) \frac{\partial \vec{\Psi}_n(\alpha, \tilde{\Omega})}{\partial t}$ for integer m [151]. To make the calculation less cumbersome, we can look at the range $\alpha \in [-1, 1]$. For $\tilde{\Omega}$ not too large and α in this range, the eigenvectors with lower energies are populated almost entirely by momentum eigenstates $|2m\hbar k\rangle$ with relatively small $|m|$. This is the case because for α in this range, the diagonal elements of the Hamiltonian will be smallest for values of m close to zero. We note that for $\tilde{\Omega} = 0$, the diagonal elements are the eigenvalues. In the limit of $\tilde{\Omega} \rightarrow 0$, each eigenvector will consist of only a single momentum eigenstate, where in general eigenvectors corresponding to momentum eigenstates with m closer to zero will have lower eigenvalues. Increasing $\tilde{\Omega}$ will allow the lower eigenvectors to spread out in momentum space to a certain extent, but this will not change the fact that the lower eigenvectors will be linear combinations of momentum eigenstates corresponding to smaller values of $|m|$. The eigenvectors

we care about for calculational purposes will be those with eigenvalues closer to the ground state eigenvalue. We can thus consider a truncated $(2n + 1) \times (2n + 1)$ Hamiltonian matrix centered around $m = 0$, where we choose n to be large enough so that for the particular dynamics being described, a sufficient number of eigenvectors and eigenvalues can be calculated.

8.5 An Example of Perturbative Adiabatic Expansion: Calculating the Non-Adiabatic Correction to the Phase Shift Evolved During a Lattice Beam Splitter

We illustrate the above method by calculating phase corrections to a lattice beam splitter. In this example, we consider the case where two optical lattices of the same depth but different accelerations are used to separate the two arms of the interferometer (after an initial momentum space splitting is achieved through Bragg diffraction). We note that the analysis here is equally applicable to the situation where two separate optical lattice waveguides are used to address the two arms of the interferometer, an example of which is illustrated in Fig. 8.5. To calculate the phase shift for applications in precision measurement, we need to determine the non-adiabatic correction to the phase difference between the two arms that accrues during the beam splitter. In practice, we do this by first calculating corrections to the ground state coefficient $b_0(t)$ and then evaluating how these corrections affect the phase difference between the arms. We note that the dominant contribution to the phase difference will come from the zeroth order term as given in Eq. (8.13).

For this example, we consider the situation shown in Fig. 8.2, where the interaction of the atoms with the lattice is divided into three distinct parts. From $t = 0$ to $t = T_{\text{ramp}}$ we ramp up the lattice, from $t = T_{\text{ramp}}$ to $t = T_{\text{ramp}} + T_{\text{accel}}$ we accelerate the lattice, and from $t = T_{\text{ramp}} + T_{\text{accel}}$ to $t = 2T_{\text{ramp}} + T_{\text{accel}} \equiv T_{\text{final}}$ we ramp down the lattice. For the sake of simplicity, the ramps are chosen to be symmetric so that

the lattice depth decrease ramp is the time reversed lattice depth increase ramp.

We assume that initially all of the population is in the ground state, so that $b_j^{(0)}(t) = \delta_{0j}$, and we make the lattice depth and velocity ramps adiabatic enough so that almost all of the population remains in the ground state. In order to find the non-adiabatic correction to the phase shift, we determine the non-adiabatic correction to the phase of the ground state for each arm.

Since to lowest order only the ground state is populated, the leading corrections to $b_0(t)$ will come at second order. The largest contribution comes from $C_{0 \rightarrow 1 \rightarrow 0}(t)$, and it is this term on which we focus. Because the ground state is non-degenerate, Eq. (8.20) and the fact that $\vec{\Psi}_j^\dagger(t) \frac{\partial \vec{\Psi}_n(t)}{\partial t} = \frac{\vec{\Psi}_j^\dagger(t) \dot{H}(t) \vec{\Psi}_n(t)}{\varepsilon_n(t) - \varepsilon_j(t)}$ for $\varepsilon_n(t) - \varepsilon_j(t) \neq 0$ [153] give us:

$$C_{0 \rightarrow 1 \rightarrow 0}(t) = - \int_0^t dt_1 \left(- \int_0^{t_1} dt_2 \frac{M_{10}(t_2)}{\Delta\varepsilon_{10}(t_2)} e^{-\frac{i}{\hbar} \int_0^{t_2} \Delta\varepsilon_{10}(t_3) dt_3} \right) \frac{M_{10}(t_1)}{-\Delta\varepsilon_{10}(t_1)} e^{\frac{i}{\hbar} \int_0^{t_1} \Delta\varepsilon_{10}(t_3) dt_3} \quad (8.21)$$

where we define $M_{10}(t) \equiv \vec{\Psi}_1^\dagger(t) \dot{H}(t) \vec{\Psi}_0(t) = \vec{\Psi}_0^\dagger(t) \dot{H}(t) \vec{\Psi}_1(t)$ and $\Delta\varepsilon_{10}(t) \equiv \varepsilon_0(t) - \varepsilon_1(t)$. Note that the two matrix elements are equal because we choose the eigenvectors to be real.

We examine the ultimate contribution of $C_{0 \rightarrow 1 \rightarrow 0}(T_{\text{final}})$ to $b_0^{(2)}(T_{\text{final}})$. Since during the ramp up and ramp down stages $M_{10}(t)$ depends only on $\dot{\tilde{\Omega}}$ but not on $\dot{\alpha}$, some portions of $C_{0 \rightarrow 1 \rightarrow 0}(T_{\text{final}})$ will be common to both arms of the interferometer, because we assume that the lattice interaction processes for the two arms differ only in the magnitude of the lattice acceleration. We denote these common terms as g_{ramp} . The remaining terms depend on the lattice acceleration and will thus differ between the arms. There will be a term g_{mixed} that depends both on $\dot{\tilde{\Omega}}$ and $\dot{\alpha}$. However, it can be shown that under the assumption that the lattice depth decrease ramp is the time reversed lattice depth increase ramp, this term is zero [151]. Finally, there will be a term g_{accel} that depends quadratically on $\dot{\alpha}$ and is not explicitly dependent on $\dot{\tilde{\Omega}}$. We note that g_{accel} implicitly depends on the maximum lattice depth $\tilde{\Omega}_{\text{max}}$, which can be seen by the fact that $\tilde{\Omega}_{\text{max}}$ affects what value the energy gap $\Delta\varepsilon_{10}$ takes on during

the acceleration stage (a deeper lattice leads to a larger energy gap). We can thus write:

$$b_0^{(2)}(T_{\text{final}}) \approx 1 + g_{\text{ramp}} + g_{\text{accel}} \quad (8.22)$$

In calculating g_{accel} , it is useful to note that $M_{10}(t)$ takes on a convenient form during the acceleration stage. Recalling the form of the Hamiltonian matrix from Eq. (8.8), we observe that $\dot{H}(t)$ will be a diagonal matrix with matrix elements $\dot{H}_{mn}(t) = -4E_r n \dot{\alpha}(t) \delta_{mn}$. We can thus write $M_{10}(t) = \dot{\alpha}(t) A_{10}(t)$, where $A_{10}(t) \equiv -4E_r \sum_n n \left(\vec{\Psi}_1(t) \right)_n \left(\vec{\Psi}_0(t) \right)_n$ is a weighted dot product.

In order to more clearly illuminate the general points we are illustrating with this example, we make the simplifying assumption that $\dot{\alpha}(t)$ is constant throughout the acceleration stage. Moreover, we assume that the lattice is deep enough so that $A_{10}(t)$ and $\Delta\varepsilon_{10}(t)$ are also constant during the acceleration stage, which is an accurate approximation for typical experimental situations. During the acceleration stage, we respectively denote these constant quantities as $\dot{\alpha}$, A_{10} , and $\Delta\varepsilon_{10_{\text{accel}}}$. Note that these assumptions, along with the assumption of mirror symmetry between the ramp up and ramp down stages, are certainly not necessary to carry out the calculation. They only serve to make the final result take a particularly simple form that provides physical insight into the process. In the absence of these assumptions, the calculation will be only slightly more complicated and can easily be performed. We note in particular that the mirror symmetry assumption is not stringent, for even when this symmetry is largely violated, the g_{mixed} term is typically an order of magnitude or more smaller than the g_{accel} term, as we verify by estimating the relevant integrals in Eq. (8.21). If needed, g_{mixed} can be calculated by evaluating these integrals. In addition, we note that the treatment given in this example can readily be generalized to the case where the lattice depth and velocity are changed simultaneously. Performing the necessary integrals, we find that:

$$g_{\text{accel}} = -i\hbar \frac{\dot{\alpha}^2 A_{10}^2}{(\Delta\varepsilon_{10_{\text{accel}}})^3} T_{\text{accel}} + \hbar^2 \frac{\dot{\alpha}^2 A_{10}^2}{(\Delta\varepsilon_{10_{\text{accel}}})^4} \left[e^{\frac{i}{\hbar} \Delta\varepsilon_{10_{\text{accel}}} T_{\text{accel}}} - 1 \right] \quad (8.23)$$

We note that for $|g_{\text{ramp}} + g_{\text{accel}}| \ll 1$, we can solve the problem by employing adiabatic expansion over a single time interval. However, there may be times when we must divide the problem into multiple parts, as discussed in Sec. 8.10. For typical experimental parameters, the term proportional to T_{accel} in g_{accel} will dominate both the second term in g_{accel} and the g_{ramp} term. We have verified that the g_{ramp} term (which embodies the non-adiabatic loading of the lattice) is typically much smaller than the first term in g_{accel} by estimating the integrals in Eq. (8.21) that correspond to g_{ramp} and by checking these estimates numerically. Thus, we can express the condition $|g_{\text{ramp}} + g_{\text{accel}}| \ll 1$ as:

$$\left| \hbar \frac{\dot{\alpha}^2 A_{10}^2}{(\Delta\varepsilon_{10_{\text{accel}}})^3} T_{\text{accel}} \right| \ll 1 \quad (8.24)$$

This condition will often hold, since in many experimentally relevant cases the acceleration time or acceleration will be sufficiently small.

We now show how to determine the correction to the phase shift between the two arms arising from the non-adiabatic correction $g_{\text{ramp}} + g_{\text{accel}}$ in the case where this correction is small. As we recall from Eq. (8.14), the coefficient of the ground state eigenvector at time T_{final} is $b_0(T_{\text{final}}) e^{i\varphi_0(T_{\text{final}})} \approx (1 + g_{\text{ramp}} + g_{\text{accel}}) e^{i\varphi_0(T_{\text{final}})}$. From now on, we adopt the notation $g_{\text{accel}}(\dot{\alpha})$ to emphasize the dependence of this quantity on $\dot{\alpha}$, and we leave g_{ramp} without an argument to emphasize that it does not depend on $\dot{\alpha}$. The non-adiabatic correction to the phase of the coefficient of the ground state eigenvector for an arm with acceleration $\dot{\alpha}$ is:

$$\phi_{\text{correction}}(\dot{\alpha}) \approx |g_{\text{ramp}}| \sin(\arg[g_{\text{ramp}}]) + |g_{\text{accel}}(\dot{\alpha})| \sin(\arg[g_{\text{accel}}(\dot{\alpha})]) \quad (8.25)$$

where we have Taylor expanded to first order in small quantities. We note that the exact expression for $\phi_{\text{correction}}(\dot{\alpha})$, which is sometimes necessary to use, is given by $\phi_{\text{correction}}(\dot{\alpha}) = \frac{1}{2i} \ln \left[\frac{1+|g_{\text{ramp}}|e^{i\arg(g_{\text{ramp}})}+|g_{\text{accel}}(\dot{\alpha})|e^{i\arg(g_{\text{accel}}(\dot{\alpha}))}}{1+|g_{\text{ramp}}|e^{-i\arg(g_{\text{ramp}})}+|g_{\text{accel}}(\dot{\alpha})|e^{-i\arg(g_{\text{accel}}(\dot{\alpha}))}} \right]$. To calculate the correction to the phase shift between two arms, we take the difference $\phi_{\text{correction}}(\dot{\alpha}_{\text{arm1}}) - \phi_{\text{correction}}(\dot{\alpha}_{\text{arm2}})$. The $|g_{\text{ramp}}| \sin(\arg[g_{\text{ramp}}])$ term is common to both arms. The non-adiabatic correction to the phase difference between an arm with acceleration $\dot{\alpha}$ and

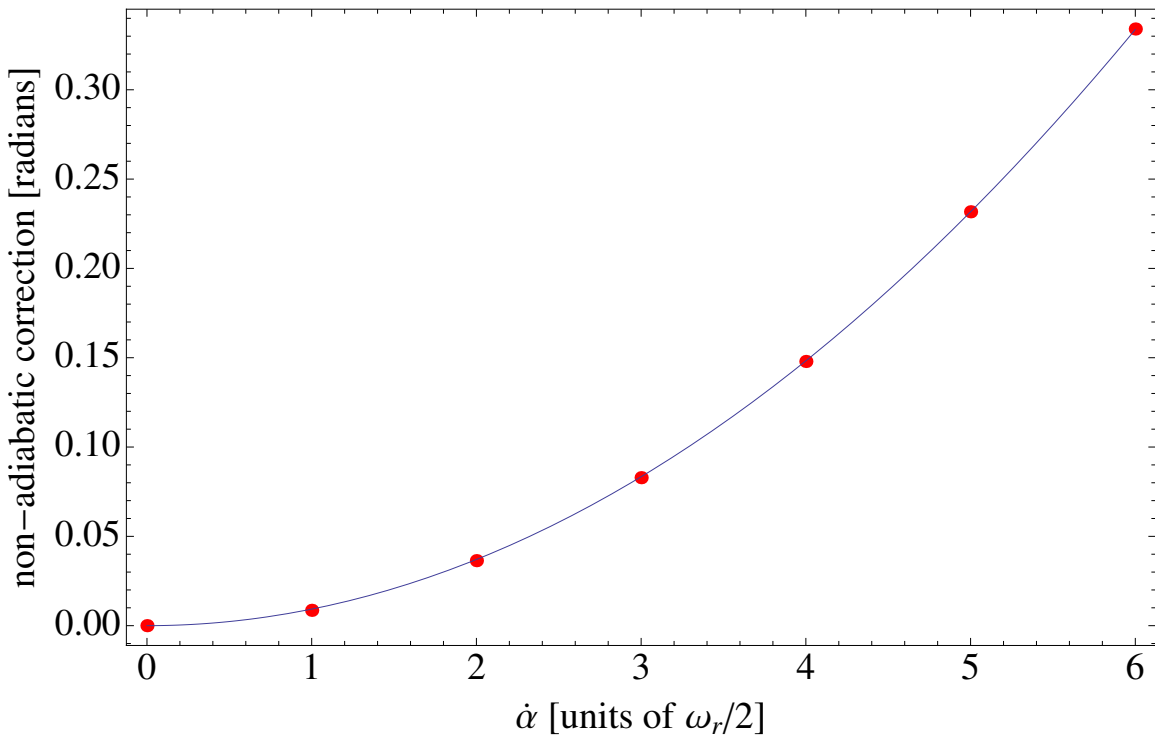


Figure 8.3: Non-adiabatic correction to the phase difference between an arm that is accelerated by an experimentally plausible lattice beam splitter and an arm that is not accelerated (which is in our notation $\delta\phi(\dot{\alpha})$), as calculated using a simplified adiabatic expansion method in which we keep only leading terms versus numerical simulations of the Schrodinger equation. The curve represents the prediction made by the adiabatic expansion method, while the points represent the numerical results.

an unaccelerated arm is:

$$\delta\phi(\dot{\alpha}) \equiv \phi_{\text{correction}}(\dot{\alpha}) - \phi_{\text{correction}}(0) \approx |g_{\text{accel}}(\dot{\alpha})| \sin(\arg[g_{\text{accel}}(\dot{\alpha})]) \quad (8.26)$$

Eqs. (8.25) and (8.26) provide us with a means to calculate the leading correction to the phase shift, and comparison with numerical results for a variety of experimentally conceivable lattice depth ramps shows excellent agreement. A comparison of the adiabatic expansion method with numerical calculations is illustrated in Fig. 8.3. In particular, Fig. 8.3 shows $\delta\phi(\dot{\alpha})$ as a function of $\dot{\alpha}$. The lattice depth ramps and acceleration time are identical to those of the acceleration sequence shown in Fig. 8.2, with an acceleration time of $16(4\omega_r)^{-1}$ and with $\tilde{\Omega}_{\max} = \frac{19.5}{8}$. The points shown in the figure come from a numerical simulation of the Schrodinger equation. In addition to the leading second order term, we keep the leading fourth order correction term in $g_{\text{accel}}(\dot{\alpha})$, $-\hbar^2 \frac{\dot{\alpha}^4 A_{10}^4 T_{\text{accel}}^2}{2(\Delta\varepsilon_{10_{\text{accel}}})^6}$, calculated in [151], which becomes significant for larger accelerations. For example, for an acceleration of $6\left(\frac{\omega_r}{2}\right)v_r$, this term is smaller than the leading second order correction by a factor of ~ 10 . We neglect corrections arising from the term g_{ramp} , for these corrections are common to both arms of the interferometer to lowest order. Even the simple approximation used to obtain the corrections agrees remarkably well with the simulations (with an rms deviation of 4×10^{-4} radians), and we note that we could easily improve this approximation by including more terms in the adiabatic expansion series. As expected, we observe that the correction scales quadratically with acceleration.

The non-adiabatic correction to the phase shift between the two arms of the interferometer for arbitrary arm acceleration differences is $\phi_{\text{correction}}(\dot{\alpha}_{\text{arm1}}) - \phi_{\text{correction}}(\dot{\alpha}_{\text{arm2}}) = \delta\phi(\dot{\alpha}_{\text{arm1}}) - \delta\phi(\dot{\alpha}_{\text{arm2}})$. Note that the leading order results depicted in Fig. 8.3 will often be sufficient, but it may sometimes be necessary to calculate higher order corrections, examples of which can be found in [151].

In an experimental implementation, the two arms of the beam splitter are addressed by two different lattices. Therefore, any imbalance in the depths of the two lattices will lead to a phase error between the arms. Where the intensities of the two

beams forming a given lattice are I_a and I_b , we note that the lattice depth is proportional to the product $\sqrt{I_a} \times \sqrt{I_b}$, meaning that intensity imbalances lead to lattice depth imbalances. We calculate that once a lattice is ramped up, the $\varepsilon_0(0, \tilde{\Omega})$ term in the expression for the lowest eigenvalue of the dressed state Hamiltonian from Eq. (8.11) is much larger than the $p_0(\alpha, \tilde{\Omega})$ term. Thus, for an interaction lasting from time t_1 to time t_2 , the dominant contribution to the phase error, which we denote as ϕ_{balance} , arising from the imbalance in the lattice depths is:

$$\phi_{\text{balance}} = -\frac{1}{\hbar} \int_{t_1}^{t_2} [\varepsilon_0(0, \tilde{\Omega}_{\text{arm1}}) - \varepsilon_0(0, \tilde{\Omega}_{\text{arm2}})] dt \quad (8.27)$$

where we note that $\varepsilon_0(0, \tilde{\Omega})$ can be calculated using the truncated matrix approximation discussed in Sec. 8.4. In order to put Eq. (8.27) in a more convenient form for making order of magnitude estimates, we use the fact that for $|\tilde{\Omega}| > 0.25$, $\varepsilon_0(0, \tilde{\Omega}) \sim -8E_r|\tilde{\Omega}|$. This result is verified by direct comparison with the values of $\varepsilon_0(0, \tilde{\Omega})$ obtained with the truncated matrix approximation. Recalling that $\tilde{\Omega} \equiv \frac{\Omega}{8\omega_r}$, it is convenient to rephrase this statement in terms of Ω as follows: for $|\Omega| > 2\omega_r$, $\varepsilon_0(0, \Omega) \sim -\hbar|\Omega|$. This range of $|\Omega|$ is of considerable experimental interest and is amenable to simple approximation. However, if needed, smaller lattice depths can be treated using the general relation given in Eq. (8.27) and the truncated matrix approximation. Substituting the above result into Eq. (8.27), we obtain:

$$\phi_{\text{balance}} \sim \int_{t_1}^{t_2} (|\Omega_{\text{arm1}}| - |\Omega_{\text{arm2}}|) dt = (\langle |\Omega_{\text{arm1}}| \rangle - \langle |\Omega_{\text{arm2}}| \rangle)(t_2 - t_1) \quad (8.28)$$

where $\langle |\Omega_{\text{arm1}}| \rangle$ and $\langle |\Omega_{\text{arm2}}| \rangle$ respectively denote the average values of $|\Omega_{\text{arm1}}|$ and $|\Omega_{\text{arm2}}|$ between time t_1 and time t_2 . Note that fluctuations in the difference between $|\Omega_{\text{arm1}}|$ and $|\Omega_{\text{arm2}}|$ that occur at frequencies that are large with respect to the beam splitter time $t_2 - t_1$ will largely average out, suppressing their net effect on the phase shift. Furthermore, in many geometries, arm 1 will be addressed by one pair of laser beams, that we call lattice A, during the splitting of the arms and then will be addressed by a second pair of laser beams, that we call lattice B, during the

recombination of the arms. Conversely, arm 2 will be addressed by lattice B during the splitting stage and by lattice A during the recombination stage. In such a geometry, the effect on the phase shift of a constant offset in depth between lattice A and lattice B will cancel, and the effect on the phase shift of fluctuations in the depth difference between lattice A and lattice B that occur at low frequencies with respect to the time scale of the interferometer sequence will be highly suppressed. Also, as we discuss in the following section, we will often be interested in the difference in the phase shifts of two interferometers in a differential configuration. If both of the interferometers remain well within the Rayleigh ranges of the laser beams so that beam divergence is a small effect, any lattice depth imbalance will be largely common to the two interferometers, suppressing its effect on the phase shift difference by orders of magnitude.

8.6 Applications: Atom Interferometers Using Optical Lattices as Waveguides

Light-pulse atom interferometer geometries have had tremendous success in performing many types of high-precision measurements. However, in many cases, we would like to be able to push the capabilities of atom interferometry by making more precise measurements using spatially compact interferometers. Atom interferometers that use optical lattices as waveguides for the atoms offer the potential to make such measurements attainable. In such a scheme, we can use an initial beam splitter composed of multiple Bragg pulses, a multi-photon Bragg pulse, or a hybrid Bragg pulse/lattice acceleration scheme as described in [23, 24, 25] to split the arms of the interferometer in momentum space. We can then control each arm independently with an optical lattice. We will once again use Bragg pulses during the π -pulse and final $\frac{\pi}{2}$ -pulse stages of the interferometer sequence, with lattices acting as waveguides between these stages. The preceding analysis has developed the theoretical machinery for calculating phase shifts for these lattice interferometers. We now examine several of the most promising applications of lattice interferometers.

8.6.1 Gravimetry and gravity gradiometry

Lattice interferometers can be used to make extremely precise measurements of the local gravitational acceleration g . We proceed to calculate the phase shift for a lattice gravimeter. It is essential to note that whenever the two arms are addressed by different lattices they will be in different dressed state frames (where we recall that a dressed state frame is defined by the velocity of the corresponding lattice and by the distance that the lattice has traveled since the beginning of the interferometer sequence). Let the velocities in the lab frame of the two lattices be denoted as $v_{\text{Lab}}^{\text{arm}1}(t)$ and $v_{\text{Lab}}^{\text{arm}2}(t)$, respectively. The lattice velocities for the two arms in their respective dressed state frames will thus be $v_{\text{Lattice}}^{\text{arm}1}(t) = v_{\text{Lab}}^{\text{arm}1}(t) + gt - v_0$ and $v_{\text{Lattice}}^{\text{arm}2}(t) = v_{\text{Lab}}^{\text{arm}2}(t) + gt - v_0$. We note that v_0 is the velocity of the atom before the initial Bragg diffraction that splits the arms in momentum space. Thus, the two arms have different momenta after the Bragg diffraction. During the lattice loading period, the two lattices must be resonant (as described in Sec. 8.3) with the respective portions of the atomic wavefunction that they are addressing. Also, let $\Delta v(t) \equiv v_{\text{Lab}}^{\text{arm}1}(t) - v_{\text{Lab}}^{\text{arm}2}(t)$ be the velocity difference between the two arms and $\Delta d(t) \equiv \int_0^t \Delta v(t') dt'$ be the distance between the two arms. Where the interferometer sequence lasts for a time T , we can derive the phase shift for a lattice gravimeter using Eq. (8.13). We note that an additional contribution $-\frac{1}{\hbar}m(v_f - v_0 + gT)\Delta d(T)$ to the phase shift will arise if the two arms of the interferometer end up in different dressed state frames (which occurs if $\Delta d(T)$ differs from zero), where mv_f is the lab frame momentum at time T of a particular momentum eigenstate in the atomic wavepacket. After averaging, it follows from the discussion in [8] that mv_f will take on the value of the center of the momentum space wavepacket. This additional contribution is calculated by boosting both arms into the freely falling frame using the relevant transformation given in Sec. 8.8 and the mathematical framework discussed in Sec. 8.9. We can thus write the phase shift as follows, where we also include a term ϕ_{Bragg} to embody the net contribution to the phase shift arising from the Bragg pulses:

$$\Delta\phi = -\frac{1}{\hbar} \int_0^T mg\Delta d(t)dt + \frac{1}{\hbar} \int_0^T \frac{1}{2}m(v_{\text{Lab}}^{\text{arm1}}(t)^2 - v_{\text{Lab}}^{\text{arm2}}(t)^2)dt - \frac{m}{\hbar}v_f\Delta d(T) + \phi_{\text{Bragg}} \quad (8.29)$$

When expressed in terms of lab frame quantities, it is apparent that the first two terms in $\Delta\phi$ correspond to the propagation phase and the third term corresponds to the separation phase, both of which typically appear in standard atom interferometer phase shift calculations [8]. We note that in the dressed state frame, ideal Bragg pulses simply yield contributions in units of $\pm\frac{\pi}{2}$ to the overall phase shift between the arms, and these contributions can easily be made to cancel so that $\phi_{\text{Bragg}} = 0$. However, we note that in some cases, corrections to the simplified picture of an ideal Bragg pulse due to such factors as gravity gradients, finite pulse and detuning effects (which can sometimes lead to a non-negligible propagation phase during the Bragg pulse), phase noise, or population loss may need to be considered. To avoid unnecessarily complicating our presentation, we will not present these corrections here. Instead, we emphasize that they are well-understood effects and refer the reader to other sources for further discussion [8, 16, 155]. Moreover, we note that these effects gain additional suppression for interferometers in a differential configuration so that they will often be below the mrad level [8], as in the case of the gravity gradiometer discussed below.

In the symmetric case, the velocities of the two arms in the lab frame are either opposite to each other or equal so that $v_{\text{Lab}}^{\text{arm1}}(t)^2 - v_{\text{Lab}}^{\text{arm2}}(t)^2 = 0$. Since we need the two arms of the interferometer to overlap at time T , ideally $\Delta d(T) = 0$. Thus, the first term in Eq. (8.29) will constitute the only contribution to $\Delta\phi$. However, in an experiment, the parameters in Eq. (8.29) will undergo small fluctuations around their desired values from shot to shot, so that the other terms in Eq. (8.29) act as a source of noise.

In order to cancel the effects of this noise, we can adopt a gradiometer setup in which an array of two or more gravimeters interacts with the same lattice beams. Although fluctuations in $\Delta d(t)$ will still affect phase differences between gravimeters, which take the form $-\frac{1}{\hbar} \int_0^T m(g_1 - g_2)\Delta d(t)dt$, modern phase lock techniques will typically allow us to control the phase differences between the lattice beams well

enough so that these effects are smaller than shot noise [156]. When measuring a gravity gradient, the value of g will vary due to the gradient over the range of a single gravimeter. For linear gradients, we can calculate the phase shift in the presence of a gravity gradient by assuming that the value of g corresponding to the gravimeter is equal to its value at the center of mass position of the atom (see [151] for a rigorous justification of this procedure). When higher order derivatives of the gravitational field become sizable in comparison to the first derivative, this simple prescription may not suffice, and we can treat the problem perturbatively. If we want to measure an acceleration as well as a gravitational gradient in a noisy environment in which the fringes of the individual gravimeters are washed out, we can use dissimilar conjugate interferometers whose phase noise is strongly correlated as suggested in [72]. Appropriate statistical methods can then be used to extract the desired acceleration signal [157, 141].

The effects on the phase shift of non-adiabatic corrections, lattice depth imbalances, and the finite spread of the atomic wavefunction in momentum space are considered in Sec. 8.4., Sec. 8.5, and Sec. 8.9. Based on the analysis in these sections, we conclude that a wide range of experimentally feasible gravimeter geometries exist that contain sufficiently adiabatic lattice depth and velocity ramps and that make use of symmetry in such a way that the net contribution of these corrections to the phase shift will be below the mrad level in a gradiometer configuration. We note that this chapter has developed the mathematical machinery to calculate any such corrections to arbitrary precision if necessary.

When two lattices are used to manipulate the arms of an atom interferometer, one lattice will be on resonance with a given arm, while the other will be highly detuned. As long as we keep this detuning large enough or employ geometries with sufficient symmetry between the arms, the net effect of the off-resonant lattices on the final phase shift can often be made to be smaller than the mrad level in a differential configuration (e.g., a gradiometer). For arm 1, the detuned lattice will manifest as an additional term in the discrete Hamiltonian, with matrix elements given by (using the same notation convention as in Eq. (8.8)):

$$H_{mn}^{\text{detuned}} = 4E_r \left[-\tilde{\Omega}_{\text{arm2}} e^{-i\beta(t)} \delta_{m,n+1} - \tilde{\Omega}_{\text{arm2}} e^{i\beta(t)} \delta_{m,n-1} \right] \quad (8.30)$$

where $\beta(t) \equiv -\int_0^t [\alpha^{\text{arm1}}(t') - \alpha^{\text{arm2}}(t')] 4\omega_r dt' = -2k\Delta d(t)$ and where $\tilde{\Omega}_{\text{arm2}}$ is the lattice depth parameter corresponding to the detuned lattice that addresses arm 2 [152]. To obtain the correction to the Hamiltonian for arm 2, which comes from the detuned lattice addressing arm 1, we replace $\beta(t)$ with $-\beta(t)$ and $\tilde{\Omega}_{\text{arm2}}$ with $\tilde{\Omega}_{\text{arm1}}$. For large detunings, $\beta(t)$ will vary rapidly with time so that the contribution from the detuned Hamiltonian will be small (i.e. the rotating wave approximation). Corrections arising from the detuned Hamiltonian can be solved for perturbatively using methods such as adiabatic perturbation theory. But we emphasize again that we can often avoid situations where this will be necessary. For example, we find from perturbation theory that to avoid population loss due to the off-resonant lattice as described in Sec. 8.3, we should choose the off-resonant lattice to have a velocity that differs from that of the particular arm of the interferometer under consideration by an amount $\Delta v \gg |\tilde{\Omega}|v_r$ (where $\tilde{\Omega}$ is the depth parameter of the off-resonant lattice). We have verified this result with numerical simulations. However, in this regime, the off-resonant lattice can still sometimes cause a non-negligible energy shift, which we estimate with perturbation theory. The energy shift for arm 1 is $\Delta E_{\text{arm1}} \approx \frac{\hbar}{8}\omega_r^{-1}(v_r/\Delta v)^2(\Omega_{\text{arm2}})^2$. The relevant quantity in determining the correction to the phase difference between the arms is the difference in energy shifts $\Delta E_{\text{arm1}} - \Delta E_{\text{arm2}}$, which is determined by the lattice depth imbalance between the arms. Where we let $\Omega_{\text{arm1}} = \Omega$ and $\Omega_{\text{arm2}} = \Omega + \Delta\Omega$:

$$\begin{aligned} \Delta E_{\text{arm1}} - \Delta E_{\text{arm2}} &\approx \frac{\hbar}{4} \frac{\Omega\Delta\Omega}{\omega_r(\Delta v/v_r)^2} \\ &\approx \hbar(0.4 \text{ s}^{-1}) \left(\frac{2\pi \times 3.77 \text{ kHz}}{\omega_r} \right) \left(\frac{20}{\Delta v/v_r} \right)^2 \left(\frac{\Omega}{5\omega_r} \right)^2 \left(\frac{\Delta\Omega/\Omega}{10^{-3}} \right) \end{aligned} \quad (8.31)$$

This result agrees with numerical simulations. For ${}^{87}\text{Rb}$, the recoil frequency value $\omega_r = 2\pi \times 3.77 \text{ kHz}$ should be used. We can use Eq. (8.31) to estimate the size of the phase shift induced by the lattice depth imbalance for an example lattice

interaction. For ^{87}Rb and assuming a lattice interaction of duration 10 ms, a lattice velocity difference of $\Delta v = 20v_r$, a lattice depth of $\Omega = 5\omega_r$, and a fractional lattice depth imbalance of $\Delta\Omega/\Omega = 10^{-3}$, the resulting phase shift is 4 mrad. For the same reasoning as in the discussion in the previous section, the net effect of lattice depth imbalances on the correction term treated here will often be further suppressed by orders of magnitude for interferometers in a differential configuration.

A lattice gravimeter can provide extraordinary levels of sensitivity. This sensitivity can be achieved over small distance scales by implementing a hold sequence in which the two arms are separated, manipulated into the same momentum eigenstate, held in place by a single lattice, and then recombined. In achieving compactness, we note that the fact that lattice interferometers are confined and can thus keep the atoms from falling under gravity during the separation and recombination stages of the interferometer as well as during the hold sequence is essential. Otherwise, for many configurations, the desired arm separation could not be reached without the atoms falling too great a distance, which would ruin the compactness of the interferometer. Hold times will be limited by spontaneous emission, which decreases contrast. Modern laser technology will allow detunings of hundreds or even thousands of GHz, making hold times on the order of 10 s within reach [39].

Gravimeter sensitivities using the hold method greatly exceed the sensitivities of light-pulse gravimeters while simultaneously allowing for a significantly smaller interrogation region. For example, for $\sim 10^7$ atoms/shot and $\sim 10^{-1}$ shots/s, a shot noise limited conventional light-pulse interferometer with a 10 m interrogation region can achieve a sensitivity of $\sim 10^{-11} \text{ g/Hz}^{1/2}$. With similar experimental parameters, a shot noise limited lattice interferometer with a 10 s hold time and an interrogation region of 1 cm will have a sensitivity of $\sim 10^{-12} \text{ g/Hz}^{1/2}$. If we expand the interrogation region to 1 m, we obtain a sensitivity of $\sim 10^{-14} \text{ g/Hz}^{1/2}$. This remarkable sensitivity has a plethora of potential applications. Extremely precise gravimeters and gravity gradiometers can be constructed to perform tests of general relativity, make measurements relevant to geophysical studies, and build highly compact inertial sensors. Moreover, the fact that lattice interferometers can operate with such high sensitivities over small distance scales makes them prime candidates for exploring short distance

gravity. One could set up an array of lattice gravimeters to precisely map out gravitational fields over small spatial regions, as shown in Fig. 8.4. The knowledge obtained about the local gravitational field could be useful in searching for extra dimensions [158] as well as in studying the composition and structure of materials. It is relevant to note the scale dependence of spatial derivatives of the gravitational field. That is, we consider a sensor a distance D_{sensor} away from a mass of radius R_{mass} . If we multiply both D_{sensor} and R_{mass} by a scale factor s , assuming fixed density, the scale dependence tells us how the size of the measured spatial derivative is affected. The mass scales as $(R_{\text{mass}})^3$, while the n th spatial derivative of the gravitational field scales as the mass divided by $(D_{\text{sensor}})^{n+2}$. Therefore, the scale dependence of the n th spatial derivative is $1/s^{n-1}$. Thus, the first spatial derivative (the gravity gradient) is scale invariant. Higher derivatives are proportional to powers of the inverse scale and are therefore more strongly affected by nearby masses.

8.6.2 Tests of atom charge neutrality

Ultra-high precision gravitational measurements are certainly among the most promising applications of lattice interferometers, but the usefulness of lattice interferometers is certainly not limited to the study of gravity. By exposing the two arms of a lattice interferometer to different electrostatic potentials, tests of atom charge neutrality with unprecedented accuracy could be achieved [159]. The main advantage of a lattice interferometer in such a measurement is that the interrogation time can be significantly increased in comparison to the interrogation time achievable in a light-pulse geometry through the use of a hold sequence. Where t_{hold} is the duration of the hold, V is the electrostatic potential difference between the two arms of the interferometer, e is the electron charge, and ϵ is the ratio of the spurious atomic charge to the electron charge, the phase shift is given by $\frac{\epsilon e}{\hbar} V t_{\text{hold}}$ [159]. Based on the results of Sec. 8.4., Sec. 8.5, and Sec. 8.9, and assuming an identical configuration to that described in [159] except for the inclusion of a hold sequence, we estimate that the phase error induced by the undesirable effects we consider will be below the proposed shot noise limit for this experiment (1 mrad). Any systematic phase error can be characterized

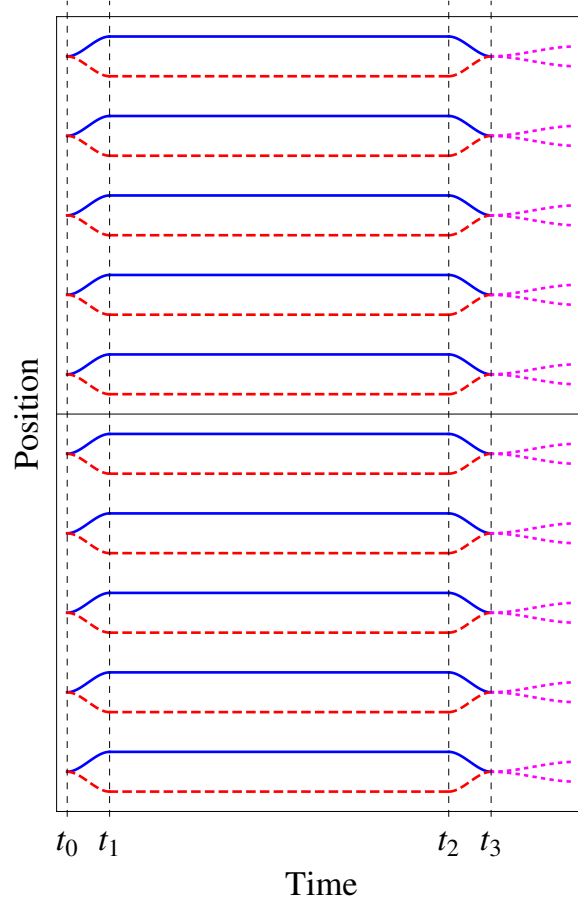


Figure 8.4: An array of lattice gravimeters such as that shown above can be used to achieve measurements of a local gravitational field with high spatial resolution. The trajectories shown hold in the lab frame. After separating the atoms in each gravimeter by a small amount, we can implement a hold sequence to greatly increase sensitivity. Bragg pulses are used at times t_0 , t_1 , t_2 , and t_3 . Such an array could be used to study general relativistic effects, search for extra dimensions, examine local mass distributions, or measure Newton's constant. In addition, the ability of lattice interferometers with hold sequences to provide extremely precise measurements with a small interrogation region makes them ideal candidates for compact, mobile sensors.

by the methods we have developed. For a hold time of 10 s and for integration over 10^6 shots, spurious atom charges can be probed down to the region of $\epsilon \sim 10^{-27}$. For comparison, the current best limit is $\epsilon \sim 10^{-21}$. The current limit is set by several different types of experiments, including monitoring the response of levitated objects to alternating electric fields and measuring the frequencies of electrically excited sound waves [160].

8.6.3 Measurements of $\frac{\hbar}{m}$ and of isotope mass ratios

The ratio $\frac{\hbar}{m}$ is of particular interest because of its direct relation to the fine structure constant. Atom interferometry has previously been used to provide exquisite measurements of $\frac{\hbar}{m}$. The most precise atom interferometric measurement to date was performed by Cadoret *et al.*, who performed an elegant experiment combining Bloch oscillations and a Ramsey-Bordé interferometer to measure the fine structure constant to within a relative uncertainty of 4.6×10^{-9} [149]. Eq. (8.29) indicates that if we apply different accelerations to the two arms of the interferometer, we will see a phase shift proportional to $\frac{m}{\hbar}$ that depends on the kinetic energy difference between the arms, which can be made extremely large. A differential configuration using conjugate interferometers (shown in Fig. 8.5) could reduce the net contribution of such unwanted effects as laser phase noise and cancel the gravitational phase shift up to gradients [72]. Such a geometry could provide an extremely precise measurement of $\frac{\hbar}{m}$, as illustrated by the fact that we can achieve a phase shift of $\sim 10^{11}$ radians for a 5 m interrogation region and a 0.6 s interrogation time, corresponding to a shot noise limited sensitivity of $\sim 10^{-14} \frac{\hbar}{m}/\text{Hz}^{1/2}$ for the experimental parameters stated above. In this situation, the dominant unwanted effect would arise from non-adiabatic corrections, and the methods for calculating these corrections that are presented in the previous sections would need to be applied (we estimate a phase error ~ 10 rad). We note that even if the shot noise limit is not reached, the technique we have proposed could still improve the $\frac{\hbar}{m}$ limit. We emphasize again that to take full advantage of the sensitivity offered by lattice manipulations in atom interferometry, the methods we develop in this chapter for calculating non-adiabatic corrections are absolutely

essential.

The fact that all terms in Eq. (8.29) are proportional to m (except for the ϕ_{Bragg} term, which as we have explained, will often be negligible) can be exploited to provide high-precision measurements of isotope mass ratios by using an interferometer geometry in which the two isotopes follow identical trajectories. Isotope mass ratios could be relevant to studies of advanced models of the structure of the nucleus [161]. Conversely, if we know the mass ratio of two isotopes sufficiently well, we can use such a geometry to precisely measure accelerations, where the two isotopes provide two dissimilar conjugate interferometers. The phase noise of these two interferometers will be extremely well correlated because they are nearly topologically identical. This also eliminates the need for the additional lattice beams required to form the second, topologically distinct interferometer that would be needed with only a single isotope. Note that this scheme to construct dissimilar, topologically identical conjugate accelerometers would not be possible for a light-pulse geometry, for the leading order phase shift of light-pulse accelerometers is independent of isotope mass.

8.6.4 Gyroscopes

Lattice interferometers can also be used to build compact and highly sensitive gyroscopes. There are multiple possible schemes in which optical lattices can enhance gyroscope sensitivity. One such scheme is to modify a typical atom-based gyroscope by replacing the Raman pulses with LMT lattice beam splitters, increasing the enclosed area of the interferometer and hence its sensitivity to rotations. The Sagnac phase shift can be written as $\frac{2m}{\hbar} \vec{\Omega} \cdot \vec{A}$, where $\vec{\Omega}$ is the rotation rate vector and \vec{A} is the normal vector corresponding to the enclosed area of the interferometer [8]. The gyroscope described in [28] achieves a sensitivity of $2 \times 10^{-8} \frac{\text{rad}}{\text{s}}/\text{Hz}^{1/2}$. Replacing the Raman pulses in this experiment with $200\hbar k$ lattice beam splitters would increase the sensitivity by a factor of 100, with a 1 Hz repetition rate (1 s measurement period). For reference, we give several rotation rates of interest. The Earth rotates around its axis by 2π rad every day, corresponding to a rotation rate of 7×10^{-5} rad/s, which could be easily measured by such a gyroscope. The Earth completes one orbit around

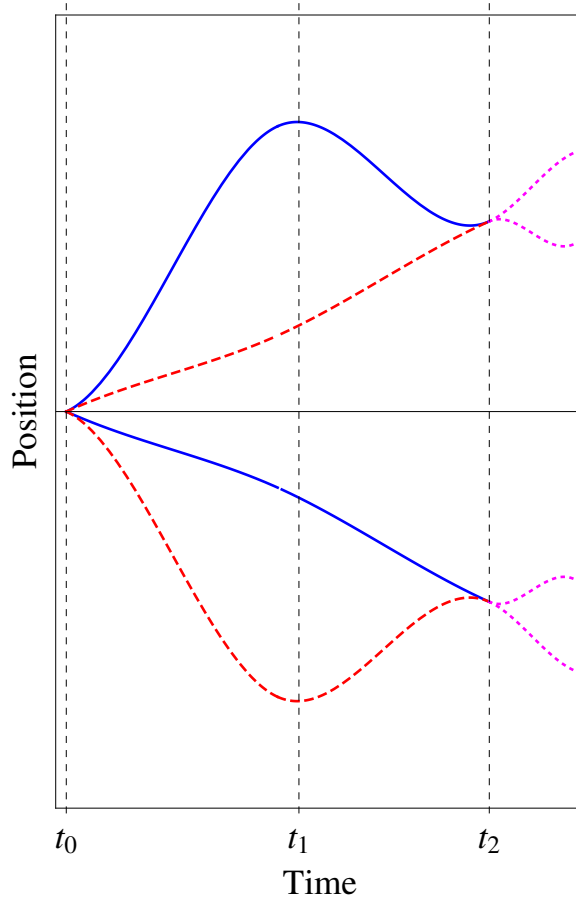


Figure 8.5: Conjugate interferometer geometry that could be used to measure $\frac{\hbar}{m}$. The trajectories shown hold in the lab frame. Bragg pulses are used at times t_0 , t_1 , and t_2 (at t_0 , a sequence of multiple Bragg pulses is necessary to split the system into the two arms of the two conjugate interferometers). The phase shift of the lower interferometer is subtracted from the phase shift of the upper interferometer, which suppresses the effects of laser phase noise and eliminates the gravitational phase shift up to gradients [72]. With such a scheme, a measurement of $\frac{\hbar}{m}$ to a part in 10^{14} may be possible, which could lead to the most accurate determination of the fine structure constant to date.

the sun per year, corresponding to a rotation rate of 2×10^{-7} rad/s. This is still well within the resolution of the proposed gyroscope. The solar system completes one orbit around the center of the galaxy every 240 million years [162], corresponding to a rotation rate of 10^{-15} rad/s. Such a small rotation rate would be much more difficult to measure. Perhaps such a measurement could be feasible by averaging over many measurements and using more ambitious interferometer parameters. A challenge would be to separate this signal from background effects. Additionally, the Earth's rotation period undergoes seasonal changes of ~ 1 ms [163], which translates into seasonal variations in the Earth's rotation rate of $\sim 10^{-12}$ rad/s. With measurement averaging, the proposed gyroscope sensitivity would be able to resolve such changes.

In the lattice gyroscope configuration mentioned above, we estimate that each beam splitter could introduce a non-adiabatic phase error of ~ 1 rad if the arms of the interferometer are not split symmetrically. However, beam splitter configurations that exploit symmetry between the arms can reduce this effect by orders of magnitude. Another option is to use optical lattices along multiple axes to provide complete control of the motion of the atoms in two or three dimensions (this control is only achieved in the region in which the lattices overlap, necessitating the use of wide beams). Analogous to a fiber-optic gyroscope, the atoms could be guided in repeated loop patterns, with the two arms rotating in opposite directions. Geometries in which atomic motion is controlled in multiple dimensions could also expand the possibilities for other applications of lattice interferometry (such as measurements of gravity) by allowing for the measurement of potential energy differences between arbitrary paths. For instance, a compact array of three orthogonal lattice gravity gradiometers could be used to measure the nonzero divergence of the gravitational field in free space predicted by general relativity [37].

8.7 Outlook

We have presented a detailed analytical description of the interaction between an atom and an optical lattice, using the adiabatic approximation as a starting point

and then proceeding to rigorously develop a method to calculate arbitrarily small corrections to this approximation using perturbative adiabatic expansion. We have applied this theoretical framework to calculate the phase accumulated during a lattice acceleration in an LMT beam splitter. Finally, we have proposed atom interferometer geometries that use optical lattices as waveguides and discussed applications of such geometries, using our theoretical methods to add rigor to this discussion. We are working toward the experimental implementation of lattice interferometers and LMT lattice beam splitters, and we hope to explore the applications we have discussed. In this experimental work, we realize that we will have to contend with a number of unwanted systematic effects, such as spatially varying magnetic fields, imperfections in the lattice beam wavefronts, and inhomogeneity of the lattice depth across the atomic cloud. We have studied these effects using both analytical and numerical methods, and we are optimistic that they can be significantly mitigated for a wide range of experimental parameters—a conclusion that we hope to verify experimentally. Many of the unwanted systematic effects that are relevant to lattice interferometers are also shared by light-pulse interferometers and can therefore be dealt with using similar methods. Therefore, we believe that it will likely be possible to realize lattice interferometers in existing apparatus originally constructed with light-pulse geometries in mind.

8.8 Additional Calculation: Boosting Between Different Frames

For the purposes of this chapter, we consider unitary transformations that consist of a translation in position space, a boost in momentum space, and a time-dependent change of phase. Such a transformation has the general form:

$$\hat{U}(t) = e^{\frac{i}{\hbar}d(t)\hat{p}}e^{-\frac{i}{\hbar}mv(t)\hat{x}}e^{\frac{i}{\hbar}\theta(t)} \quad (8.32)$$

We note that the translation $d(t)$, the boost $v(t)$, and the phase $\theta(t)$ are independent parameters. We now consider the Hamiltonian in a frame that is freely falling with

gravity, which takes the form:

$$\hat{H}_{FF} = \frac{\hat{p}^2}{2m} + 2\hbar\Omega(t) \sin^2 \left[k\hat{x} - k(D_{Lab}(t) + \frac{1}{2}gt^2) \right] \quad (8.33)$$

We can transform from the freely falling frame to the lab frame by applying the appropriate Galilean transformation $\hat{U}_{FF}(t)$, which corresponds to specifying $d(t) = \frac{1}{2}gt^2$, $v(t) = gt$, and $\theta(t) = \frac{1}{3}mg^2t^3$, so that $\hat{H}_{Lab} = \hat{U}_{FF}(t)\hat{H}_{FF}\hat{U}_{FF}^\dagger(t) + i\hbar \left(\frac{\partial}{\partial t} \hat{U}_{FF}(t) \right) \hat{U}_{FF}^\dagger(t)$.

It is useful from a calculational standpoint to transform to a third frame, with a Hamiltonian resembling that describing the atom-light interaction from the point of view of dressed states. We note that although we could have performed a boost directly from the lab frame to the dressed state frame, it is useful to introduce the freely falling frame for pedagogical reasons, since it is the frame in which calculations for atom interferometry are often performed. In Sec. 8.9, we use the transformation between the freely falling frame and the dressed state frame to highlight the parallels between a lattice beam splitter and a typical light pulse beam splitter.

The Hamiltonian in the dressed state frame is $\hat{H}_{DS} = \frac{\hat{p}^2}{2m} - (v_{Lab}(t) + gt - v_0)\hat{p} + 2\hbar\Omega(t) \sin^2(k\hat{x})$. We absorb the initial velocity v_0 of the atom in the lab frame (and hence also in the freely falling frame) into the dressed state frame, so that velocity v_0 in the lab frame corresponds to velocity zero in the dressed state frame. The unitary transformation that transforms from the dressed state frame to the freely falling frame is $\hat{U}_{DS} = e^{\frac{i}{\hbar}mv_0\hat{x}} e^{-\frac{i}{\hbar}(D_{Lab}(t) + \frac{1}{2}gt^2)\hat{p}} e^{-\frac{i}{\hbar}(\frac{1}{2}mv_0^2t)}$, so that $\hat{H}_{FF} = \hat{U}_{DS}(t)\hat{H}_{DS}\hat{U}_{DS}^\dagger(t) + i\hbar \left(\frac{\partial}{\partial t} \hat{U}_{DS}(t) \right) \hat{U}_{DS}^\dagger(t)$.

8.9 Additional Calculation: Generalizing to the Case of a Finite Wavepacket

In Sec. 8.2, we discretized the Hamiltonian using the basis of momentum states $|2n\hbar k\rangle$ for integer n . We now generalize our results to the case of a finite wavepacket.

Throughout our analysis, we have worked mainly in the dressed state frame, since this frame is particularly convenient for describing phase evolution in a lattice. However, since different momentum states correspond to different dressed state frames,

in order to calculate effects due to finite wavepacket momentum spread, we need to use a common reference frame. Phase shift calculations for light-pulse atom interferometers are often performed in the freely falling frame. Thus, we present the general results derived in this section in the freely falling frame.

In Sec. 8.2, we considered a particular dressed frame in which the initial velocity of the atom is boosted to zero. We now introduce an unboosted dressed state frame that is related to the freely falling frame by a translation in position space with no boost in momentum space, so that the unitary transformation $\hat{U}_{DS_0} = e^{-\frac{i}{\hbar}(D_{Lab}(t) + \frac{1}{2}gt^2)\hat{p}}$ transforms from the unboosted dressed state frame to the freely falling frame. The Hamiltonian in this frame is:

$$\hat{H}_{DS_0} = \frac{\hat{p}^2}{2m} - (v_{Lab}(t) + gt)\hat{p} + 2\hbar\Omega(t) \sin^2(k\hat{x}) \quad (8.34)$$

Now, say that before the lattice acceleration, the state that we are accelerating is described by $|\Psi_{FF}(t_0)\rangle$ in the freely falling frame. We can then transform this state vector to the unboosted dressed state frame, describe its evolution to the final time t_f in this frame, and transform back to the freely falling frame. Where $\hat{T}_{DS_0}(t', t)$ is the time evolution operator that takes us from time t to time t' in the unboosted dressed state frame, we can write:

$$|\Psi_{FF}(t_f)\rangle = \hat{U}_{DS_0}(t_f)\hat{T}_{DS_0}(t_f, t_0)\hat{U}_{DS_0}^\dagger(t_0)|\Psi_{FF}(t_0)\rangle \quad (8.35)$$

Denoting the initial momentum space wavefunction in the freely falling frame as $\Psi_{FF}(p, t_0) \equiv \langle p|\Psi_{FF}(t_0)\rangle$, we can express Eq. (8.35) as:

$$|\Psi_{FF}(t_f)\rangle = \int dp \hat{U}_{DS_0}(t_f)\hat{T}_{DS_0}(t_f, t_0)|p\rangle e^{\frac{i}{\hbar}(D_{Lab}(t_0) + \frac{1}{2}gt_0^2)p}\Psi_{FF}(p, t_0) \quad (8.36)$$

We now consider how each momentum eigenstate $|p\rangle$ evolves in the unboosted dressed state frame. That is, we must calculate $\hat{T}_{DS_0}(t_f, t_0)|p\rangle$ for each p . In order to do so, we introduce a class of boosted dressed state frames DS_p parameterized by p , so that momentum p in the unboosted dressed state frame (which is just the frame DS_0)

corresponds to momentum zero in the frame DS_p . In essence, where $v \equiv \frac{p}{m}$, frame DS_p travels with velocity v with respect to the unboosted dressed state frame. In frame DS_p , the Hamiltonian takes the form:

$$\hat{H}_{DS_p} = \frac{\hat{p}^2}{2m} - (v_{\text{Lab}}(t) + gt - v)\hat{p} + 2\hbar\Omega(t) \sin^2(k\hat{x}) \quad (8.37)$$

where we note that the unitary transformation that transforms from frame DS_p to the unboosted dressed state frame is:

$$\hat{U}_p(t) = e^{\frac{i}{\hbar}p\hat{x}} e^{-\frac{i}{\hbar}[-(D_{\text{Lab}}(t) + \frac{1}{2}gt^2)mv + \frac{1}{2}mv^2t]} \quad (8.38)$$

Where $\hat{T}_{DS_p}(t_f, t_0)$ is the time evolution operator in frame DS_p , we can write:

$$\begin{aligned} \hat{T}_{DS_0}(t_f, t_0) |p\rangle &= \hat{U}_p(t_f) \hat{T}_{DS_p}(t_f, t_0) \hat{U}_p^\dagger(t_0) |p\rangle \\ &= e^{\frac{i}{\hbar}[-(D_{\text{Lab}}(t_0) + \frac{1}{2}gt_0^2)mv + \frac{1}{2}mv^2t_0]} \hat{U}_p(t_f) \hat{T}_{DS_p}(t_f, t_0) |0\rangle \end{aligned} \quad (8.39)$$

The problem of determining the evolution of the momentum eigenstate $|p\rangle$ in the unboosted dressed state frame thus reduces to evolving the momentum eigenstate $|0\rangle$ in the frame DS_p , which we know how to do from the preceding sections. We assume that the momentum space wavefunction is narrow enough so that the momentum eigenstates we consider are resonant with the lattice (that is, as we recall from Sec. 8.3, the magnitudes of their velocities with respect to the lattice are less than v_r). Where the lattice acceleration is chosen so as to transfer a momentum of $2n\hbar k$ to the atom, the result from Sec. 8.3 tells us that the time evolution in Eq. (8.39) yields:

$$\hat{T}_{DS_p}(t_f, t_0) |0\rangle = e^{i\phi_p} |2n\hbar k\rangle \quad (8.40)$$

for the following phase factor relevant to the phase shift of the interferometer:

$$\phi_p = \frac{m}{2\hbar} \int_{t_0}^{t_f} v_{\text{Lattice}}^p(t)^2 dt \quad (8.41)$$

where $v_{\text{Lattice}}^p(t) \equiv v_{\text{Lab}}(t) + gt - v$ is the lattice velocity in frame DS_p . For the sake of pedagogy, at the moment we neglect the phase arising from the lattice depth, the phase arising from the small periodic variations in the lowest eigenvalue, and the phase arising from non-adiabatic corrections, where we note that we could calculate these contributions if needed. Evaluating the integral in Eq. (8.41), substituting this result into Eq. (8.39), and applying the transformation $\hat{U}_p(t_f)$, we obtain:

$$\hat{T}_{\text{DS}_0}(t_f, t_0) |p\rangle = e^{i\frac{m}{2\hbar} \int_{t_0}^{t_f} (v_{\text{Lab}}(t) + gt)^2 dt} |p + 2n\hbar k\rangle \quad (8.42)$$

We can now evaluate Eq. (8.36), which gives us the final result:

$$|\Psi_{\text{FF}}(t_f)\rangle = \int dp |p + 2n\hbar k\rangle e^{i\phi_{\text{FF}}(p)} \Psi_{\text{FF}}(p, t_0) \quad (8.43)$$

where:

$$\phi_{\text{FF}}(p) = \frac{m}{2\hbar} \int_{t_0}^{t_f} (v_{\text{Lab}}(t) + gt)^2 dt - 2nk(D_{\text{Lab}}(t_f) + \frac{1}{2}gt_f^2) - \frac{p}{\hbar}\Delta D \quad (8.44)$$

for $\Delta D \equiv (D_{\text{Lab}}(t_f) + \frac{1}{2}gt_f^2) - (D_{\text{Lab}}(t_0) + \frac{1}{2}gt_0^2)$.

Observe that the second term in Eq. (8.44) is what would typically be called the laser phase in a light-pulse atom interferometer for an n th-order beam splitter. We note that as long as the resonance condition is met for the momentum eigenstates we are considering so that they are accelerated, the phase evolved during a lattice acceleration in the DS_0 dressed state frame, is independent of p , as shown in Eq. (8.42). (This is true up to non-adiabatic corrections and the small periodic variations in the ground state eigenvalue). This makes dressed state frames particularly convenient for performing calculations involving wavepackets. In contrast, in the freely falling frame, the accumulated phase ϕ_{FF} is dependent on p , but this dependence cancels in the final expression for the phase shift between the two arms of an interferometer as long as the distance travelled by the atom while locked into a lattice is the same for both arms. Note that momentum dependent contributions to the total phase shift must arise when we treat the problem purely in terms of dressed states, since the

total phase shift is an observable quantity and must therefore be independent of the frame in which it is calculated. The key point to realize is that if the total distance traveled in the lattice is not the same for both arms, then the two arms will end up in two different dressed state frames.

We now consider the effect on phase evolution of the periodic term $p_0(\alpha, \tilde{\Omega})$ in the expression for the ground state eigenvalue of the dressed state Hamiltonian given in Eq. (8.11). This term leads to a momentum dependent correction $\delta\phi_p$ to the evolved phase ϕ_p described in Eq. (8.41), where:

$$\delta\phi_p = -\frac{1}{\hbar} \int_{t_0}^{t_f} p_0 \left(\frac{v_{\text{Lattice}}^p(t)}{v_r}, \tilde{\Omega}(t) \right) dt \quad (8.45)$$

We remind the reader here that $p_0 \left(\frac{v_{\text{Lattice}}^p(t)}{v_r}, \tilde{\Omega}(t) \right)$ is an energy, so the right side of the above equation indeed has units of phase. We note that $p_0 \left(\frac{v_{\text{Lattice}}^p(t)}{v_r}, \tilde{\Omega}(t) \right)$ can be calculated using the truncated matrix approximation described in Sec. 8.4. Since $p_0 \left(\frac{v_{\text{Lattice}}^p(t)}{v_r}, \tilde{\Omega}(t) \right)$ is periodic in $v_{\text{Lattice}}^p(t)$ with period $2v_r$, the contribution $\delta\phi_p^{\text{arm}1} - \delta\phi_p^{\text{arm}2}$ of this correction term to the phase difference between the two arms of an interferometer will be highly suppressed if both arms load the atom into the lattice near the center of the zeroth band (as discussed in Sec. 8.3) and undergo a nearly integral number of Bloch oscillations so that the effects of this periodic variation in the ground state eigenvalue will be largely common to the two arms, as verified by estimation of the integral in Eq. (8.45) and by numerically solving the Schrodinger equation.

8.10 Additional Calculation: Perturbative Adiabatic Expansion at Higher Orders

In order to calculate non-adiabatic corrections at arbitrary order, we define $C_{a \rightarrow b \rightarrow \dots \rightarrow m \rightarrow n \rightarrow j}(t)$ recursively in the natural way based on the notation of Sec. 8.4:

$$C_{a \rightarrow b \rightarrow \dots \rightarrow m \rightarrow n \rightarrow j}(t) \equiv - \int_{t_0}^t C_{a \rightarrow b \rightarrow \dots \rightarrow m \rightarrow n}(t') \vec{\Psi}_j^\dagger(t') \frac{\partial \vec{\Psi}_n(t')}{\partial t'} e^{i[\varphi_n(t') - \varphi_j(t')]} dt' \quad (8.46)$$

For arbitrary order p , we can then write:

$$b_j^{(p)}(t) = C_j(t) + \sum_{n \neq j} C_{n \rightarrow j}(t) + \sum_{n \neq j} \sum_{m \neq n} C_{m \rightarrow n \rightarrow j}(t) + \dots + \sum_{n \neq j} \sum_{m \neq n} \dots \sum_{a \neq b} C_{a \rightarrow b \rightarrow \dots \rightarrow m \rightarrow n \rightarrow j}(t) \quad (8.47)$$

where the last term includes p sums and $C_j(t) \equiv b_j^{(0)}(t_0)$.

The convergence of the perturbative series depends on the time interval of the solution. As long as the Hamiltonian does not vary at an infinitely fast rate, we can always work on a small enough time scale so that the series converges rapidly. To solve the problem on time scales for which the series does not converge quickly, we can simply break the problem into multiple parts. This method provides with us with a means to describe the system for a Hamiltonian that changes arbitrarily fast in time. Having a slowly varying Hamiltonian just serves to allow us to solve the problem without dividing it into as many parts (much of the time we will not have to divide the problem at all, and in Sec. 8.5 we derive conditions for when this will be the case), thus making the calculation significantly easier.

Chapter 9

Current Work: Equivalence Principle Test

This chapter presents ongoing work toward an equivalence principle test with atom interferometry in the 10 m atomic fountain apparatus. The measurement concept is to run simultaneous interferometers with ^{85}Rb and ^{87}Rb to make a differential acceleration measurement between the two species, with common atom optics laser beams driving the Bragg transitions for the beam splitters and mirrors. The use of common beams to drive simultaneous interferometers allows for common mode cancellation of interferometer phase noise from vibration of the retroreflection mirror and from laser phase noise. Another reason why it is essential to operate the interferometers simultaneously is to ensure that signals from the time variation of Earth's gravitational field, due to tides and seismic effects, are common to the two interferometers. The differential acceleration signal is extracted from the correlations of the ^{85}Rb and ^{87}Rb phases on each shot. We have demonstrated dual species $^{85}\text{Rb}/^{87}\text{Rb}$ interferometry with long interrogation times ($T = 1$ s pulse spacing) and LMT atom optics transferring up to $10\hbar k$, observing a high degree of common mode noise cancellation. Current work is aimed at improving signal by producing a colder dual species atom source and implementing an optimized detection scheme.

9.1 Overview

Given its fundamental importance to general relativity, there is widespread interest in testing the equivalence principle¹. Equivalence principle (EP) tests compare the accelerations g_1 and g_2 of two freely falling objects with different composition. Typically, these tests are quantified in terms of the Eötvös parameter

$$\eta \equiv \frac{|g_1 - g_2|}{\frac{1}{2} |g_1 + g_2|}. \quad (9.1)$$

Currently, the most stringent EP tests use lunar laser ranging or torsion pendula, and have $\eta \sim 10^{-13}$ [164, 165]. When making precision measurements to test physical theories, it is generally useful to perform experiments with a variety of systems, each with a different set of possible systematic errors. An approach that has received growing interest is to test the equivalence principle by using dual species atom interferometry to make a differential acceleration measurement. So far, these dual species atom interferometry based tests have reached $\eta \sim 10^{-8}$ [166]. It is a goal for the field to bridge the gap between atom interferometry and lunar laser ranging/torsion pendula and ultimately to push beyond the $\eta \sim 10^{-13}$ level. Through the use of large area, dual species atom interferometry in the 10 m atomic fountain, we are working toward this goal.

9.2 Magnetic Lensing and Launching of the Dual Species Cloud

The laser and evaporation cooling process for the dual species atom source is described in Sec. 2.3.2. After the evaporation, there are $\sim 10^7$ ^{87}Rb atoms and $\sim 10^6$ ^{85}Rb atoms. As for the ^{87}Rb only cloud, we can further reduce the velocity spread after the evaporation by applying a magnetic lensing sequence (see Ch. 6). For the ^{87}Rb only lensing described in Ch. 6, an experimental challenge was to tune the parameters of the lens (e.g., the quadrupole gradient) so that the oscillations in the radial and

¹As mentioned in Sec. 1.3.3, we focus on the weak equivalence principle.

vertical cloud sizes reached a maximum at the same time. The dual species situation is more challenging, because there are more oscillations that need to be matched. The radial and vertical size oscillations for both species need to all reach a maximum at the same time. Moreover, at this particular time, the oscillating vertical center-of-mass velocities for ^{85}Rb and ^{87}Rb need to be well-matched so that the lattice can efficiently launch both species. Data showing these oscillations is displayed in Fig. 9.1. The plotted cloud widths and center-of-mass positions are from Gaussian fits to absorption images.

In principle, it should be possible to adjust the quadrupole gradient and TOP bias field as functions of time to make the lens meet all these constraints. However, this represents a large parameter space that we have not yet fully explored. For the moment, we have chosen the quadrupole gradient and TOP bias field so that the constraints are approximately met, with some tradeoffs. In particular, as shown in Fig. 9.1, both the radial and vertical ^{85}Rb size oscillations are near a maximum, and the vertical center-of-mass velocities for ^{85}Rb and ^{87}Rb are overlapped. The radial and vertical ^{87}Rb size oscillations deviate somewhat from a maximum, causing the ^{87}Rb cloud after the lens to be hotter than the ^{85}Rb cloud. With this lensing sequence, the cloud sizes are ~ 1 cm after the atoms are launched up the full height of the fountain and fall back down into the detection region. Further optimization of the lens parameters, as suggested above, may be able to yield colder dual species clouds.

9.3 Atom Optics for the Dual Species Interferometer

A useful feature of an equivalence principle test with ^{85}Rb and ^{87}Rb is that the optical properties of the two species are similar enough [60, 61] so that Bragg transitions can be driven for both species with a common pair of spectral components. For the dual species work, we use the same high power atom optics laser system described in Chs. 2 and 7, with the same sequential $2\hbar k$ Bragg LMT atom optics sequences as those in

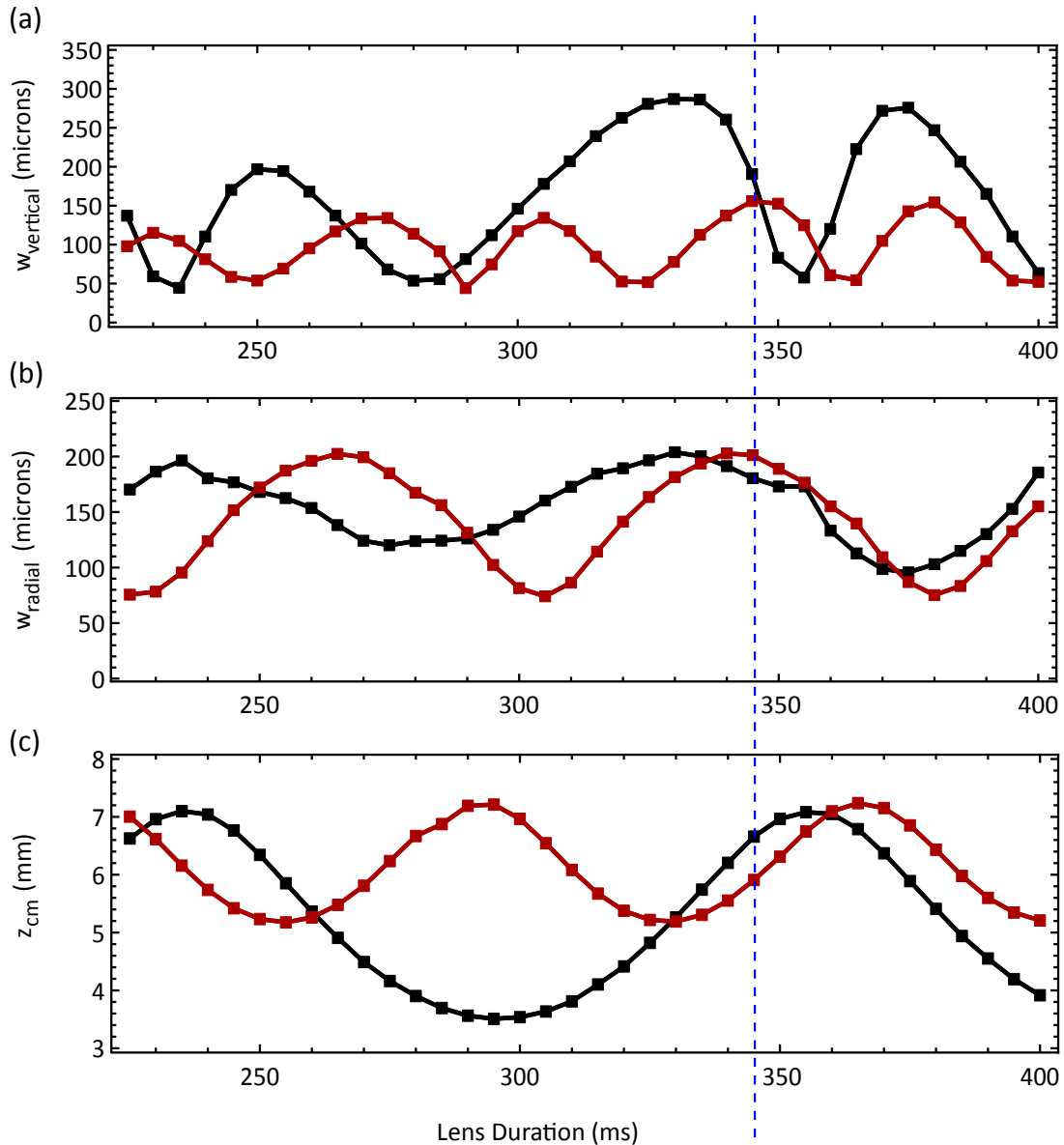


Figure 9.1: Oscillations in a dual species magnetic lens. Black curves correspond to ^{87}Rb , and red curves to ^{85}Rb . (a) Oscillations of the vertical cloud widths w_{vertical} . (b) Oscillations of the radial cloud widths w_{radial} . (c) Oscillations of the vertical center-of-mass positions z_{cm} . The lensing potential is abruptly turned off after 345 ms of oscillation, indicated by the dashed blue line.

Ch. 7.

The number of photon recoils transferred by the LMT beam splitters using this current atom optics scheme is limited by the $\approx 2\%$ difference in the recoil velocities $v_{r85} = \frac{\hbar k}{m_{85}}$ and $v_{r87} = \frac{\hbar k}{m_{87}}$ of the two species, where m_{85} is the mass of ^{85}Rb and m_{87} is the mass of ^{87}Rb . An initial velocity selection pulse selects a narrow vertical velocity slice from both the ^{85}Rb and ^{87}Rb clouds, so that at the beginning of the interferometer, both clouds have approximately the same velocity and velocity spread. As additional sequential $2\hbar k$ momentum kicks are delivered to one of the interferometer arms during the first LMT beam splitter sequence, the velocities v_{85} and v_{87} of the ^{85}Rb and ^{87}Rb clouds start to become mismatched due to the different recoil velocities. For momentum $n\hbar k$ already transferred by the beam splitter, $v_{85} = nv_{r85}$ and $v_{87} = nv_{r87}$ (up to a common initial offset value), and so this velocity mismatch is

$$\Delta v_{85/87} \equiv v_{85} - v_{87} = n\hbar k \left(\frac{1}{m_{85}} - \frac{1}{m_{87}} \right) \quad (9.2)$$

From Eq. 1.10, the detuning of the ^{85}Rb resonance frequency from the ^{87}Rb resonance frequency for the next $2\hbar k$ Bragg transition in the beam splitter sequence is

$$\delta_{85/87} = (2n + 2)\hbar k^2 \left(\frac{1}{m_{85}} - \frac{1}{m_{87}} \right) = 2\pi \times (n + 1)355 \text{ Hz.} \quad (9.3)$$

Above $10\hbar k$, this relative Doppler detuning between the two species reaches many kHz and becomes a sizeable fraction of the ~ 20 kHz Rabi frequency (see Fig. 9.2(a)). Therefore, both species cannot be simultaneously transferred efficiently. Figure 9.2b presents data illustrating this point. This data consists of measurements of the fractional atomic population remaining as a function of the number of photon momentum recoils transferred by the first beam splitter. To better measure the population loss, the initial $\pi/2$ pulse was replaced by a π pulse so that all atoms underwent a sequence of $2\hbar k$ Bragg transitions. Population loss curves for ^{85}Rb were measured under three conditions: with the Bragg beams on resonance with the ^{85}Rb Bragg transitions, with the Bragg beams on resonance with the ^{87}Rb Bragg transitions, and a compromise condition with the Bragg beams tuned midway between the ^{85}Rb and ^{87}Rb resonances. The population loss for ^{85}Rb was dramatically worse for the latter two cases

for momentum transfer above $10\hbar k$.

For this reason, our current atoms optics scheme is not suitable for LMT atom optics much above $10\hbar k$ in the context of dual species interferometry. This should be sufficient for an initial equivalence principle test. Future iterations of the experiment might seek to increase the amount of LMT through the use of atom optics techniques that are less sensitive to Doppler detunings, such as ARP-based methods (see Ch. 4) or optical lattice manipulations (see Ch. 8). Another possibility is to implement a Raman atom optics scheme. Due to the different hyperfine splittings of the two species, the two species would need to be addressed by different sets of optical sidebands. Although more complicated, such an implementation would allow the frequencies of the spectral components driving transitions for the two species to be tuned on resonance independently.

9.4 Imaging the Output Ports of Dual Species Interferometers

As described in Sec. 2.5, we use CCD cameras to detect the atoms with spatially resolved fluorescence imaging. By the time the atoms fall back down into the detection region, the upper and lower interferometer output ports for a given species are spatially separated and can be independently resolved. However, the upper (lower) output port for ^{85}Rb is spatially overlapped with the upper (lower) output port for ^{87}Rb . We therefore delay the detection of ^{87}Rb by 1.5 ms so that its output ports fall to a lower position in the camera's field of view, below the ^{85}Rb output ports (with a simple change to the timing file running the experiment, we can also make it so that the detection is instead delayed for ^{85}Rb). Once the fluorescence light is turned on for a given species, the atoms of that species are quickly brought to rest and no longer fall downward.

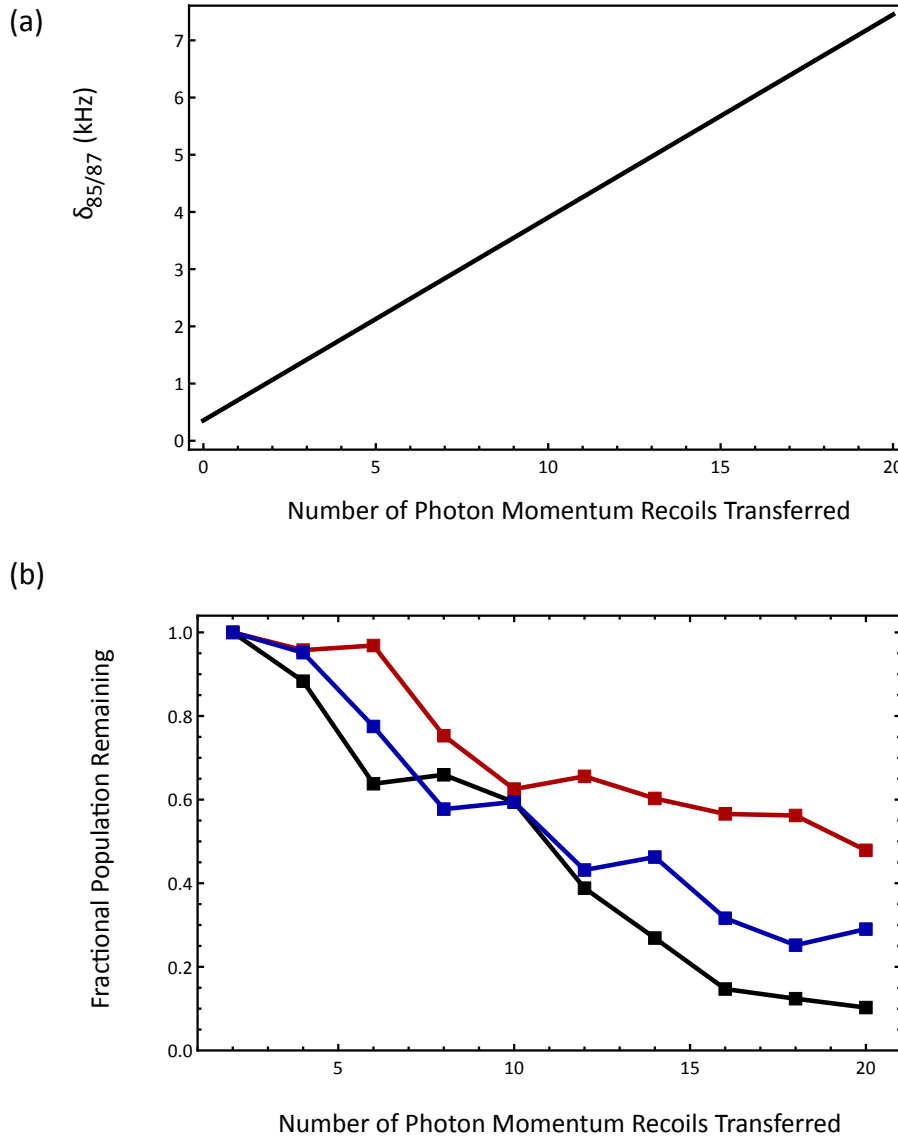


Figure 9.2: Transfer efficiency for dual species LMT atom optics. (a) Relative Doppler detuning $\delta_{85/87}$ between the two species as a function of momentum transferred (see Eq. 9.3). (b) Measurement of fractional population remaining for ^{85}Rb as a function of the number of photon momentum recoils transferred by the first beam splitter under three conditions: atom optics lasers on resonance with the ^{85}Rb Bragg transitions (red), atom optics lasers on resonance with the ^{87}Rb Bragg transitions (black), and atom optics lasers halfway between the resonances for ^{85}Rb and ^{87}Rb (blue). Transfer efficiency is significantly reduced when the lasers are moved away from the ^{85}Rb resonances.

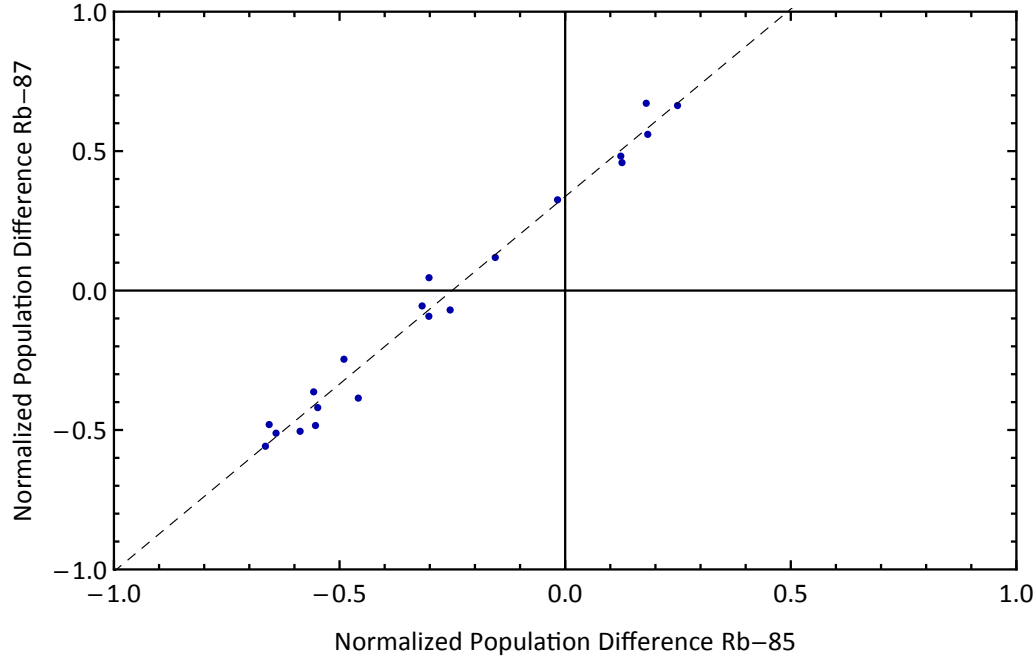


Figure 9.3: Data for a $2\hbar k$ dual species interferometer with $T = 1.04$ s. Parametric plot of the normalized population difference between the output ports for ^{85}Rb and ^{87}Rb (P_{85} and P_{87}). The dashed line with positive slope through the data points illustrates the in-phase correlation of the ^{85}Rb and ^{87}Rb interferometers.

9.5 Preliminary Dual Species Interferometry Data

9.5.1 The Differential Signal

For a dual species interferometer, the signal we ultimately want to measure is the differential phase $\delta\phi$ between the ^{85}Rb interferometer and the ^{87}Rb interferometer. For each experimental shot, we can extract the normalized population differences P_{87} and P_{85} between the two output ports of the two interferometers. Where C_{87} is the contrast of the ^{87}Rb interferometer and C_{85} is the contrast of the ^{85}Rb interferometer, these normalized population differences are given by

$$\begin{aligned} P_{87} &= C_{87} \sin(\phi) + A_{87} \\ P_{85} &= C_{85} \sin(\phi + \delta\phi) + A_{85}, \end{aligned} \quad (9.4)$$

for a common phase ϕ shared by the two interferometers and for constant offsets A_{87} and A_{85} . As discussed in Sec. 1.3.2, due to the large acceleration sensitivity of the interferometers, ϕ varies by a large amount from shot-to-shot, preventing the observation of a stable shot-to-shot fringe pattern for each individual interferometer. Since this fluctuating phase is common to the two interferometers, the differential phase $\delta\phi$ can be estimated by observing correlations in P_{87} and P_{85} [141]. For the data we have taken so far, $\delta\phi$ is close to zero, so the variations in P_{87} and P_{85} are in phase with each other. For a parametric plot with P_{85} on one axis and P_{87} on the other, the data points therefore lie approximately along a line with positive slope. Such plots are shown for a $2\hbar k$ interferometer in Fig. 9.3 and a $10\hbar k$ interferometer in Fig. 9.4. For larger $\delta\phi$, the points in such a plot would lie on an ellipse [141].

The correlations between the two interferometers can also be seen using principal component analysis (see Fig. 7.5 and the discussion thereof). Figure 9.5(a) shows a principal component from a data set of images of the dual species interferometer over 20 shots, illustrating that the upper (lower) port of the ^{85}Rb interferometer is correlated with the upper (lower) port of the ^{87}Rb interferometer. This principal component also shows that the upper ports are anti-correlated with the lower ports, which is a result of interference contrast.

9.5.2 Preliminary Analysis: Maximum Likelihood Estimation of the Differential Phase

We estimate the differential phase $\delta\phi$ using maximum likelihood analysis, which was also used and discussed in detail in Ch. 7. For the maximum likelihood estimation, we use Eq. 9.4 as a model for the two interferometer signals. To model amplitude noise in the output ports, the offsets A_{87} and A_{85} are treated as random variables with

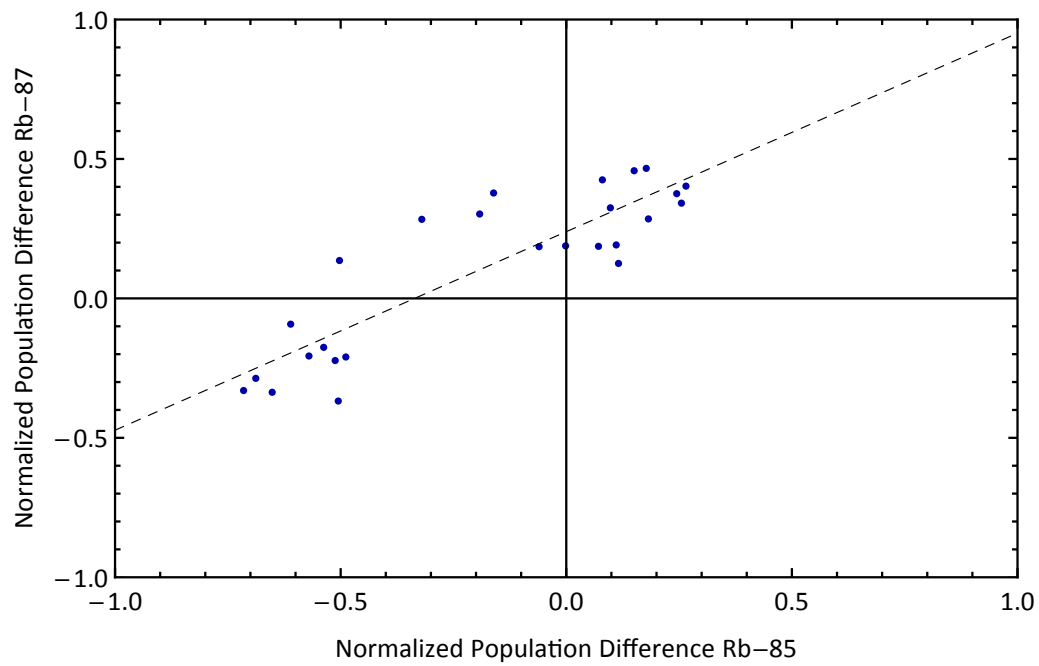


Figure 9.4: Data for a $10\hbar k$ dual species interferometer with $T = 1.04$ s. Parametric plot of the normalized population difference between the output ports for ^{85}Rb and ^{87}Rb (P_{85} and P_{87}). The dashed line with positive slope through the data points illustrates the in-phase correlation of the ^{85}Rb and ^{87}Rb interferometers.

normally distributed probability density functions (PDFs). The means and standard deviations of these PDFs are estimated from the data. Maximum likelihood estimation is used separately on the ^{85}Rb and ^{87}Rb data points to estimate the contrasts C_{87} and C_{85} and their respective uncertainties. Subsequently, using just the ^{87}Rb data, maximum likelihood estimation is once again applied to find PDFs for the overall phase ϕ of each shot. Finally, these PDFs, the information about the contrast, and the model in Eq. 9.4 are used for a maximum likelihood estimation of $\delta\phi$ for the data set, incorporating the ^{85}Rb data.

The uncertainty in $\delta\phi$ given by the maximum likelihood analysis, combined with knowledge of the interferometer scale factor, allows us to determine the statistical uncertainty of the measurement. For the $k_{\text{eff}} = 2\hbar k$ interferometer, the interferometer phase shift $-k_{\text{eff}}gT^2$ has magnitude 1.7×10^8 rad. For a typical data set of 20 shots, $\delta\phi$ is consistent with zero with statistical uncertainty 0.055 rad, corresponding to a statistical uncertainty in the Eötvös parameter of 3×10^{-10} . After averaging over five sets of 20 shots, the statistical uncertainty in the Eötvös parameter is 1.4×10^{-10} . For the $k_{\text{eff}} = 10\hbar k$ interferometer, the interferometer phase shift has magnitude 8.5×10^8 rad, and the statistical uncertainty in the differential phase is 0.08 rad after 20 shots. This corresponds to a statistical uncertainty in the Eötvös parameter of 9×10^{-11} . At the moment, the statistical resolution is limited by detection noise. As described in Sec. 9.7, upgrades to the system to dramatically improve the detection signal-to-noise are currently underway.

9.5.3 Phase Shear Readout

An alternate method that we may ultimately use to determine the differential phase shift is to use phase shear readout [41]. This involves purposefully imprinting a phase gradient across the atom cloud, so that the output ports have a spatially dependent interference fringe. For each of the two interferometers, the position of this interference fringe relative to a fixed point in the fluorescence image allows the interferometer phase to be determined (modulo 2π) in a single shot, without the need for additional measurements to determine the interferometer contrast and output port

offsets. This makes phase determination insensitive to noise in the contrast or in the offsets. Note that phase shear readout with a vertical spatial fringe across the cloud was used in Fig. 7.5.

For the dual species interferometer, we demonstrated that phase shear readout can be implemented by adding an additional tilt to the retroreflection mirror angle of $60 \mu\text{rad}$ before the final beam splitter, leading to horizontal spatial fringes across the cloud [41]. The fringes can be seen through principal component analysis, as shown in Fig. 9.5(b). Ongoing work will assess the merits of phase shear readout as compared to standard readout (counting atoms in the ports) for an improved atom source (see Sec. 9.7).

9.6 Consideration of Systematic Effects

A critical aspect of the equivalence principle test will be to experimentally study systematic errors. The differential phase shifts arising from a number of possible systematic effects—including gravity gradients, rotations, and magnetic field gradients—have been studied in detail theoretically in [8]. The coupling of the initial positions and velocities of the two atom clouds to gravity gradients is essential to consider. If the initial kinematics for the two clouds are systematically different, gravity gradients can cause the two clouds to experience different effective gravitational accelerations during the interferometer. A possible strategy for managing this effect is to use spatially resolved imaging to measure the initial positions and velocities for each shot. The initial position could be measured by applying a short absorption imaging pulse while the atoms are still in the 3D MOT chamber, such that only a small fraction of the atoms absorb photons and are lost from the signal. The initial velocity could be measured through time-of-flight imaging with the spatially resolved fluorescence images of the interferometer output ports.

Another recently suggested strategy for mitigating systematic errors from gravity gradients is to hop the atom optics laser frequency ν by an amount $\delta\nu = (\Gamma T^2/2) \nu$ for the mirror pulse only [167], where Γ is the gravity gradient. As shown in [167], this eliminates all couplings of the initial kinematics to the gravity gradient from the phase

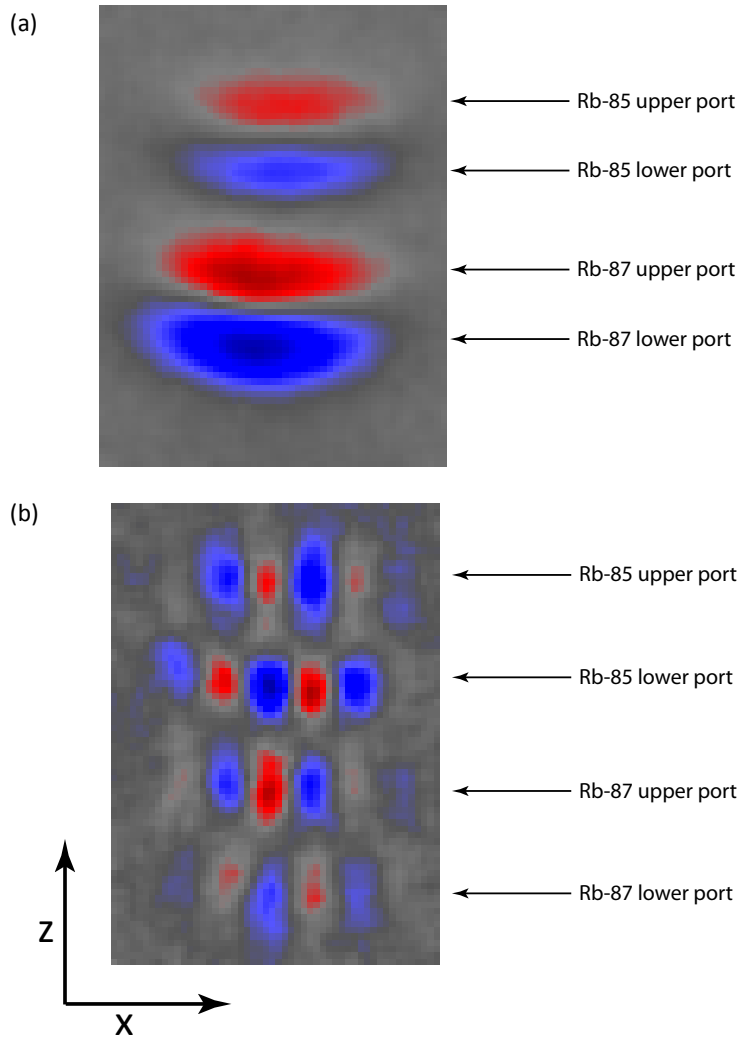


Figure 9.5: Principal component analysis for $2\hbar k$ dual species interferometry. Red and blue regions are anti-correlated, while regions of the same color are correlated with each other. (a) Principal component showing the correlation between the ^{85}Rb and ^{87}Rb interferometers. The upper (lower) port of the ^{85}Rb interferometer is correlated with the upper (lower) port of the ^{87}Rb interferometer. Interference is indicated by the anti-correlation of the two upper ports with the two lower ports. (b) Principal component showing horizontal fringes induced by tilting the retroreflection mirror before the final beam splitter. The fringes on the two upper (lower) output ports have the same phase, showing the correlation between the two interferometers.

shift. The frequency change $\delta\nu$ would be on the order of 1 GHz for our experiment, which could easily be implemented by shifting the phase modulation frequencies of the atom optics lasers. By measuring the local gravity gradient and implementing the corresponding frequency shift $\delta\nu$, it might be possible to ease constraints on the initial kinematics by several orders of magnitude. Additional systematic effects could come from spatial variations in the gravity gradient over the interferometer region arising from the local mass distribution. Ultimately, we will likely want to measure the gravity gradient as a function of height using shorter time interferometers.

As discussed in Sec. 2.7.1, magnetic field gradients are another potential source of systematic error, because ^{85}Rb and ^{87}Rb have different second order Zeeman coefficients. It will be helpful to measure the magnetic field along the height of the interferometer region by using interferometers with magnetically sensitive states. Another possible method to characterize systematic effects from magnetic field gradients is to alternate between running the interferometers with atoms in the upper ground state hyperfine level versus the lower ground state hyperfine level, as the second order Zeeman coefficients for the upper and lower hyperfine levels have opposite signs [60, 61].

9.7 Upgrades Underway

As mentioned in Sec. 9.5.2, the statistical sensitivity of the dual species interferometer is currently limited by detection noise. The signal suffers from the fact that the atom clouds are hotter than desired. This leads the clouds to have a large transverse size at the time of fluorescence detection, so that number of counts on a given camera pixel is reduced. Moreover, the hotter clouds lead to increased atom loss from the velocity selection pulse, further reducing signal. In order to have a reasonable number of counts per pixel, we need to use a relatively long fluorescence imaging time of 10 – 11 ms, leading to increased atom cloud heating and causing neighboring output ports to be significantly blurred together, which is not desirable for a clean signal. It is possible to increase the output port spacing by adding an additional π pulse after the final beam splitter to increase the momentum splitting of the two output ports for a given

interferometer to $4\hbar k$. However, if the spacing between the ports is increased enough to eliminate blurring, the four output ports (two from each interferometer) do not fit into the field of view of a single camera. This latter problem can be solved by using a pair of vertically offset cameras, an upgrade that we plan to implement shortly.

Current work is aimed at improving the signal by implementing an optical dipole lens after the lattice launch to reduce the transverse velocity spread of the clouds, as done in Ch. 6 for ^{87}Rb only. Additionally, we plan to try evaporation in an optically plugged trap, which was previously implemented for ^{87}Rb only [11, 12] and could lead to a colder dual species source with more atoms. With these improvements to detection and the dual species atom source, we hope to be able to reach phase resolution corresponding to the atom shot noise limit with $\sim 10^5 - 10^6$ atoms of each species per shot. The atom shot noise limit is a bound on how precisely the interferometer phase can be measured on a single shot by counting how N atoms are distributed between two interferometer output ports (this is called count data, and the statistics describing it is called counting statistics). The interferometer phase specifies the probability that each atom will end up in one output port versus the other. For a given phase, the number of atoms measured in each of the two output ports therefore follows a binomial distribution. The variance of the binomial distribution limits the degree to which a measured distribution of atoms between the two ports can be used to determine the phase. For N atoms contributing to the measurement, the atom shot noise limit on the phase resolution per shot is $1/\sqrt{N}$.

Chapter 10

Conclusion

This thesis presents the development of several new methods for large momentum transfer (LMT) atom optics and the use of these methods to realize atom interferometers with very large momentum transfer beam splitters ($100\hbar k$) for the first time. Furthermore, we have shown that the considerable challenges associated with combining LMT atom optics with long duration atom interferometry can be overcome, allowing us to demonstrate truly macroscopic interferometers in a 10 m atomic fountain. Data is presented showing the application of these macroscopic interferometers to a test of the equivalence principle with ^{85}Rb and ^{87}Rb .

We have also used a combination of magnetic and optical dipole lensing to prepare and measure ensembles of ^{87}Rb atoms with record-low effective temperatures of 50 pK. In order to achieve this, we studied the factors that limit lens performance and developed techniques to mitigate them. Atom sources at these extremely low effective temperatures will be crucial for a variety of future experiments, including envisioned atom interferometers with interrogation times of tens or even hundreds of seconds.

Additionally, through the use of coherent combination and frequency doubling, we have demonstrated a suitable atom optics laser source at 780 nm with a record-high power for such a source of 43 W. A variant of this laser source was essential to the success of the large area interferometry experiments in the 10 m atomic fountain.

The 10 m atomic fountain has an exciting future ahead of it. At the moment,

progress on the equivalence principle test is continuing. The dual species interferometer statistical sensitivity that we have already demonstrated suggests that this test will exceed previous atom interferometry tests of the equivalence principle by multiple orders of magnitude, and we are optimistic that our apparatus will be competitive with the most precise equivalence principle tests realized using other methods. After the equivalence principle test, there are many exciting directions for the apparatus to explore. The apparatus could be used to measure the gravitational potential from a well-characterized test mass, leading to a new measurement of Newton's gravitational constant. It would be interesting to build a prototype atomic gravitational wave detector by implementing large area interferometers in a gravity gradiometer setup with a long baseline of multiple meters¹. To this end, it would intriguing to push atom interferometry in the 10 m fountain to its physical limits, using $1000\hbar k$ beam splitters (possibly optical lattice based) to separate the interferometer wave packets by 10 m. Moreover, the use of a refocusing lens to allow the atoms to be caught and relaunched multiple times, per the demonstration in Ch. 6, could enable the interferometer duration to be pushed to > 10 s.

¹The interferometers in Ch. 7 are gravity gradiometers with a baseline equal to the millimeter cloud size. Despite the short baseline, the large intrinsic acceleration sensitivity of the interferometers allows the gravity gradient sensitivity to be significant: for the largest momentum transfer, a gravity gradient of $10^{-7} g/m$ leads to a ~ 1 rad differential phase shift between the upper and lower parts of the atom cloud. The sensitivity of a gravity gradiometer grows linearly with the baseline length, so an increase of the baseline length to the full 10 m height of the fountain would lead to a four order of magnitude increase in gravity gradient sensitivity.

Bibliography

- [1] Alexander D. Cronin, David E. Pritchard, and J. Schmiedmayer. Optics and interferometry with atoms and molecules. *Reviews of Modern Physics*, 81(3):1051–1129, July 2009.
- [2] H. J. Metcalf and P. van der Straten. *Laser Cooling and Trapping*. Springer-Verlag, New York, 1999.
- [3] Peter W. Graham, Jason M. Hogan, Mark A. Kasevich, and Surjeet Rajendran. New Method for Gravitational Wave Detection with Atomic Sensors. *Physical Review Letters*, 110(17):171102, April 2013.
- [4] P. R. Berman, editor. *Atom Interferometry*. Academic Press, New York, 1997.
- [5] M. Kasevich and S. Chu. Atomic interferometry using stimulated Raman transitions. *Phys. Rev. Lett.*, 67(2):181–184, July 1991.
- [6] M. Kozuma, L. Deng, E. W. Hagley, J. Wen, R. Lutwak, K. Helmerson, S. L. Rolston, and W. D. Phillips. Coherent Splitting of Bose-Einstein Condensed Atoms with Optically Induced Bragg Diffraction. *Physical Review Letters*, 82(5):871–875, 1999.
- [7] P. Storey and C. Cohen-Tannoudji. The Feynman path integral approach to atomic interferometry: A tutorial. *J. Phys. II (France)*, 4:1999, 1994.
- [8] J. M. Hogan, D. M. S. Johnson, and M. A. Kasevich. Light-pulse atom interferometry. In E. Arimondo, W. Ertmer, and W. P. Schleich, editors, *Proc. Int.*

- School Phys. Enrico Fermi, Course CLXVIII*, pages 411–447. IOS Press, June 2009.
- [9] H. Müntinga, H. Ahlers, M. Krutzik, A. Wenzlawski, S. Arnold, D. Becker, K. Bongs, H. Dittus, H. Duncker, N. Gaaloul, C. Gherasim, E. Giese, C. Grzeschik, T. W. Hänsch, O. Hellmig, W. Herr, S. Herrmann, E. Kajari, S. Kleinert, C. Lämmerzahl, W. Lewoczko-Adamczyk, J. Malcolm, N. Meyer, R. Nolte, A. Peters, M. Popp, J. Reichel, A. Roura, J. Rudolph, M. Schiemangk, M. Schneider, S. T. Seidel, K. Sengstock, V. Tamma, T. Valenzuela, A. Vogel, R. Walser, T. Wendrich, P. Windpassinger, W. Zeller, T. van Zoest, W. Ertmer, W. P. Schleich, and E. M. Rasel. Interferometry with Bose-Einstein Condensates in Microgravity. *Physical Review Letters*, 110(9):093602, February 2013.
 - [10] J. M. McGuirk, M. J. Snadden, and M. A. Kasevich. Large area light-pulse atom interferometry. *Phys. Rev. Lett.*, 85(21):4498–4501, November 2000.
 - [11] Susannah Dickerson. *Long-Time Atom Interferometry for Precision Tests of Fundamental Physics*. Doctoral thesis, Stanford University, 2014.
 - [12] Alex Sugarbaker. *Atom Interferometry in a 10 m Fountain*. Doctoral thesis, Stanford University, 2014.
 - [13] A. Peters, K. Y. Chung, and S. Chu. High-precision gravity measurements using atom interferometry. *Metrologia*, 38:25–61, 2001.
 - [14] Peter J. Martin, Bruce G. Oldaker, Andrew H. Miklich, and David E. Pritchard. Bragg Scattering of Atoms from a Standing Light Wave. *Physical Review Letters*, 60(6):515–518, 1988.
 - [15] David M. Giltner, Roger W. McGowan, and Siu Au Lee. Atom Interferometer Based on Bragg Scattering from Standing Light Waves. *Physical Review Letters*, 75(14):2638–2641, 1995.

- [16] H. Müller, S.-W. Chiow, and S. Chu. Atom-wave diffraction between the Raman-Nath and the Bragg regime: Effective Rabi frequency, losses, and phase shifts. *Phys. Rev. A*, 77:023609, Feb 2008.
- [17] H. Müller, S.-W. Chiow, Q. Long, S. Herrmann, and S. Chu. Atom Interferometry with up to 24-Photon-Momentum-Transfer Beam Splitters. *Phys. Rev. Lett.*, 100(18):180405, May 2008.
- [18] S. S. Szigeti, J. E. Debs, J. J. Hope, N. P. Robins, and J. D. Close. Why momentum width matters for atom interferometry with Bragg pulses. *New J. Phys.*, 14(2):023009, 2012.
- [19] Michael M. T. Loy. Observation of Population Inversion by Optical Adiabatic Rapid Passage. *Physical Review Letters*, 32(15):814–817, 1974.
- [20] Nikolay V. Vitanov, Thomas Halfmann, Bruce W. Shore, and Klaas Bergmann. Laser-Induced Population Transfer by Adiabatic Passage Techniques. *Annu. Rev. Phys. Chem.*, 52:763–809, 2001.
- [21] Boyan T. Torosov, Stéphane. Guérin, and Nikolay V. Vitanov. High-fidelity adiabatic passage by composite sequences of chirped pulses. *Physical review letters*, 106(23):233001, June 2011.
- [22] Krish Kotru, David L Butts, Joseph M Kinast, and Richard E Stoner. Large-Area Atom Interferometry with Frequency-Swept Raman Adiabatic Passage. *Physical review letters*, 115(10):103001, September 2015.
- [23] J. Hecker Denschlag, J. E. Simsarian, H. Häffner, C. McKenzie, A. Browaeys, D. Cho, K. Helmerson, S. L. Rolston, and W. D. Phillips. A Bose-Einstein condensate in an optical lattice. *J. Phys. B.: At. Mol. Opt. Phys.*, 35:3095–3110, 2002.
- [24] P. Cladé, S. Guellati-Khélifa, F. Nez, and F. Biraben. Large momentum beam splitter using bloch oscillations. *Phys. Rev. Lett.*, 102(24):240402, Jun 2009.

- [25] Holger Müller, Sheng-wei Chiow, Sven Herrmann, and Steven Chu. Atom interferometers with scalable enclosed area. *Physical Review Letters*, 102(24):240403, June 2009.
- [26] G. D. McDonald, C. C. N. Kuhn, S. Bennetts, J. E. Debs, K. S. Hardman, M. Johnsson, J. D. Close, and N. P. Robins. $80 \hbar k$ momentum separation with Bloch oscillations in an optically guided atom interferometer. *Physical Review A*, 88(5):053620, November 2013.
- [27] Ekkehard Peik, Maxime Ben Dahan, Isabelle Bouchoule, Yvan Castin, and Christophe Salomon. Bloch oscillations of atoms, adiabatic rapid passage, and monokinetic atomic beams. *Physical Review A*, 55(4):2989–3001, 1997.
- [28] T. L. Gustavson, P. Bouyer, and M. A. Kasevich. Precision Rotation Measurements with an Atom Interferometer Gyroscope. *Physical Review Letters*, 78(11):2046–2049, 1997.
- [29] Susannah M. Dickerson, Jason M. Hogan, Alex Sugarbaker, David M. S. Johnson, and Mark A. Kasevich. Multiaxis Inertial Sensing with Long-Time Point Source Atom Interferometry. *Physical Review Letters*, 111(8):083001, August 2013.
- [30] M. J. Snadden, J. M. McGuirk, P. Bouyer, K. G. Haritos, and M. A. Kasevich. Measurement of the Earths Gravity Gradient with an Atom Interferometer-Based Gravity Gradiometer. *Physical Review Letters*, 81(5):971–974, 1998.
- [31] R. Bouchendira, P. Cladé, S. Guellati-Khélifa, F. Nez, and F. Biraben. New Determination of the Fine Structure Constant and Test of the Quantum Electrodynamics. *Phys. Rev. Lett.*, 106(8):080801, February 2011.
- [32] G. Rosi, F. Sorrentino, L. Cacciapuoti, M. Prevedelli, and G. M. Tino. Precision measurement of the newtonian gravitational constant using cold atoms. *Nature*, 510(7506):518–521, 2014.

- [33] A. Bonnin, N. Zahzam, Y. Bidel, and A. Bresson. Simultaneous dual-species matter-wave accelerometer. *Phys. Rev. A*, 88(4):043615, October 2013.
- [34] D. Schlippert et al. Quantum Test of the Universality of Free Fall. *Phys. Rev. Lett.*, 112(20):203002, May 2014.
- [35] C. C. N. Kuhn et al. A Bose-condensed, simultaneous dual-species Mach-Zehnder atom interferometer. *New J. Phys.*, 16(7):073035, 2014.
- [36] R. Geiger et al. Detecting inertial effects with airborne matter-wave interferometry. *Nat. Commun.*, 2:474, January 2011.
- [37] Savas Dimopoulos, Peter Graham, Jason Hogan, and Mark Kasevich. General relativistic effects in atom interferometry. *Physical Review D*, 78(4):042003, August 2008.
- [38] M. Arndt and K. Hornberger. Testing the limits of quantum mechanical superpositions. *Nat. Phys.*, 10(April):271–277, 2014.
- [39] S. Dimopoulos, P. Graham, J. Hogan, M. Kasevich, and S. Rajendran. Atomic gravitational wave interferometric sensor. *Phys. Rev. D*, 78(12):122002, December 2008.
- [40] Jason M. Hogan, David M. S. Johnson, Susannah Dickerson, Tim Kovachy, Alex Sugarbaker, Sheng-wei Chiow, Peter W. Graham, Mark A. Kasevich, Babak Saif, Surjeet Rajendran, Philippe Bouyer, Bernard D. Seery, Lee Feinberg, and Ritva Keski-Kuha. An atomic gravitational wave interferometric sensor in low earth orbit (AGIS-LEO). *General Relativity and Gravitation*, 43(7):1953–2009, May 2011.
- [41] A. Sugarbaker, S. M. Dickerson, J. M. Hogan, D. M. S. Johnson, and M. A. Kasevich. Enhanced Atom Interferometer Readout through the Application of Phase Shear. *Phys. Rev. Lett.*, 111(11):113002, September 2013.

- [42] J. M. McGuirk, G. T. Foster, J. B. Fixler, M. J. Snadden, and M. A. Kasevich. Sensitive absolute-gravity gradiometry using atom interferometry. *Physical Review A*, 65(3):033608, February 2002.
- [43] Sean M. Carroll. *Spacetime and Geometry: An Introduction to General Relativity*. Addison-Wesley, San Francisco, 2004.
- [44] R. P. Feynman, R. B. Leighton, and M. Sands. *The Feynman Lectures on Physics Volume III*. Addison-Wesley, Reading, MA, 1965.
- [45] B. P. Abbott et al. Observation of Gravitational Waves from a Binary Black Hole Merger. *Physical Review Letters*, 116(6):061102, February 2016.
- [46] K. Kawabe and the LIGO Collaboration. Status of LIGO. *Journal of Physics: Conference Series*, 120(3):032003, 2008.
- [47] J. R. Smith and the LIGO Collaboration. The path to the enhanced and advanced LIGO gravitational-wave detectors. *Classical and Quantum Gravity*, 26(11):114013, 2009.
- [48] F. Acernese et al. Methods of gravitational wave detection in the VIRGO Interferometer. *AIP Conference Proceedings*, 924:187, 2007.
- [49] Shane L. Larson, William A. Hiscock, and Ronald W. Hellings. Sensitivity curves for spaceborne gravitational wave interferometers. *Phys. Rev. D*, 62(6):062001, Aug 2000.
- [50] Douglas D. Osheroff. Superfluidity in ^3He : Discovery and Understanding. In G. Ekspong, editor, *Nobel Lectures, Physics 1996-2000*. World Scientific Publishing Co., 2002.
- [51] Steven Chu. The Manipulation of Neutral Particles. In G. Ekspong, editor, *Nobel Lectures, Physics 1996-2000*. World Scientific Publishing Co., 2002.
- [52] Wolfgang Ketterle. When Atoms Behave as Waves: Bose-Einstein Condensation and the Atom Laser. In Tore Frängsmere, editor, *The Nobel Prizes 2001*, volume 1995, pages 118–154. Nobel Foundation, 2001.

- [53] S. Chu, J. E. Bjorkholm, A. Ashkin, J. P. Gordon, and L. W. Hollberg. Proposal for optically cooling atoms to temperatures of the order of 10^{-6} K. *Optics Letters*, 11(2):73, February 1986.
- [54] Jason Hogan. *Towards Precision Tests of General Relativity Using an Atom Interferometer*. Doctoral thesis, Stanford University, 2010.
- [55] David Johnson. *Long Baseline Atom Interferometry*. Doctoral thesis, Stanford University, 2011.
- [56] N. S. Bhaskar and C. M. Kahla. Cesium Gettering by Graphite-Improvement in the Gettering Efficiency. *IEEE Transactions on Ultrasonics, Ferroelectrics, and Frequency Control*, 37(5):355–358, 1990.
- [57] D. M. S. Johnson, J. M. Hogan, S. w. Chiow, and M. A. Kasevich. Broadband optical serrodyne frequency shifting. *Opt. Lett.*, 35(5):745–747, Mar 2010.
- [58] V. I. Kovalev and R. G. Harrison. Threshold for stimulated Brillouin scattering in optical fiber. *Optics Express*, 15(26):17625–17630, 2007.
- [59] Susannah Dickerson, Jason M. Hogan, David M. S. Johnson, Tim Kovachy, Alex Sugarbaker, Sheng-wei Chiow, and Mark A. Kasevich. A high-performance magnetic shield with large length-to-diameter ratio. *The Review of Scientific Instruments*, 83(6):065108, June 2012.
- [60] D. A. Steck. Rubidium 85 D Line Data. Technical report, 2008.
- [61] D. A. Steck. Rubidium 87 D Line Data. Technical report, 2008.
- [62] Sheng-wei Chiow, Tim Kovachy, Hui-Chun Chien, and Mark A. Kasevich. 102 $\hbar k$ Large Area Atom Interferometers. *Physical Review Letters*, 107(13):130403, September 2011.
- [63] C. J. Bordé. Atomic interferometry with internal state labelling. *Phys. Lett. A*, 140(12):10 – 12, 1989.

- [64] Tim Kovachy, Jason M. Hogan, David M. S. Johnson, and Mark A. Kasevich. Optical lattices as waveguides and beam splitters for atom interferometry: An analytical treatment and proposal of applications. *Physical Review A*, 82(1):013638, July 2010.
- [65] I. T. Jolliffe. *Principal Component Analysis*. Springer, New York, 2002.
- [66] Stephen R. Segal, Quentin Diot, Eric A. Cornell, Alex A. Zozulya, and Dana Z. Anderson. Revealing buried information: Statistical processing techniques for ultracold-gas image analysis. *Physical Review A*, 81(5):053601, May 2010.
- [67] B. P. Anderson. *Bose-Einstein condensation and macroscopic interference with atomic tunnel arrays*. Ph.d. thesis, 2000.
- [68] C. Orzel, A. K. Tuchman, M. L. Fenselau, M. Yasuda, and M. A. Kasevich. Squeezed States in a Bose-Einstein Condensate. *Science*, 291:2386–2389, 2001.
- [69] Wei Li, Ari K. Tuchman, Hui-Chun Chien, and Mark A. Kasevich. Extended coherence time with atom-number squeezed states. *Physical review letters*, 98(4):040402, January 2007.
- [70] J. Stenger, S. Inouye, A. P. Chikkatur, D. M. Stamper-Kurn, D. E. Pritchard, and W. Ketterle. Bragg Spectroscopy of a Bose-Einstein Condensate. *Physical Review Letters*, 82(23):4569–4573, 1999.
- [71] A. Imamoglu, M. Lewenstein, and L. You. Inhibition of Coherence in Trapped Bose-Einstein Condensates. *Physical Review Letters*, 78(13):2511–2514, 1997.
- [72] Sheng-Wey Chiow, Sven Herrmann, Steven Chu, and Holger Müller. Noise-immune conjugate large-area atom interferometers. *Physical review letters*, 103(5):050402, July 2009.
- [73] Holger Müller, Sheng-wey Chiow, Sven Herrmann, Steven Chu, and Keng-Yeow Chung. Atom-Interferometry Tests of the Isotropy of Post-Newtonian Gravity. *Physical Review Letters*, 100(3):031101, January 2008.

- [74] Tim Kovachy, Sheng-wei Chiow, and Mark A. Kasevich. Adiabatic-rapid-passage multiphoton Bragg atom optics. *Physical Review A*, 86(1):011606, July 2012.
- [75] L. M. K. Vandersypen and I. L. Chuang. NMR techniques for quantum control and computation. *Reviews of Modern Physics*, 76:1037–1069, 2005.
- [76] M. H. Levitt and R. Freeman. NMR Population Inversion Using a Composite Pulse. *Journal of Magnetic Resonance*, 33:473–476, 1979.
- [77] R. Tycko. Broadband Population Inversion. *Physical Review Letters*, 51(9):775–777, 1983.
- [78] Malcolm H. Levitt. Composite Pulses. *Progress in NMR Spectroscopy*, 18:61–122, 1986.
- [79] Ingela Roos and Klaus Mølmer. Quantum computing with an inhomogeneously broadened ensemble of ions: Suppression of errors from detuning variations by specially adapted pulses and coherent population trapping. *Physical Review A*, 69(2):022321, February 2004.
- [80] Charles D. Hill. Robust controlled-NOT gates from almost any interaction. *Physical review letters*, 98(18):180501, May 2007.
- [81] H. Häffner, C. F. Roos, and R. Blatt. Quantum computing with trapped ions. *Physics Reports*, 469(4):155–203, December 2008.
- [82] Boyan T. Torosov and Nikolay V. Vitanov. Smooth composite pulses for high-fidelity quantum information processing. *Physical Review A*, 83(5):053420, May 2011.
- [83] Svetoslav S. Ivanov and Nikolay V. Vitanov. High-fidelity local addressing of trapped ions and atoms by composite sequences of laser pulses. *Opt. Lett.*, 36(7):1275–1277, Apr 2011.

- [84] Svetoslav S. Ivanov and Nikolay V. Vitanov. Scalable uniform construction of highly conditional quantum gates. *Physical Review A*, 84(2):022319, August 2011.
- [85] G. T. Genov, B. T. Torosov, and N. V. Vitanov. Optimized control of multistate quantum systems by composite pulse sequences. *Physical Review A*, 84(6):063413, December 2011.
- [86] J. K. Stockton, K. Takase, and M. A. Kasevich. Absolute geodetic rotation measurement using atom interferometry. *Physical review letters*, 107(13):133001, September 2011.
- [87] J. E. Debs, P. A. Altin, T. H. Barter, D. Döring, G. R. Dennis, G. McDonald, R. P. Anderson, J. D. Close, and N. P. Robins. Cold-atom gravimetry with a Bose-Einstein condensate. *Physical Review A*, 84(3):033610, September 2011.
- [88] Shau-Yu Lan, Pei-Chen Kuan, Brian Estey, Philipp Haslinger, and Holger Müller. Influence of the Coriolis Force in Atom Interferometry. *Physical Review Letters*, 108(9):090402, February 2012.
- [89] C. P. Slichter. *Principles of Magnetic Resonance*. Springer, Berlin, 1978.
- [90] S.-W. Chiow, T. Kovachy, J. M. Hogan, and M. A. Kasevich. Generation of 43 W of quasi-continuous 780 nm laser light via high-efficiency, single-pass frequency doubling in periodically poled lithium niobate crystals. *Opt. Lett.*, 37(18):3861–3863, September 2012.
- [91] B. V. Zhdanov, J. Sell, and R. J. Knize. Multiple laser diode array pumped Cs laser with 48 W output power. *Electronics Letters*, 44(9):2008, 2008.
- [92] Boris V. Zhdanov, Adam Stooke, Gregory Boyadjian, Adam Voci, and R. J. Knize. Rubidium vapor laser pumped by two laser diode arrays. *Optics Letters*, 33(5):414–415, 2008.
- [93] Jason Zweiback and William F. Krupke. 28W average power hydrocarbon-free rubidium diode pumped alkali laser. *Optics Express*, 18(2):1444–1449, 2010.

- [94] G. K. Samanta, S. Chaitanya Kumar, K. Devi, and M. Ebrahim-Zadeh. Multicrystal, continuous-wave, single-pass second-harmonic generation with 56% efficiency. *Optics Letters*, 35(20):3513–3515, 2010.
- [95] S. Chaitanya Kumar, G. K. Samanta, K. Devi, and M. Ebrahim-Zadeh. High-efficiency, multicrystal, single-pass, continuous-wave second harmonic generation. *Optics Express*, 19(12):11152–11169, 2011.
- [96] Krishnan R. Parameswaran, Jonathan R. Kurz, Rostislav V. Roussov, and Martin M. Fejer. Observation of 99% pump depletion in single-pass second-harmonic generation in a periodically poled lithium niobate waveguide. *Optics Letters*, 27(1):43–45, 2002.
- [97] Luke R. Taylor, Yan Feng, and Domenico Bonaccini Calia. 50W CW visible laser source at 589nm obtained via frequency doubling of three coherently combined narrow-band Raman fibre amplifiers. *Optics Express*, 18(8):8540–8555, 2010.
- [98] R. J. Thompson, M. Tu, D. C. Aveline, N. Lundblad, and L. Maleki. High power single frequency 780nm laser source generated from frequency doubling of a seeded fiber amplifier in a cascade of PPLN crystals. *Optics Express*, 11(14):1709–1713, 2003.
- [99] F. Lienhart, S. Boussen, O. Carraz, N. Zahzam, Y. Bidel, and A. Bresson. Compact and robust laser system for rubidium laser cooling based on the frequency doubling of a fiber bench at 1560nm. *Applied Physics B*, 89(2-3):177–180, September 2007.
- [100] V. Ménoret, R. Geiger, G. Stern, N. Zahzam, B. Battelier, A. Bresson, A. Landragin, and P. Bouyer. Dual-wavelength laser source for onboard atom interferometry. *Optics Letters*, 36(21):4128–4130, 2011.
- [101] S. S. Sané, S. Bennetts, J. E. Debs, C. C. N. Kuhn, G. D. McDonald, P. A. Altin, J. D. Close, and N. P. Robins. 11 W narrow linewidth laser source at 780nm for laser cooling and manipulation of Rubidium. *Optics Express*, 20(8):8915–8919, 2012.

- [102] T. Kovachy et al. Matter Wave Lensing to Picokelvin Temperatures. *Phys. Rev. Lett.*, 114(14):143004, April 2015.
- [103] Stefan Nimmrichter and Klaus Hornberger. Macroscopicity of Mechanical Quantum Superposition States. *Physical Review Letters*, 110:160403, 2013.
- [104] Angelo Bassi, Kinjalk Lochan, Seema Satin, Tejinder Singh, and Hendrik Ulbricht. Models of wave-function collapse, underlying theories, and experimental tests. *Reviews of Modern Physics*, 85(2):471–527, April 2013.
- [105] G. Wilpers, T. Binnewies, C. Degenhardt, U. Sterr, J. Helmcke, and F. Riehle. Optical Clock with Ultracold Neutral Atoms. *Physical Review Letters*, 89(23):230801, November 2002.
- [106] Olaf Mandel, Markus Greiner, Artur Widera, Tim Rom, Theodor W. Hänsch, and Immanuel Bloch. Controlled collisions for multi-particle entanglement of optically trapped atoms. *Nature*, 425(6961):937–40, October 2003.
- [107] Waseem S. Bakr, Jonathon I. Gillen, Amy Peng, Simon Fölling, and Markus Greiner. A quantum gas microscope for detecting single atoms in a Hubbard-regime optical lattice. *Nature*, 462(7269):74–7, November 2009.
- [108] A. E. Leanhardt, T. A. Pasquini, M. Saba, A. Schirotzek, Y. Shin, D. Kielpinski, D. E. Pritchard, and W. Ketterle. Cooling Bose-Einstein condensates below 500 picokelvin. *Science*, 301(5639):1513–5, September 2003.
- [109] Hubert Ammann and Nelson Christensen. Delta Kick Cooling: A New Method for Cooling Atoms. *Physical Review Letters*, 78(11):2088–2091, March 1997.
- [110] E. Maréchal, S. Guibal, J.-L. Bossennec, R. Barbé, J.-C. Keller, and O. Gorceix. Longitudinal focusing of an atomic cloud using pulsed magnetic forces. *Physical Review A*, 59(6):4636–4640, June 1999.
- [111] M. Morinaga, I. Bouchoule, J.-C. Karam, and C. Salomon. Manipulation of Motional Quantum States of Neutral Atoms. *Physical Review Letters*, 83(20):4037–4040, November 1999.

- [112] S. Myrskog, J. Fox, H. Moon, J. Kim, and A. Steinberg. Modified δ -kick cooling using magnetic field gradients. *Physical Review A*, 61(5):053412, April 2000.
- [113] Pierre Meystre. *Atom Optics*. Springer-Verlag, New York, 2001.
- [114] Eric Cornell, Chris Monroe, and Carl Wieman. Multiply loaded, ac magnetic trap for neutral atoms. *Physical Review Letters*, 67(18):2439–2442, October 1991.
- [115] David A. Smith, Aidan S. Arnold, Matthew J. Pritchard, and Ifan G. Hughes. Experimental single-impulse magnetic focusing of launched cold atoms. *Journal of Physics B: Atomic, Molecular and Optical Physics*, 41(12):125302, June 2008.
- [116] C. Monroe, W. Swann, H. Robinson, and C. Wieman. Very cold trapped atoms in a vapor cell. *Physical Review Letters*, 65(13):1571–1574, September 1990.
- [117] I. Shvarchuck, Ch. Buggle, D. Petrov, K. Dieckmann, M. Zielonkowski, M. Kemmann, T. Tiecke, W. von Klitzing, G. Shlyapnikov, and J. Walraven. Bose-Einstein Condensation into Nonequilibrium States Studied by Condensate Focusing. *Physical Review Letters*, 89(27):270404, December 2002.
- [118] Juris Kalnins, Jason Amini, and Harvey Gould. Focusing a fountain of neutral cesium atoms with an electrostatic lens triplet. *Physical Review A*, 72(4):043406, October 2005.
- [119] W. J. Engelen, M. A. van der Heijden, D. J. Bakker, E. J. D. Vredenbregt, and O. J. Luiten. High-coherence electron bunches produced by femtosecond photoionization. *Nature Communications*, 4:1693, January 2013.
- [120] B. Dubetsky and M. Kasevich. Atom interferometer as a selective sensor of rotation or gravity. *Physical Review A*, 74(2):023615, August 2006.
- [121] E. Giese, W. Zeller, S. Kleinert, M. Meister, V. Tamma, A. Roura, and W. P. Schleich. The interface of gravity and quantum mechanics illuminated by Wigner phase space. *arXiv:1402.0963v1*, 2014.

- [122] Vladimir Minogin, James Richmond, and Geoffrey Opat. Time-orbiting-potential quadrupole magnetic trap for cold atoms. *Physical Review A*, 58(4):3138–3145, October 1998.
- [123] E. Hodby, G. Hechenblaikner, O. M. Maragò, J. Arlt, S. Hopkins, and C. J. Foot. Bose-Einstein condensation in a stiff TOP trap with adjustable geometry. *Journal of Physics B: Atomic, Molecular and Optical Physics*, 33(19):4087–4094, October 2000.
- [124] Stefan Nimmrichter. *Macroscopic Matter-wave Interferometry*. PhD thesis, 2013.
- [125] E. Schrödinger. Die gegenwärtige Situation in der Quantenmechanik. *Naturwissenschaften*, 23:807–812, 1935.
- [126] M. A. Hohensee, B. Estey, P. Hamilton, A. Zeilinger, and H. Müller. Force-Free Gravitational Redshift: Proposed Gravitational Aharonov-Bohm Experiment. *Phys. Rev. Lett.*, 108(23):230404, June 2012.
- [127] T. Kovachy, P. Asenbaum, C. Overstreet, C. A. Donnelly, S. M. Dickerson, A. Sugarbaker, J. M. Hogan, and M. A. Kasevich. Quantum superposition at the half-metre scale. *Nature*, 528(7583):530–3, December 2015.
- [128] B. Julsgaard, A. Kozhekin, and E. S. Polzik. Experimental long-lived entanglement of two macroscopic objects. *Nature*, 413(September):400–403, 2001.
- [129] A. Aspect, J. Dalibard, and G. Roger. Experimental Test of Bell’s Inequalities Using Time-Varying Analyzers. *Physical Review Letters*, 49(25):1804–1807, 1982.
- [130] M. Giustina et al. Bell violation using entangled photons without the fair-sampling assumption. *Nature*, 497(7448):227–230, May 2013.
- [131] V. Jacques et al. Experimental Realization of Wheelers Delayed-Choice Gedanken Experiment. *Science*, 315(5814):966–968, 2007.

- [132] A. G. Manning, R. I. Khakimov, R. G. Dall, and A. G. Truscott. Wheeler's delayed-choice gedanken experiment with a single atom. *Nature Physics*, 11:539–542, 2015.
- [133] Ch. J. Bordé et al. Observation of optical Ramsey fringes in the $10 \mu\text{m}$ spectral region using a supersonic beam of SF₆. *J. Phys. (Paris)*, 42:C8,15–19, 1981.
- [134] D. W. Keith, C. R. Ekstrom, Q. A. Turchette, and D. E. Pritchard. An Interferometer for Atoms. *Physical Review Letters*, 66(21):2693–2697, 1991.
- [135] M Kasevich and S Chu. Measurement of the Gravitational Acceleration of an Atom with a Light-Pulse Atom Interferometer. *Applied Physics B Photophysics and Laser Chemistry*, 54:321–332, 1992.
- [136] M. Zawisky, M. Baron, R. Loidl, and H. Rauch. Testing the world's largest monolithic perfect crystal neutron interferometer. *Nucl. Instrum. Meth. A*, 481(13):406 – 413, 2002.
- [137] B. Brezger, L. Hackermüller, S. Uttenthaler, J. Petschinka, M. Arndt, and A. Zeilinger. Matter-Wave Interferometer for Large Molecules. *Physical Review Letters*, 88(10):100404, February 2002.
- [138] K.-Y. Chung, S.-w. Chiow, S. Herrmann, S. Chu, and H. Müller. Atom interferometry tests of local Lorentz invariance in gravity and electrodynamics. *Physical Review D*, 80(1):016002, July 2009.
- [139] Sandra Eibenberger, Stefan Gerlich, Markus Arndt, Marcel Mayor, and Jens Tüxen. Matter-wave interference of particles selected from a molecular library with masses exceeding 10,000 amu. *Physical chemistry chemical physics : PCCP*, 15(35):14696–700, September 2013.
- [140] S. Gupta, K. Dieckmann, Z. Hadzibabic, and D. E. Pritchard. Contrast Interferometry using Bose-Einstein Condensates to Measure h/m and α . *Physical Review Letters*, 89(14):140401, September 2002.

- [141] G. T. Foster, J. B. Fixler, J. M. McGuirk, and M. A. Kasevich. Method of phase extraction between coupled atom interferometers using ellipse-specific fitting. *Optics Letters*, 27(11):951–953, 2002.
- [142] L. P. Parazzoli, A. M. Hankin, and G. W. Biedermann. Observation of Free-Space Single-Atom Matter Wave Interference. *Phys. Rev. Lett.*, 109(23):230401, December 2012.
- [143] W. H. Greene. *Econometric Analysis*. Pearson, Boston, 2012.
- [144] M. Zych, F. Costa, I. Pikovski, and C. Brukner. Quantum interferometric visibility as a witness of general relativistic proper time. *Nature communications*, 2:505, January 2011.
- [145] K. Bongs, R. Launay, and M. A. Kasevich. High-order inertial phase shifts for time-domain atom interferometers. *Applied Physics B*, 84(4):599–602, August 2006.
- [146] Christian J. Bordé. Quantum Theory of Atom-Wave Beam Splitters and Application to Multidimensional Atomic Gravito-Inertial Sensors. *General Relativity and Gravitation*, 36(3):475–502, 2004.
- [147] Kathryn Moler, David S. Weiss, Mark Kasevich, and Steven Chu. Theoretical analysis of velocity-selective Raman transitions. *Physical Review A*, 45(1):342–348, 1992.
- [148] M. Büchner, R. Delhuille, A. Miffre, C. Robilliard, J. Vigué, and C. Champañois. Diffraction phases in atom interferometers. *Physical Review A*, 68(1):013607, July 2003.
- [149] Malo Cadoret, Estefania de Mirandes, Pierre Cladé, Saïda Guellati-Khélifa, Catherine Schwob, François Nez, Lucile Julien, and François Biraben. Combination of Bloch oscillations with a Ramsey-Bordé interferometer: new determination of the fine structure constant. *Physical review letters*, 101(23):230801, December 2008.

- [150] A. Wicht, E. Sarajlic, J. M. Hensley, and S. Chu. Phase shifts in precision atom interferometry due to the localization of atoms and optical fields. *Physical Review A*, 72(2):023602, August 2005.
- [151] T. Kovachy. *Optical Lattices in Atom Interferometry: An Analytical Treatment and Proposal of Applications*. Senior thesis, Harvard University, 2009.
- [152] Vladimir S. Malinovsky and Paul R. Berman. Momentum transfer using chirped standing-wave fields: Bragg scattering. *Physical Review A*, 68(2):023610, August 2003.
- [153] D. J. Griffiths. *Introduction to Quantum Mechanics*. Pearson Education, Upper Saddle River, NJ, 2005.
- [154] R. P. Feynman and A. R. Hibbs. *Quantum Mechanics and Path Integrals*. McGraw-Hill, New York, 1965.
- [155] C. Antoine. Matter wave beam splitters in gravito-inertial and trapping potentials: generalized ttt scheme for atom interferometry. *Applied Physics B*, 84(4):585–597, July 2006.
- [156] H. Müller, S.-W. Chiow, Q. Long, C. Vo, and S. Chu. A new photon recoil experiment: towards a determination of the fine structure constant. *Applied Physics B*, 84(4):633–642, July 2006.
- [157] John K. Stockton, Xinan Wu, and Mark A. Kasevich. Bayesian estimation of differential interferometer phase. *Physical Review A*, 76(3):033613, September 2007.
- [158] Nima Arkani-Hamed, Savas Dimopoulos, and Gia Dvali. The hierarchy problem and new dimensions at a millimeter. *Physics Letters B*, 429:263–272, 1998.
- [159] Asimina Arvanitaki, Savas Dimopoulos, Andrew A. Geraci, Jason Hogan, and Mark Kasevich. How to test atom and neutron neutrality with atom interferometry. *Physical review letters*, 100(12):120407, March 2008.

- [160] C. S. Unnikrishnan and G. T. Gillies. The electrical neutrality of atoms and of bulk matter. *Metrologia*, 41(5):S125, 2004.
- [161] D. Lunney. Nuclear Masses: Experimental programs, theoretical models and astrophysical interest. In N. Prantzos and S. Harissopoulos, editors, *Nuclei in the Cosmos V*, pages 296–302, Paris, 1998. Editions Frontieres.
- [162] Frances Hess. *Earth Science*. McGraw-Hill, New York, 2002.
- [163] R. Hide and J. O. Dickey. Earth’s variable rotation. *Science*, 253(5020).
- [164] James G. Williams, Slava G. Turyshev, and Dale H. Boggs. Progress in lunar laser ranging tests of relativistic gravity. *Phys. Rev. Lett.*, 93:261101, Dec 2004.
- [165] S. Schlamminger, K.-Y. Choi, T. A. Wagner, J. H. Gundlach, and E. G. Adelberger. Test of the equivalence principle using a rotating torsion balance. *Phys. Rev. Lett.*, 100:041101, Jan 2008.
- [166] Lin Zhou, Shitong Long, Biao Tang, Xi Chen, Fen Gao, Wencui Peng, Weitao Duan, Jiaqi Zhong, Zongyuan Xiong, Jin Wang, Yuanzhong Zhang, and Ming-sheng Zhan. Test of Equivalence Principle at 10^{-8} Level by a Dual-Species Double-Diffraction Raman Atom Interferometer. *Physical Review Letters*, 115(1):013004, July 2015.
- [167] A. Roura. Circumventing Heisenberg’s uncertainty principle in atom interferometry tests of the equivalence principle. *arXiv:1509.08098v1*, 2015.